RESIDUAL STRESS CHARACTERISATION IN FORGINGS FOR AERO-ENGINE APPLICATION

A thesis submitted to The University of Manchester for the degree of

Doctor of Engineering

in Faculty of Engineering and Physical Sciences

2013

James Rolph

School of Materials

Table of contents

List of Figures

List of Tables

Abstract

Residual stresses are the stresses which are present within a component without any external load. They can be introduced through any number of manufacturing processes and in-service conditions, meaning that they are almost ubiquitous in engineering components. The characterisation of residual stress is an important field of research particularly in an engineering context since the effects of residual stress sum with the loads. As a result, the performance of a component can be greatly enhanced, or significantly reduced, by the presence of residual stress depending on the sign of the stress and the applied load.

In this EngD thesis the focus has been on the development of residual stress through the manufacturing processes of aero-engine forgings, specifically the turbine disc. The forgings studied were sub-scale geometries of the disc, forged from the nickel-base superalloy RR1000. The overall aim of this work is to improve the understanding of the residual stress generation and relaxation through implementation of advanced experimental characterisation techniques, with a view to improving current stress predicting process modelling capabilities. With this in mind the work has focussed on the use of neutron diffraction and the contour method to characterise residual stress experimentally, while residual stress predictions have been made using finite element modelling.

The findings of this research indicated that very large residual stresses were generated as a result of the quenching process, and that these stresses were then relaxed and redistributed by ageing heat treatments and material removal by machining. The results obtained through the two experimental techniques exhibited very strong agreement, indicated a robust experimental process. Comparisons to the finite element predictions highlighted some issues with the current model; in particular it was found that the simulation of quenching could be improved by better definition of the heat transfer at the surface. Furthermore, the level of stress relaxation during ageing was consistently over predicted in the model. This result is thought to be the result of an over-prediction of the level primary creep in the alloy. Subsequent studies will investigate this behaviour further using the newly developed in-situ heat treatment capabilities which have developed as part of this research.

Declaration

No portion of the work referred to in the thesis has been submitted in support of an application for another degree or qualification of this or any other university or other institute of learning

Copyright Statement

Acknowledgements

Chapter 1

Introduction

This EngD project is focussed on furthering the understanding of residual stress generation and evolution through the manufacturing processes of aerospace forgings. As such, this section aims to contextualise the work in terms of the significance of residual stress to aero-engine components, and the ways in which they can occur during manufacture. As a research project of commercial relevance, the following sections also aim to illustrate the motivation of this work with regard to the industrial sponsor, Rolls-Royce Plc. The structure of the thesis is also outlined here for the benefit of the reader.

1.1 Background

1.1.1 Residual Stress

Residual stresses are, by definition, the stresses, which remain within a material without any external forces or load. Since they are internal to the component, they are often not apparent externally and are therefore difficult to account for. They are also highly prolific, being present in almost all engineering components as a result of any number of manufacturing processes and/or service conditions. However, from a theoretical point of view, the origin of residual stress can be thought of simply in terms of a misfit between neighbouring regions of material. This can occur as a result of three distinct mechanisms (1):

1. Thermal gradients. In heating or cooling a material it is expected that thermal expansion or contraction will result in a volumetric change of the material. If this occurs at different rates, or to different extents within a component, a thermal gradient is setup which leads to the generation of strain. Given a sufficiently high level of strain, the material will deform plastically with the result that once all thermal processing has ceased, a residual strain (and hence stress) will remain. One way in which this can occur is quenching. The rapid cooling process causes the outer regions to cool ahead of the interior. This sets up thermal gradients which ultimately cause plasticity at the surface and the generation of residual stress (2).

2. Plastic deformation. When sufficient load is applied to a component, e.g. a bending moment on a beam, some regions will deform plastically while others are far enough away from the load point to remain elastic. Upon removal of the load, the elastic regions will attempt to relax back to a zero stress state but will be constrained by the regions adjacent to it, which were deformed plastically. The results in a residual stress induced by a localised plastic deformation. One beneficial use of plastically induced residual stress is that created by shot peening. The surface of a component is bombarded by small round 'shots', which plastically deform the surface layer to generate a compressive surface that helps to resist the initiation of surface cracking (3).

3. Chemical misfit. In certain alloys it is possible for a phase transformation to bring about a volumetric increase/decrease at a particular temperature. If this occurs in a localised manner there will be a misfit generated around that region and strain will result. One example of this would be the process of welding in Martensitic steel. The high temperatures within the weld pool and the heat affected zone (HAZ) are sufficient to cause localised phase transformations which bring about a change in volume, and therefore generate strain (4). It is also possible for compositional changes within a phase to create misfit, typical examples of which are nitriding and carburising. During this process diffusion of Nitrogen and Carbon atoms at the surface bring about a localised volume change and hence a strain hardening effect.

Irrespective of origin, residual stress has a direct impact on mechanical performance since it sums with the applied load. In plastically deformable materials the combined residual and applied stress field determines the yield point, as such the residual stress state can retard or accelerate the onset of plastic deformation. The fact that the residual stress sums with the load means that it can be of significant benefit or detriment to the mechanical performance depending on the sign of the residual stress and the applied load. Under tensile load, tensile residual stresses in particular are generally perceived as having a detrimental affect on component life since they accelerate the initiation of cracks around defects and the growth of existing cracks. Conversely, compressive stress resists the initiation of cracks and helps to slow the rate of crack propagation (5).

1.1.2 Manufacture of Aero-space Forgings

In this project the focus has been on the manufacture of the turbine disc, which is forged using polycrystalline Nickel-base Superalloy. This group of alloys represents one of the most compositionally complex materials ever developed, and the manufacturing process is a reflection of this. While almost every manufacturing stage will in some way impact the residual stress, the forging process and the processes which follow are the most significant. Without going into substantial detail over each process, it is possible make generalisations to understand the implications with regard to residual stress.

In the context of aero-space components, forging is typically used to make near net geometries from the raw billet without compromising the microstructure. Since this requires exceptionally large amounts of plastic deformation it is not unsurprising that large strains and residual stresses can result. However, the forging process is often made in a number of stages to gradually bring the component to the final shape, which reduces the strain rate and hence lowers the total residual stress.

Following forging, the near net shape component is typically exposed to a sequence of heat treatment processes. This will usually involve a high temperature heat treatment (>1000°C in Ni Superalloy) to solutionise particular alloying elements, before a rapid quench to trap the desired microstructure. Further 'fine tuning' of the microstructure is made by ageing heat treatments, which hold the alloy at a lower temperature for a specified time to enable elemental diffusion to occur between the various phases. In terms of residual stress, the quenching from high temperature generates thermal gradients which if large enough generate residual stress. The subsequent ageing process will typically partially relax the quenching stresses by enabling creep processes to occur.

Upon completion of the microstructural optimisation, the only process, which remains is that of machining to obtain the final high tolerance component geometry. The machining process removes regions of material to achieve the desired geometry, however the material removed will contain residual stresses generated during prior processing. Since residual stresses balance across any single component, the removal of a region of stress requires the remaining stresses to re-balance to maintain equilibrium, this occurs as a distortion of the part.

1.2   Motivation and Commercial Relevance

The motivation for improving the understanding of residual stress in aero-engine components can be considered separately in terms the manufacturing processes and the in-service performance.

1.2.1 Manufacturing

As outlined in the previous section, the manufacturing processes are known to generate and redistribute residual stresses at various stages of manufacture. In the later stages of manufacture, the component is machined down to the fine tolerance of the finished part. The removal of material presents a problem however, since removal of a stressed region requires the remaining residual stresses to rebalance. This occurs via a distortion of the part. Turbine manufacturers accept the fact that this distortion is unavoidable, and so instead attempt to machine areas of the disc in a such a way as to achieve zero net distortion. In order to do this it is crucial to have an accurate knowledge of the residual stress state immediately prior to machining. Practically this cannot be achieved through measurement of every component. Therefore, this knowledge is based on a process model. The model aims to simulate all of the prior processing which contributed to the residual stress state, i.e. quenching and ageing, and then use to predict the stresses of the part to be machined. Similarly, the model can be used to trial different combinations of material removal across the part to come up with a solution to give zero net distortion.

The commercial benefit to having an accurate prediction of the residual stress through manufacture is therefore clear. Processes can be tailored to take residual stress into account and thereby reduce the tendency for components to be machined out of tolerance. However, this approach relies on the model being an accurate representation of the manufacturing processes; to ensure that this is the case it is important for the predictions to be validated through experimental results. Traditionally validations were made using techniques such as x-ray diffraction and hole drilling, but such techniques are only capable of very near surface measurement, thereby leaving the bulk stresses an unknown quantity. The experimental techniques employed in this study, namely, neutron diffraction and the contour method, offer a significant advantage in this respect since they are capable of measurement deep within the bulk. The data generated in this study is therefore a means to carry out

more thorough validation of the process model and ultimately improve the knowledge of residual stress development through manufacture.

1.2.2 In-service Performance

Aero-engine manufacturers are constantly looking to improve the power output and efficiency of their gas turbines. It can be shown that the efficiency of a gas turbine is directly related to the maximum difference in gas temperature across the entire engine (6). Therefore engine designers seeking to improve the efficiency often look to increase the peak gas temperature, also known as the turbine entry temperature (TET). By designing engines to operate at higher temperatures, the loading on components such as the turbine disc and blades is increased. As stated previously, the residual stress sums with the loading stress and as such has a direct impact on the performance of the component. If the residual stress is not known with great confidence then any new design must be over-engineered to have a large safety margin as a contingency for the possibility of significant residual stress. The alternative to this would mean risking the failure of a component, which is obviously not an option.

As was the case with manufacture, the residual stress with regard to in-service performance is taken into account as part of a model. The model in this case also includes the thermal loading and stress experienced by each component during service in order to determine the operating parameters of the engine, and the total service life of individual components. It is therefore clear that if the residual stress after manufacture can be predicted with greater accuracy, then it is possible to optimise the design further and take advantage of the additional loading capacity of the component. Furthermore, accurate residual stress predictions can be fed into lifing models, and thereby increase the time spent in the air as opposed to in the workshop being maintained. However, in order for the residual stress predictions to be accurate it is necessary for the results to be validated and optimised through studies such as this. Only by carrying out experimental validations can the confidence in the modelled results be increased and the prospective commercial benefits of more fuel efficient designs, and increased service intervals be made a reality.

1.3 Aims and Objectives

The origins and effects of residual stress has long been acknowledged by both academic and industrial parties. However, the development of new techniques and

robust methodologies to characterise residual stress has largely been the remit of academic and scientific interest. While their cannot be doubt that a deeper understanding of residual stress is beneficial to industry, the difficulty in quantifying residual stress reliably often leads to components simply being over-engineered to compensate for the difficulty in characterising residual stress.

This research project sits strategically between the academic and industrial interest. The broad aim of this project is to apply new and developing stress characterisation techniques to industrial problems, in this case that of gas turbine manufacturing processes. Specifically, the objectives of this project are as follows:

- To characterise bulk residual stress in Nickel Superalloy turbine discs using the latest available techniques and demonstrate the robustness of such measurements for validation of finite element models.
- To develop the existing techniques for future studies, in particular the technique of in-situ measurement of stress relief during ageing.
- To monitor the development of residual stress through manufacture, specifically levels of stress generated during quenching and the extent to which they relax and redistribute during subsequent ageing and machining operations.
- To validate the current finite element predictions using the experimental data, and identify and investigate any shortcomings in the current predictions.

1.4 The EngD Scheme

The Engineering Doctorate (EngD) is a postgraduate research degree with an industrial focus. The research content forms the same scientific depth as a traditional PhD, but with a topic, which is suited to an industrial partner. The EngD scheme was introduced by the UK Engineering and Physical Sciences Research Council (EPSRC) in the early 1990's to address the need for PhD level graduates with an awareness of the industrial and commercial implications of their research. With this in mind, the EngD typically lasts four years, which allows 3 years for completion of the research, and a further year for taught content and personal development aimed at improving commercial and industrial awareness.

For this project concerning the development of residual stress in aero-space forgings, the industrial partner was Rolls-Royce plc. There was also considerable input and

involvement from the US forging company ATI Ladish, and Rolls-Royce Corporation (US). As a company, Rolls-Royce needs very little introduction being steeped in such a long history in the aerospace (and automotive) industry as to be a household name. In the present day, the organisation has four primary business interests in the gas turbine industry, namely, civil and defence aerospace, marine propulsion, and energy generation. This project is based solely within the remit of the civil aerospace sector; a sector in which Rolls-Royce is currently the second largest producer of gas turbines world-wide. The headquarters for Rolls-Royce UK are located in Derby, they serve as a hub for the commercial aspects of the organisation, as well as housing large facilities for manufacturing, development and testing.

1.5   Structure of Thesis

This thesis differs from the traditional format, in that it has been submitted in the so called 'alternative format' or paper-based format. The alternative format contains all of the usual chapters of a traditional thesis such as a literature review, experimental methods and conclusions, but differs by reporting the technical content in the form of scientific papers. The papers themselves have either been published, and hence have already been peer reviewed, or have been prepared in a format ready to be published.

The reason for choosing this format is that much of the experimental work carried out in this study was made using neutron diffraction instruments at large research facilities. Specifically; SALSA, at the Institut Laue Langevin (ILL), Grenoble, France; STRESS-SPEC at the FRM-II, Munich, Germany; and ENGIN-X at ISIS, Oxford, UK. At such facilities there is a strong emphasis on publishing the findings from each experiment in order to advance the field of research and enable continual funding and development of the facilities. This being the case, it was deemed important that the work carried out was published in the public domain, which makes this project ideally suited to the alternative format. Following this introduction (Chapter 1) this thesis is structured as follows.

Chapter 2 covers all aspects of the literature relevant to the field of residual stress characterisation and of Nickel-based superalloys. It also considers the manufacturing processes for a Nickel-based superalloy turbine disc with regard to the generation of residual stress.

Chapter 3 describes the experimental methods implemented as part of this study with reference to some prior work where necessary.

Chapters 4-9 comprises the technical chapters, which in this case relates to individual publications. While each of the papers had to be written in such a way as to be understood as a single document, there is a an overriding theme to each paper which allows them to be placed into a logical order:

- Chapters 4-5 concern the development of techniques. Chapter 4 covers the issue of d_0 characterisation for diffraction based strain measurement. Chapter 5 describes the development of a novel in-situ heat treatment setup to allow the relaxation of stresses during ageing to be measured directly. This paper has been published in the journal - Comptus Rendus Physique – as an invited paper.

- Chapters 6 and 7 look into the residual stress development through heat treatment. This was split into two parts; Chapter 6 looked into the process of quenching while Chapter 7 considered the subsequent ageing processes. Both chapters also include comparisons to current finite modelling efforts of the same processes.

- Chapter 8 builds on the work carried out in chapter 5 to extract further data from the in-situ heat treatments and make comparisons to models set up to simulate the same heat treatment processes

- Chapter 9 takes a broader look at the manufacturing process as a whole, documenting the evolution of residual stress on a larger disc taken through the stages of quenching, ageing and machining. This paper has been published as part of the peer reviewed proceedings of TMS Superalloys 2012.

Since each publication is written to be understood as a stand-alone document it should be noted that a degree of repetition across the publications is unavoidable where similar techniques have been employed.

Chapter 10 begins by summarising each of the publications and it draws upon all of the findings to form a set of technical conclusions. Following on from this, the conclusions are discussed in a commercial context and recommendations for future work are made.

Chapter 2

Literature Review and Background

This literature review aims to give the reader an overview into each of the topics covered, while highlighting relevant aspects of the large volume of prior work which has lead up to this research being carried out. Of particular importance are the origins and consequences of residual stress and the means by which it can be characterised. A considerable focus will also be Nickel-base superalloys, particularly their development within the aerospace industry, the manufacturing processes, and the significance of residual stress during manufacture and service life.

2.1 Residual Stress

2.1.1 Origins and Effects

Residual stresses are defined as the stresses which remain in a material without an applied force while at constant temperature. In a condition of no external force the material is in equilibrium, as a result residual stresses are always balanced across a single component (7).

Residual stresses can be found in three variations which are distinguishable by the length scales over which they balance (Figure 1). Type I stress, also termed macrostress, balance over the largest length scale, which is that of the component geometry. In a polycrystalline material they are assumed to remain continuous from one grain to the next. The combination of a number of grains creates a long-range misfit, which generates the macrostress (8).

Type II stresses balance over a smaller length scale, that of the order of the individual grain size. They are homogeneous for each grain, but discontinuous across neighbouring grains, the stress originates from misfits between each grain. Polycrystalline materials are particularly prone to developing type II stresses due to the thermal anisotropy of the crystal structure. This effect combined with mis-orientated grains gives differing thermal expansion in any particular direction between neighbouring grains, creating stress (8).

Type III stresses are created by dislocations, interstitial atoms, vacancies in the lattice, or any other discontinuity in the material. As a result they balance on a scale smaller than that of an individual grain and act in a localised field. Together type II and type III stresses are termed microstress (8).
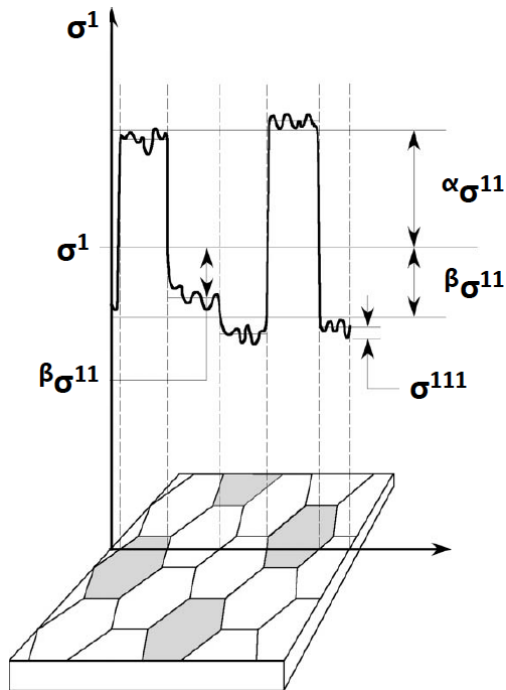
Figure 1: A schematic illustration of type I, II and III residual stress. Equilibrium occurs over the scale of the component for type I, a single grain for type II and within a localised field in type III. (1).

The residual stress state of a material at any particular point is the superposition of all three types of stress. However for large engineering components, the macroscopic stress is most frequently considered to have the greatest affect on the performance of the bulk material (8, 9).

Residual stress is generated through any combination of three distinct mechanisms. The first of these is inhomogeneous thermal conditioning. This involves heating or cooling of a part in a non-homogeneous manner such that the different levels thermal expansion/contraction creates residual stress within a part. A typical example of this is quenching, rapid cooling of the surface around a still hot core results in plastic strain and on final equilibrium a residual stress (10). The second mechanism is plastic deformation, processes such as forging, drawing, rolling, which permanently deform the material, result in induced residual stress (11). The third and final mechanism is volumetric phase change, a process whereby strain is generated as a material

undergoes a phase change which brings with it an increase or decrease in volume (11). A typical example of this is the martensitic phase transformation in steel (12).

The effect of residual stress on the material performance can be either detrimental or beneficial depending on the sign of the stress and the component loading and environment. The primary reason for this is that the residual stress adds directly to the loading stress in service; therefore it can either reduce total stress by partially cancelling the load, or increase total stress by adding further to the load (8). One well established example of beneficial residual stress is that resulting from mechanical surface treatments such as shot peening. The process of shot peening creates a thin layer of compressive residual stress which counteracts crack initiation and growth at the surface and doing so improves fatigue life and damage tolerance (13). In contrast to this, the effect of tensile stress would be to reduce fatigue life by adding to the applied load and promoting the initiation and growth of cracks (5).

Given the effects of residual stress on component performance it is clear that in order to accurately predict the service life of a component it is necessary to know both the applied load and the residual stress state. Whilst it is relatively easy to calculate the applied load on a component, the level of residual stress remains hidden and difficult to quantify (14). Therefore in order to make accurate lifing predictions it is necessary to carry out residual stress characterisations either through measurement or simulation.

2.1.2 Residual Stress Characterisation

In the following sections the means by which residual stress can be characterised in engineering materials will be discussed with reference to prior investigations of a similar nature. As highlighted in the previous section, it is the macrostress which is of primary concern in terms of material performance. It is therefore also the focus of this review in terms of characterisation.

What follows is an overview of the more widely used techniques available for characterisation; a specific and detailed account of the techniques employed in this investigation has been provided in the experimental methods chapter (Chapter 3). The techniques discussed have been broken down into three categories, non-destructive techniques, destructive techniques, and simulation.

2.1.2.1 **Non-destructive techniques**

Non-destructive techniques are those which are capable of residual stress characterisation without disrupting the component. In practice these are most commonly the diffraction based techniques, although there are others including the ultrasonic (15) and magnetostriction (16) techniques which can be employed in some instances. It should be noted that diffraction techniques often require a coupon machined out of the component as a stress free reference, making them not truly non-destructive in some instances.

2.1.2.1.1 Diffraction theory for measurement of strain

It is not possible to directly measure the stress in a material; first the strain has to be measured and then the value of stress can be calculated from this. The principle means by which strain is measured in diffraction techniques is to use the crystal lattice as a three-dimensional strain gauge. The strain in the lattice is calculated as a change in length of the inter-planar distance d^{hkl} where *hkl* are the Miller indices of a particular crystallographic plane. The relationship between the lattice strain in a direction (ϕ,ψ) and the inter-planar distance $d^{hkl}(\phi,\psi)$ of planes orientated normal to the same direction, is given by the following expression. (17, 18)

$$\varepsilon_{\phi\psi} = [d^{hkl}(\phi,\psi) - d_0^{hkl}]/d_0^{hkl} \tag{1}$$

The value of d is obtained through measuring the angle (2θ) of peak intensity of diffracted x-rays (or neutrons). The process of diffraction is illustrated in Figure 2
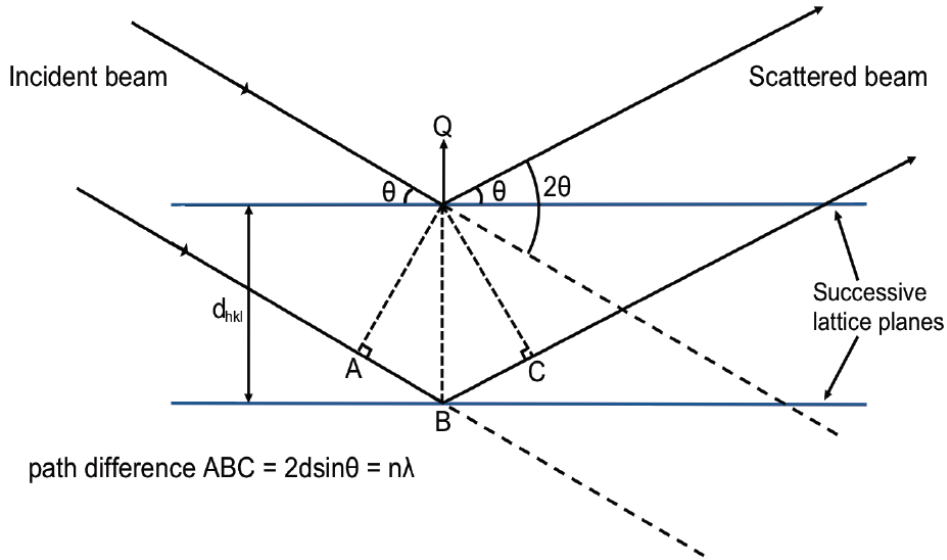
Figure 2: Atomic lattice planes as a strain gauge. Q represents the scattering vector, 2θ the diffraction angle, and d_{hkl} the inter-planar spacing. Adapted from (18).

From Figure 2 it can be seen that the path difference can be related directly to the lattice spacing. Bragg's law states that the path length difference must be in integer number of wavelengths in order for constructive interference to occur, all path lengths which are not an integer number of wavelengths will bring about destructive interference. In other words, diffraction will only be observed when the path length difference is equal to nλ. Mathematically this can be expressed in Bragg's law

$$n\lambda = 2dsin\theta \tag{2}$$

Where λ is the wavelength of the incident radiation, and θ is the incident angle. Therefore for a given λ there will be an angle θ which allow diffraction to be observed as a peak in intensity. By measuring the diffraction angle θ, it is a trivial step to deduce the inter-planar spacing, d^{hkl}. (19).

It should be noted that obtaining d^{hkl} alone is not sufficient to calculate strain. From equation 2 it can be seen that d_0 – the strain free lattice spacing – is also required. A variety of methods exist for determining d_0, each of which are discussed in later sections. In principle a d_0 value can also be obtained through diffraction in the same manner described, the only stipulation being that the portion of lattice measured is free from strain.

In the final step, stress is calculated from the measured strain. To fully characterise the stress in a homogeneous, isotropic sample requires strain measurement in three

orthogonal directions, (σ_x σ_y σ_z), as well as six shear directions (τ_{yx} τ_{zx} τ_{xy} τ_{zy} τ_{xz} τ_{yz}), which gives the full stress tensor. However (τ_{ij}) and (τ_{ji}) are not independent of each other; from rotational invariance it can be deduced that they are equal in magnitude and direction, as such, only three measurements are required to quantify the shear stress. Furthermore, it is possible in most engineering components to deduce the principle directions from symmetry considerations. It is possible to calculate the stress by measuring strain in three orthogonal principal directions in combination with the following relation (8, 20),

$$\sigma_x = \frac{E_{hkl}}{(1+v_{hkl})(1-2v_{hkl})}\left[(1-v_{hkl})\varepsilon_x + v_{hkl}(\varepsilon_y + \varepsilon_z)\right] \text{ and } \sigma_y = \cdots \qquad (3)$$

Where E and v represent the elastic constants of the material. Note that E and v are specific to the lattice plane for a d-spacing measurement, but may represent the bulk properties if strain has been calculated through the change in lattice parameter. When measuring d-spacing, the choice of lattice plane must be made with the following considerations

The chosen diffraction plane should have a high multiplicity; in terms of diffraction this means that a large number of grains are contributing to the diffracted intensity, as such it provides a strong peak to background ratio and therefore a low uncertainty in the observable peak shift. In addition, given the available wavelengths of an instrument, a lattice plane must be selected such that the diffraction angle is appropriate for the measurement. This includes consideration of possible texture, as well as picking a lattice plane which diffracts at close to 90° if a cubic gauge volume is desired.

Furthermore, a lattice plane must be chosen which has an elastic response representative of the bulk material, and which is not sensitive to the effects of plastic deformation. Specifically, the stress-strain response of the chosen lattice plane must be as close to linear as possible even when the material has plastically deformed. In this way, stress can be calculated from the measured strain using an appropriate diffraction elastic constant (DEC). However, for the stress-strain response to remain linear when plastic deformation has occurred it is necessary to chose a lattice plane which does not accumulate type-II (intergranular) stress. Studies have been made to characterise the lattice plane responses under load and thus make recommendations as to which plane to choose for accurate macrostress measurement (21) and (22). In

Nickel-base superalloy it is widely accepted that the best hkl lattice planes for strain measurement are the (111) and (311), and that the (220) plane should be avoided (23).

2.1.2.1.2 Laboratory x-rays

Laboratory x-rays are produced by accelerating electrons at a target, also known as an x-ray tube. The scattering of the electrons with the target causes two things, firstly the emission of Bremsstrahlung, and secondly the emission of characteristic x-rays. The Bremsstrahlung is a spectrum of photon energies emitted as electrons are decelerated to varying extents within the target, it is thus a continuous spectrum. The characteristic x-rays are caused by the incoming electron colliding with a bound electron in the lowest electron orbit (K-shell) and ejecting it, thus creating a vacancy. As the vacancy is filled by an electron from the next most outer orbit (L-shell) a photon is emitted which is of characteristic wavelength to the target material. It therefore appears on the spectrum as a sharp spike, known as the Kα line. By applying filters to the emitted spectrum from the x-ray tube it is possible to remove the Bremsstrahlung and select only the Kα emission to generate a monochromatic x-ray beam (18). The x-rays produced in this way typically have a wavelength less than 0.1nm, or energies less than 10keV.

One of the issues with diffracting laboratory x-rays is that the method used to generate them does not result in a perfectly monochromatic beam, meaning that there is small range of wavelengths either side of the characteristic wavelength. As a result of this, the diffraction peaks produced through laboratory x-rays measurements are broadened. To minimise the effect of this, it is recommended that a higher order diffraction plane is selected when carrying out a diffraction measurement, i.e. the largest value of 2θ that is convenient to measure (18).

Laboratory x-rays scatter off of the electron cloud. As a result, the scattering interaction increases with atomic number (Z) and hence increased electron density around the nucleus. The penetration of x-rays into a material can therefore be correlated directly to the atomic number of the material (Figure 4) (17). In most engineering materials lab x-ray penetration is of the order of tens of microns which restricts strain measurement to the surface. This in itself is not necessarily a disadvantage since stress characterisation can be made at the surface using the $\sin^2\psi$ technique (18, 24). Using this approach, the plane stress condition at the surface

enables the direct measurement of the in-plane stresses with out the need to obtain a value for d_0. The methodology is as follows:

In a bi-axial stress condition the stress-strain relation for a diffraction measurement can be written as follows (9).

$$\varepsilon_{\phi\psi} = \frac{d_{\phi\psi} - d_0}{d_0} = \left(\frac{1}{2}\right)S_2\sigma_\phi \sin^2\psi + S_1(\sigma_{11} + \sigma_{22}) \tag{4}$$

Where S_1 and S_2 are the diffraction elastic constants, ϕ represents the in-plane angle, and ψ the surface tilt. Rearrangement of equation 4 allows d to be made the subject.

$$[d_{\phi\psi}] = \left[d_0\left(\frac{1}{2}\right)S_2\sigma_\phi\right]\sin^2\psi + [d_0 S_1(\sigma_{11} + \sigma_{22}) + d_0]$$

$$[Y] \quad = [\qquad m \qquad] \, x \quad + [\qquad c \qquad] \tag{5}$$

From the form of the above equation it can be seen that a plot of d vs. $\sin^2\psi$ will have a gradient which is directly related to the in plane stress. A further rearrangement produces the following relation which allows the calculation of the in plane stress.

$$\sigma_\phi = \frac{2}{S_2} \cdot \frac{1}{d_0}\left(\frac{\delta d_{\phi\psi}}{\delta \sin^2\psi}\right) \tag{6}$$

Although this relation is still dependant on d_0 it can be assumed that d_0 is equal to the measured d-spacing d^{hkl}, as the difference is small enough to create negligible error in the value of stress. It should also be noted that equation 6 is independent of the value of ϕ. Therefore it is not necessary to have any knowledge of the principal axis to calculate the stress (8, 18).

Application of the $\sin^2\psi$ technique is well established, successful studies have been made on a variety of materials including, steels (25), titanium alloys (26), nickel-base superalloys (27) and assorted coatings (28).

2.1.2.1.3 Hard x-rays

Hard x-rays, also known as synchrotron x-rays are those which have an energy of 20-300keV. Synchrotron x-rays are produced at very short wavelengths, this has the advantage of increased energy and therefore penetration into engineering materials. Furthermore they have a flux up to a million times greater than lab x-rays which means that acquisition times as low as one second are achievable. However, the disadvantage of such short wavelengths is that diffraction occurs at very low angles of incidence. Therefore at very high x-ray energies the diffracting gauge volume is

elongated in the plane perpendicular to the scattering vector, which reduces the spatial resolution in this direction. The low scattering angle can also lead to prohibitively large path lengths in large components when measuring strain in two or more orthogonal directions.

The x-rays generated at a synchrotron are a white beam, i.e. a continuous spectrum inclusive of all wavelengths. Therefore the user is presented with the choice of either diffracting all wavelengths, or using a monochromator to select a single wavelength. When using a single wavelength, strain is measured through a $\theta/2\theta$ scan (Figure 3) to capture the peak shift and hence change in lattice spacing (24). When diffracting all wavelengths an energy dispersive spectrum can be captured (Figure 3), each intensity peak representing an *hkl* lattice plane. Strain can either be determined on multiple lattice planes, or the entire spectrum can by used in a refinement process to deduce the lattice parameter (29). Owing to the low diffraction angle, a third option of low angle transmission is available to the user (Figure 3). In this arrangement diffraction rings are captured which enables strain to be measured as a radial shift in the diffraction ring (24).
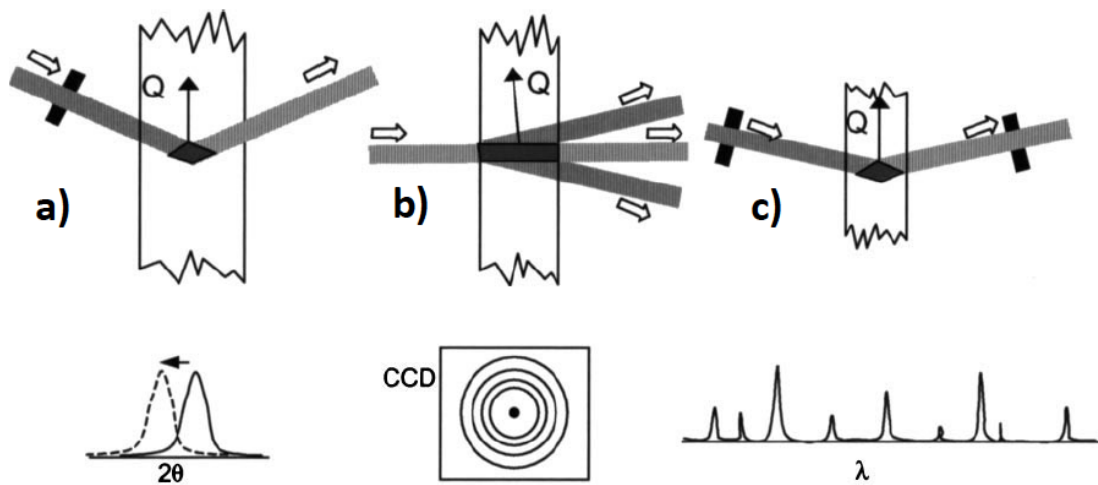
Figure 3: Synchrotron x-ray setups; a) 2θ scanning, b) low angle transmission and c) energy dispersive (14).

2.1.2.1.4 Neutrons

In terms of diffraction, neutrons differ significantly from x-rays since they scatter off the atomic nuclei as opposed to the electron cloud. As a result of this, the scattering properties for different materials does not increase monotonically with atomic number (Z), as was the case with x-rays. In fact the scattering properties of two atoms in

sequence (i.e. Z and Z+1), can be very different, this is illustrated in Figure 4, with a comparison to the x-ray scattering behaviour.
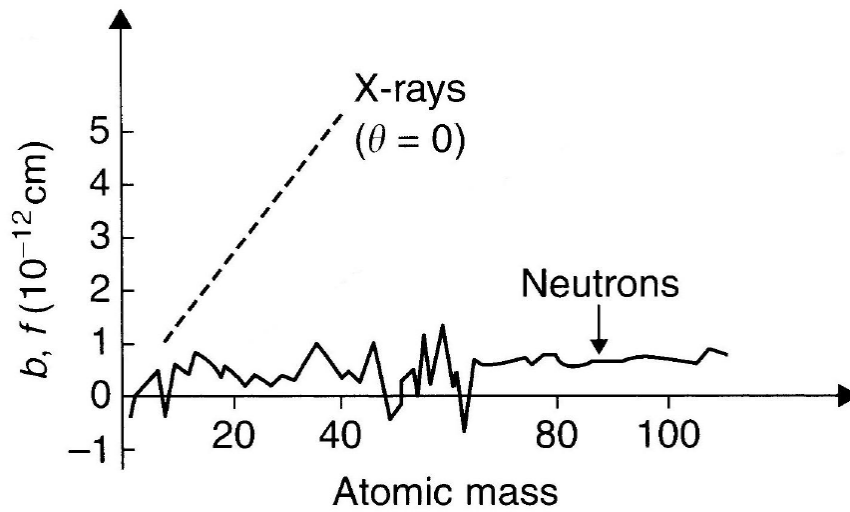
Figure 4: Neutron and x-ray scattering interactions with atomic mass (17)

As the trend in Figure 4 shows, the neutron scattering length can have positive and negative values; while materials such as Fe, Al, Ni and Zr have positive values and hence scatter well, others like Ti, H, and Mn have negative values and scatter poorly. Alloys containing appreciable quantities of poor neutron scatterers will require additional time to achieve a strong diffraction signal.

The trends shown in Figure 4 also highlight another difference in scattering behaviour; that the probability of a scattering interaction is much lower in neutrons in comparison to x-rays. As a result of this, the typical penetration depth into most engineering materials using neutrons is of the order of cm as opposed to μm using laboratory x-rays (8). A comparison between the typical penetration depths for laboratory and synchrotron x-rays as well as neutrons has been given in Table 1.

Table 1: Typical attenuation lengths for x-rays and neutrons in common engineering materials. Adapted from (8)

Measurement technique		Attenuation length (mm) for 63.2% intensity decrease			
	Typical λ (Å)	Al	Ti	Fe	Ni
Lab x-ray (Cu Kα)	1.54	0.076	0.011	0.004	0.023
Synchrotron x-ray	0.08	39	14	7	5
Thermal neutrons	1.8	96	17	8.3	4.8

The process of strain measurement through neutron diffraction depends on the neutron source, which can be either a constant flux reactor, or a pulsed spallation

source. A strain scanning instrument on a reactor source uses a monochromator crystal to select a single wavelength of neutron to diffraction. As such they are well suited to diffracting from a single *hkl* lattice plane in order to measure strain as a shift in line profile of a single reflection.

A pulsed source contrasts significantly from a reactor since it uses a white spectrum of neutrons, i.e. all wavelengths, and measures strain in the so called time of flight (TOF) setup. This approach uses a fixed diffraction angle (usually 90°) and measures the time of flight from source to detector to calculate the neutron energy and hence wavelength. Since all wavelengths are used, the TOF spectrum is a sequence of peaks generated from each hkl lattice plane when the wavelength satisfies Bragg's law at $2\theta=90°$. For a chosen peak, strain can be observed as shift in the time of flight, hence strain is calculable as $\varepsilon= \Delta t/t$.

Each neutron diffraction setup has its advantages depending on the nature of the measurement. A reactor source is well suited to the characterisation of macrostress providing that a single reflection can be chosen which accurately represents the bulk behaviour

In contrast to this, the TOF setup measures multiple lattice planes simultaneously, it is therefore well suited to measuring strain in multiphase or composite materials, and materials in which intergranular stress is to be characterised. Measurement of multiple lattice planes also enables the determination of the lattice parameter through a Rietveld refinement (30). The Rietveld refinement fits the entire spectrum but with a weighting on reflections which are known to be the most reliable in that material, and from this calculates the lattice parameter.

Whether diffracting through TOF or 2θ setup, the use of neutrons presents an additional consideration over x-ray diffraction. Where x-rays interact with the surface over an area, neutrons penetrate the surface and therefore interact with a volume. As such it is necessary to define a volume over which the neutrons interact with the material known as the gauge volume. The size and shape of the gauge volume therefore defines the spatial resolution over which strain and hence stress will be characterised. It is important to consider that all strains measured within the gauge volume will be averaged, therefore any steep stress gradients will be averaged over unless a smaller gauge volume is defined.

Definition of the gauge volume must be made with consideration to the divergence of the neutron beam. While x-rays, and synchrotron x-rays in particular provide highly parallel beams, neutrons are highly divergent and therefore require neutron optics which take this into account (31). The gauge volume can be defined through two mechanisms. The first mechanism is to use neutron absorbing (usually Cadmium) slits before and after the beam interacts with the sample (Figure 5). The slits do little to control the divergence but offer very high flux. In order to minimise the divergence effect it is best to place the slits as close to the sample as possible.
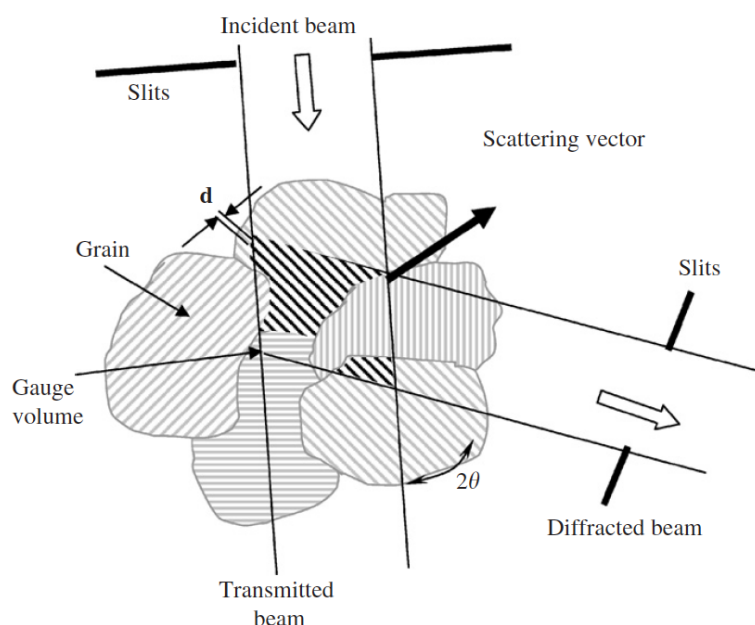
Figure 5: Definition of gauge volume through primary and secondary slits. (32)

When using slits it is possible to alter the spatial resolution by increasing/decreasing the gauge width either by motorised jaws or using a piece of Cadmium with a different window size cut through it. Using this approach an improved spatial resolution is always achievable through a smaller slit width, however the consequence of this is that fewer neutrons interact with the sample, and time required to achieve good counting statistics increases accordingly. Therefore, the choice of gauge volume is a compromise between the desired spatial resolution and the time available on the instrument (32).

The second means by which a gauge volume can be defined is to use collimators in place of the slits. Collimators guide the neutrons down to the point of interest within the sample. The advantage of this approach is that it reduces the effect of divergence, which allows larger distances to be maintained between the neutron optics and the

sample. The downside to collimators is a lack of flexibility; one collimator is calibrated to a single gauge width. Therefore in order to increase/decrease the gauge volume an entirely new collimator must be put in place and re-aligned to the beam, a time consuming process. The number of available collimators is also significantly less than slits due to the high cost associated with manufacturing collimators in comparison to slits.

Neutron diffraction strain scanning is now an established technique with diffraction instruments available in most parts of the world. The number of instruments has recently become sufficient to warrant a study to characterise the level of consistency across facilities through a round robin study of standardised sample (33). Out of such studies and through the collaboration of the facilities involved, a standard has been outlined to guide the implementation of neutron diffraction strain studies (23). By following the standardised approach to strain measurement an uncertainty of $\pm 100 \mu \varepsilon$ can be achieved which translates to $\sim \pm 25MPa$ in most engineering materials. Comparison of neutron diffraction data to other stress characterisation techniques have shown it to be robust and accurate providing a considered approach is taken (34) and (35).

2.1.2.1.5   *Obtaining the strain free lattice spacing*

As discussed in Section 2.1.2.1, the measurement of strain through diffraction requires a value of the strain-free lattice spacing d_0 (or strain-free lattice parameter a_0). It has been argued that in order to achieve a specific uncertainty in strain/stress the strain free lattice spacing should be measured to an uncertainty which is half that of the main measurement (36). As such, a successful experiment depends on careful consideration as to how a stress free lattice spacing will be accurately quantified for every measurement point. A number of approaches have been reviewed in the literature (8, 37), an overview of the more prevalent techniques has been given here.

Stress-free coupons

As it is normally the macrostress that is of principal concern in engineering components, a macrostress-free sample can be used to obtain a value for d_0. This can be created by cutting up cubes or combs from the same sample (or an identically processed one), with dimensions that are too small to allow the build up of macrostresses. A value for the d-spacing is then measured in the same way as any other measurement point. Note that the microstresses are not relieved in a cube, but

this does not present a problem because the same microstresses affect d^{hkl} and d_0. Therefore any variation due to microstress will effect both measurements equally, and not contribute to the difference that is used to measure macrostress (37).

The disadvantage of measuring the strain free lattice spacing using coupons is that it is time consuming, particularly if any variation in d_0 is expected in which case a number of coupons or a comb have to be manufactured and measured. In addition, the procurement of stress-free coupons will either require duplicate samples, or machining out of the original samples. The procurement of additional material is often not viable due to time and financial constraints, while the machining out process renders the technique destructive (37).

The $sin^2\psi$ technique

The $sin^2\psi$ technique has already been discussed in terms of the way in which it can be used to calculate in-plane stresses using laboratory x-ray diffraction. However, with some additional working it can also be used to obtain a value for the strain-free lattice spacing.

Obtaining d_0 through the $sin^2\psi$ technique is largely the same experimental process as for stress measurement. Measurements are made at two in-plane angles $\phi=0°$ and $\phi=90°$ over tilt-angles of ψ ranging from 0-45°. The value for d_0 is calculated from the data by realising that for a biaxial stress state, there will be a value of ψ, let this be ψ^*, where $d = d_0$. Therefore we set $d = d_0$, and the left hand side of equation 4 becomes zero, rearranging this we come up with the following relation (37).

$$sin^2\psi^2 = \frac{S_1}{\frac{1}{2}S_2}\left[1 + \sigma_{11}/\sigma_{22}\right] \tag{7}$$

Since σ_{11} and σ_{22} are calculable from the gradients of the d vs. $sin^2\psi$ plots, we find that the whole right hand side of equation 7 is known and it is possible to deduce ψ^* – the angle at which $d=d_0$. Substituting ψ^* for ψ in the Bragg law (equation 2) d_0 is calculated directly (37)

$$d_0 = \frac{\lambda}{2sin\psi^*} \tag{8}$$

Stress-balance

The stress balance approach takes an existing dataset of d-spacings and iterates through values of d_0 until a solution is found such that the force and moment balances

across a selected cross section. This relies on two key principles to give an accurate value. The first is that the geometry of the sample allows a cross section to be selected which can confidently be said to balance. The second is that the number of measurements made adequately covers the selected cross-section. One example of a viable stress balance condition, is that the axial stress should balance across a cross section parallel to the axis of a disc (38).

One of the primary advantages of this approach is that it does not require an explicit measurement of d_0. However caution should be exercised when employing this technique since anomalous data points can skew the d_0 solution. The stress-balance also has the disadvantage that it is only applicable when a global d_0 can be applied to the data. As such, the stress-balance is typically applied as a first iteration in analysis, or as a check to the validity of a measured d_0; it is not recommended that a stress balance be relied upon as the sole source of d_0 value (37).

Far-field measurement

This technique requires knowledge of a region of the material that is known to be stress-free, often predicted through modelling. A routine d-spacing measurement can then made in this region and the results obtained taken to be the value for d_0. The most important factor in this method is to ensure that the region is truly stress free. As such it is necessary to have a well validated model, with detailed knowledge of the material and the processing parameters. This technique is particularly desirable as it is truly non-destructive, and involves very little extra time or sample preparation to make the measurement. The disadvantages with this approach is that the it relies heavily on a well validated model, and that d_0 is assumed to be invariant with position, which is not always the case (9).

2.1.2.2 Destructive techniques

A destructive residual stress characterisation technique is so called because it requires removal of material, thus damaging the component. Material is removed in order to bring about a mechanical relaxation of stress which can be measured and from this the residual stress back calculated. Owing to the process of measurement, they are also known as mechanical relaxation techniques.

2.1.2.2.1 Hole drilling

Characterisation through hole drilling is made via measurement of mechanical relaxation of the residual stress as a result of localised material removal, in this case a drilled hole. The deformation is usually measured through an arrangement of strain gauges around a drilled hole and from this the data obtained to back calculate the original residual stress profile (Figure 6).
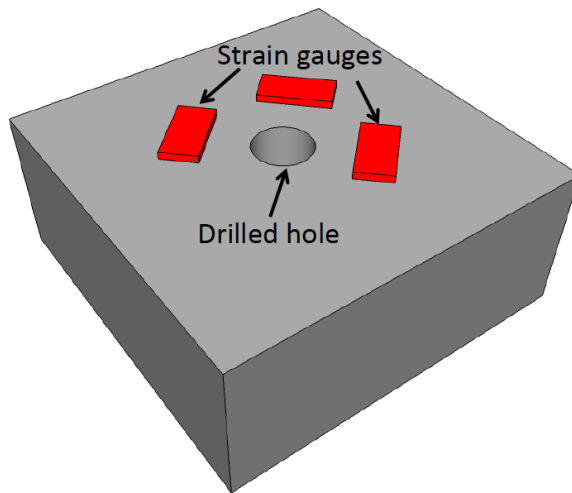
Figure 6: Illustration of the strain gauge placement for a typical hole drilling measurement

Using this approach data is obtained such that the in-plane stresses in proximity to the hole can be calculated. It is also possible to make a depth resolved measurement of the in-plane stress by incremental hole drilling, although uncertainty increases beyond a depth equal to the diameter (14). Uncertainty also increases when measurements are made in residual stress fields which exceed ~50% yield due to localised plasticity (39).   Despite such drawbacks, hole drilling is one of the most widely used characterisation techniques owing to the fact that it is relatively easy to implement, cheap, and well established (40).

2.1.2.2.2 The contour method

The contour method is a relatively new technique developed by (41) which characterises residual stress by sectioning a sample in half, and then measuring the deformation on the cut surface to determine the residual stress prior to the cut. It is particularly attractive as a technique since it allows the determination of a full 2D map of the stresses normal to the cut face from a single measurement process.

Characterisation is made possible through Bueckner's superposition principle (42) which allows the measured contour to be analytically forced back to planarity and the

inverse of this operation used to determine the residual stress. One of the advantages of this approach is that the deformation is measured at the same location as material removal, i.e. at the cut face. This obviates the need for complex calculations to invert the remotely measured deformation to calculate the stress at the point of material removal, for example at the base of drilled hole. The technique also has the significant advantage of being insensitive to microstructure, and not limited to materials which diffract (41).

To date the technique has been applied successfully in a number of studies. The first measurements were made and successfully validated through numerical simulations and measurement of a specimen of known residual stress (41). Since then the technique has been shown to accurately characterise bulk stress in real world engineering problems including quenching stresses (43) and stresses in ex-service railway rails (44). It is also been shown to be well suited to residual stress measurement in welded components (45), and welds of dissimilar metals through friction welding (46). This is largely owing to the fact that the technique is not sensitive to the microstructural or chemical variations which occur in the weld. Execution of the contour method is made up of three distinct stages; cutting, surface measurement, and data analysis; this has been illustrated schematically in Figure 7 and briefly explained in the sections that follow.
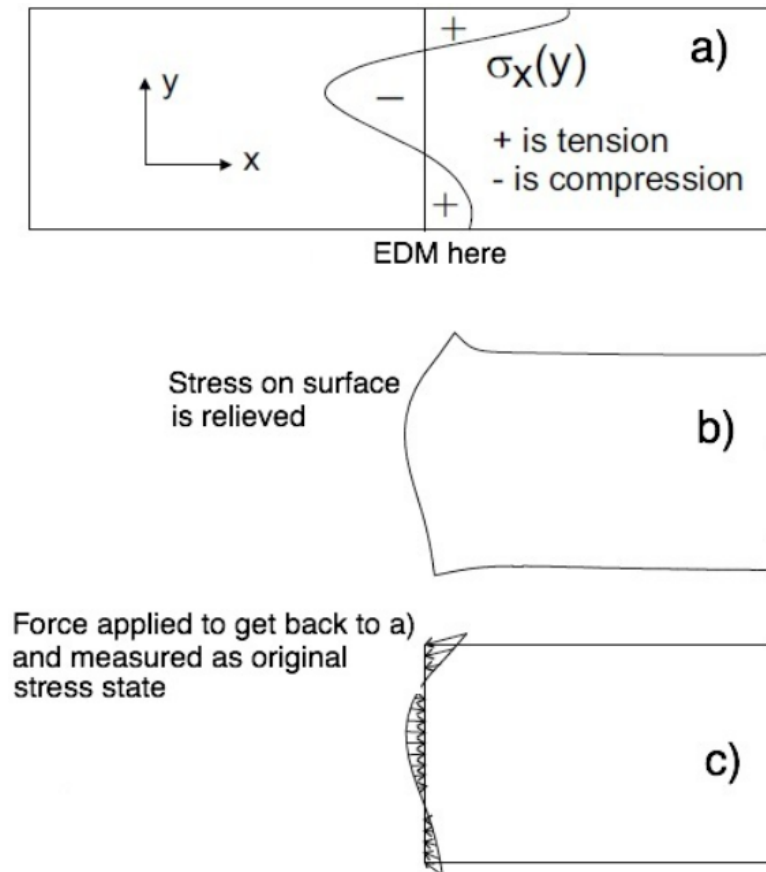
Figure 7: Implementation of the contour method. a) EDM cutting of the component complete with residual stress profile, b) stress relief at the surface, c) measurement of the surface profile and calculation of residual stress (41).

The cutting process

The first stage of the contour method is to cut the sample in half. In order to bring about a deformation which is wholly representative of the relaxed stress the cut is carried in such a way as to meet two requirements specified by (41). Firstly, the cutting process must not contribute in any way to the stress of the component i.e. zero plasticity at the cut tip. Secondly, the cut should have zero width (in an idealised case). More realistically, the cut should have constant but very small width, since this will remove as little material as possible, and is symmetric in terms of material removed from each half. The later requirement in particular has been shown to play an important in reducing errors in analysis (47).

To meet the stringent requirements of the cut, a specific cutting technique known as electro-discharge machining (EDM) is employed and used in a specific set up known as 'skim cut' settings. This setup is usually reserved for the final cut on high tolerance parts, however it is required here since it removes the very minimum

amount of material, and cuts at a much slower speed (48). Using this setup it is possible to cut a component in half without influencing the residual stress (41).

Surface measurement

On completion of the cut, the resulting surface contour is measured on both halves. The process of surface contour measurement is carried out in one of two ways, either through use of a coordinate measurement machine (CMM) or a laser scanner. In either case the aim of the measurement is to accurately capture the surface contour and to identify the sample edges in the data. The only significant factor for either surface measurement is the resolution, or point density, which is set to be high enough to account for the steepest expected stress gradient. Identification of the sample edges is made by a drop in reflected intensity of the laser beam, or when using a CMM, through a separate perimeter scan. It is important that the edges are identified at this stage, since the contour from both halves must be aligned in the analysis stages.

Data analysis

The final stage of the contour method is data analysis and stress calculation, in a typical measurement it is likely to require the greatest proportion of user time since there are many steps to work through. Typically, data analysis is made up of the following stages:

To begin with, the raw displacement data requires some pre-processing and cleaning of anomalous data points. In particular it has been found that the measured surface contour near to the sample edges is highly unreliable when using either CMM or laser scanned data (49). As a result of this, it is common to remove a small (~1mm width) region of data from each of the edges at the start of data analysis to remove edge effects. Once both contour halves have been cleaned of outliers the two datasets are aligned to allow the average of the displacements to be calculated. Taking the average of both halves is known to be a crucial step in the analysis since it cancels out all forms of anti-symmetric error which are commonly induced by the relaxation of shear stresses or a non planar cut (47).

Before residual stress calculations can be made based on this contour it is necessary to smooth the data to remove experimental noise. This is particularly important in the contour method since the stresses are highly sensitive to the displacement, thus any experimental noise would translate to unrealistic localised variations in stress. The

process of data smoothing has been developed by (50) using a spline fit (51). The spline fit first creates a number of localised points known as 'knots' across the contour and then uses a low order polynomial to fit to the area around the knot. This has the flexibility to allow for large deformations between knots which would otherwise be over smoothed if a polynomial function was to be fitted to the entire surface. It is however, necessary to choose a knot spacing appropriate to the measurement to ensure that steep gradients are not smoothed out where they occur. This can be prevented by assessment of the residuals between the fit and the raw data and then increasing the knot spacing accordingly.

The final stage of the analysis is to take the spline fit and incorporate it in a finite element model to calculate the stresses. The model is setup to generate a mesh representing one half of the component without any surface deformation on the cut face. This surface therefore represents the internal plane along which the EDM wire made the cut through the sample; this condition is used as the initial boundary condition. The deformed surface is then used as the final condition and the model finds the nodal displacements required to get from the flat surface to the measured contour. By assuming elastic isotropy it is then possible to convert the nodal displacements into values for stress using the bulk elastic properties for the material (41).

Accuracy

It is difficult to accurately quantify the level of accuracy in the contour method due to the fact that the most significant uncertainties are created during the cutting phase. The issue is therefore how to identify and de-convolute the cutting errors from the accurately recorded contour which resulted from stress relief. The sources of error generated during cutting have been categorised by Prime (47) as being either symmetric or anti-symmetric (Figure 8).
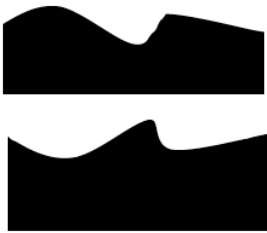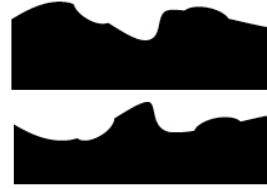
CUT PROFILE	MEASUREMENT OF EACH HALF	
ANTI-SYMMETRIC		AVERAGES OUT NO EFFECT
SYMMETRIC		DOES NOT AVERAGE OUT. CONTRIBUTES TO CALCULATED STRESS

Figure 8: Symmetric and anti-symmetric errors generated during the cutting process. Adapted from (47, 52)

Anti symmetric errors are those which result in a contour which is equal and opposite on both cut faces. Typically this will occur as a result of the relaxation of shear stresses or the deviation of the cut from a straight line. In each case the resulting error on one face will be met by an equal and opposite error on the opposite face. When averaging the displacement of both halves this error drops out of the data and does not go on to affect the final stress calculation.

Symmetric errors are those which by definition create an equal effect on both faces, either an increase, or decrease in the amount of material removed. Such errors create a bigger issue for stress calculation since they do not cancel out by averaging the contour of both halves, and cannot be easily distinguished from the deformation by stress relief. The sources of symmetric errors can be broken down into two sub categories:

- Irregularities in the rate of material removal irrespective of residual stress. Any of a number of factors including material heterogeneities, changes in component thickness, or wire vibrations can lead to a localised change in the removed material.
- Irregularities in the rate of material removal as a result of the residual stress. This includes the effects of plasticity, and a phenomenon known as the 'bulge effect' (47). In these cases, the stress field causes an opening or closing of the cut tip ahead of the wire which alters the cut width accordingly.

The irregularities, which occur regardless of the residual stress, are relatively easy to correct using a second stress-free reference cut. The reference cut, made after completion of the contour measurement, is carried out parallel to the first cut at a distance of 1-2mm behind the original cut face using an identical setup. Since the cutting plane is so close to the free surface there should be no relaxation of stresses normal to the cut. It is therefore reasonable to assume that any departure from planarity is the result of irregularities intrinsic to the EDM machine and the material being cut, rather than the relaxation of stress. The measured deformations in a stress free cut can therefore be applied as a correction to the original contour (47).

Irregularities in material removal rate, which are caused by the relaxation of residual stress, are less readily measurable and hence more difficult to correct. However, recent work carried out by Prime (47) has brought about a method which allows correction of the bulge effect using finite element modelling. To carry out the correction, the model is initially setup as a complete component including the measured stresses (with bulge error), and an accurate representation of the clamping. The cut is then simulated by sequential removal of nodes along the cut path and the resulting deformations recorded. Note that since the model is a simulated cutting process, there will be no bulge effect or asymmetric material removal to affect the deformation. As such, the modelled deformation can used to correct the measured deformation and the stress recalculated. The corrected stress is used as the initial stress in the model and the process repeated until a convergence is reached (47).

While recent efforts have demonstrated that much of the error which originates from the cutting process can usually be corrected with additional work, it cannot be argued that the corrections are convenient or without time penalties. It is therefore prudent to minimise as much as possible the generation of errors in the first place. This, it has been shown, can be achieved by thorough and symmetric clamping of the part (47).

2.1.3 Residual Stress Prediction

Prediction of residual stress in this case refers to the use of the finite element method (FEM). Using FEM, the component in question is broken down into elements which are joined together at nodes. The process of stress analysis is carried out through application of equilibrium conditions at the nodes, which effectively breaks the large analysis down into smaller constituent parts. When applying the FEM approach to residual stress, field quantities such as displacement and temperature are modelled

during processes such as mechanical working, heat treatment and machining. By summing together the results from each element it is possible to model almost any variation of component geometry. Owing to the fact that the FEM approach makes many repeated calculations for each element, implementation must be made using a computer.

The field of stress modelling through the finite element method is exceptionally large, with many variations on the approach taken depending on the specific problem. A number of comprehensive sources of information including (53, 54), and (55), can be found in the literature. What follows is a brief overview of the most recent work using the FEM approach to model residual stress appropriate to this project, principally during heat treatment processes.

2.1.3.1.1 Residual stress modelling during heat treatment

In the context of this study, heat treatment is taken to consist of two distinct processes; quenching and ageing/stress relief. During quenching the cooling of a component at the surface sets up thermal gradients which results in the generation of residual stress. Modelling of the quenching process therefore requires characterisation of the heat extraction at the surface in combination with an accurate knowledge of the thermal properties of the material. This information coupled with an accurate dataset for the mechanical properties enables calculation of the thermally induced strains and hence the generation of residual stress during quenching.

Recent studies into modelling quench-induced residual stress include those carried out on the nickel superalloy IN718 on cylinders (10) and turbine discs (56, 57). The approach taken to model quenching stress comprised of the following stages.

- Invoking symmetry. In order to speed up the modelling process, lines of symmetry were used to model a 3D part as a 2D part. In particular, modelling of a disc geometry enabled the use of a 2D axi-symmetric model provided that processing is applied equally around the circumference.

- Meshing. The number of elements was chosen to balance the required resolution with the time available to solve the model. A typical mesh size was approximately $1mm^2$.

- Setup of boundary conditions. The heat extraction through the surface was modelled through a heat transfer function. This was characterised

experimentally through quenching trials using near surface thermo-couples to measure the rate at which heat was lost at the surface.

- Specification of thermal and mechanical material properties. The conduction, specific heat capacity, and thermal expansion specific to that material was employed. This allowed calculation of the thermal strains as the component cooled. In order to characterise the stress, mechanical properties including quantities such as Young's modulus, Poisson ratio, and Proof stress were also required. The thermal and mechanical properties were obtained through prior experiments characterising the material over the temperature ranges required.

- Final model setup. Each of the quenching models were setup as rate independent elastic-plastic using an iso-tropic hardening law.

In the studies listed above, comparisons made between predicted and experimental data indicated a good level of agreement. However, the use of an iso-tropic hardening law has recently been called into question when modelling quench stresses. The issue stems from the fact that quenching causes a degree of reverse yielding, as such it should be expected that material hardening is subject to the Bauschinger effect - a reduction in flow stress upon reverse yielding (58). However, the isotropic hardening model does not include any influence of the Bauschinger effect, in order for this to be taken into account it is necessary to employ a kinematic hardening model (59). One of the few studies which employed kinematic hardening to simulate quench induced stress was that carried out by (2) on the residual stress generated during quenching of stainless steel spheres. The study also included a comparison of the isotropic and kinematic hardening laws and found a discernible drop in simulated stress brought about by the use of a kinematic hardening law.

The simulation of ageing/stress relief has most frequently been carried out in studies concerning post weld heat treatment. Studies include those made by Karadge et al. on post weld heat treatments (PWHTs) on inertia friction welds of the nickel superalloy Udimet 720li (60), as well as by Tawfik et al. on the PWHT of flash butt welded railway rails (61). There are fewer studies in the context of a quenched component, however one such study has been carried out by Hossain et al. on the creep relaxation of quenched stainless steel cylinder and sphere geometries (62). The approach taken by Hossain et al. was to setup the component geometry complete with the quench stress, and then take the entire component through the thermal cycle of ageing as one

entity. This assumes that the thermal gradients through ageing are zero as a result of the slow heating and cooling rates. While at an elevated temperature, stress relaxation was simulated through an empirically derived law for primary and secondary creep specific to the material. The results obtained showed a strong correlation to experimental data obtained through neutron diffraction indicating that the approach was an accurate approximation to the actual ageing process.

2.2   Nickel-base Superalloys

Nickel-base Superalloys are a class of material which have developed out of the gas turbine industry to meet the requirement for materials with superior high temperature properties.   Since Nickel superalloys have emerged almost exclusively from this application it is appropriate to consider the development of Nickel superalloy in the context of the gas turbine. A gas turbine can be broken down into many sections, for the purposes of this discussion it has been broken down by the material used.
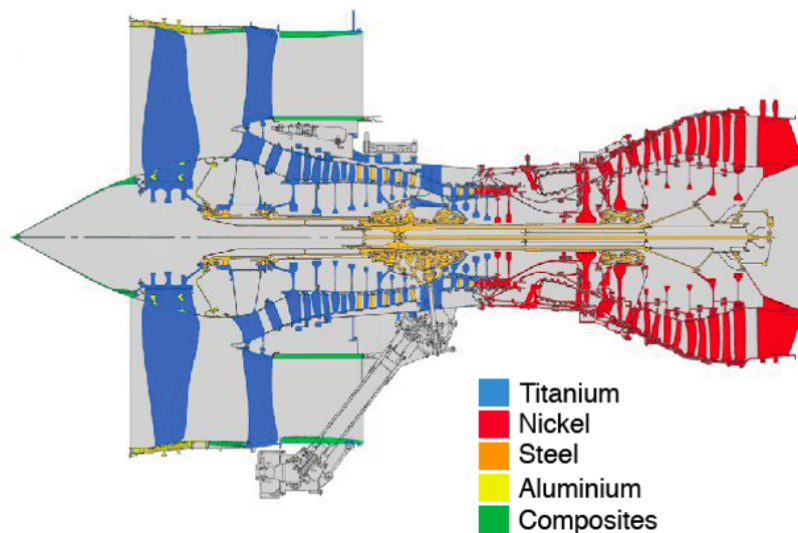
Figure 9: Materials employed in a typical aero-engine (63).

It is clear from Figure 9 that the overall trend is for the front sections of the engine to employ titanium and steel alloys, while the rear sections are exclusively Nickel superalloy (63). The reasons for this trend are primarily related to temperature and weight. The front sections of the engine prior to combustion operate at much lower temperatures, as such they can be manufactured from steel and titanium alloys. Titanium alloys in particular are used where weight is a concern since they are known to be both strong and lightweight. However as temperatures begin to exceed ~600°C titanium alloys suffer from increased oxidation and even heavily alloyed steels see a fall off in strength (64). As the temperatures rise beyond 600°C, Nickel superalloy is required in order to maintain high strength and resistance to corrosion and oxidation (63).

Since their inception in the late 1920s (65), the development of Nickel superalloys has been a relentless strive for higher temperature capabilities. The driving force for improved high temperature properties in Nickel superalloys can be traced back to the fundamentals of gas turbine operation, the Carnot heat cycle (6). Using the Carnot

cycle, it can be shown that the efficiency of a gas turbine is directly related to the maximum difference in gas temperature achieved during the cycle (63).

$$\eta = 1 - \frac{T_2}{T_1} \tag{9}$$

Since it is not practical to significantly reduce the gas intake temperature, turbine designers have continuously sought to push for higher peak temperatures to improve power and efficiency. The drive for increased gas temperatures places greater demands on all aspects of the engine, but none more so than the turbine sections which experience the highest temperatures. It is therefore the turbine section of the engine, which dictates the temperature limits, and therefore requires development of more advanced high temperature materials such as Nickel superalloy in order for the turbine to become more efficient. The relationship between the development of more advanced gas turbines and the turbine entry temperature (TET) shows a clear correlation (Figure 10) (66).
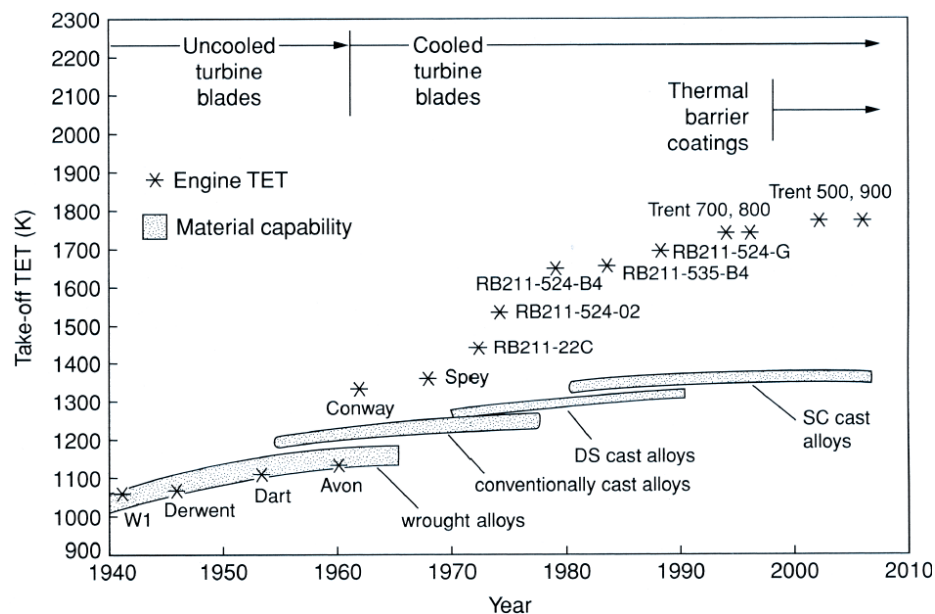
Figure 10: Development of turbine entry temperature with advances in aero-engine design and material processing (66).

At the time of writing, Nickel-base superalloys remain by far the material of choice for the extreme in-service environment of a gas turbine. As such, the development of new alloys, as well as maximising the potential of existing alloys, remains part of gas turbine development (4, 63).

2.3   Composition

Nickel-base superalloys are one of the most complex alloy groups made by man, often containing ten or more alloying elements. The proportions required in a turbine alloy will vary depending on the precise requirements although some general trends can be found. The composition of several nickel-base superalloys can be found in Table 2 (67)

Table 2: Chemical compositions (wt%) of a number of nickel-base superalloys.

Alloy	Ni	Cr	Co	Mo	W	Nb	Ti	Al	Fe	C	Other
RR1000	52.3	15.0	18.5	5.0	-	-	3.6	3.0	-	0.027	0.015B, 2Ta, 0.06Zr, 0.5Hf
Astroloy	56.5	15.0	15.0	5.25	-	-	3.5	4.4	<0.3	0.06	0.03B, 0.06Zr
Inconel X750	73.0	15.5	-	-	-	1.0	2.5	0.7	7.0	0.04	0.25 max Cu
René 88	56.4	16.0	13.0	4.0	4.0	0.7	3.7	2.1	-	0.03	0.03 Zr
Udimet 720Li	57.0	16.0	15.0	3.0	1.25	-	5	2.5	-	0.025	0.03Zr
Udimet 720	55.0	18.0	14.8	3.0	1.25	-	5	2.5	-	0.035	0.03Zr
IN718	52.5	19.0	-	3.0	-	5.1	0.9	0.5	18.5	0.08	0.15 max Cu
Waspaloy	57.0	19.5	13.5	4.3	-	-	3.0	1.4	2.0	0.07	0.06B, 0.09Zr

As shown in Table 2, an array of different compositions are used when developing an alloy, in some cases a small change will create significant differences in alloy performance. The roles of a wide variety of elements in nickel superalloy are summarised in Table 3 (67).

Table 3: The effect of alloy elements on material properties and performance for nickel-base superalloys.

Effect	Alloying Elements
Solid-solution strengtheners	C, B, Al, Ti, Co, Cr, Fe, Mo, W, Ta, Nb, Re
Carbide formers	
MC	W, Ta, Ti, Mo, Nb, Hf
MC_7C_3	Cr
$M_{23}C_6$	Cr, Mo, W
M_6C	Mo, W, Nb
Carbonitrides: M(CN)	C, N
Form γ' $Ni_3(Al,Ti)$	Al, Ti, Cr, Mo, W, Ta, Nb
Raise γ' solvus and solidus temperature	Co
Hardening precipitates of intermetallics	Al, Ti, Nb
Oxidation and corrosion resistance	Al, Cr, Y, La, Ce
Improve hot corrosion resistance	La, Th
Sulfidation resistance	Cr, Co, Si
Improve creep resistance	B, Ta
Increase rupture strength	B
Grain-boundary refiners/grain size control	B, C, Zr, Hf
Retard γ' coarsening	Re
Increase misfit	Re

2.4 Microstructure and Mechanical Properties

The microstructure of Nickel-base superalloys can be broken down into the component phases of, the matrix (γ), the precipitate (γ'), and Carbides and Borides (Figure 11). Examination of each of the phases individually and in combination provides an insight in to the mechanical behaviour of the alloy as a whole.

Primary Gamma Prime
(Gamma Prime not Solutioned During Heat Treatment)
1–10 microns

Tertiary Gamma Prime
(Gamma Prime Precipitated at Low Temperatures on Cooling from the Solution Treatment)
5–10 nm After Quenching
15–50 nm After Ageing

Secondary Gamma Prime
(Gamma Prime Formed at High Temperatures on Cooling from the Solution Heat Treatment)
70–120 nm

γ–Grains
(Limited in Size by Zener Pinning by Primary Gamma Prime During Solutioning)
5–22 microns (ASTM 8–12)

Figure 11: A schematic illustration of the typical microstructure of a γ/γ' Nickel-base superalloy (68).

2.4.1 The γ matrix.

The γ phase is a continuous disordered matrix in which all other phases present in the superalloy are distributed. Alloying elements having similar atomic radii to Nickel (e.g. Cr, Co, Mo) are able to dissolve into the matrix and thus partition there to form the γ phase. The γ phase contributes to the overall strength of the alloy through solid solution strengthening, and in a polycrystalline alloy, through the presence of grain boundaries.

In Nickel superalloys solid solution strengthening occurs in the γ phase when elements of significantly different atomic radii to Nickel are dissolved into the phase.

The effect of this is to create localised lattice strain fields through interstitial or substitutional dissolution of atoms, which acts to impede to movement of dislocations. The strengthening effect can be increased by either; dissolving more solute atoms, or using solute atoms with a greater radii difference to the matrix phase. The limiting factor to this is the precipitation of a new phase, which occurs once the limit of solubility is reached. Hence there is a finite amount of solid solution strengthening that can be achieved in an alloy before precipitates appear and precipitation strengthening begins. (67)

In nickel superalloys the disordered γ phase is typically strengthened by addition of elements such as tungsten, molybdenum, chromium and cobalt (69). It has also been shown that creep strength can be improved through solid solution strengthening of the γ phase with the addition of gold, palladium, rhodium or iridium (63).

As previously mentioned, in polycrystalline form the γ phase also contributes strength to the alloy due to the presence of grain boundaries. In commercial Nickel-base superalloys, the grain size ranges from 5μm up to 150μm depending on the precise application (64). The choice of grain size must be made with considerations to the applied load, the operating temperature, and the effects of fatigue and creep.

Small grain sizes are typically used when yield strength and resistance to fatigue are of primary concern (67). In contrast, large grains sizes, have the advantage of improved resistance to creep owing to the reduction in total grain boundaries (64). The choice of γ grain size is therefore a compromise between the desired mechanical properties for the component. However, recent developments in alloy microstructures for disc application are looking to overcome this compromise by using what is known as a dual microstructure. A dual microstructure disc uses a fine grain microstructure at the bore, and a coarse grain at the rim. This is achieved by simultaneously carrying out a super-solvus heat treatment on the rim, and a sub-solvus heat treatment on the bore. Such a heat treatment is made possible by heavily insulating the bore region while taking the rim over the γ' solvus temperature. This causes the grain boundary primary γ' to be dissolved into the matrix at the rim, but retained in the bore. As a result the grains at the rim are coarsened while those in the bore are not, leaving them as fine grain. The resulting dual-microstructure allows the fine grain bore to resist the greatest loads and fatigue, while the coarse grain rim benefits from improved

resistance to creep (70). Figure 12 shows the variation in microstructure across a test forging subject to the DMHT process as carried out by (71).
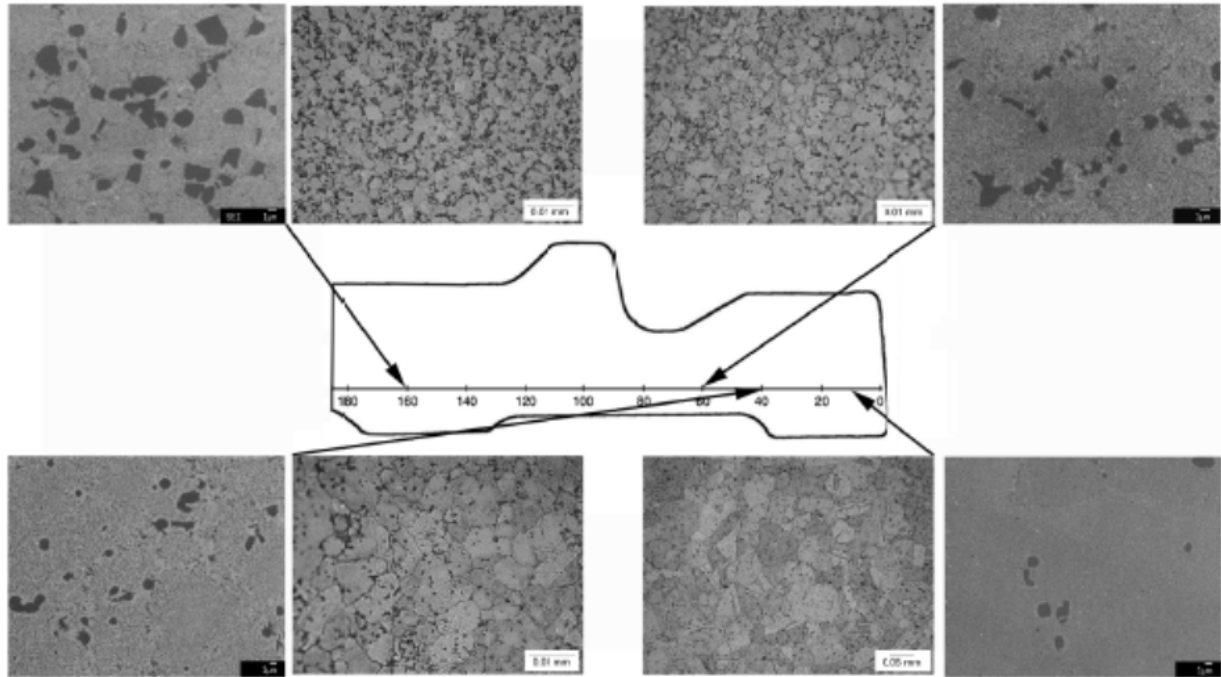
Figure 12: Variation in microstructure across an RR1000 dual microstructure AE2100 forging (71).

2.4.2 The γ′ precipitate

The γ′ phase forms as a precipitate in the γ matrix and is in many ways responsible for high temperature properties of the alloy. The γ′ phase itself is made up of the Ni_3(Al,Ti,Ta) phase, although Ni_3Al is usually the more prevalent. The Ni-Al binary phase is similar to the γ phase in that it is also an FCC structure, however it differs significantly since it is an ordered phase, meaning that the atoms sit at specific locations Figure 13. More specifically the γ′ phase is a primitive cubic $L1_2$ structure, which means that the Al/Ti/Ta atoms sit at the cube corners, and the Ni sit on the cube faces. This ordered structure is energetically preferable to the disordered structure, hence an investment of energy is required to break the ordering (72).
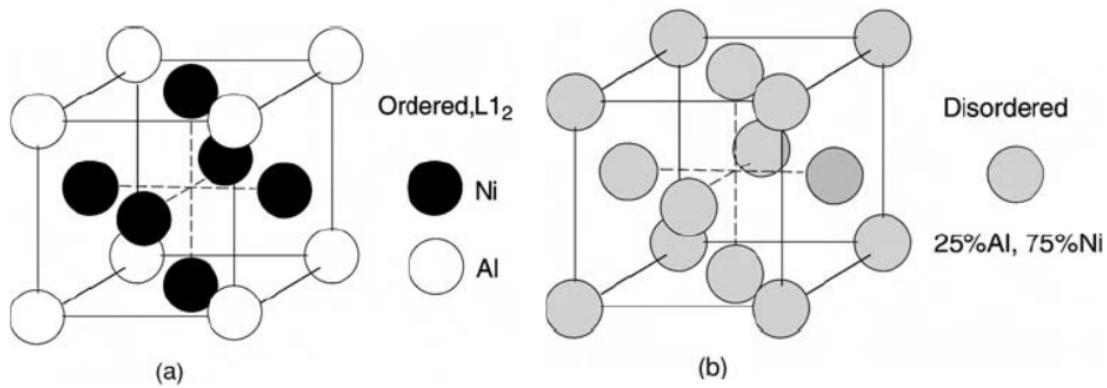
Figure 13: Atomic arrangement in the a) ordered L1$_2$ structure (γ') and b) the disordered matrix (γ) (63).

The L1$_2$ ordering of the γ' precipitates is the source of their individual strength, since deformation of the precipitate would require the ordering to be broken which would require energy. The way in which the precipitate strengthens the alloy is best explained by considering a dislocation approaching a precipitate. The three possible outcomes for the dislocation are:

1. The dislocation cuts through the precipitate and carries on out of the other side.
2. The dislocation is able to climb to adjacent glide planes in order to move around the precipitate
3. The dislocation does not have the energy to do either of the above and remains pinned by the precipitate, effectively halting the deformation

Each scenario is considered in order to understand the overall strength imparted by the γ' precipitate.

In the first case the dislocation must enter the precipitate. However, for this to happen it is necessary to break the ordering of the γ' phase and create a so called anti-phase boundary, which is energetically costly. The cutting of a precipitate by a dislocation has been explained schematically in Figure 14.
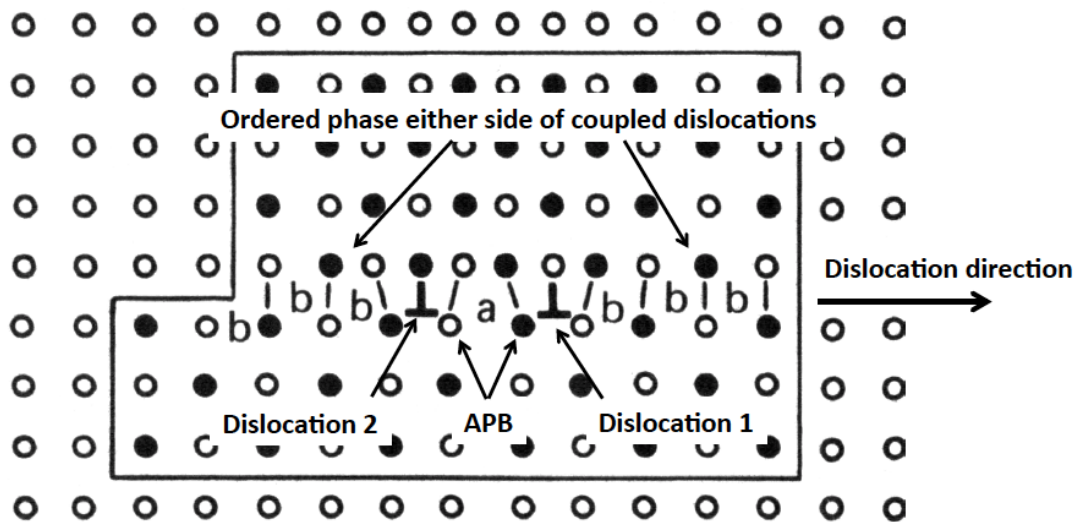
Figure 14: Schematic illustration of the development of APBs as a dislocation enters an ordered precipitate (73).

An important feature of Figure 14 is the presence of a second dislocation following through the precipitate to allow the precipitate to re-order back to the original state. It is the requirement of this second dislocation to follow the first that results in much of the imparted strength. The two dislocations are said to be coupled, and it is the degree of coupling along with the APB energy which determines the energy cost of two dislocations cutting through the precipitate.

Strongly coupled dislocations are said to be spaced by approximately the diameter of the particle, whereas weakly coupled dislocations are spaced by a distance much greater than the particle diameter. Strongly coupled dislocations are required in order to cut large precipitates since the total APB energy to cut the particle increases with the diameter. As a result, the second dislocation is required to enter the precipitate before the first one leaves in order for the cut to be completed. However, strongly coupled dislocations require energy input since the two dislocations are forced to be close together despite being mutually repulsive of each other. Weakly coupled dislocations are able to cut smaller precipitates and require less energy since they are far apart from each other (63).

The second possibility for a dislocation approaching a precipitate, is for it to go around it, a process known as Orowan looping (74). Looping, as the name suggests is the process by which a dislocation climbs to successive glide planes in order to by-pass the precipitate all together. To determine whether a dislocation will loop or cut a precipitate, it is necessary to consider the γ′ precipitate size distribution.

Given a fixed volume fraction of uni-modal γ′ the inter-particle distance can be said to be directly related to the particle radius. Increasing the particle radius will increase the energy required to cut the precipitate and therefore the strength of the alloy, but it will also increase the distance between precipitates. Therefore once the inter-particle distance increases beyond a certain point it becomes energetically more favourable for dislocations to loop and bow around the precipitate than to cut through Figure 15. At this point the energy required for a dislocation to translate through the alloy is reduced and consequently the strength falls (67, 73)
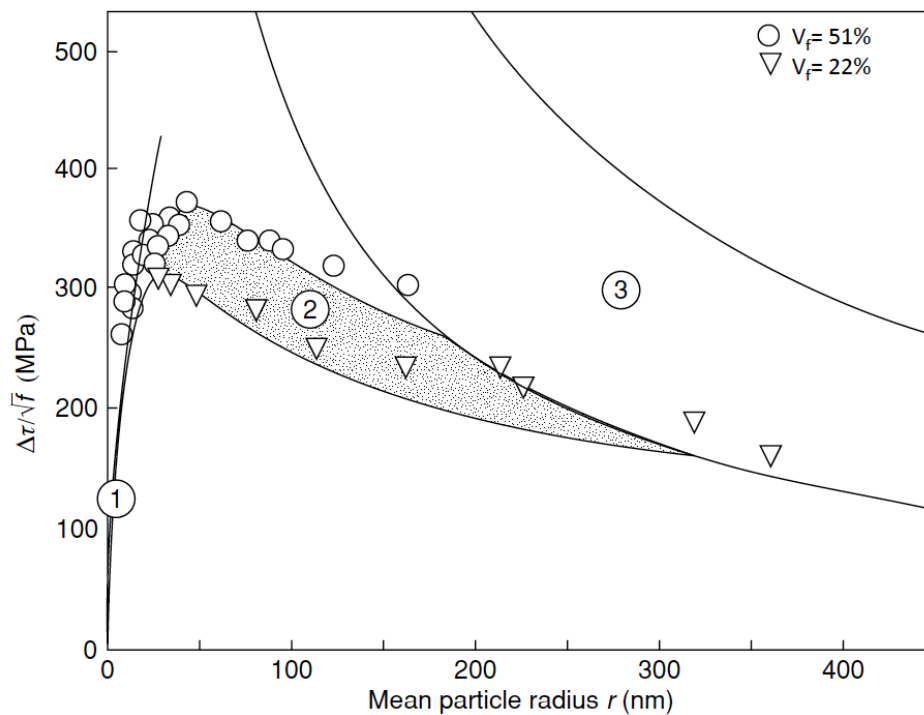
Figure 15: The increase in critical resolved shear stress for Nimonic 105 with a γ′ V_f of 51% and 22%. In regime 1, hardening is by weakly coupled pairs, regime 2 by strongly coupled pairs, and in regime 3 by the Orowan mechanism. The transition from weak to strong coupling is associated with peak strength (75).

Given the results shown Figure 15 it is crucial to alloy strength that the size distribution of the γ′ precipitates is optimised to achieve the maximum strengthening benefit. To achieve this, Nickel base superalloys are subjected to a solution heat treatment followed by an ageing heat treatment which dissolves and then grows the γ′ precipitates to desired size. From Figure 15 the desired size for optimum ageing and maximum strength would be that of approximately 50nm. However, it should be noted that this value is dependant on the specific alloy and on the γ′ volume fraction as indicated in Figure 15. The peak strength is achieved when the mean particle radius and hence particle spacing is as small as possible while still requiring strongly

coupled dislocations to cut the particle. It is in this microstructural configuration that the dislocation is most likely to be pinned by the precipitate and the deformation halted.

2.4.3 Carbides

In Nickel-base superalloys, carbides form when the more reactive elements meet the carbon atoms to form MC carbides, where the M represents metals including Cr, Mo, Ti, Ta, or Hf (63). The MC phases are usually found at the grain boundaries owing to the larger atomic radii of the carbon atoms. At the grain boundaries MC carbides have been found to have a profound beneficial effect on the creep properties of the alloy by acting as inhibitors to grain boundary sliding (76). The amount of Carbon required to strengthen the boundaries is as low as 0.025 wt%, one of the smallest additions. Anything significantly greater than this promotes the precipitation of carbide phases with little additional benefit to alloy performance. In some cases an excess of carbide phase is thought to aid the nucleation of the brittle σ phase, thereby reducing alloy performance (63).

2.5 Manufacture

The manufacture of Nickel-base superalloys includes many different processing stages, the combination of which will depend on the application. This review will give a brief overview of the processing required for polycrystalline alloys for turbine disc application, with additional attention paid to the processes which are known to affect the residual stress.

To begin with it is necessary to create an ingot. The conventional means by which an ingot is manufactured is the cast and wrought method of vacuum metallurgy (77). Using this approach the alloying elements are melted down through vacuum induction melting (VIM), electro-slag refining and then vacuum arc re-melting. The melting processes are conducted under vacuum to prevent oxidation of alloying elements which would be of significant detriment to the alloy strength. This is particularly important when elements such as Ti, Cr, and Al are present as they produce strong oxides which are difficult to remove later in the process. The ingot is then subjected to mechanical work including a sequence of forging and cogging processes, to further refine the microstructure and ultimately produce a chemically homogeneous and microstructurally refined billet (78).

The cast and wrought route is typically used in nickel superalloys which have a γ′ content not exceeding 45 vol.%, alloys such as IN718, Waspaloy and UDIMET 720Li. However, the latest generation of alloys such as RR1000, have a very high γ′ volume faction (~50%), and require a more advanced approach known as powder metallurgy (P/M) to guarantee homogenisation of the alloying elements.

The P/M process (Figure 16) begins in a similar fashion to the cast and wrought approach with a vacuum induction melt of the feedstock. However, once a melt has been achieved the process takes a different route and the molten metal is atomised using a high pressure inert gas resulting in small spherical molten droplets which cool rapidly to form a very fine (~50μm) powder. These are then sieved to control the size distribution, then collected into a can, placed under a vacuum and sealed ready for the consolidation process. (78, 79)

Consolidation is a particularly important step in the P/M route, firstly because it is critical to the integrity of the part, and secondly due to its ability to alter the microstructure. It is usually carried out either by hot isostatic pressing (HIPing), extrusion, or a combination of the two. Extrusion reduces the material cross section and further refines the microstructure. It also has the advantage of forcing out remaining impurities through diffusion. HIPing is similarly capable of refining the grain structure but with the advantage of creating high isotropy in the ingot due to the even pressure and temperature distribution around the can (63, 79).
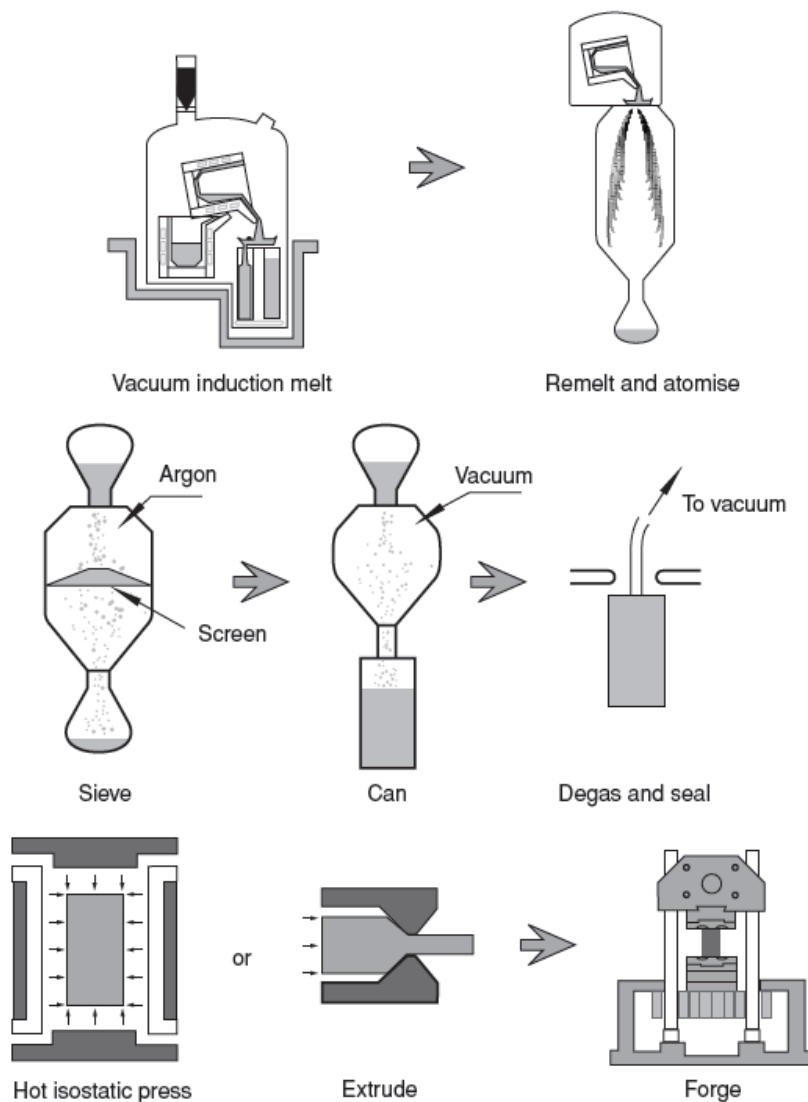
Figure 16: A schematic illustration of the powder metallurgy technique (78).

Once a billet has been produced, by either approach, the alloy is forged to take it close to the final geometry and to further refine the microstructure. In the case of P/M processed alloys it is normal for the forging to be carried out isothermally to reduced strain rates and allow the disc to be forged to near final geometry whilst controlling recrystallization (63, 80).

Once a near net geometry has been produced through forging, a sequence of heat treatments are performed which produce the final microstructure. This begins with a sub-solvus solution heat treatment which dissolves most of the γ´ back into the matrix but retains the primary γ´ on the grain boundaries to prevent coarsening of the grains. The temperatures required to do this are very high, usually >1000°C; the part is then held for a number of hours at this temperature. As a result of the high temperature, it

is typically assumed that all residual stresses generated by prior processes are removed during the heat treatment.

The cooling rate from sub-solvus solution heat treatment is critical to the microstructure of the component since it governs the re-precipitation of the γ´. Conventional cooling methods include water, oil and forced air quenching, water quenching being the fastest cool and forced air being the slowest. A fast cooling rate can be used to keep more of the γ´ suspended in the matrix, thus allowing the precipitates to be grown in subsequent ageing heat treatments in a controlled manner. A slower cooling rate may be used if some γ´ precipitation and growth is desired at this stage, possibly in order to create a bi, or tri-modal distribution of γ´ particle sizes.

The rate of cooling during quenching has an additional affect, however, as it leads to the generation of residual stress. The level of residual stress is directly linked to the thermal gradients produced during quenching, and is therefore found to increase with the rate of cooling. As a result, fast quenching techniques such as water quenching often lead to very large stresses being generated within the component.

Following quenching, the components are exposed to an ageing heat treatment. This is usually carried out at a lower temperature (~700°C depending on the alloy), and over a longer duration (up to 30 hours). During the age, the temperature is sufficient to allow elemental diffusion to occur which results in the precipitation and coarsening of γ´. The microstructure and mechanical properties of the alloy can be altered significantly by the choice of ageing time and temperature. A study of the superalloy UDIMET 720Li found that ageing at 700°C coarsened the tertiary γ´ but had little to no affect on the secondary γ´. Furthermore, there was an optimum duration for the age of ~30hrs which provided the greatest strength (68).

Apart from optimising the microstructure, the ageing heat treatment can also enable the residual stresses in the component to relax in the same manner as a conventional anneal. Typically the relaxation process is expected to occur through a creep mechanism and is therefore directly correlated to the initial stress state, and the ageing time and temperature. If the temperature is high enough, the creep relaxation will consist of an initial rapid primary creep stage followed by an approximately linear secondary creep (62). However, recent work concerning post weld heat treatment on inertia friction welds of the nickel superalloys 720Li, RR1000, and IN718 found that

ageing temperatures set for microstructural optimisation were in some cases too low to have a large impact on the relaxation of residual stress (81).

The final process for a Nickel-superalloy component is high tolerance machining to the final geometry. The component is expected to distort during this process since the removal of material will cause rebalancing of the residual stress (11, 82). To avoid creating a part which is out of tolerance, material must be removed in a specific order such that the net distortion after all machining operations have been completed is zero. It is only possible to determine this order by having an accurate knowledge of the bulk residual stresses after ageing, or by a significant amount of empirical work.

To summarise, the manufacturing process for a Nickel-superalloy consists of a number of mixing, melting and consolidation processes to produce a billet. From this point onwards there are four distinct stages: forging, solution heat treatment (including quenching), ageing, and machining. In terms of residual stress, it can be said that in general, quenching generates, ageing relaxes, and machining re-balances residual stress. The presence and evolution of residual stress through the manufacturing process is significant particularly since it governs the manner in which machining processes can be carried out. Beyond the manufacturing process the presence of residual stress takes on an even greater significance since it has a large impact on the in service performance and therefore the life of the component (5) and (83).

Chapter 3

Experimental methods

In the sections that follow a detailed description of the approaches taken as part of this investigation has been provided. While some reference has been made to previous work where appropriate, the focus has been maintained on the methodology of this study. A wider discussion on the techniques employed with reference to much of the prior work has been given in Chapter 2.

3.1 Neutron Diffraction

Neutron diffraction was employed extensively throughout this investigation as a means to measure strain and hence characterise residual stress. Some of the experiments were very similar in terms of the methodology taken, therefore the methods described in this section are an amalgamation of more than one experiment in most cases.

3.1.1 Constant Flux Source – STRESS-SPEC and SALSA

Two neutron diffraction instruments at reactor sources were used during this investigation to measure strain: STRESS-SPEC (84) at the FRM2 Munich, Germany, and SALSA (31) at the ILL, Grenoble, France. The two instruments are in principle very similar; they are both materials diffractometers primarily designed to measure strain situated at a constant flux reactor source. Owing to their similarity, the instrumental setup for a strain scanning experiment was very similar in each case. As such, references to 'the diffractometer' refers to either instrument, where differences occur the instrument will be specified.

3.1.1.1 Instrument setup

As already mentioned, the diffractometer was situated at a reactor source. In such a facility a single wavelength of neutron is selected using a monochromator crystal setup at the instrument. At STRESS-SPEC the user is able to select from a Ge(511), Si(400) or PG(002) crystal with a take-off angle from the guide tube of 35°-110° resulting in wavelengths ranging from 1 – 2.4Å. At SALSA a double-bent focusing Si crystal monochromator with take off angles of 55°-125° enables measurement with

wavelengths from 1.3 – 3Å. In either case, the wavelength range is ideally suited to providing neutrons of a similar wavelength to the lattice spacing in most engineering materials.

For strain measurement of Nickel Superalloy it is recommended that either the (311) or the (111) hkl lattice plane is used to avoid contributions from intergranular strains (21). In this case the (311) lattice plane was selected: at STRESS-SPEC this was measured using $\lambda=1.55$Å resulting in $2\theta\approx93°$, while at SALSA a wavelength of $\lambda=1.64$Å gave $2\theta\approx98°$. This wavelength was selected in each case since it provided a near cubic gauge volume – which gave an equal spatial resolution in all directions.

Having selected the wavelength of incoming neutrons, the next stages are concerned with defining the optics to get the neutrons in and out of the sample. This can either be achieved through Cadmium slits, which only allow a selected cross section of the beam through, or by employing radial collimators which guide the neutrons down to a volume within the sample. Each approach has it's advantages: Slits are often employed since they are comparatively easy to setup and align, they also offer superior flux, and therefore faster measurement (31). However, collimators are typically favoured when divergence becomes an issue (85), in particular when the beam optics cannot be placed close to the sample surface.

Measurements carried out at STRESS-SPEC were made using Cadmium slits (Figure 17). On the primary side, a Cadmium plate with a machined window was placed in a holder at the end of the beam optics. On the secondary side a computer controlled set of vertically oriented Cadmium 'jaws' were set to control the beam height. Both the primary and secondary slits were placed as close as possible to the sample in order to reduce the affect of beam divergence. This fully defined a volume in which the neutrons were interacting with the sample and being detected, this is known as the gauge volume. For all experiments made on STRESS-SPEC this was set to $4x4x4mm^3$ to balance count times with spatial resolution.
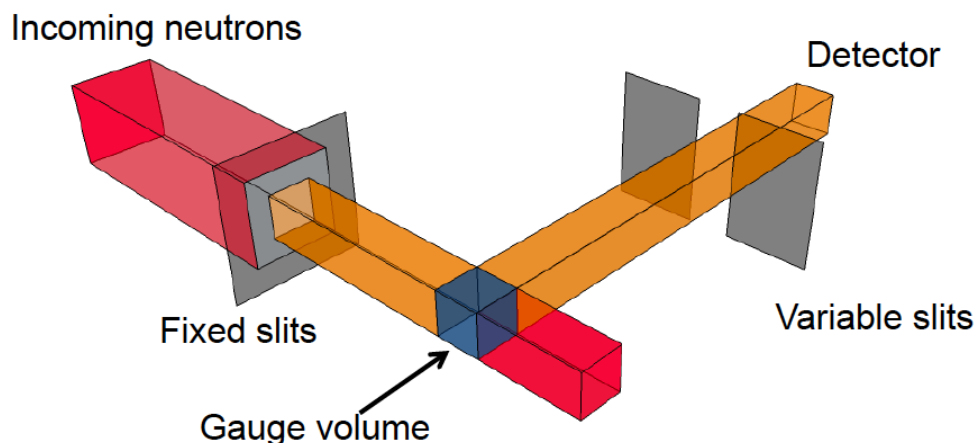
Figure 17: Gauge volume definition using a combination of variable and fixed slits.

Measurements carried out on SALSA were broadly very similar. However, the monochromator setup on SALSA differs such that it provides a more vertically divergent beam at the instrument (31). When using slits this rapidly elongates the gauge volume in the vertical direction which can be an issue if a vertical spatial resolution is required. For the sample geometries measured in this investigation (a disc) this applied to the measurement of hoop strain. To reduce the divergence in this direction a 2mm collimator was place in the primary beam behind the slit, which was still required in order to define a gauge volume. Using this setup, it was found that the vertical divergence could be reduced to produce a gauge height of 4mm at a 60mm slit distance to the gauge volume. All other orientations were made using slits to enable faster count times. To calibrate between measurements made using different optical setups, a stress-free powder sample was measured in each case.

It was essential that the samples were mounted securely and accurately to maintain spatial resolution. On each diffractometer this was achieved using the precision machined flat table top with threaded holes designed to allow secure mounting of samples. On SALSA the table was manipulated using a six-axis HEXAPOD (31), while at STRESS-SPEC the table moved along three orthogonal axis and rotated. In either case the movement of the table was computer controlled to allow alignment of the gauge volume to within ~0.1mm.

The final setup process was to align the sample to the instrument. Preliminary alignment was made using a laser fired to visualise the path of the neutron beam. A more accurate alignment was then made using a theodolite and/or a mounted video camera aligned to the centre of the gauge volume. Final alignment was made in each

case through entrance scans – the intensity profile as the neutron beam entered the sample was fitted, and from this the location of the surface deduced.

3.1.1.2 Data acquisition and analysis

The actual measurement process was implemented through a sequence of computer scripts to automate the movement of the sample table for precise alignment of the gauge volume. Where ever possible, multiple samples were mounted simultaneously to reduce the need for sample changes and frequent realignment. The intensity profile was recorded using a 2D position sensitive detector which was binned by diffraction angle to provide a single line profile of the peak. Acquisition times were high for this alloy owing to the high Cobalt content (18.5wt%) which is highly absorbing of neutrons. At SALSA the acquisition times were typically no greater than 70 minutes, while at FRM2 this increased marginally to 90 minutes. In either case, the raw data was processed using analysis software developed at the instrument by fitting a Gaussian profile to the peak and subtracting the background. This enabled the peak position to be determined which in combination with a stress free reference value permitted the calculation of strain section 3.2.

3.1.1.3 Uncertainty and errors

A number of sources of error can be considered for a diffraction strain measurement a discussion of which can be found in (36). In investigations such as this, which span more than one instrument, it is important to consider the interplay of systematic errors inherent to each setup. Such an effect has been observed in a round robin study on a standardised sample across a wide number of neutron strain scanning instruments (23). In order to compensate for the variations between setups used here, a stress free powder sample was measured when ever a new experimental setup was implemented.

The actual level of uncertainty for a given strain measurement is typically quantified using the uncertainty in peak position from the fitted profile. It can be calculated using the following relation (36).

$$u_\varepsilon = \frac{1}{tan\theta}[(\delta\theta_0)^2 + (\delta\theta)^2]^{\frac{1}{2}} \tag{10}$$

Quantifying the level of uncertainty in this way had the advantage that it was readily available and so allowed fine tuning of the count times to achieve the desired level of accuracy in the measurement.

3.1.2 Pulsed Source – ENGIN-X

The Engin-X instrument is part of the ISIS facility at the Rutherford Appleton Laboratory in Oxford, UK (86). The neutrons are generated from a spallation source, meaning that they arrive at the instrument as a white spectrum in pulses. The method for strain measurement at such an instrument is known as the Time of Flight (TOF) setup and differs significantly from a continuous source, it has been discussed in Chapter 2. In this study, the Engin-X instrument was chose for a specific experiment to capture stress relaxation during ageing using an in-situ heat treatment. The instrument was particularly well suited to the measurement since it was capable of rapid measurement in two strain directions simultaneously.

3.1.2.1 **Instrument setup**

The neutrons arrived at the instrument as white beam in pulses of 50Hz. The neutron optics at ENGIN-X combine the use of a slit in the primary beam and radial collimators in the secondary beam to define the gauge volume (Figure 18).
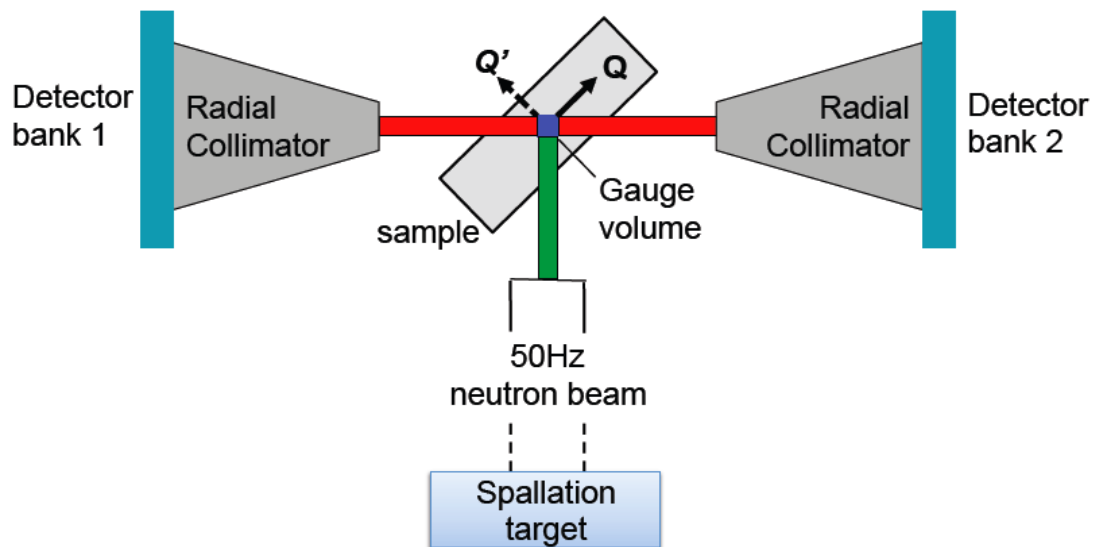
Figure 18: Layout of ENGIN-X instrument at ISIS, RAL, Oxford, UK (86)

The slits in the primary beam are motorised and hence controllable through a computer, they are capable of a 0.2-20mm and 0.2-10mm window in the vertical and horizontal respectively. The radial collimators are mounted immediately in front of each of the detectors and are of fixed width. Therefore this dimension of the gauge volume can only be set in accordance with the available collimators, which are 0.5, 1, 2, 3 and 4mm in width. To enable the fastest acquisition times the largest (4mm) collimators were selected for this study.

The in-situ heat treatment added a further dimension to the experimental setup. In order to heat the forging (76mm dia. 25mm depth) a heated blanket of sintered alumina beads containing high resistance Ni-Cr wire was clamped firmly in contact with the sample. To reduce the heat radiating away into the surroundings, and maintain a homogeneous temperature within the heated blanked, a series of insulating layers were arranged around the outside. Through a sequence of preliminary tests it was found that almost all of the layers placed around the forging would attenuate the neutron beam to a certain extent. As a consequence it was necessary to arrange a window in the heated blanket, clamp, and outer heat proof blankets to avoid compromising the measurement. A schematic diagram of the experimental setup has been given in Figure 19a.
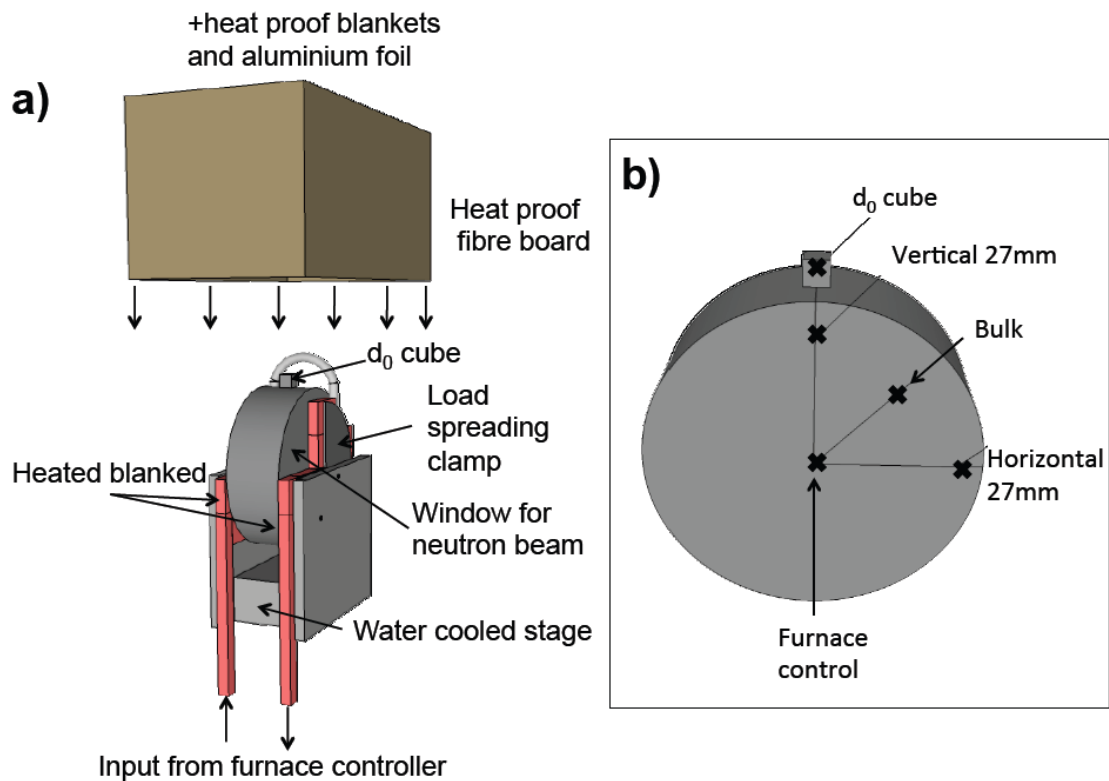
Figure 19: a) Schematic illustration of the in-situ heat treatment setup, b) distribution of thermo-couples on sub-scale forging for temperature control.

The temperature across the forging was monitored using five surface mounted thermo-couples distributed as indicated in Figure 19b. The central thermo-couple was used to control the power through the heated blanket and hence the temperature of the forging. Using this setup it was possible to maintain the temperature across the forging to within 10°C.

Alignment of the sample was made in the usual manner, preliminary alignment using a theodolite followed by entry scans to achieve full alignment.

3.1.2.2 Data acquisition and analysis

Using the white neutron beam, all velocities and hence all wavelengths were diffracted. At the constant diffraction angle ($2\theta=\pm90°$) each lattice plane within the gauge volume diffracted the wavelength which satisfied Bragg's law ($\lambda=2d\sin\theta$) at the fixed angle. The resulting spectrum is a contribution from each lattice plane, a typical example of which is given in Figure 20.
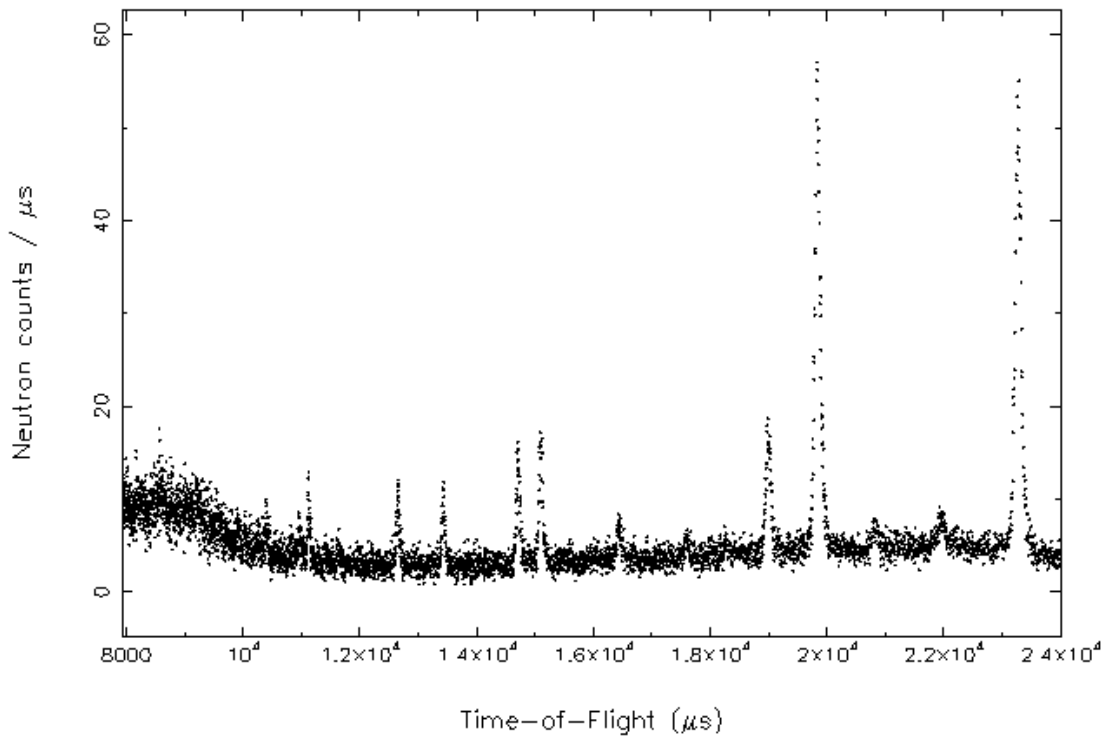
Figure 20: A time of flight (TOF) spectrum as obtained on Engin-X while measuring strain in RR1000 Nickel Superalloy.

Calculation of strain was made by fitting a single peak as opposed to a Rietveld fit (30) to maintain continuity with previous experiments. The (311) lattice plane was again chosen for this as a result of the low sensitivity to intergranular strain and good approximation to bulk behaviour (21). Note that the above diffraction pattern was captured in two direction simultaneously owing to the two horizontally opposed detector banks. This had the significant advantage of providing strain measurement in two directions at the same time. Furthermore, by placing the gauge volume in the centre of the disc, the hoop, radial and axial stresses were characterised from a single acquisition.

Strain measurements during the in-situ heat treatment were made with the emphasis on achieving high time resolution to enable to the stress relaxation process to be captured. As a result, the targeted acquisition time was in the region of 15-20mins per point. In order to achieve this it was accepted that the uncertainty in peak position, and hence strain, would increase.

3.2 X-ray Diffraction

The use of x-ray diffraction in this study was limited to the $\sin^2\psi$ technique, specifically it's use to calculate a value for d_0, the theory of which has been explained in Chapter 2.

3.2.1 Bruker Laboratory X-ray Diffractometer

3.2.1.1 Instrument setup

The instrument used in this study was a Bruker D8 Discover with GADDS 2D area detector. During operation x-rays are generated by virtue of a tube source and transmitted via a foil filter and collimator to remove fluorescence and deliver a parallel beam with spot size ~1mm. The x-rays are diffracted from the surface of the sample and detected by the 2D area detector at an angle 2θ which corresponds to the lattice plane of interest.

The sample was aligned to the beam using a unique laser video camera system (87) which enabled precise positioning and focus of the beam on the sample surface (Figure 21). The laser is mounted directly above the camera at angle such that the spot falls within the centre of the camera's field of view once the stage is set at the correct height. For each measurement location on the surface (x and y position) the stage height (z) is varied until the laser spot is aligned to the camera cross hairs. The values for x, y and z for each measurement location are then imported into an automation script to drive the diffractometer. The script also automates the measurement of tilt angle (ψ), and orientation (ϕ), to gather the data necessary to make a $\sin^2\psi$ analysis (Chapter 2).
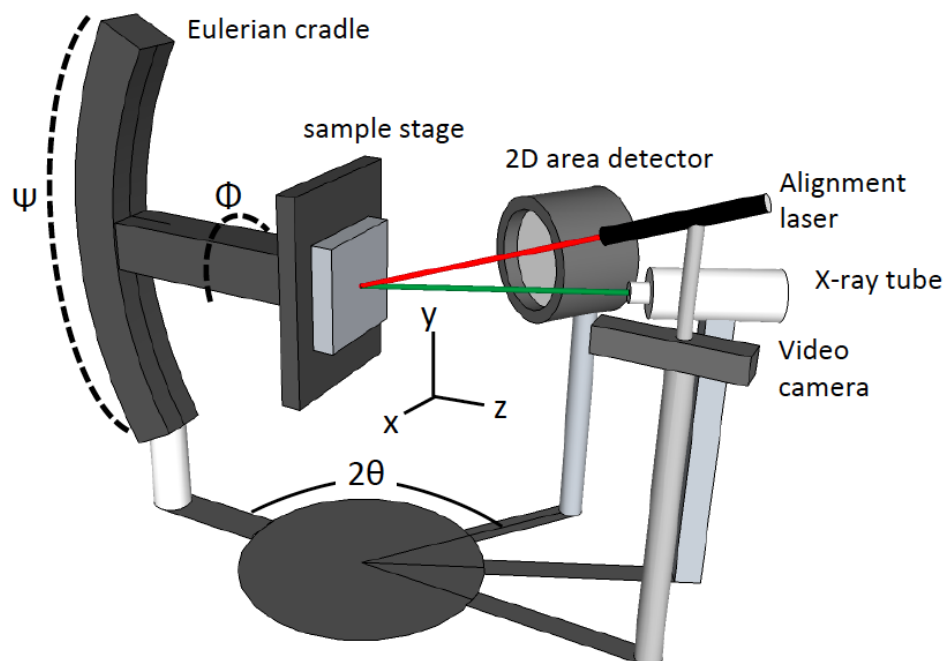
Figure 21: Layout of the Bruker D8 Discover with GADDs, including laser video camera alignment system (87).

3.2.1.2 Data acquisition and analysis

The $\sin^2\psi$ technique requires measurement of each data point in two orthogonal sample orientations (ϕ) over a range of tilt angles (ψ) (section 2.1.2.1). In this particular setup, ψ was varied in steps of 5° from 0° (stage normal aligned to the x-ray beam) up to 45° using the Eularian cradle as illustrated in Figure 21. This measurement process was carried out in two orthogonal stage orientations $\phi= 0°$ and $\phi= 90°$ (Figure 21).

For each measurement position (x, y, z, ϕ and ψ) the GADDs 2D detector recorded a section of the diffraction ring(s) which fell within the 2θ window of the detector. The detector was significantly wider than the width of the peak, as such it was necessary to integrate the data over a smaller window in 2θ to only include contributions from the lattice plane of interest. The integrated intensity produced a single line profile which was fitted using a sliding gravity approach built into the software package, BRUKER STRESSplus. The sliding gravity approach operates by taking regions of data from the top of the peak in 10% intervals from the maximum intensity down to 80 or 90% of the maximum intensity. The average of the peak position from each of these fits is then taken as the fitted peak position and this value of 2θ converted into a value for the lattice spacing, d, using Bragg's law. This approach to peak fitting has

been found to be a very robust process which allows for high repeatability and less influence from peak asymmetry or artifacts in the data (88).

Carrying out the above process provided a value for the d-spacing for each tilt angle ψ (0-45°) and orientation of ϕ (0° and 90°) for all measurement locations on the sample surface. A typical dataset for a single measurement location has been provided in Figure 22, the two orientations and tilt angles are clearly visible.
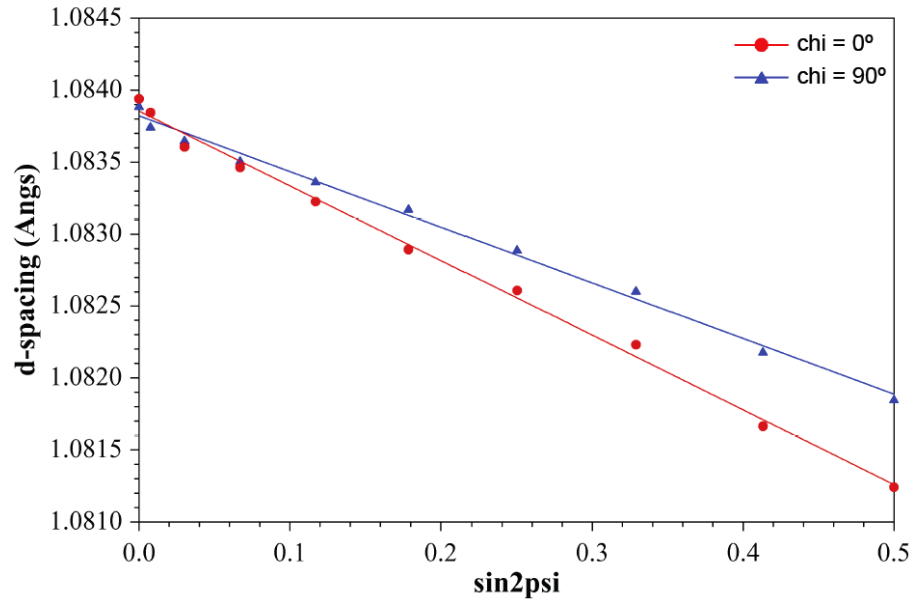
Figure 22: A typical $\sin^2\psi$ plot used to calculate d_0 from the intercept and gradient of the linear fit using Equation 11.

From the data shown in Figure 22, it was possible to determine a value for d_0 using the biaxial stress equation for a typical $\sin^2\psi$ measurement (Chapter 2) to generate two simultaneous equations (for $\phi=0°$ and $\phi=90°$) and solve for d_0 to obtain the following relation.

$$d_0 = (intercept \; \phi = 0°) + \frac{v}{1+v}(gradient \; \phi = 0° + gradient \; \phi = 90°) \qquad (11)$$

3.3 The Contour Method

The contour method is a relatively new technique developed by (41) to obtain the residual stress after making a cut. A review of the technique has been given in Chapter 2, what follows is a description of the implementation made in this study. The methodology has been broken down into the three principle process required to make the measurement, namely, cutting, surface measurement and data analysis.

3.3.1 Cutting

In all instances the cut was made using Wire Electro-Discharge Machining (EDM) as carried out by Rotadata Ltd Derby. The wire EDM process operates by passing an electrical current through a thin wire in proximity to a conductive part, this results in a spark arcing across the gap, vaporising a small volume of material. The part is typically submerged in de-ionised water to act as a di-electric and stabilise the erosion of material, while fresh wire is fed in from above and collected below (Figure 23).
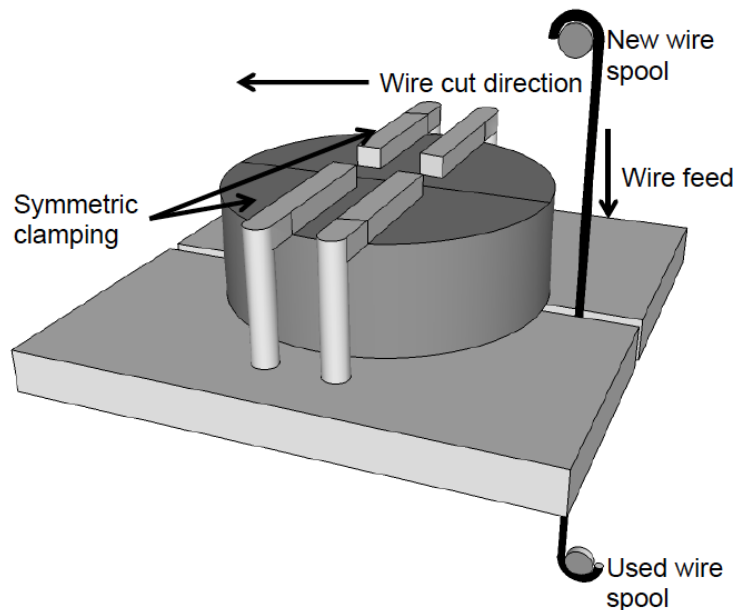
Figure 23: Sample clamping for EDM cutting. The entire assembly is submerged in de-ionised water with the exception of the wire spools.

For each of the samples cut here, the EDM machine was set to a specific setting known as 'skim cut' Table 4. This setup is so named because it is usually employed to get the final high tolerance geometry when machining a component, it is therefore a slow and non-aggressive cut which removes the minimum of material. This makes the skim cut setting ideal for the contour method measurement since the requirements are for a cut which does not contribute to the residual stress state, and has 'zero width' (Chapter 2). It is important that this distinction is made, since the typical wire EDM process involves a preliminary rough cut followed by the final skim cut. This is of no use for stress analysis since the first rough cut is not completely stress free and removes too much material, thereby destroying much of the useful data. The skim cut settings used for all samples characterised using the contour method are given in Table 4

Table 4: Contour method EDM cutting parameters

Wire type	Brass (uncoated)
Wire diameter (mm)	0.30
Wire feed rate (internal machine value)	12
Cutting speed (mm/min)	0.25
Wire voltage (internal value for skim cut)	14
Water flushing rate (L/min)	8
Clamping arrangement	Part clamped to two rails within the tank either side of cutting plane

A further stipulation of the cutting process was that material should be removed uniformly across the cut to avoid the generation of errors (Chapter 2). Studies made by M. Prime (47), have shown that it is possible to minimise the generation of errors during the cut by taking care to secure the part thoroughly on both halves. This prevents movement of the part as the stresses relax during the cut. Each sample cut as part of this study was sufficiently large to allow secure clamping on both sides and thus minimise the possibility of movement.

3.3.2 Surface Measurement

The deformed surface can be measured in one of two ways, either a coordinate measuring machine (CMM) touch probe, or a non-contact laser scanner, the latter was chosen in this study. A NanoFocus μscan profilometer (89) was used for all surface contour measurements. Through the characteristic interference of the outgoing and reflected laser light the NanoFocus μscan system is capable of measuring relative changes in surface height to a precision of up to 0.02μm over a 300x200mm surface area. However, this high level of precision restricts the measurement range to a maximum change in surface height of 1mm.

For this particular setup, each disc half was placed individually in a clamp on the stage and the laser module adjusted to bring it close to the sample surface for alignment (Figure 24). Since the working distance was limited to a range of 1mm, it was important for vertical alignment that the sample was flat and that the working distance was set to be in the mid range of the change in contour. This was achieved

by a manual process of adjusting the laser module height and clamping arrangement until the laser could be scanned across the entire surface within a 1mm total change in working distance. The sample was aligned laterally using the built-in camera arrangement to identify the x-y coordinates of the sample edge and then scanning 5mm further to ensure the entire surface and the edge profile was captured. The stage was set to raster the sample at a speed of 10mm/s and measure at intervals of 100μm in both the x and y directions across the sample surface.
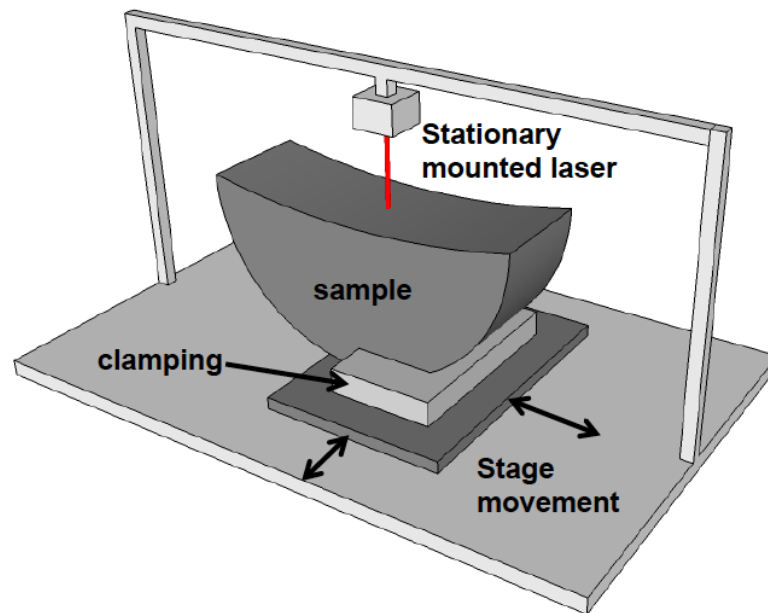
Figure 24: Schematic of the μscan NanoFocus con-focal laser scanner. Note that the laser remains stationary and the clamped sample moves underneath to scan the surface.

Upon completion of the scan the data was masked to identify all regions where the reflectivity was less than 30% (typical signal data was ~80%). The mask therefore identified the regions where the laser had passed over the edge of the sample and left only the data from the surface. The data was then exported for further analysis as a simple comma separated variable data file containing x-y position with height, z.

3.3.3 Data Analysis

The two stages prior to data analysis are relatively standardised techniques, and as such are easy to document and replicate. However, the process of analysing the surface contour data in order to calculate stress has required the development of a new set of procedures specific to the technique. It is therefore to be expected that the precise analysis route will depend on the needs of the experimenter that develops the analysis code. For this implementation of the contour method, the Matlab (90)

routines developed by Johnson (50) and Xiong (91) were used for each of the following steps, with one or two minor alterations made where necessary.

The raw data was imported into Matlab and visualised; the raw contour measurement of a sample which had aged for two hours at 760°C following a water quench is shown in Figure 25, Note that the masked area where the laser passed over the edge is clearly shown as a masked region, and that a number of outliers are still present.
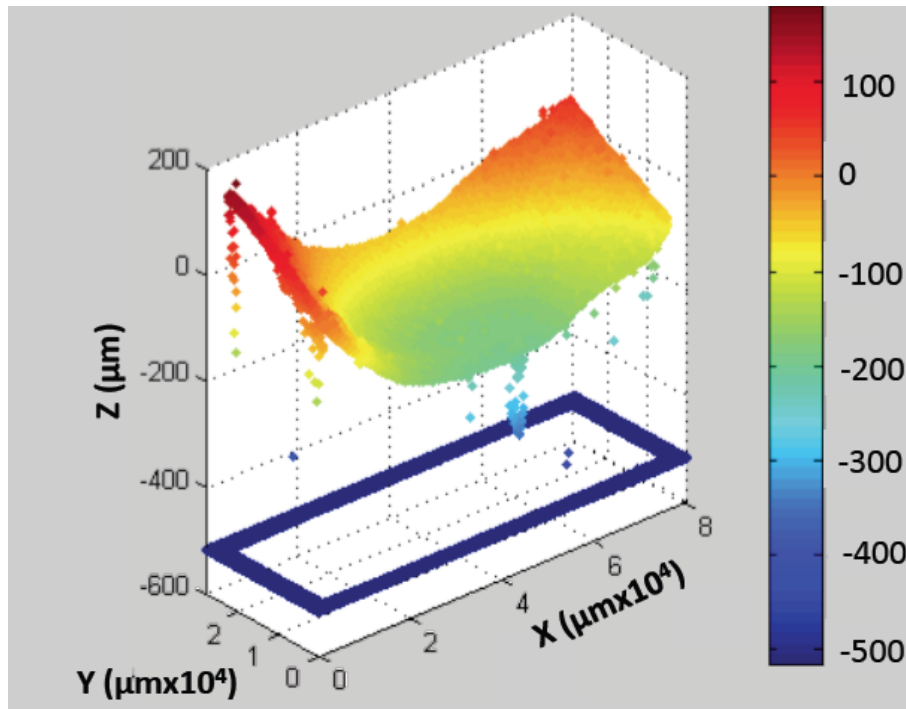
Figure 25: Surface contour raw data – water quenched and aged for two hours @ 760°C. The masked region is visible at approximately z=-550μm

The first step in analysis was to clean the raw data files and remove outliers from each half. An automated routine removed any isolated data points far from the measured contour, after which it was possible to remove data manually. For each of the samples measured here it was found that as the EDM wire exited the forging it left a small lip which remained in the measured surface contour. It was therefore necessary to manually remove a region of contour data ~1mm in width from one end of the contour to remove this feature.

The cleaned data from each half was then aligned and averaged. Alignment was made using an automated routine which began by extracting the data from the outermost points of the contour and setting this as the outline of the component. In order to align the two outlines it was necessary to define the axis over which the two

halves were rotated to provide access to the inner faces. This could either be the x or y axis, as illustrated in Figure 26 for the samples measured here.
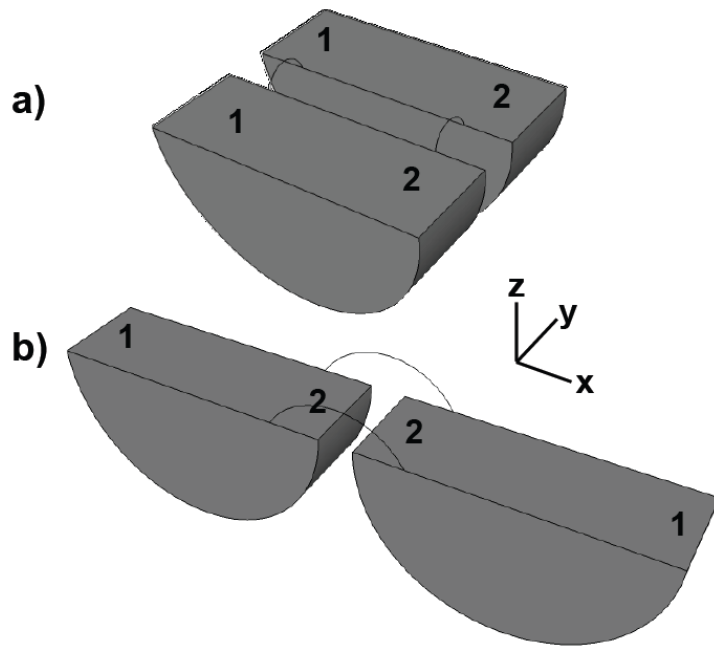
Figure 26: Ways in which the top half can be rotated away from the bottom half, a) about the x-axis, and b) about the y-axis

Given the rotation axis, the routine aligned the two outlines by fixing one half as a reference and translating the other half to minimise the sum of the distances between the corresponding points on each half. The aligned contours could then be averaged. As detailed in Chapter 2, the averaging of both halves is one of the key steps in the contour method since it removes all contributions from shear stress relaxation, and errors generated from a non-planar cut (47). The aligned and averaged contour data for the sample aged for two hours is given in below in Figure 27. The contours shown in Figure 27 clearly highlight a near symmetric contour about the sample centre. Furthermore the contour indicates a tensile bore and compressive rim, which is the expected stress distribution following quenching. The data also clearly indicates a few isolated data outliers, these are removed in the subsequent fitting stage.
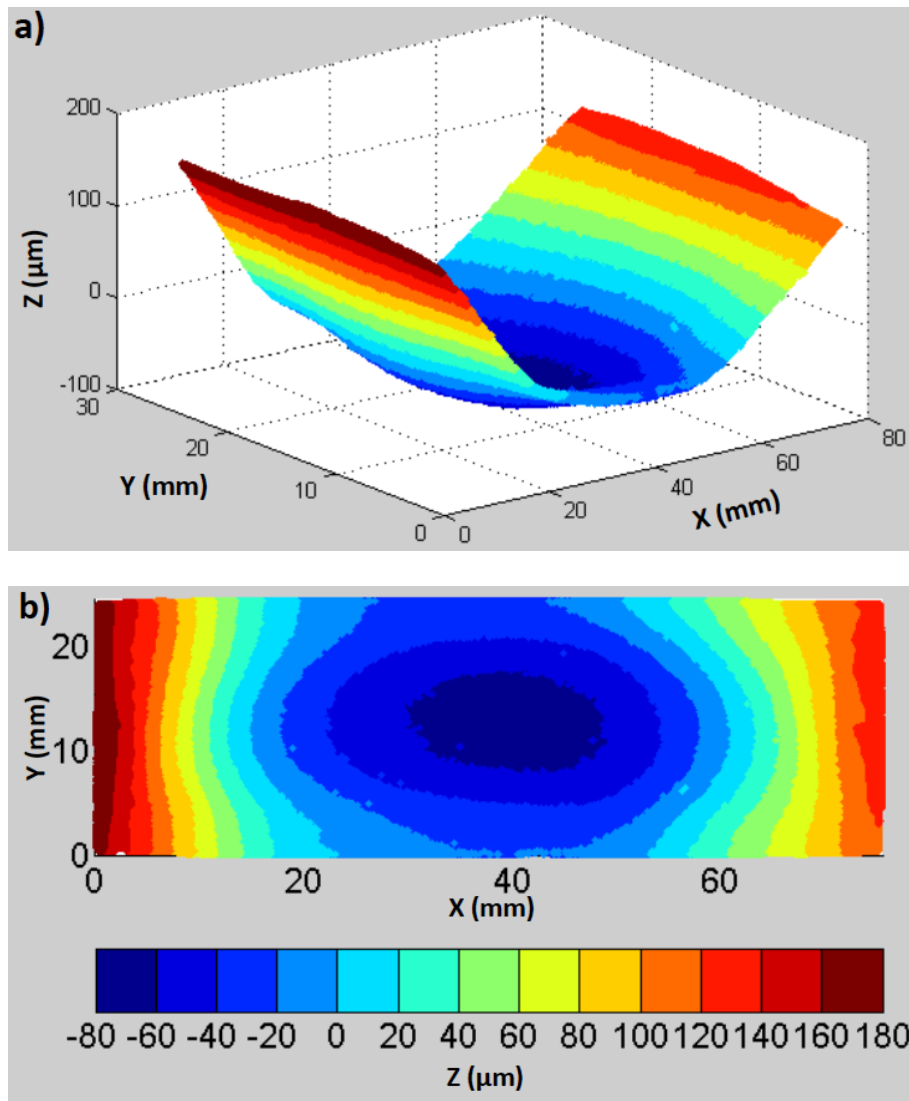
Figure 27: Cleaned surface contour data – water quenched and aged for two hours @ 760°C. a) isometric view and b) XY planar view.

The final stage of data manipulation before generating the stress model was to fit a surface to the averaged data-set. The fitted surface acts to smooth the data, removing the experimental noise which would otherwise translate in to unrealistic extreme localised variations in stress. The fitting routine employed here was that of a spline fit (92), as adapted for the contour method by Xiong and Johnson (50, 91). The adapted routine is highly automated, allocating a greater knot density for the spline fit where the change in displacement is steep, and reducing this where it is not. The spline fit and residuals between the fit and the raw data are then plotted to ensure that the data is not noisy or over smoothed in any regions. The residuals and spline fit for the two hour aged sample are shown in Figure 28. The residuals (a) indicate a number of outliers which are removed by the fitting process to give the final spline fit (b).
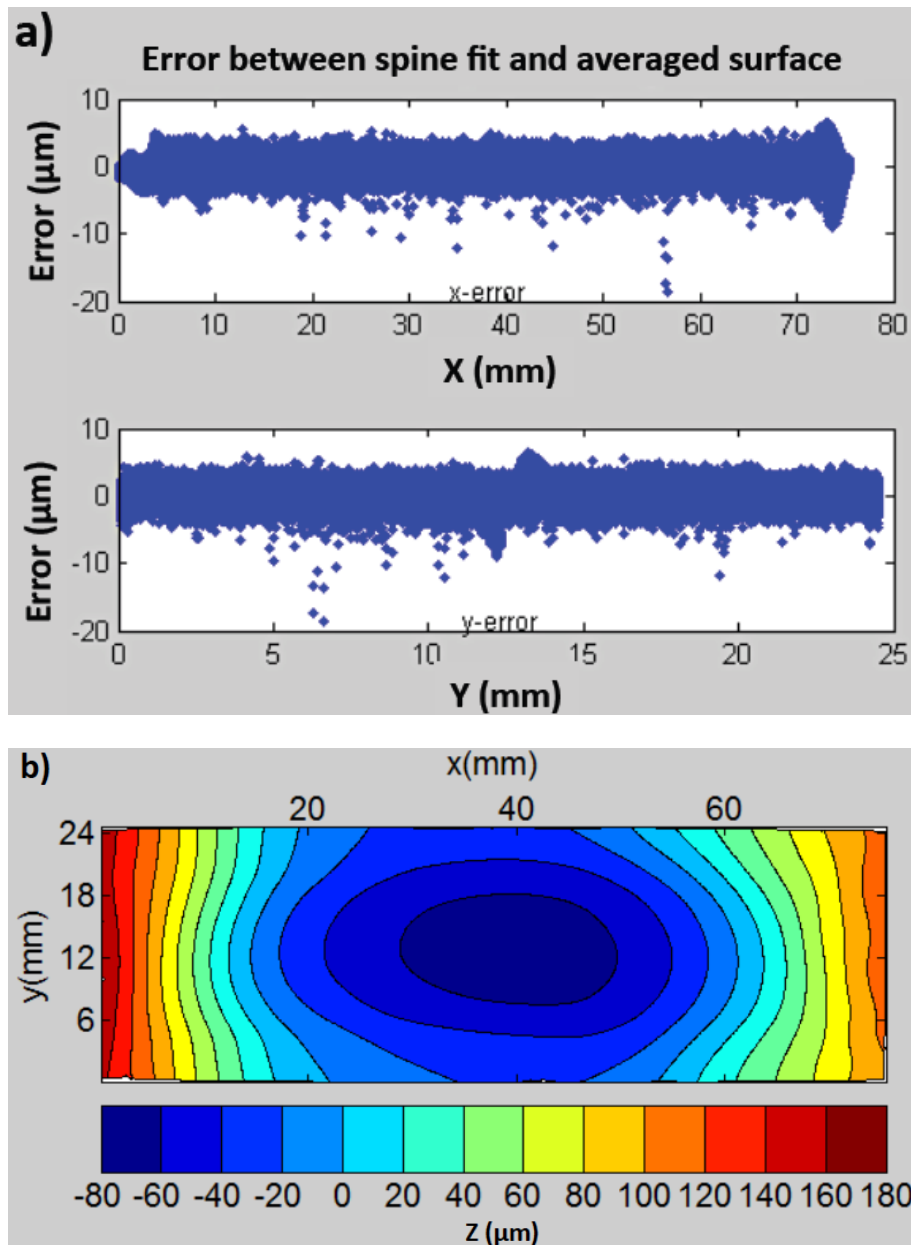
Figure 28: a) Residuals between spline fit and surface contour data and b) spline fit of the contour (sample: water quenched and aged for two hours @ 760°C)

The next step requires Abaqus CAE (93) to generate the finite element model. The aim of this modelling stage is to create a 3D mesh of one half of the component without any deformation on the cut face. To achieve this the component outline was imported, then extruded and cut to form a half disc shape using built in Abaqus functions. The component was meshed with quadratic elements using a dense mesh at the cut face (~0.5mm length) which reduced to a coarse mesh (~3mm length) close to the back face. This enabled the model to be precise in the region of the cut face, but reduced the total number of elements in the model to allow faster analysis times. The mesh was then written as a 'job file' (saved as *.inp) to be imported back into

Matlab to generate the nodal displacement file. The displacement for each node to get from the undeformed mesh (Abaqus file) to the deformed contour (spline fit) is calculated using a Matlab routine developed by Johnson (50) and written as the boundary condition for the model. The routine also requires two nodes to be selected to prevent movement of the component, and the user to input bulk elastic properties for the final stress calculation. The final step in the routine is to write an Abaqus input file using all of this information which can then be solved using the Abaqus standard/implicit solver.

Completion of the analysis generates an Abaqus output file which can be opened and viewed using the Abaqus CAE visualisation package, along with a data file which contains the x-y coordinates and a z value, which is the stress normal to the x-y plane. This file was then opened and plotted in Matlab using scripts built around the 'contour_plot' Matlab command by Johnson (50). The data could be plotted either as a contour plot to visualise the entire stress map, or as a line scan. Since it was expected that the contour method data would be compared to results obtained by neutron diffraction, a modification was made at this point to allow for a 'gauge volume averaging' effect. The modification addressed the fact that while a neutron diffraction data point averaged the stress over the gauge volume, which in this case was 4mm^3, the contour method data did not. Therefore a direct comparison of the data would show poor agreement in areas of steep stress gradient. To compensate for this, a script was developed to designate 'gauge areas' on the contour map and average the stress values within the area to simulate the measurement process of the neutron diffraction gauge volume.

3.4 Finite Element Modelling

All finite element modelling carried out in this study was made using the Rolls-Royce in house analysis code SCO3 (94).

3.4.1 Thermal characterisation of processes

Before an accurate model could be developed, it was necessary to experimentally characterise some of the processes to be simulated. Of particular importance was the quenching process, the rapid heat extraction which occurs during quenching is complex and hence very difficult to predict using an entirely theoretical approach. The route taken was to carry out quenching trials using a 304 stainless steel (304SS)

sample of identical geometry with embedded thermo-couples to capture the rate of heat extraction from the disc. The 304SS sample was used in place of an RR1000 forging since it was less costly to procure and was easier to machine holes to place the thermo-couples. Furthermore, 304SS is a good analogue to RR1000 for the purpose of this study since it is also an FCC lattice structure, and is not subject to any phase changes over the course of the heat treatment. The arrangement of embedded thermo-couples within the sub-scale forging geometry used in this investigation is given in Figure 29. This setup was used to characterise the solution, quenching and ageing heat treatments. Thermocouple 1 captured the bore, thermocouples 2 and 3 captured the bulk region, and thermocouples 4 and 5 captured the rim.
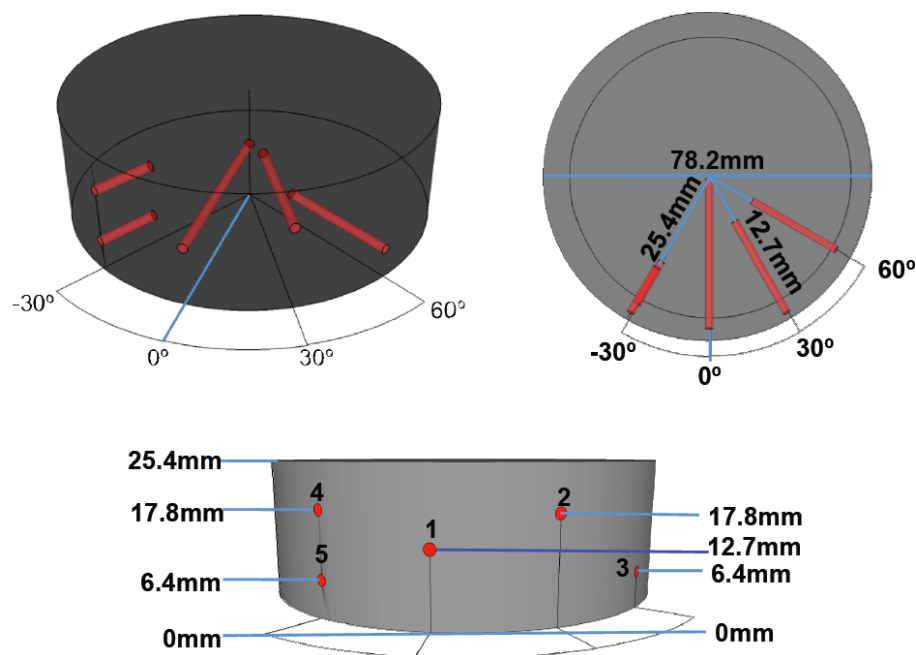
Figure 29: Distribution of embedded thermo-couples in the sub-scale forging.

The thermocouples remained in the part during heating to solution, and during transfer to the quench tank, thus fully capturing the process. The transfer was implemented using a basket which could be lowered rapidly into the quench tank. Data from the thermocouples indicate a typical transfer time of 8-20 seconds. The physical arrangement of the forgings within the basket was such that they were not in contact with any other parts to allow for a repeatable and reliable quench to be carried out. The quenchant was not agitated during either oil or water quenching. The air cool was a **still air** cool with the part place outside of the furnace in ambient conditions, again with minimal surface contact. During quenching the thermo-couple

data indicated the expected trend, near surface regions cooled first followed by the core (Figure 30).
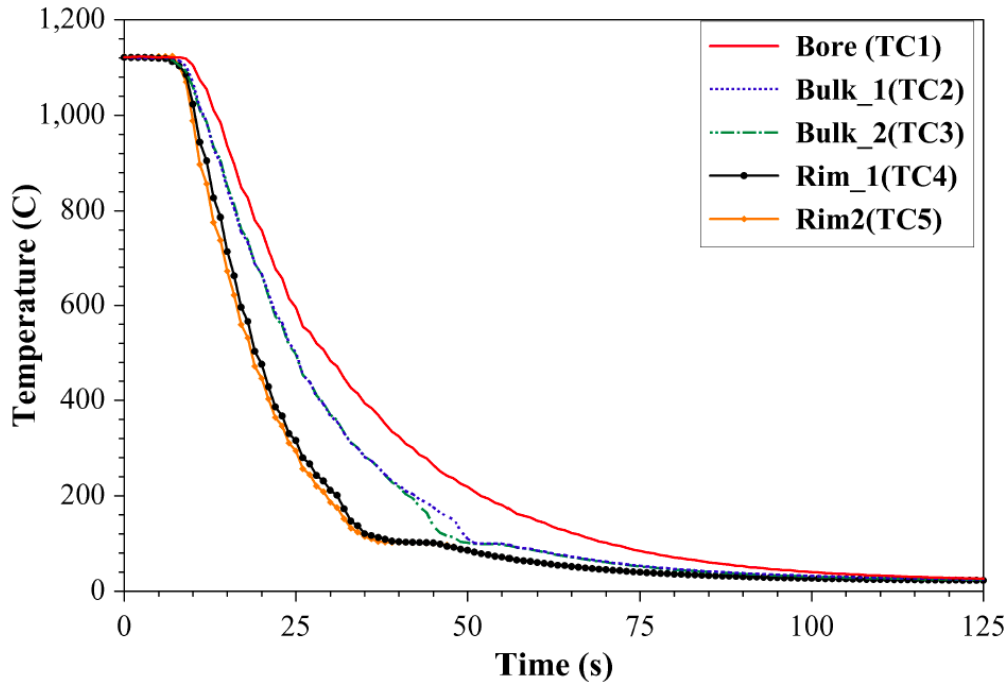
Figure 30: Cooling data generated by embedded thermo-couples, in this from a water quench from solution heat treatment.

The temperature differential between the near surface and core thermo-couples was used to derive a heat transfer coefficient (HTC) to be implemented in the model The HTC was calculated across the entire temperature range of the quench using equation 12. The value of thermal conductivity used in equation 12 was that of the 304SS. However, this does not prevent the curve being used for the RR1000 part since the HTC primarily represents the heat extraction at the surface rather than the internal conduction of heat within the component. The HTC is therefore characteristic of the quenchant, quench tank arrangement and the surface geometry of the part, rather than the thermal conductivity of the material. However, it should be stipulated the HTC curve was applied to a model which used the thermal conductivity of RR1000 in order predict the generation of residual stress.

$$HTC = \frac{k\left(abs(T_B - T_A)\right)}{(T_B - T_{water})d} \tag{12}$$

Where k is the thermal conductivity, T_A, T_B and T_{water} are the temperatures at thermo-couples A, B and of the water, and d the distance between the two thermo-couples

Using this equation and the data captured in Figure 30, it was possible to generate the following HTC curves for air, oil and water quenching.
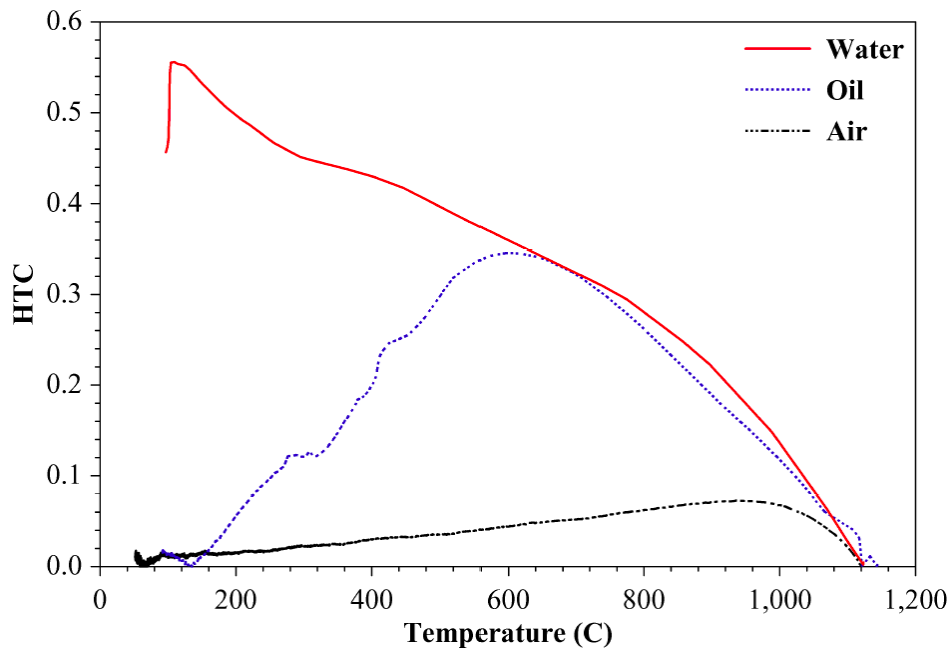
Figure 31: Heat transfer coefficient (HTC) curves for air, oil and water quenches.

While the curves in Figure 31 were derived from a realistic quenching trial it was recognised that the positioning of the thermo-couples presented a problem when employing the HTC as a surface boundary condition in the model. The issue was that the near surface thermo-couple was still at least 6mm from the surface. This meant that the heat flux characterised was not as extreme as the surface condition. Application of the derived HTC was therefore made using an additional weighting factor to increase the effectiveness of the HTC at the surface. The derivation of the weighting factor is explained as part of the model implementation.

3.4.2 Model implementation

The modelling process began by generating the part mesh. Since the heat treatment processes were carried out equally around the entire disc, it was possible to simulate the them using a 2D axi-symmetric model (Figure 33). The mesh was generated using triangular elements of ~1mm length from the bore to the rim, and a constraint placed on a single node at the bore to prevent rigid body movement.

3.4.2.1 **Material Properties**

The material properties of RR1000 were obtained directly from the Rolls-Royce materials database which is populated using data from detailed material characterisation. Given a specific composition, the characterisation follows a process as shown in Figure 32.

Material characerisation process:
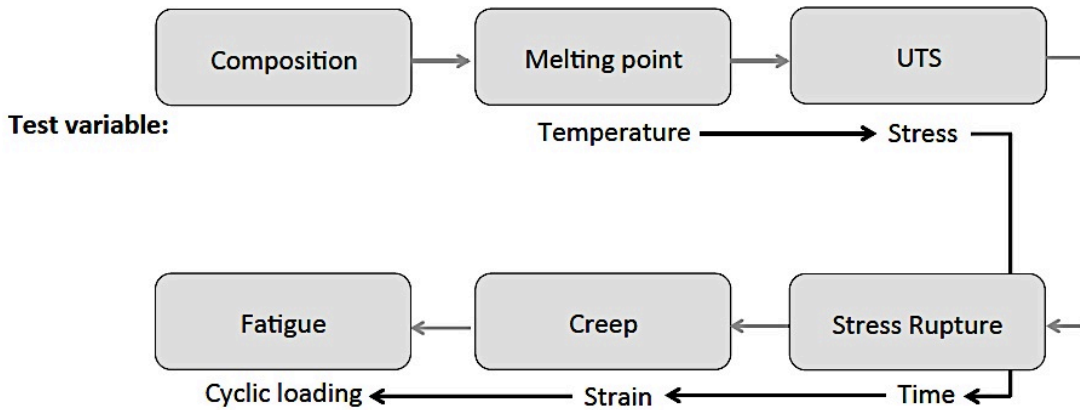
Figure 32: The material characterisation process, testing must occur sequentially to build up material data. Adapted from (95)

As detailed in Figure 32, characterisation begins with the capture of all thermal properties, quantities such as melting point, thermal conductivity, specific heat capacity and thermal expansion. From this point stress is introduced to understand the mechanical behaviour. Elastic properties such as the Young's modulus and Poisson ratio are captured using elastic tensile tests across the required temperature ranges. Plastic properties such as the proof stress curves are also captured at this point by taken the material to yield. Moving beyond yield the time to rupture for a given stress and temperature allows the measurement of the stress rupture life. A hyperbolic tangent fit to the stress rupture test data is then implemented to derive creep curves, the fit equation is given in equation 13 (96).

$$\sigma = \sigma_i \left[1 + \tanh\left(k \ln \left(\frac{\varepsilon}{\varepsilon_i} \right) \right) \right] \tag{13}$$

Where σ_I and ε_I are functions of temperature and time. The σ_I parameter is 0.5*UTS, and ε_I is the strain at the point of minimum strain rate when the applied stress is σ_i. k is a fitting parameter. This is henceforth known as the CT07 hyperbolic tangent representation of creep strain (96). The final part of the characterisation process is to carry out cyclic loading tests to derive the material hardening behaviour and ultimately the fatigue properties.

As a relatively new alloy, but one which has been the focus of much recent work, RR1000 has been tested and documented thoroughly meaning that the quality of the data is known to be very high. However, since alloy development and testing must be

offset by a commercial benefit, all material testing, and thus all available data, is that of the production grade alloy. While the test samples featured in this study followed commercial processing up until heat treatment, the sub-scale geometry required a more aggressive quench to generate high levels of residual stress. As a result it was expected that some disparity in microstructure and hence mechanical properties may be apparent in some samples in comparison to the available material data.

3.4.2.2 Quenching

Modelling of the quenching process consisted of heat extraction in two distinct phases, the first being transfer from furnace to quench tank and the second being immersion in the quench tank. During the transfer period (~8s) the model was setup using an emissivity constant of 0.8. After this point the HTC curve was applied as a surface boundary condition to model the convection and heat extraction in the quench tank. As mentioned in the previous section, it was expected that the HTC curve would not extract heat at a fast enough rate at the surface, therefore the curve was applied to the surface with a weighting factor. It was also expected that the rate of heat extraction would vary by surface region, i.e. a faster rate at the rim in comparison to the bore. To allow for this in the HTC, the model was broken down into multiple domains to create 13 surface regions as illustrated in Figure 33.
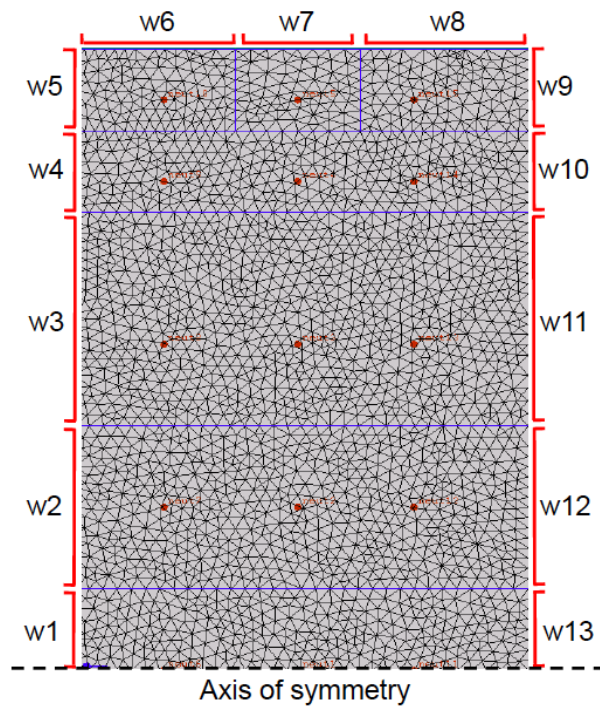
Figure 33: 2D axi-symmetric mesh of a sub-scale disc forging with surface regions for weighting factor indicated.

A unique weighting factor was applied to each of the 13 surface regions. The value of the weighting factor was determined using an optimisation process to match the modelled cooling rate to that of the thermo-coupled quench.

Optimisation of the weighting factors was made using the iSight software package (97). The iSight software automated the running of the model by using the iSight specific 'pointer' algorithm to select different combinations of weighting factor in an attempt to reach the user defined target(s). In this case the targets were assigned as 6 points extracted from the time-temperature plots from each thermo-couple. To prevent the optimisation from attempting unrealistic weighing factor combinations, i.e. very significant differences between neighbouring regions, a control was enforced whereby neighbouring weighting factors had to be within 2/3 of the combined average. Using this approach it was possible to determine a set of weighting factors for each quench and thus create a thermally accurate model.

It must be noted that during this phase the aim was to characterise the heat extraction based on the data provided by the quenching trial. As such the material properties employed had to be those of 304 stainless steel rather than Nickel Superalloy. Once the weighting factors were determined, they could be applied along with the HTC curve as boundary conditions to the stress analysis model using material properties appropriate to the Nickel Superalloy.

3.4.2.3 **Plasticity modelling**

Having characterised the heat extraction during quench it was now possible to run the model using a structural analysis to establish the thermal strains and hence the potential generation of residual stress. The generation of residual stress is dependant on the level of plastic deformation which occurs as a result of the thermal gradient across the component. As such it was necessary to run the model non-linearly using a material specific hardening law to simulate the plasticity and thus generate residual stress.

3.4.2.3.1 *Hardening law*

As the name suggests, the isotropic hardening law allows for equal hardening in all strain directions. The isotropic hardening law has been widely used to model plasticity during quenching and so is the natural first choice (10, 57). In a uniaxial case isotropic hardening dictates that whatever material hardening is achieved in

tension is retained once unloaded and then loaded in compression. However, for polycrystalline metals this is thought to be unrealistic owing to the Bauschinger effect (58). The Bauschinger effect describes material hardening in tension at the expense of that in compression (or vice-versa). Taking the Bauschinger effect into account requires a new hardening law known as the kinematic hardening law. The two hardening laws can be visualised using a yield surface as shown in Figure 34.
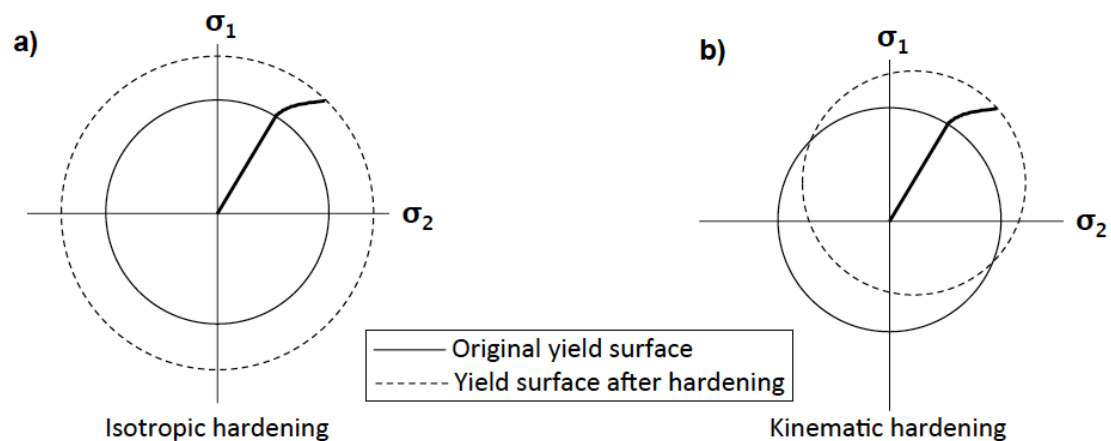
Figure 34: Yield surface representation of isotropic and kinematic hardening in a biaxial stress field.

Isotropic hardening can be expressed as an expansion of the yield surface, whereas kinematic hardening is a translation of the yield surface. Under monotonic loading the hardening behaviour is identical, however once reverse loading occurs the kinematic model yields far earlier than the isotropic model owing to the included Bauschinger effect. The isotropic model is therefore more suited to monotonic loading, while the kinematic model to cyclic loading.

In the SC03 package, kinematic hardening is no longer modelled explicitly, instead it is taken into account using an Mroz multilayer hardening law. The Mroz law uses multiple yield surfaces to achieve a mixture of both isotropic and kinematic hardening, details of the model theory can be found in (98). In SC03 the Mroz model is setup in such a way as to allow the hardening behaviour to transition from monotonic to cyclic behaviour, thereby mixing the isotropic and kinematic hardening models. Initial simulations were carried out exclusively using the isotropic model but this was found to give a poor match to experimental results in the rapidly quenched samples. As a result, quenching simulations were run twice, first using the isotropic and then the Mroz hardening laws to allow for a comparison to made.

3.4.2.4 **Ageing**

After quenching, the remaining two simulations were of the ageing and machining processes. From the thermo-couple data it was observed that the ageing process resulted in an almost homogeneous heating rate across the entire geometry. As such the ageing process was simulated by taking the entire part through the same rate of heating and cooling according to the thermo-couple characterisation. Throughout this heat treatment, the creep model was enabled to allow the quenched stresses to relax. As described in the previous sections, RR1000 creep behaviour was modelled using a the CT07 hyperbolic tangent creep strain representation derived by Rolls-Royce.

3.4.2.5 **Machining**

The machining process was modelled only in terms of the re-balancing of stress which resulted from regions of material being removed. As such the stresses imparted at the surface by the machining process itself was not taken into account. To simulate this process, the stresses prior to machining were imported into the model, and then the elements representing areas to be machining away were removed. Re-running the model at this stage thus allowed the stresses to re-balance and hence predict the residual stress in the post machined condition.

3.4.2.6 **Data extraction**

Each of the models could be visualised as a contour plot indicating the stresses in a particular direction (i.e. hoop, radial or axial) across the 2D geometry. Data extraction for comparison to other techniques was made by selecting a line scan and extracting the data as an x-y coordinate complete with the stress at that point.

3.5 Microstructural Characterisation

While the bulk of this study has been to characterise the manufacturing process in terms of residual stress, it is recognised that the heat treatment processes have been designed to achieving the optimum microstructure. In view of this, a microstructural characterisation was made using a scanning electron microscope (SEM) to asses the impact of the various quenches and ageing heat treatments on the γ/γ' microstructure.

3.5.1 Sample preparation

All samples, irrespective of heat treatment, were prepared in the following way. A small coupon was extracted from the centre of the forging by EDMing out a 6x6mm

cross section matchstick and then taking a slice from the centre ~6mm in width. Each coupon was mounted in phenolic resin for the grinding and polishing stages. Grinding was carried out using progressively finer silicon carbide paper down to a standard ANSI grit size of 1200. Polishing consisted of a 6μm followed by a 1μm diamond polish, and then finally a two hour polish using colloidal silica polish (OPS).

The final stage before using the microscope, was to remove the coupon from the resin and carry out a chemical etch. In this case the chemical etch is used to dissolve the γ′ precipitates, thus leaving behind holes in the surface which can be imaged as topological features with the SEM. The etchant is a so called 'Nickel two part' etch which is made using the chemicals detailed in Table 5.

Table 5: Chemical composition of the Nickel Two Part etch

Part I	Part II
150ml H_2O	15ml HNO_3
150ml HCl	25ml H_2O
2.5g MoO_3	30ml part I

Each coupon was washed using soapy water and ethanol, before being immersed in the etchant for 20-30s and then rinsed thoroughly in water.

3.5.2 Scanning Electron Microscope

To guarantee a high quality image, the later stages of sample preparation, in particular the etch, were carried out very shortly before imaging in the microscope. Each coupon was individually mounted on a secure stage and place inside an FEI Sirion Field Emission Gun Scanning Electron Microscope (FEG-SEM). The microscope is capable of imaging using many different setups, for the images captured here the microscope was setup to image secondary electrons using a through lens detector. Secondary electrons are those which are released from the outer shell of an atom through inelastic scattering of the incident electrons. The advantage to imaging secondary electrons is that they typically on travel a few nm through the material before being reabsorbed. As a result of this, the detected secondary electrons can be said to originate from a very thin layer, and as such provide a high resolution image of the topology of the surface (99).

Imaging of the intragranular γ' was made at 20000x magnification in each case. At this magnification it was possible to clearly observe and analyse the size distribution of the secondary γ' and compare this across the quenched and aged conditions.

Chapter 4

The Effect of d0 Reference Value on a Neutron Diffraction Study of Residual Stress in a γ/γ´ Nickel-base Superalloy

This paper was submitted for publication in the *Journal of Strain Analysis for Engineering Design* on 6th September 2012. The paper that follows is in the form in which it was submitted to the journal. This research was performed with Dr. Naveed Iqbal, Dr. Michael Hoffman, Dr. Alex Evans, Professor Michael Preuss, Dr. Mark Hardy, and Dr. Mike Glavicic

The lead author of this paper is the author of this thesis; all of the content which follows are the words of the lead author, and all of the data gathered and presented here is the result of investigations implemented by the lead author. In terms of co-author involvement, Dr. Naveed Iqbal, Dr. Michael Hoffman, and Dr. Alex Evans assisted with all aspects of data acquisition through neutron diffraction. Essential guidance and feedback was provided through Professor Michael Preuss, Dr. Mark Hardy, and Dr. Mike Glavicic.

The effect of d_0 reference value on a neutron diffraction study of residual stress in a γ/γ´ Nickel-base superalloy.

J. Rolph[1], N. Iqbal[1], M Hoffman[2], A. Evans[3], M. C. Hardy[4], M. G. Glavicic[5], M. Preuss[1]

[1] Materials Science Centre, University of Manchester, Grosvenor St, Manchester, M13 9PL, UK

[2] FRM2, TU München, Lichtenbergstr. 1, 85747 Garching, Germany

[3] Institut Laue-Langevin, BP 156, 6, rue Jules-Horowitz, 38042 Grenoble cedex 9, France

[4] Rolls-Royce plc, PO Box 31, Moor Lane, Derby, DE24 8BJ, UK

[5] Rolls-Royce Corporation, Indianapolis, IN, USA

Abstract

A nickel-base superalloy sub-scale disc has been studied using neutron diffraction to characterise the residual stress distribution following heat treatment. Strain has been calculated using measured neutron diffraction d-spacings in combination with d_0 reference values obtained using three distinct methods. Namely; measurement of a stress-free cube, a $\sin^2\psi$ characterisation (used independently and as a correction factor), and an axial stress-balance. In addition, data obtained using the contour method has been included since it allows comparison of diffraction based data to a technique that does not require a d_0 value. In terms of residual stress, agreement between all d_0 measurement techniques and the contour method was high, with the exception being those made using the $\sin^2\psi$ technique. An offset of approximately 350MPa was observed in this data and a possible systematic error ascribed to a unique diffraction characteristic of a γ/γ´ nickel-base superalloy. A global d_0 value obtained using a stress balance or stress-free cube was found to be reliable throughout the sample bulk in cases where thermal processing was carried out at a slow rate, such as ageing. However, d_0 differences equivalent to 400με were observed between central and surface regions when a global d_0 was applied to a water quenched sample.

1. Introduction

Residual stresses are introduced into an engineering component through a number of widely used manufacturing steps including; forging, heat treatment and machining. The level of residual stress within a component is known to affect performance as it can promote or retard failure mechanisms (Withers, 2007). Characterisation of residual stress following manufacture is therefore a crucial part of understanding the in-service capabilities of any single component. The measurement techniques used to determine residual stressγ´ include destructive techniques such as slicing and hole drilling, as well as non-destructive techniques such as neutron and x-ray diffraction (Withers and Bhadeshia, 2001). In each case residual stress is calculated from the measured elastic strain and material specific elastic properties.

In a diffraction experiment, the inter-planar spacing can be derived from the measured diffraction angle 2θ as given by Bragg´s law (Eq. (1)).

$$\lambda = 2d\sin\theta \tag{1}$$

The inter-planar spacing acts as an atomic strain gauge, measurable through equation 1. When using neutron diffraction for stress analysis, strain is calculated by comparing a specific hkl lattice spacing, d^{hkl}, or the lattice parameter a, to a reference value representing a stress free lattice spacing, also known as d_o^{hkl} or a_0 (Eq. (2)).

$$\varepsilon = \frac{d^{hkl} - d_0^{hkl}}{d_0^{hkl}} = \frac{a - a_0}{a_0} \tag{2}$$

When using a specific lattice plane for stress determination, it is important to choose one that is insensitive to intergranular strain development during plastic deformation, as this would affect any elastic strain determination in components with plasticity induced stored energy (Stone et al., 1999b). The lattice parameter a is considered to be free of such intergranular strain development (Dye et al., 2001).

By measuring strain in the three principal directions it is possible to calculate stress using the following relation.

$$\sigma_x = \frac{E_{hkl}}{(1 + v_{hkl})(1 - 2v_{hkl})}\left[(1 - v_{hkl})\varepsilon_x + v_{hkl}(\varepsilon_y + \varepsilon_z)\right] \quad \text{and} \quad \sigma_y = ..etc. \tag{3}$$

Where the principal strain directions are denoted as x, y, z and E_{hkl} and v_{hkl} represent plane specific diffraction elastic constants. In the case when strain is based on lattice

parameter measurements, conventional bulk elastic properties can be used. The elastic constants used in this particular study are given in Table 1. These properties are specific for RR1000, which is a γ' precipitation strengthened polycrystalline nickel base superalloy for disc application that was investigated in the present study. The γ' precipitates are an ordered phase with a $L1_2$ crystal structure while the γ matrix is face centre cubic (fcc). The two phases have a cube-cube orientation relationship and, due to an almost identical lattice parameter, γ' is often coherent with the γ matrix. In RR1000 the volume fraction of γ' is close to 50%.

The measured strain, and hence calculated stress, is highly sensitive to the d_0 value. Consequently, it is recommended that an uncertainty half that of the d-spacing is sought to reduce inaccuracies (Wimpory et al., 2009). One of the most widely used d_0 measurement techniques is to remove a coupon from the sample that is of sufficiently small dimension to have zero type I stress. This coupon is measured during the neutron diffraction experiment alongside the actual component to obtain the required d_0. However, in cases of significant d_0 variations due to dramatic microstructural variations, a large number of cubes or a comb type sample are required to account for the d_0 value at each measurement location. If a more detailed d_0 characterisation is required, a $\sin^2\psi$ technique can be employed across a sample surface to map d_0 to a resolution depending on the chosen spot size. Further detail on d_0 measurement including the $\sin^2\psi$ technique can be found in the in-depth review given by (Withers et al., 2007).

In the present paper we report the observed variations in residual stress calculated from the same neutron diffraction data using three techniques to characterise d_0: A stress-free cube measurement, an axial stress balance, and a $\sin^2\psi$ lab x-ray diffraction measurement. A fourth d_0 dataset was generated by using the $\sin^2\psi$ data as a position dependant correction factor for the stress-free cube measurement. The material studied was a γ' strengthened nickel-base superalloy, which displays a complex diffraction spectrum due to the matrix (γ) and precipitates (γ') having almost identical lattice parameters. In order to determine the validity of the three independent d_0 techniques additional residual stress analysis was carried out using the contour method (Prime, 2001). This method consists of sectioning a sample, thus relaxing the residual stress, and then measuring the newly created (and deformed) surface contour to infer the original residual stress distribution. As this method is

based on a completely different approach without the requirement of knowing a d_0 value, it was considered to be most appropriate for validation. The focus of this paper is to draw together these datasets to study the impact of d_0 characterisation on the final residual stress calculated using diffraction techniques.

2. Experimental description

Material

ATILadish Forgings provided two sub-scale forgings of the nickel-base superalloy RR1000. The nominal chemical composition of RR1000 is given in Table 2. The samples were of small disc shape with a diameter of 76.2mm, and a thickness of 25.4mm (Figure 1). Prior to any measurement, the samples were processed as follows.

Each specimen was cut from a large pancake forging at the same radial distance to ensure a closely matched thermo-mechanical history for each part. Sample 1 (S1) was sub γ´-solvus heat treated at 1120°C for 4 hours followed by water quench. Sample 2 (S2) was subjected to an identical heat treatment but with the addition of a 2 hours ageing heat treatment at 760°C.

The water quench process was chosen in this sub-scale geometry to achieve high levels of residual stress despite the small geometry of the sample, whilst an ageing temperature of 760°C was chosen because it is a typical stress relief/ageing temperature for γ´ strengthened nickel-base superalloys.

Residual stress analysis by neutron diffraction

All neutron diffraction measurements were carried out at the dedicated strain scanning instrument STRESS-SPEC at FRM-II, Germany (Hofmann et al., 2006).

Both samples were mounted simultaneously on a computer controlled translator table and aligned initially using a theodolite, and then more carefully using entry scans with the neutron beam. For the measurement of strain in RR1000 the Ni (311) reflection was chosen for its low sensitivity to plastic strain and good representation of the bulk (Stone et al., 1999a). Using a wavelength of $\lambda = 1.55$ Å the (311) diffraction peak was recorded at $2\theta = 92°$, which provided an approximately cubic gauge volume.

In order to calculate stress it was necessary to measure strain in three perpendicular directions, namely hoop, radial and axial as indicated on Figure 1. Five measurements were made along each of three line scans; the centre line (CL) and ±7mm from CL, making a total of fifteen points. In order to balance spatial resolution with count statistics, a gauge volume of 4x4x4 mm^3 was chosen and defined using primary and secondary slits.

Data analysis was carried out during and immediately after completion of each measurement point using an FRM-2 in-house software package known as StressTex. This software allowed fitting and subtraction of the background, followed by a Gaussian fit of a single peak to obtain a value of d-spacing. However, in a γ′ strengthened nickel base superalloy, such as RR1000, any fundamental reflection contains contributions from both the γ and γ′ phases, thereby making a Gaussian fit an averaging of both phases. As such the measured strain and subsequently calculated stress is an average over both phases; this is widely accepted to be a good representation of bulk behaviour when measuring the (311) reflection {Stone, 1999 #137}{Cihak, 2006 #169}. However, whilst this holds true while measuring on either a neutron or x-ray diffraction instrument, it has the potential to be an issue when directly combining the two. This is related to Titanium having a negative neutron scattering factor (Rauch and Waschkowski, 2003) and since Titanium is a γ′ stabilising element it partitions to the γ′ phase and reduces the γ′ fundamental peak intensity when using neutron diffraction while this effect is not expected when using x-ray diffraction. As a result, strain calculations made using a neutron derived d-spacing in conjunction with an x-ray derived d_0 are likely to generate systematic errors.

During the neutron diffraction experiment, the fit uncertainty value was used as a guide to check that the count times per point were sufficient to generate reliable data. For this experiment the aim was to calculate stress to an accuracy of ±50MPa or less, which on this instrument meant achieving a fit uncertainty of approximately 2θ=0.025° (~220με) in each direction.

Figure 2a shows a comparison of the fit uncertainty with measurement position for S1 in transmission orientation. Count times were kept the same for each point shown with the exception of points at 35mm radial distance. These points could be counted for half the time due to their proximity to the rim and hence reduced neutron path

length. Overall, Figure 2a shows a general trend that the fit uncertainty falls once the measurement position approaches the sample rim. This is due to the diffracted neutron beam leaving through side of the sample, thus requiring a shorter path length.

In reflection orientation (Figure 2b) we observe very similar uncertainties along the CL, but reduced uncertainties along the ±7mm line. Note that the +7mm and -7mm scans have identical path lengths in this case owing to the sample being rotated 180° in 2θ to access the -7mm line scan through the back face. The data shown in Figure 2 indicates that for the most part the ±220µε limit was adhered to but for a handful of measurement points. In these locations, time limitation forced a compromise to be made and uncertainties rose as a result.

The fit uncertainty was used to calculate errors in the residual stress values as described by (Wimpory et al., 2009). However, as has been observed by (Frankel, 2008), the uncertainty in fit does not necessarily reflect the uncertainty in residual strain and stress. It is possible that a poor fit, if applied to each peak equally, may map a peak shift without issue despite not fitting the peak to a high accuracy. It was therefore worth comparing a fit uncertainty to an uncertainty obtained by making a repeat measurement under identical conditions. In this experiment, it was noted that at the sample centre the hoop and radial measurements were essentially the same point; therefore the difference between the values obtained could be used as a typical error.

Characterisation of d_0

Measurement of d_0 using neutron diffraction was carried out using cubes of sufficiently small size to have zero macrostress as discussed in (Withers et al., 2007). Due to a lack of additional material such measurements had to be carried out at a later date to the primary neutron diffraction measurement as made on Stress-Spec. A 6x6x6mm^3 cube was extracted at mid-diameter and thickness, using conventional cutting techniques and mounted on the strain scanning instrument SALSA at the ILL, Grenoble, France. A 4x4x4mm^3 gauge volume was aligned carefully using entry scans to ensure full gauge volume immersion within the sample, which was crucial to avoid pseudostrains generated by partial immersion (Johnson et al., 2003). Measurements were made using the same setup on the (311) hkl plane with a relatively long count time to ensure good count statistics and low peak position

uncertainty. It must be noted that the use of two separate diffraction instruments for a single investigation can bring about additional uncertainty in the final stress calculations. To overcome this a calibration measurement was made on both on Stress-Spec and SALSA using an RR1000 powder sample.

The $\sin^2\psi$ technique is widely known as a technique to measure stress without the need for a d_0 value (Withers et al., 2007). However, it has been shown to be equally applicable to determination of d_0 (Hauk, 1997). It is in this format that the $\sin^2\psi$ technique has been employed in this investigation.

To obtain a full d_0 map and thus generate accurate residual stress data, a $\sin^2\psi$ measurement was undertaken at each neutron measurement point (Figure 1). Application of the $\sin^2\psi$ technique to these points using x-rays required a slice to be removed from each sample to gain access. To extract the slice, a first cut was made using electro-discharge machining (EDM) in ´skim cut´ mode. The cut was carried out across the diameter of the sample at the same circumferential position as the neutron diffraction line scans. Thus the free surface revealed was that on which the three neutron line scans were made. EDM was chosen for the first cut as it allowed a contour method measurement to be made on the cut faces, details of which are provided in the next section. Following the initial EDM cut, a second conventional cut was made across the diameter parallel to the first to extract a 5mm thick slice from one sample half. This process was followed for S1 and S2, with the result that a 5mm thick cross-sectional slice was extracted from each sample.

As final preparation before measurement, the face of each slice cut with EDM was ground and polished back to the base material. This was essential since the EDM cutting process generates a re-cast layer along the surface, which can affect the d_0 value for the sample.

The instrument chosen for the $\sin^2\psi$ measurement was a Bruker AXS D8 lab-based x-ray diffractometer coupled to a GADDS 2D area detector. The instrument was setup with a Fe tube, which, when driven at 20KV and combined with a sequence of foil filters, produced a monochromatic Kα beam at λ=1.94Å. In the case of the Bruker instrument, the beam is passed through a collimator to give a spot size of ~1mm, and an approximately parallel beam. To acquire d_0 data relevant to the neutron study the (311) plane was chosen again, which in this setup gave a 2θ angle of ~127°.

Both slices were mounted simultaneously on a translational sample stage attached to an Eulerian cradle that is capable of rotation around the beam focus point. This setup allowed translation in x, y, and z, and rotation in 2θ, ψ, and ϕ. In this way it was possible to undertake $\sin^2\psi$ measurements in two orthogonal directions, $\phi=0$ and $\phi=90°$, with ψ ranging from 0-45° in steps of 5°.

Alignment on the Bruker system is carried out by rotating the stage to place the sample surface perpendicular to a laser and camera system. The laser and camera are set at an angle to each other such that the laser beam falls in the centre of the camera cross-hairs when the sample surface is the correct distance from the x-ray source. Each measurement point was aligned in this way by moving the laser and camera to a point and re-focusing, thus generating a set of x, y, and z positions which were executed within a customised script.

Each diffraction peak was fitted using the Bruker STRESSplus software package. A sliding gravity approach was used to obtain the peak centre in 2θ and this was written into a stress report along with the angle of ψ and ϕ. Using Bragg´s law to convert from 2θ to d-spacing, we obtain a data set of d-spacing values over a range of $\sin^2\psi$ angles for the two orthogonal directions in ϕ. As described in (Hauk, 1997), the relationship between $\sin^2\psi$ and d-spacing is linear providing there are not significant shear stresses present. A linear fit was therefore carried out for each ϕ direction and the gradient of each fit used to calculate the d_0 value.

As a data check, the linearity of each $\sin^2\psi$ vs. d-spacing plot was calculated as an r^2 value, also known as a Pearson correlation coefficient (Weisstein), where an r^2 value of one indicating perfect linear relationship. By calculating r^2 for each measurement point and setting a limit of 0.9 it was possible to filter the entire data set and identify $\sin^2\psi$ plots that contained anomalous data points. The points were then marked as such and removed from the data set.

The x-ray d_0 values obtained were incorporated into the final residual stress calculations in two distinct ways. Firstly, by using a powder sample of RR1000 measured on both instruments to calibrate between neutron and x-ray d-spacings. The ratio of powder d-spacings measured on each instrument was used as a multiplication factor to convert from x-ray d_0 values to neutron d_0 values. Secondly, by normalising the x-ray d_0 value with respect to the location from which a d_0 stress-free cube was

measured, in this case at mid diameter and thickness. The normalised d_0 variation could then be multiplied by the d_0 value obtained from the stress-free cube to give a full d_0 map without the use of a powder calibration.

Prior to d_0 characterisation by x-ray diffraction, a preliminary study was carried out to assess the precision of the alignment system and to obtain a characteristic error for this technique on this instrument. This study was carried out in two stages:

The first stage tackled the issue of sample alignment. The technique employed was to take measurements whilst moving systematically through the focus point of the beam and to assess to what degree the focus point affected the d_0 value obtained. Following this, the instrument was repeatedly de-focused and re-focused upon the same point and the variation in the value of z recorded each time. These two exercises revealed the correlation between focus and d-spacing, and the fundamental limit to the accuracy of this alignment system (Figure 3).

From Figure 3a one can see a linear relationship between the focus point and the d-spacing measured. To ease comparison with experimental error this is also expressed in terms of microstrain. The limits of repeatable focusing are shown as dashed lines. They indicate a focusing accuracy of ±0.02mm, which translates to ±25με. Since diffraction experiments errors of approximately ±100με are generally expected (Webster et al., 2002), it was concluded that focal alignment is expected to add only a very minor experimental inaccuracy.

The second stage of this preliminary study assessed the inherent error in the instrument. The method employed was to measure a point, move each of the motors to a new position, and then return to the same point and re-measure. This was repeated ten times to observe the instrumental scatter in d-spacing, and then converted into microstrain to be expressed as an error (Figure 3b).

It can be seen from Figure 3b, that the instrumental error was no greater than ±60με, with the standard deviation being ±30με. Having conducted this study, it was possible to conclude that the d_0 measurements are expected to have an experimental accuracy better than ±80με.

Finally, the third approach to determine a correct d_0 was the application of a stress balance as described in (Withers et al., 2007). The axial component of stress was forced to balance across a circumferential sweep of the central line scan (CL). This

approach required the compressive axial stress at the rim surface to balance with a tensile region immediately behind it; much of the remaining line scan had near zero axial stress. The central line scan was chosen in this case since the neutron diffraction data points were found to be the most reliable away from the steeper stress gradients closer to the surface.

The Contour Method

The contour method for measuring residual stress is a relatively new technique, which measures a full cross sectional map of residual stress normal to a cut surface. The technique is based upon the elastic relaxation of residual stresses causing a surface deformation immediately following a cut. The deviation of the surface contour from a planar surface is measured and then used to calculate the original residual stress distribution (Prime, 2001).

Each sample was sectioned in half using EDM. The EDM cut was made across the sample diameter using a very slow cut rate, also known as a ´skim cut´; this was chosen so as to ensure the cutting process did not contribute to the residual stress state of the sample. Details of the cutting parameters have been given in Table 3. Each sample half was placed on a Nanofocus confocal laser profilometer to measure the surface contour. This instrument has a theoretical vertical precision of approximately 10nm, for stress contour measurements this at least two orders of magnitude greater than required. The laser profilometer was set up to measure at 100µm intervals across the entire surface, generating a total of approximately 227,000 measurement points per sample surface. Measurement locations with a reflectivity lower than 80% indicated the laser had moved over the sample edge; these data points were masked off and set to a default low value. This data was then exported for analysis in commercially available data manipulate and finite element software packages.

The surface contour from each sample face was imported individually and run through a script to remove the masked points from the data and identify the sample outline. Following this, the data was manually checked for artefacts and any identifiable outliers removed. In this case it was necessary to remove 5mm of data from the end of the sample to eliminate artefacts generated as the EDM wire exits the work-piece (Frankel, 2008).

The two datasets, one for each face, were aligned by minimisation of misfit strain between the corresponding outlines of each half. After alignment an average of the two displacements was made. The averaging process allowed all stresses, except those normal to the surface, to cancel out with those on the opposite face. The displacement left over after averaging was therefore said to be solely generated by the relaxation of residual stresses normal to the cut (Prime, 2001). Finally, experimental noise was removed; this was achieved by implementing a bi-variant spline fit to the averaged surface as described by (Prime et al., 2004). The spline fit to the contour therefore represented the displacement from which bulk residual stress would be calculated.

In order to model accurately the sample geometry, the measured outline was used directly as the starting point from which a 3D mesh was generated. This was achieved through extruding the outline back by the sample radius and then forming a semi-circular shape out of the extruded block. The part was meshed using quadratic elements with a bias to allow a dense mesh near the deformed surface and a coarse mesh further back. The typical mesh length at the surface was 1mm, which increased to 3.5mm length at the curved back-face of the sample. The fully meshed part was combined with the spline fit of the contour to form the initial and final conditions for the finite element model.

Since the contour method assumes elastic isotropy, residual stress can be calculated from the relaxation data using bulk material properties. Using the bulk Young´s modulus and Poisson ratio (Table 1), with the sample mesh as an initial state, and the surface contour as the final state, a model is generated. By solving this model a 2D map of the residual stress normal to the cut surface was generated.

3. Results and Discussion

d_0 variation

Figure 4 shows d_0 variation with radial distance as characterised using the $\sin^2\psi$ technique in S1 and S2, with the data being expressed as ´raw´ d-spacing and in terms of microstrain. The reference point for the microstrain calculation was mid diameter and depth for each sample. The calculated microstrain is therefore a measure of significance in d_0 variation rather than a real and measured strain in the sample.

Figure 4a shows the d_0 variation with radial distance across three line scans in S1. It is clear from the data that a trend exists for the d_0 value to increase near to the sample rim, and that the degree to which this is occurring varies with sample depth. Across the centre line scan only a marginal increase of d_0 value is seen, whereas at +7mm and particularly at -7mm stronger trends are visible. A possible explanation for this may exist through considering the thermal history of the sample with respect to measurement position. The water quench process will rapidly cool the sample exterior whilst the interior will lag behind and cool at a slower rate. In this transient period, thermally dependant elemental diffusion processes within the alloy will exist for longer in the sample core than in the regions close to the surface. The net result of this would be to cause a variation in chemical composition of the γ and γ' phases with respect to proximity to the surface. Since the (311) diffraction peak measured to calculate d_0 is made up from both the γ and γ' phases this would lead to a change in peak shape and therefore a shift in the fitted Gaussian. This in turn would alter the stress-free lattice spacing and it is postulated would lead to a d_0 variation such as that shown in Figure 4.

The d_0 variation of S2 is shown in Figure 4b. Comparing Figures 4 a and b, it is apparent that the aging heat treatment has reduced significantly the d_0 variation. The additional ageing heat treatment will have allowed the chemical compositions of γ and γ' to evolve towards equilibrium and reducing the effect of the initial different cooling rates as a result of the quenching process.

Figure 5 shows the potential impact on an arbitrary stress calculation if an apparent d_0 variation such as that seen in Figure 4 is ignored, this has been termed a 'pseudostress'. To calculate the pseudostress the microstrain data displayed in Figure 4 was assumed to be equal in the three principal directions and stresses were calculated using Eq. (3). The aim of Figure 5 is to assess the simplified use of a global d_0 on the accuracy of the calculated residual stresses. Figure 5a demonstrates that significant pseudostresses are calculated of up to 200MPa in the regions near the rim and close to each sample face, i.e. at ±7mm from CL. However, along the CL, pseudostresses do not exceed ±50 MPa except for the point closest to the rim. In contrast to this, the aged sample (S2) generates pseudostresses for all three line scans, which, with the exception of a single point, are within ±50MPa, (Figure 5b). In view

of this, consideration should be given not only to the thermal processing, but also to the measurement locations within the sample.

d_0 measurement technique and stress calculation

The residual stress profile along the CL and CL +7mm scans of S1 and S2 are shown in Figure 6 and 7 respectively. Data from the -7mm scan has not been included since the neutron diffraction data was incomplete along this line scan, thus preventing any useful comparison from being made. Four methods were used to obtain the d_0 reference value; x-ray $\sin^2\psi$ measurement, stress balance, stress-free cube measurement, and position dependant correction of the cube data using the $\sin^2\psi$ findings. The d_0 measurements obtained from the x-ray $\sin^2\psi$ approach were calibrated against the neutron diffraction data by having a powder measurement on both sources. The residual stresses that resulted from each method have been plotted for comparison. In addition, residual stress data obtained by the contour method measurement technique is added to both line scans.

In both Figure 6 and 7 along the CL and +7mm line scans the agreement between each of the d_0 measurement techniques is high with the exception of the xrd method, which shows a relatively consistent offset of ~400MPa. The consistency of the offset in this data points to a systematic error generated as a result of using x-ray diffraction to obtain a d_0 value for neutron diffraction data. Furthermore, the calculated stresses are in some cases significantly above yield (~1200MPa) which indicates an erroneous result. As already discussed, it is suspected that this is the result of the differing diffraction characteristics of the γ/γ' peak when using neutrons and x-rays in combination.

The axial stress balance can be compared to the cube d_0 since they both generate a single global d_0 value for the entire sample. In both S1 and S2 the two d_0 approaches gave almost identical residual stress profiles indicating the stress balance to be a good approximation of the measured d_0 in this case. However, it is acknowledged that a stress balance is subject to comprehensive measurement of a valid cross section, the symmetry of the stress distribution, and the uncertainty of each data point. Given this, the stress balance is best used as a first approximation before a more thorough d_0 characterisation is carried out, as was the case in this investigation.

The cube d_0 with and without the XRD correction factor can be compared along each line scan, the differences indicate the significance of a full d_0 characterisation on final residual stress calculations. Figure 6a, the WQ CL scan, indicates the correction factor only alters the residual stress at the 35mm location, and by approximately -100MPa. In addition, the correction factor result agrees more closely with the contour method data, although a 300MPa discrepancy still exists between the two datasets at this location. From the bore through to the 30mm location the correction factor has very little effect, indicating minimal d_0 variation in this region. The WQ +7mm line scan shows a similar trend to the CL scan, in particular that very little d_0 variation is observed at the bore. However, at the 30mm and 35mm locations the correction factor has an impact on the residual stress of -100MPa and -200MPa respectively. As with the CL scan, the correction factor produces stronger agreement between the contour method and neutron diffraction data, pointing to a real effect which is being accounted for in the XRD correction factor. In the WQ sample the rapid quench has resulted in the near surface regions cooling faster than those close to the bore; it is thought that such differential cooling has resulted in a change in alloy composition close to the surface, and thus in d_0 value.

Figure 7 plots the same two line scans as S1 but for the 2hr aged (S2) sample. Along the CL scan (Figure 7a) the cube d_0 with and without XRD correction show very little difference in final residual stress value, only at the 35mm location is a change of approximately -50–100MPa is visible. Along the +7mm a very similar trend is observed, with the correction factor only playing a role at the 35mm location, altering the measured residual stress there by -100-150MPa. As with S1, the generation of this d_0 variation is thought to originate in the differential cooling of the quench. However the addition of an ageing process is likely to allow further elemental diffusion to occur, which will further alter the composition and thus the d_0 value. Comparing the near rim locations in the CL and +7mm scans for S1 and S2, it can be seen that the ageing process appears to have marginally reduced the impact of the XRD correction factor. This trend agrees with what should be expected, since the XRD data (Figure 4 and 5) showed a reduced pseudostress effect in S2 compared to S1 when assuming a uniform d_0. Overall the results indicate an ageing heat treatment allows a partial reversal of the chemical composition gradient setup by the quenching process, which is observed as a reduced d_0 variation.

4. Conclusions

The d_0 variation within a forging following heat treatment shows a correlation to the measurement location, in particular with proximity to the sample surface. It is believed this is related to the elemental diffusion between phases set up by the differential cooling rates as the sample surface cools more rapidly than the interior. It was found that although a global d_0 can be applied to the sample, a pseudostress will result once this d_0 is used near to the surface. In the most extreme case a pseudostress of 200MPa was generated in a water quenched sample. In comparison, the aged sample generated a maximum pseudostress of 100MPa, with most other measurement locations being less than 50MPa. The reduced d_0 variation in the aged condition is thought to be the result of elemental diffusion during aging, which works to create a more stable chemical composition of γ and γ' setup by the quench.

The Nickel superalloy powder calibration between the d-spacings measured using x-rays and neutrons was found to be unreliable in this alloy. The presence of Titanium, which has a negative scattering factor when using neutrons, is thought to have generated an offset in the powder d-spacing when compared to the x-ray measurement. However, data from each experiment remained valid, and an alternative means of calibrating between the two datasets was found using a stress-free cube as measured on the neutron beam line. An axial stress balance was also conducted and the residual stress values obtained compared. Whilst in this case reasonable agreement was seen, it was acknowledged that the stress balance method of obtaining a d_0 is open to a number of inaccuracies and should be treated as an estimate rather than a final characterisation.

The $\sin^2\psi$ measurement was employed as a position dependant correction factor to the stress-free cube measurement of d_0. In the subsequent stress calculations the corrected d_0 differed from the stress-free cube in regions close to the surfaces of the specimen, where more rapid cooling had taken place. In both the water quenched and aged samples this improved agreement in the neutron diffraction and contour method data. In view of this trend, it is felt that during strain measuring diffraction experiments in quenched specimens, the measurement line scans are chosen with consideration to the d_0 variation. If a global d_0 (i.e. single cube or far field measurement) is to be used, strain measurement locations should avoid near surface regions or accept a large uncertainty due to measured pseudo-strains. If accurate bulk

and near surface measurements are required, a more detailed d_0 study should be carried out to account for variation across each line scan. In a γ/γ' Nickel superalloy the $\sin^2\psi$ technique is ideally suited to a full d_0 characterisation, providing it is used as a position dependant correction factor to global d_0, as opposed to a direct d_0 measurement technique.

Acknowledgements

List of tables:

Table 1: Material properties of RR1000 {Grant, 2011 #176}

Material Properties of RR1000	
Young´s modulus (bulk)	224 GPa
Poisson ratio (bulk)	0.33
(311) Diffraction elastic constant	203 GPa
(311) Poisson ratio	0.3

Table 2: Nominal composition of Nickel superalloy RR1000

Alloy	Ni	Cr	Co	Mo	Ti	Al	C	B	Ta	Zr	Hf
RR1000	52.3	15.0	18.5	5.0	3.6	3.0	0.027	0.015	2	0.06	0.5

Table 3: EDM cutting parameters

Cutting parameters for RR1000 sub-scale forgings	
Wire type	Brass (uncoated)
Wire diameter (mm)	0.30
Wire feed rate (internal machine value)	12
Cutting speed (mm/min)	0.25
Wire voltage (internal value for skim cut)	14
Water flushing rate (L/min)	8
Clamping arrangement	Part clamped to two rails within the tank either side of cutting plane

Figure 1: Schematic diagram of the sub-scale ´hockey puck´ forgings with a) the measured gauge volumes indicated, and b) the neutron path and strain directions.
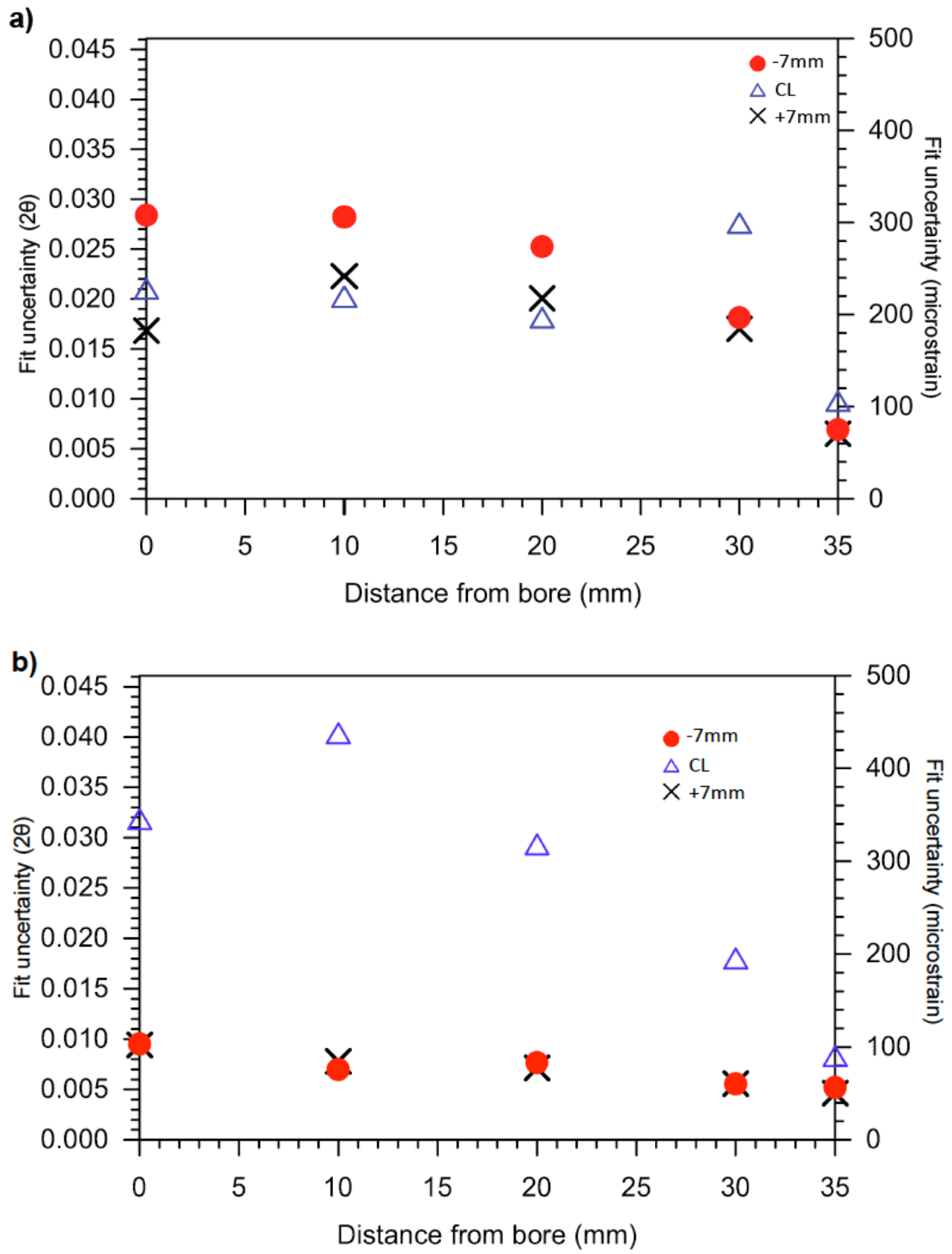
Figure 2: Fit uncertainty with measurement location in a) transmission and b) reflection in sample 1 (water quenched)
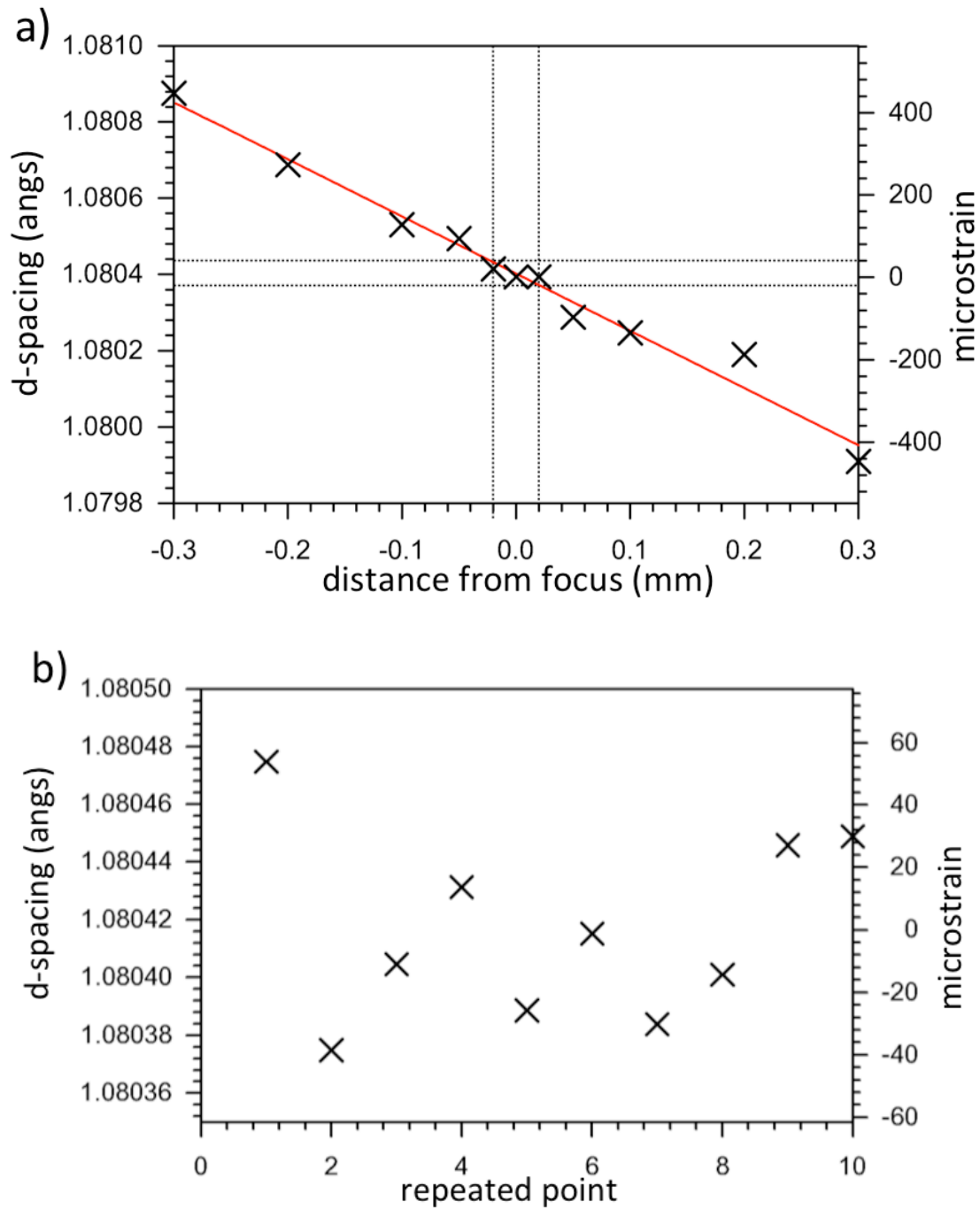
Figure 3: a) The shift in d-spacing measured as a result of changing the focus point with respect to the sample surface. b) The instrumental scatter of the Bruker GADDS diffractometer when measuring the d-spacing on the Nickel superalloy RR1000
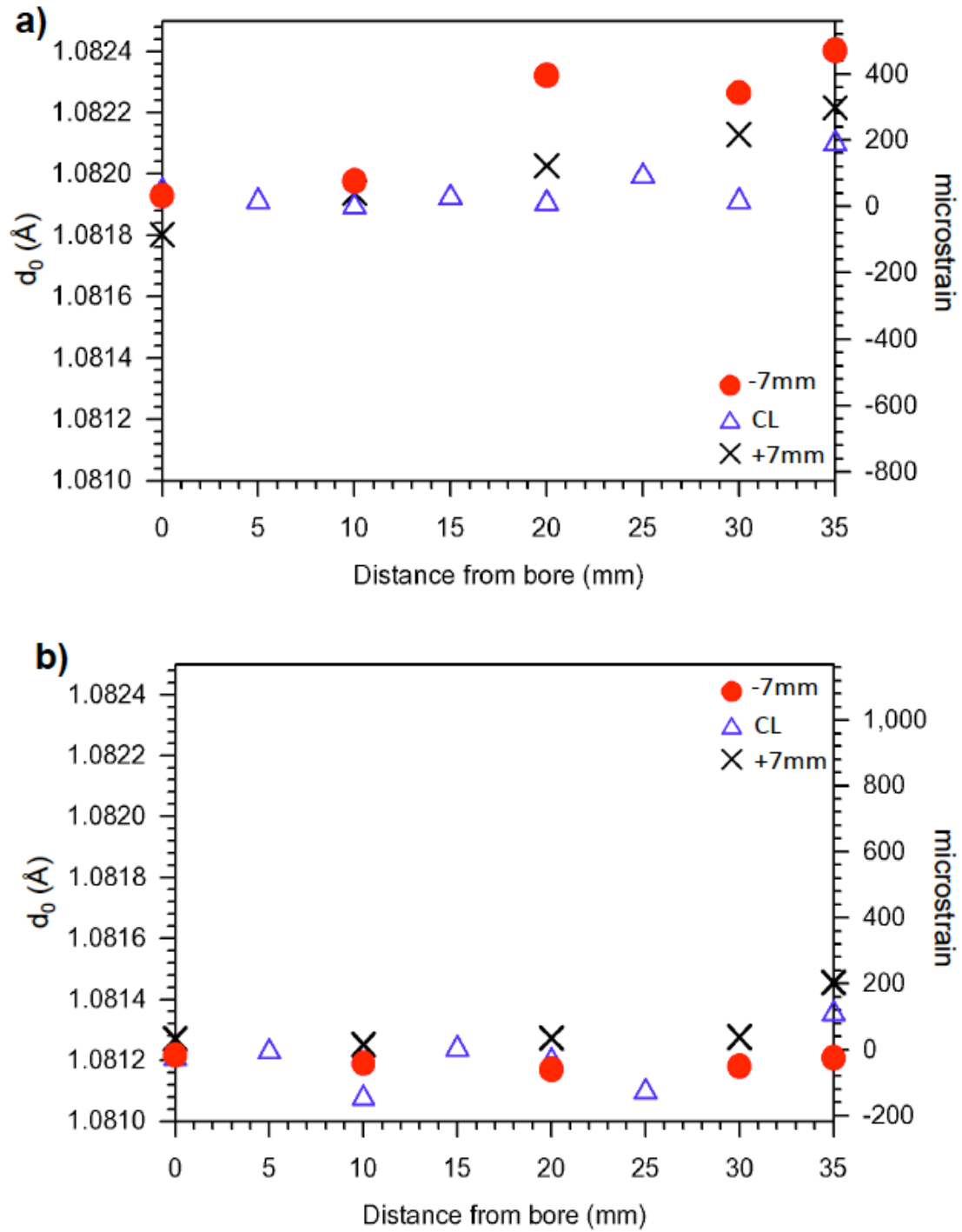
Figure 4: d_0 value with measurement position in a) sample 1 (water quenched) and b) sample 2 (water quenched and aged). Typical error ±50με
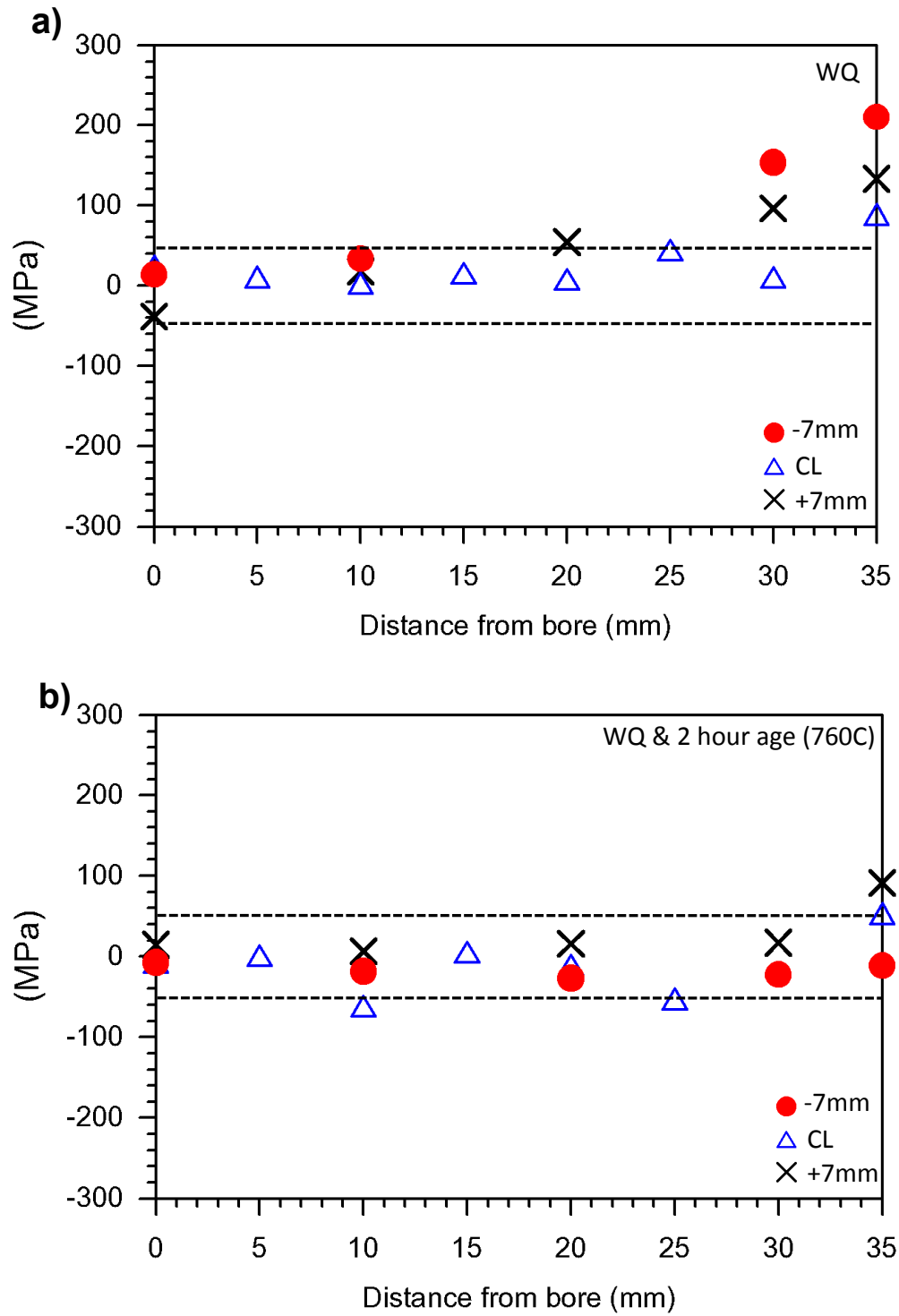
Figure 5: d_0 value with measurement position expressed in terms of ´pseudostress´ in a) sample 1 (water quenched) and b) sample 2 (water quenched and aged). Typical error ±30MPa
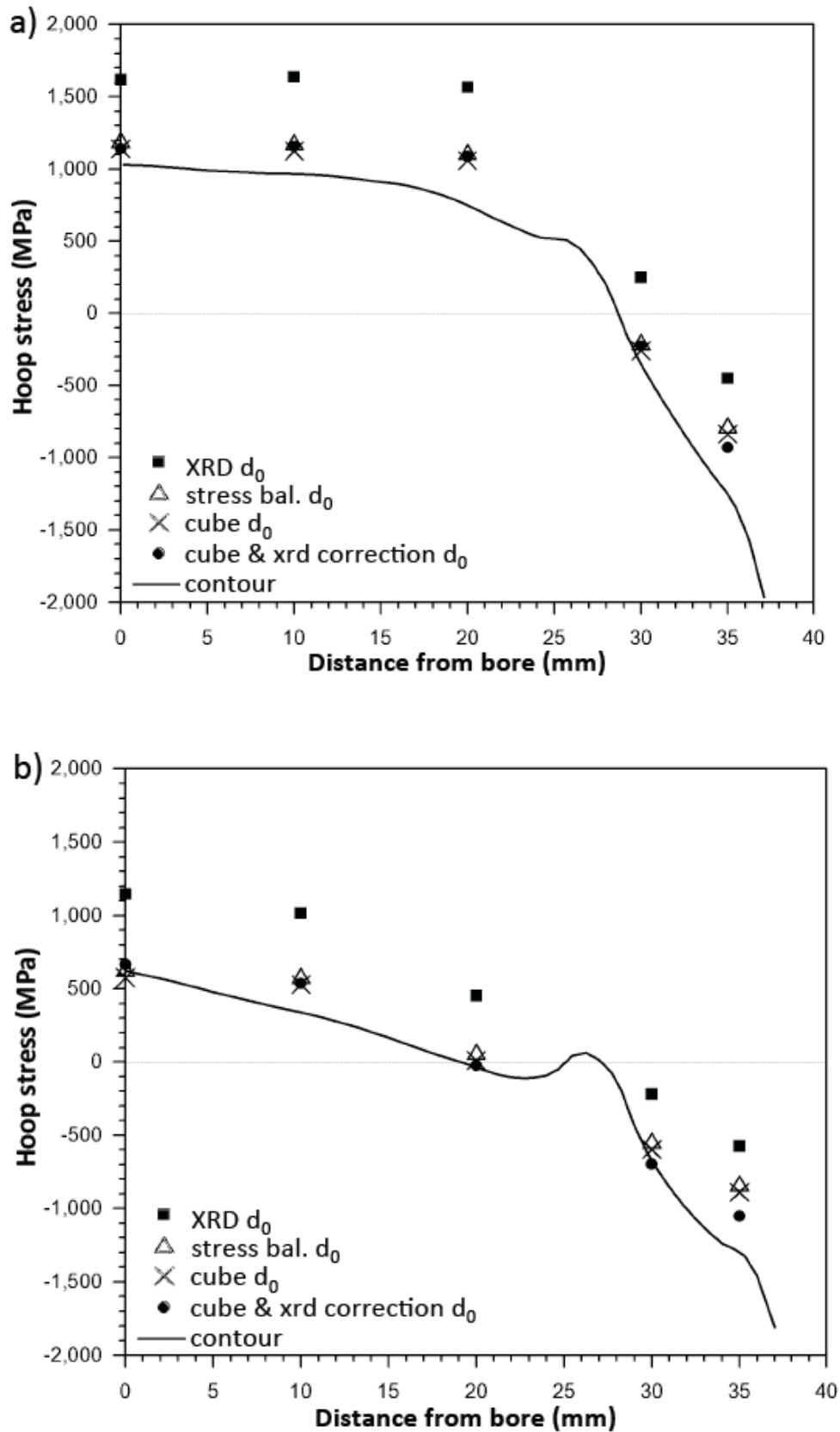
Figure 6: A comparison of d_0 measurement techniques in terms of calculated residual stress (hoop) as applied to neutron diffraction data from the a) CL line scan and b) +7mm line of **sample 1** (water quenched).
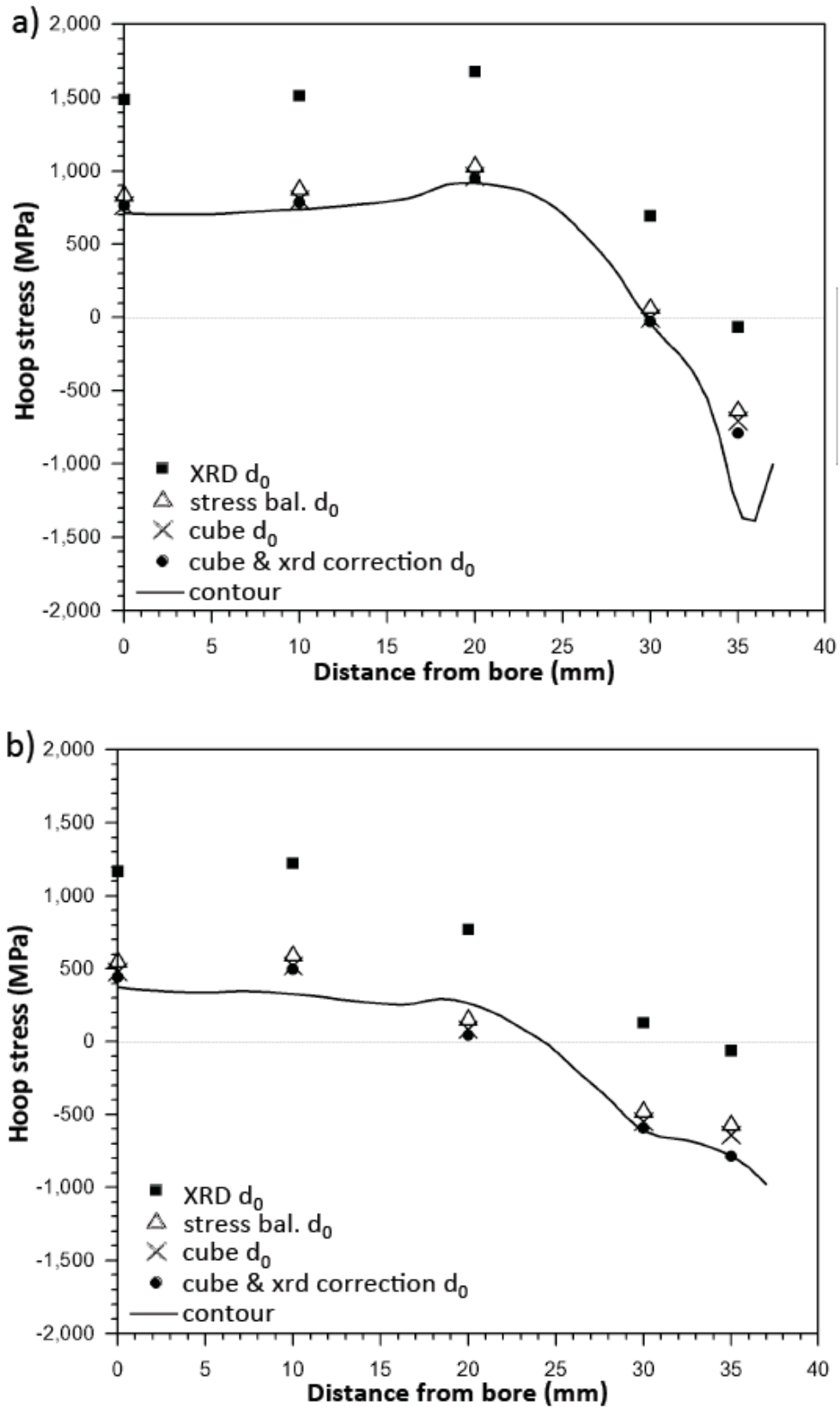
Figure 7: A comparison of d_0 measurement techniques in terms of calculated residual stress (hoop) as applied to neutron diffraction data from the a) CL line scan and b) +7mm line of **sample 2** (2hr age).

References

ALLEN, A., ANDREANI, C., HUTCHINGS, M. T. & WINDSO, C. G. 1981. Measurement of internal stress within bulk materials using neutron diffraction. *NDT International*, 249-254.

DYE, D., STONE, H. J. & REED, R. C. 2001. A two phase elastic–plastic self-consistent model for the accumulation of microstrains in Waspaloy. *Acta Materialia,* 49, 1271-1283.

FRANKEL, P. G. 2008. *Residual Stresses in Aerospace Components.* EngD, University of Manchester.

HAUK, V. 1997. *Structural and Residual Stress Analysis by Nondestructive Methods: Evaluation - Application - Assessment*, Elsevier.

HOFMANN, M., SCHNEIDER, R., SEIDL, G. A., REBELO-KORNMEIER, J., WIMPORY, R. C., GARBE, U. & BROKMEIER, H.-G. 2006. The new materials science diffractometer STRESS-SPEC at FRM-II. *Physica B*, 1035-1037.

JOHNSON, M. W., DAYMOND, M. R., FITZPATRICK, M. E. & LODINI, A. 2003. *Analysis of Residual Stresses by Diffraction Using Neutron and Synchrotron Radiation,* London, Taylor and Francis.

PRIME, M. B. 2001. Cross-sectional Mapping of Residual Stresses by Measuring the Surface Contour After a Cut. *Transactions of the ASME,* 123, 162-168.

PRIME, M. B., SEBRING, R. J., EDWARDS, J. M., HUGHES, D. J. & WEBSTER, P. J. 2004. Laser surface contouring and spline data smoothing for residual stress measurement. *Experimental Mechanics,* 44, 176-184.

RAUCH, H. & WASCHKOWSKI, W. 2003. *Neutron Data Booklet,* Philadelphia, Old City Publishing.

STONE, H. J., HOLDEN, T. M. & REED, R. C. 1999a. Determination of the plane specific elastic constants of waspaloy using neutron diffraction. *Scripta Materialia,* 40, 353-358.

STONE, H. J., HOLDEN, T. M. & REED, R. C. 1999b. On the generation of microstrains during the plastic deformation of Waspaloy. *Acta Materialia,* 47, 4435-4448.

WEBSTER, G. A., YOUTOS, A. G., OHMS, C. & WIMPORY, R. C. 2002. Draft standard for the measurement of residual stresses by neutron diffraction. *Recent Advances in Experimental Mechanics*, 467-476.

WEISSTEIN, E. W. 2011. Correlation Coefficient.

WIMPORY, R. C., OHMS, C., HOFMANN, M., SCHNEIDER, R. & YOUTSOS, A. G. 2009. Statistical Analysis of residual stress determinations using neutron diffraction. *International Journal of Pressure Vessels and Piping*, 48-62.

WITHERS, P. J. 2007. Mapping residual and internal stress in materials by neutron diffraction. *C. R. Physique,* 8, 806-820.

WITHERS, P. J. & BHADESHIA, H. K. D. H. 2001. Residual Stress Part 1 - Measurement Techniques. *Materials Science and Technology,* 17, 355-365.

WITHERS, P. J., PREUSS, M., STEUWER, A. & PANG, J. W. L. 2007. Methods for obtaining the strain-free lattice parameter when using diffraction to determine residual stress. *Journal of applied crystallography,* 40, 891-904.

Chapter 5

Stress Relaxation Through Ageing Heat Treatment – a Comparison Between In-situ and Ex-situ Neutron Diffraction Techniques

This paper was submitted for an invited publication in the Journal *Comptus Rendus Physique* on 1st September 2011 and accepted for publication on 5th October 2011. It was included as part of a special publication on the use of large scale facilities for research in metallurgy. The article was published online on 28th January 2012, and published in the April 2012 edition *of Comptus Rendus Physique.* The paper that follows is in the form in which it appears in the journal. This research was performed with Dr, Alex Evans, Dr. Ania Paradowska, Dr. Michael Hoffman, Professor Michael Preuss, and Dr. Mark Hardy.

The lead author of this paper is the author of this thesis; all of the content which follows are the words of the lead author, and all of the data gathered and presented here is the result of investigations implemented by the lead author. In terms of co-author involvement, Dr. Alex Evans and Dr. Ania Paradowska helped to design and implement the novel in-situ neutron diffraction heat treatment setup. Dr. Michael Hoffman assisted with all aspects of the ex-situ neutron diffraction experiment. Essential guidance and feedback was provided through Professor Michael Preuss, and Dr. Mark Hardy.

Contents lists available at SciVerse ScienceDirect

Comptes Rendus Physique

www.sciencedirect.com

Use of large scale facilities for research in metallurgy

Stress relaxation through ageing heat treatment – a comparison between in situ and ex situ neutron diffraction techniques

Relaxation des contraintes lors de traitements thermiques – une comparaison des techniques in-situ et ex-situ de diffraction des neutrons

James Rolph [a], Alex Evans [b], Ania Paradowska [c], Michael Hofmann [d], Mark Hardy [e], Michael Preuss [a],*

[a] *The University of Manchester, School of Materials, Manchester, M13 9PL, United Kingdom*
[b] *Institut Laue-Langevin, BP 156, 6, rue Jules-Horowitz, 38042 Grenoble cedex 9, France*
[c] *ISIS, Rutherford Appleton Laboratory, Didcot, OX11 OQX, United Kingdom*
[d] *FRM2, TU München, Lichtenbergstr. 1, 85747 Garching, Germany*
[e] *Rolls-Royce plc., PO Box 31, Derby, DE24 8BJ, United Kingdom*

ARTICLE INFO

ABSTRACT

The effect of ageing heat treatment on the relaxation of residual stress in a water quenched polycrystalline nickel-base superalloy has been measured using neutron diffraction. Two separate experiments have been conducted; the first experiment was an ex situ study in which samples were individually processed with varying degrees of age time before measurement. The second experiment was an in situ heat treatment, which required heating and then holding the sample at ageing temperature while measuring strain using neutron diffraction. The in situ experiment was carried out twice using the same setup to assess the repeatability of the technique and found to be repeatable within experimental error. The agreement between in situ and ex situ experiments was found to be reasonable, particularly the manner in which the stresses relaxed with time. In both studies it was found that initial stress relaxation was rapid, approximately 200 MPa in 15–30 min, after this a slower linear relaxation remained for the rest of the ageing heat treatment. This behaviour suggests creep may be the means by which stress relaxation takes place in this material during ageing.

© 2011 Published by Elsevier Masson SAS on behalf of Académie des sciences.

RÉSUMÉ

Nous présentons l'étude par diffraction des neutrons de l'effet de traitements thermiques de vieillissement sur la relaxation des contraintes résiduelles dans des polycristaux de superalliages à base nickel trempés à l'eau. Deux expériences distinctes ont été menées ; la première consiste en une étude ex-situ au cours de laquelle les échantillons ont subi différents niveaux de vieillissement avant les mesures. La deuxième est un traitement thermique in-situ, qui a nécessité de chauffer puys de maintenir l'échantillon en température pendant la mesure par diffraction des neutrons. La technique in-situ a été conduite deux fois en utilisant le même dispositif expérimental afin de déterminer sa répétabilité, qui s'est avérée bonne, à l'incertitude des mesures près. Un agrément satisfaisant entre les techniques ex- et in-situ est obtenu, particulièrement en ce qui

* Corresponding author.
   E-mail address: michael.preuss@manchester.ac.uk (M. Preuss).

concerne la manière avec laquelle les contraintes sont relaxées au cours du temps. Dans les deux études nous obtenons que la relaxation des contraintes est initialement rapide, environ 200 MPa en 15 à 30 min, puis on observe une relaxation linéaire plus lente pendant le reste du traitement. Ce comportement suggère que la relaxation des contraintes au cours du traitement de vieillissement a lieu par un mécanisme de fluage.

© 2011 Published by Elsevier Masson SAS on behalf of Académie des sciences.

1. Introduction

Residual stresses can be introduced into a material through a number of widely used manufacturing techniques including forging, heat treatment and machining. The level of residual stress within a component is known to affect performance as it can promote or retard failure mechanisms [1]. Characterisation of residual stress following manufacture is therefore a crucial part of understanding the in-service capabilities of any single component. Neutron diffraction is one of the variety of techniques available to measure strain and hence calculate residual stress within engineering alloys [2]. The technique makes use of Bragg's law; $\lambda = 2d\sin\theta$, to relate the diffraction angle (θ) to inter-planar spacing (d) within the crystal structure. By measuring diffracted neutrons of known wavelength, the crystal lattice structure of a material becomes a '3D atomic strain-gauge', where inter-planar spacings can be read from the diffraction angle and used to calculate strain.

The main advantage of neutron diffraction over other techniques is the ability to measure strain deep within the material bulk [3]. However, as a means to measure stress relaxation following ageing heat treatment, current studies have largely been limited to ex situ experiments. This means that in order to measure the level of stress relaxation, a sequence of samples must be measured each having experienced a different level of ageing. Two major issues arise with this method. The first is the shear quantity of samples required obtaining detailed time resolution in stress relaxation; a sample must be prepared and measured for each data point. The second issue is in sample to sample variability; heat treatment processes such as quenching and ageing are difficult to repeat to a high precision. As a result, stress relaxation measured using ex situ samples are subject to a scatter generated by even the most minor uncertainty in processing.

The alternative to measuring ex situ is to carry out stress relaxation in situ. This involves heating the sample to ageing temperature on the instrument whilst diffracting neutrons. In measuring in situ, the issues affecting ex situ are overcome; time resolution is only limited to the speed of the instrument, and sample-to-sample variation is non-existent. In addition to this, possible alignment errors are removed since alignment need only be carried once for an entire ageing experiment. In the present paper we compare the results obtained using both in situ and ex situ neutron diffraction ageing experiments on an advanced nickel based superalloy for disc application.

2. Experimental description

2.1. Sample preparation

2.1.1. Ex situ samples

Four sub-scale forgings of the nickel-base superalloy RR1000 were provided by ATI Ladish Forging. The nominal composition of RR1000 is given in Table 1. RR1000 is an advanced polycrystalline superalloy for high temperature application that is strengthened by almost 50 vol% γ'. The samples were of simple disc shape with a diameter of 76.2 mm, and a thickness of 25.4 mm (Fig. 1). Prior to any measurement, the samples were processed as follows.

Each sample was cut from a large pancake, forging at the same radial distance to ensure a closely matched thermo-mechanical history for each part. Sample 1 (S1) was sub-γ'-solvus heat treated followed by water quench. Samples 2 (S2), and 3 (S3) were both processed as S1 but with the addition of a 15 and 120 min ageing heat treatment at 760 °C respectively.

The water quench process was chosen in this sub-scale geometry to achieve high levels of residual stress despite the small geometry of the sample, whilst an ageing temperature of 760 °C was chosen since it is a typical ageing temperature of a γ' strengthened nickel-base superalloy.

2.1.2. In situ samples

As with the ex situ study, ATI Ladish Forging provided sub-scale forgings of the nickel superalloy RR1000 in the same geometry. Two samples were required for this study; sample 4 (S4) and sample 5 (S5), each of which were subjected to the same sub γ'-solvus heat treatment as S1–S3 followed by a water quench. Thus before any in situ ageing, S1, S4, and S5 were all processed identically, and were expected to have identical residual stress distributions.

Table 1
Alloy composition.

Alloy	Ni	Cr	Co	Mo	Ti	Al	C	B	Ta	Zr	Hf
RR1000	52.3	15.0	18.5	5.0	3.6	3.0	0.027	0.015	2	0.06	0.5

(a)

(b)
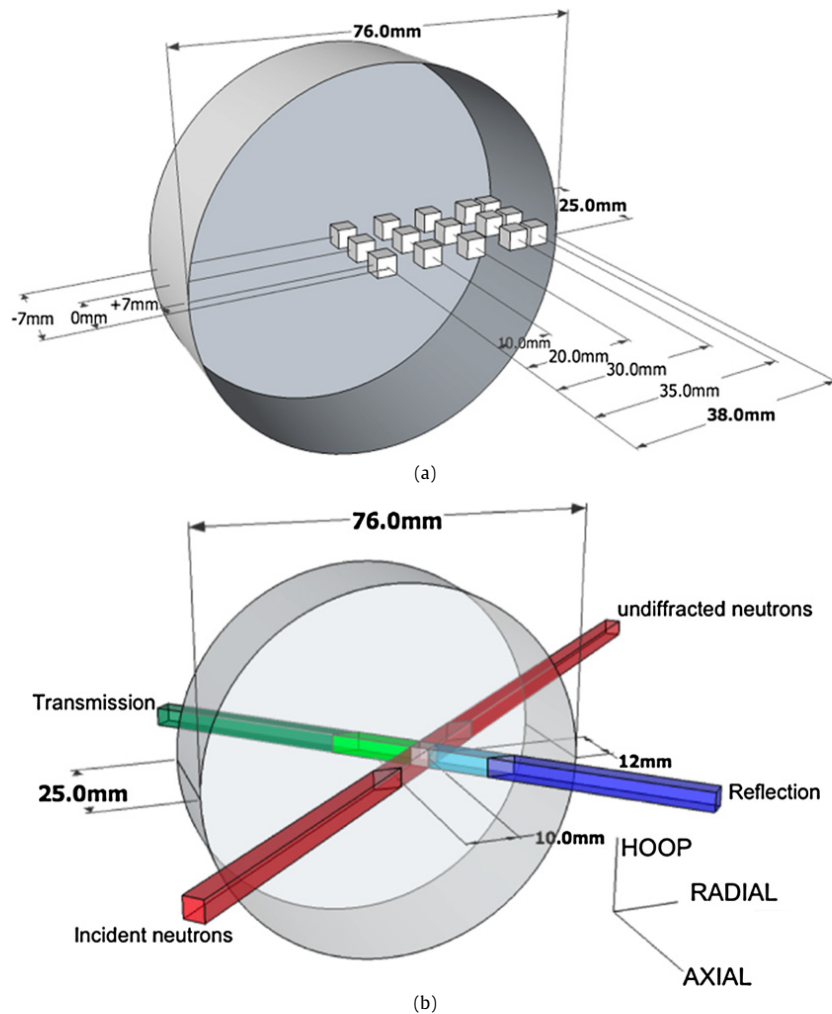
Fig. 1. Schematic diagram of the ex situ experimental sample setup; with (a) the location of gauge volumes within the sample, and (b) the measured strain directions.

2.2. Ex situ experiment – setup

All ex situ experiments were carried out at the dedicated strain scanning instrument STRESS-SPEC at FRM-II, Germany [4].

The FRM-II neutron source is of the reactor type, which means a single neutron wavelength and hence single reflection is chosen for the duration of the experiment. For the measurement of strain in RR1000 the (311) reflection was chosen for its low sensitivity to plastic strain and good representation of the bulk [5]. Using a wavelength of $\lambda = 1.55$ Å the (311) diffraction peak was recorded at $2\theta = 92°$, which provided an approximately cubic gauge volume. It should be noted that the two main phases in nickel-based superalloys are the fcc matrix (γ) and the intermetallic L1$_2$ precipitates (γ'). Due to the similar crystal structure and size of the two phases, any fundamental reflection consist of overlapping γ and γ' reflections.

Samples were mounted in pairs on a computer controlled translator table and aligned initially using a theodolite, and then again using entry scans with the neutron beam. In order to calculate stress it was necessary to measure strain in three perpendicular directions, namely hoop, radial and axial as indicated in Fig. 1(b). Measurements were made along three line scans with five points per line at -7 mm, 0 mm, and $+7$ mm with respect to the centre thickness. In order to balance spatial resolution with count statistics, a gauge volume of $4 \times 4 \times 4$ mm^3 was chosen and defined using primary and secondary slits.

Measurement of strain using diffraction always requires a value for d_0 or strain-free lattice spacing. In this study d_0 values were obtained by extracting cubes from each sample of sufficiently small dimension as to be relieved of all macrostress [6]. A $6 \times 6 \times 6$ mm^3 cube was taken from each sample at mid-diameter and thickness, using electro-discharge machining (EDM) to extract a core, and conventional cutting to form a cube. Each cube was then measured in a follow up experiment at the SALSA strain scanning instrument at the ILL Grenoble [7]. A $4 \times 4 \times 4$ mm^3 gauge volume was aligned using entry scans to ensure full gauge volume immersion within the sample after which two measurements were made
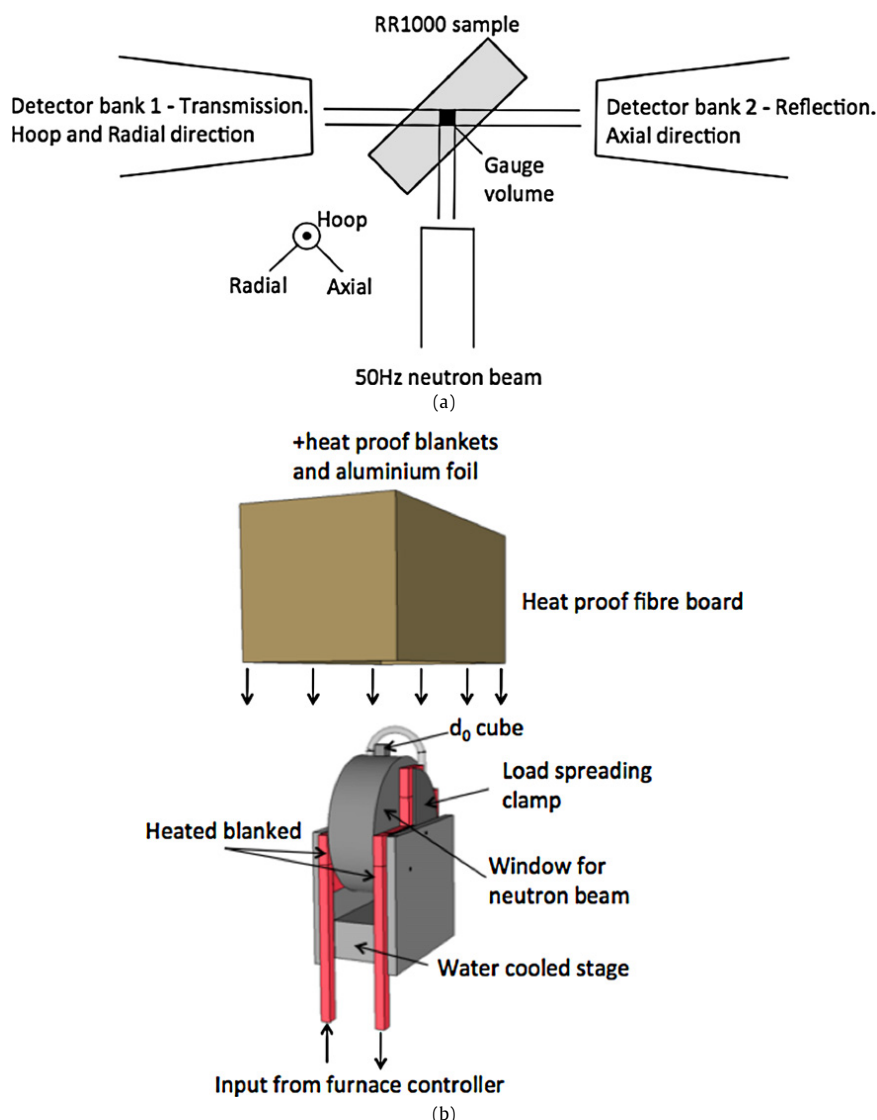
Fig. 2. Schematic diagram of the in situ experimental sample setup; with (a) the sample as placed on the instrument, and (b) the heated blanket arrangement and insulation.

using the same 311 *hkl* plane as the bulk measurements. In each case a relatively long count time was used to ensure good count statistics and a low peak position uncertainty. It was expected that absolute *d*-spacing values would differ between instruments; therefore, to calibrate between the two experiments a container of RR1000 powder was measured in each case.

2.3. In situ experiment setup

The strain-scanning instrument ENGIN-X (ISIS, UK) was chosen for in situ heat treatment. To bring each sample up the required temperature a heated 'blanket' arrangement was used. The blanket was made up from bead and/or block shaped elements of sintered alumina each containing resistance heating Ni Cr wire. From the sample geometry, heating elements were designed to wrap around the surface and thus through conduction, heat each sample to the required temperature. To allow the neutron beam to pass into the sample and back out unobstructed, a window was left open in the heated blanket as indicated in Fig. 2(b).

Prior to any in situ measurement, a sequence of thermo-couple heating tests was carried out on a spare nickel super-alloy sample. A schematic indicating thermo-couple location is given in Fig. 3. Through comparison to thermo-couple data provided by ATI Ladish Forging it was found that heating and cooling rates could be matched well to the ex situ samples. In particular, the cooling rate from 760 °C was found to be well replicated by turning off the furnace and then removing any insulation around the sample at approximately 500 °C. Results from this test also indicated that the quantity and positioning of insulation around the heated blanket and sample were crucial to achieving temperature uniformity. In a layer by layer structure our final setup was; nickel sample, heated blanked, stage and clamping, a 'box' arrangement of heat proof fibre
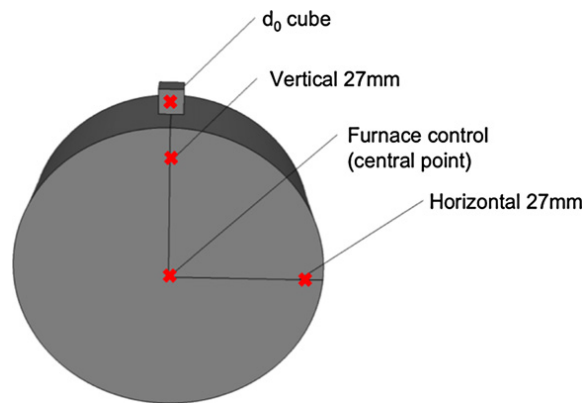
Fig. 3. Location of the type-K thermo-couples on the 'hockey puck' sample during the in situ experiment.

board placed over the top, heat proof blankets wire tied around the box, and finally aluminium foil wrapped around the outside (Fig. 2(b)). A second test was made on the beam line at room temperature to assess the impact of the insulating material on the neutron count statistics. It was found that while aluminium foil and fibreboard made little difference to the data, the heatproof blankets strongly attenuated the beam. As a result, the placement of the blankets was adjusted so as to maintain a similar window to the heating blanket.

For the measuring of a d_0 value, four $6 \times 6 \times 6$ mm^3 cubes had been extracted from an identically processed water quenched sample using EDM machining prior to the experiment. Before mounting on the instrument, each sample had one of the cubes attached to the sidewall using ceramic glue (Fig. 2(b)). Great care was taken in this process to maintain conductive contact between the cube and the sample by only using a small amount of glue around the edge of the cube. To ensure the cube reached the same temperature as the sample, part of the heating blanket was designed to loop over the top of this region to add heat. Extra insulation was also placed around the cube mounting area to prevent heat loss from the sample top. We were able to verify the effectiveness of these measures in maintaining temperature uniformity using a thermo-couple spot welded to the cube.

Each sub-scale forging complete with d_0 cube was placed in the heating blanket and then the entire setup clamped to a small stage containing a water-cooled base. The stage was mounted on a computer controlled translation table, which in combination with a theodolite allowed for sample alignment to within 0.2 mm. Sample clamping was made using two load spreading steel plates and four small bolts to sandwich the blanket against the sample face. The use of just four small diameter bolts for clamping was important to reduce conduction from the heating blanket to the stage.

The d_0 cube was aligned separately using the theodilite and measured using a $4 \times 4 \times 4$ mm^3 gauge volume to ensure full immersion of the gauge volume. The d_0 cube was measured at room temperature, while heating to temperature, at the beginning and end of the 760 °C hold period, and finally once back at room temperature again. This allowed data to be gathered on the thermal expansion of the alloy during heating, plus account for d_0 variation before, during, and after heat treatment.

The heating blanket was controlled using a Eurotherm furnace controller, which set the input current according to a centrally mounted control thermo-couple. Temperature uniformity was monitored throughout every experiment using type-K thermo-couples spot welded to the sample using small vanadium plates, as shown in Fig. 3. Using the described setup, we were able to maintain temperature to within 10 °C across the entire sample.

As a spallation source, ISIS generates neutron pulses with wavelengths ranging from ~ 0.5 to 6 Å. ENGIN-X receives the neutron pulse through a neutron guide tube via two rotating chopper arms which can reduce the neutron bandwidth depending on the needs of each experiment [8]. In this experiment the beam chopper was set to 50 Hz to give a bandwidth of $\lambda \approx 0.7$–2.2 Å, which improved count times and included the Ni(311) reflection. It was important to include this reflection as it was planned to use single peak fitting of the (311) reflection to maintain consistency across both experiments.

Whilst at heat treatment temperature, strain was scanned at a single location at the centre of the sample, this location was chosen for two reasons. Firstly, it is the location of peak tensile stress in the hoop and radial direction (Fig. 4). Secondly, at the sample centre the hoop and radial directions are the same. Thus on ENGIN-X the two detector system allowed to measure effectively all three strain directions simultaneously (Fig. 2(a)). Before and after the heat treatment, measurements were made at room temperature using longer count times to give an accurate assessment of the level of stress relaxation.

In planning this experiment, the gauge volume was chosen to be the same $4 \times 4 \times 4$ mm^3 gauge volume as the ex situ experiment, which on ENGIN-X is defined by the choice of collimator in addition to motorised slits. However, with this gauge volume and a path length of 35 mm count times approached 40 min per point, a time resolution less than that of the ex situ experiment (15 min). It was therefore necessary to open the slits and rock the collimators to increase the gauge volume to $8 \times 8 \times 8$ mm^3 and reduce count times to 15 min. Normally this would create an issue in averaging out stress gradients over such a large gauge volume. However from ex situ studies (Fig. 4) and finite element modelling it was known that the sample centre did not contain any steep stress gradients over this gauge volume. When measuring at locations other than sample centre, such as the d_0 cube, the gauge volume was reduced back to $4 \times 4 \times 4$ mm^3.
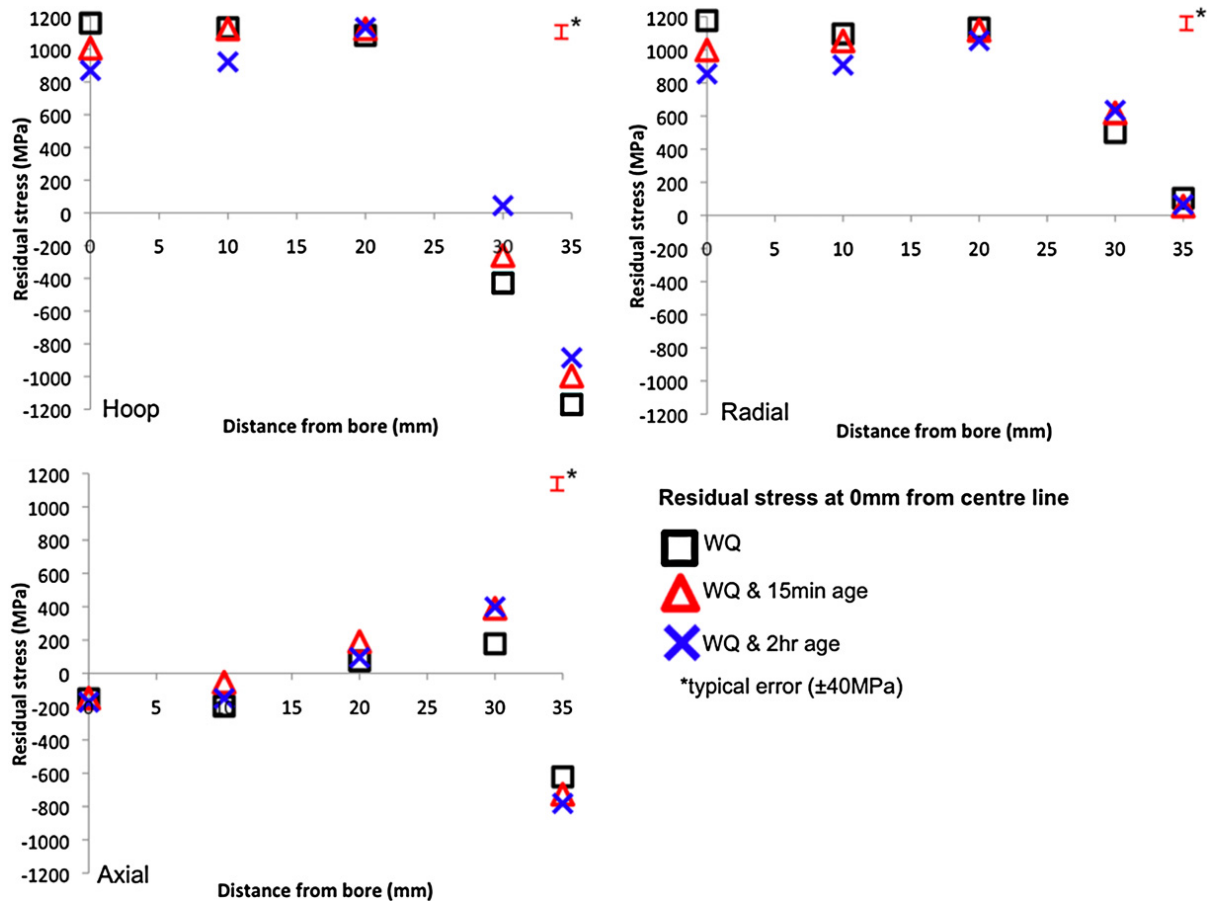
Fig. 4. Residual stress measurements made ex situ after water quench (WQ), WQ plus 15 min age at 760 °C, and WQ plus 2 h age at 760 °C.

Table 2
Material properties of nickel-superalloy RR1000.

Material properties of RR1000	
Young's modulus (bulk)	224 GPa
Poisson ratio (bulk)	0.326

Although a large gauge volume was used in this experiment to reduce count times, typical peak fit uncertainties in this experiment were high at approximately $\pm 250\ \mu\varepsilon$ or ± 150 MPa in this particular material. Although this is greater than the recommended 100 $\mu\varepsilon$ accuracy it was a necessary compromise to achieve the required time resolution in stress relaxation.

The first in situ sample, S4, was heated in stages from 25 to 200, 400, 600 and finally 760 °C and held for 5 min at each temperature to allow a d_0 measurement to be carried out. Once at temperature the gauge volume was positioned at the centre of the sample and measurements were made at approximately 15–20 min intervals throughout the hold time. Sample 4 was held to within ± 1 °C of 760 °C for 8 h by controlling the furnace using the arrangement of thermo-couples as indicated in Fig. 3. Before cooling, a final d_0 was measured to check for any variation during the hold time. The furnace was then turned off and all insulation removed at ~ 500 °C to cool the sample back down to room temperature. This process was repeated as closely as possible for sample 5.

2.4. Diffraction data analysis

Data analysis for both STRESS-SPEC and ENGIN-X was carried out by using in-house software to fit a Gaussian profile to the (311) reflection and hence derive the (311) lattice plane (d) spacing. In the same way, the data from each stress-free cube measurement was converted into a value of stress-free d-spacing, or d_0. The d and d_0 values were used to calculate strain in each of the three principal directions and then residual stress calculated from Eq. (1).

$$\sigma_x = \frac{E_{hkl}}{(1 + \nu_{hkl})(1 - 2\nu_{hkl})}\left[(1 - \nu_{hkl})\varepsilon_x + \nu_{hkl}(\varepsilon_y + \varepsilon_z)\right] \quad \text{and} \quad \sigma_y = \cdots, \quad \text{etc.} \tag{1}$$

where the principle strain directions are denoted as x, y, z and E_{hkl} and ν_{hkl} represent plane specific diffraction elastic constants. The elastic constants used in this particular study of the alloy RR1000 are given in Table 2.
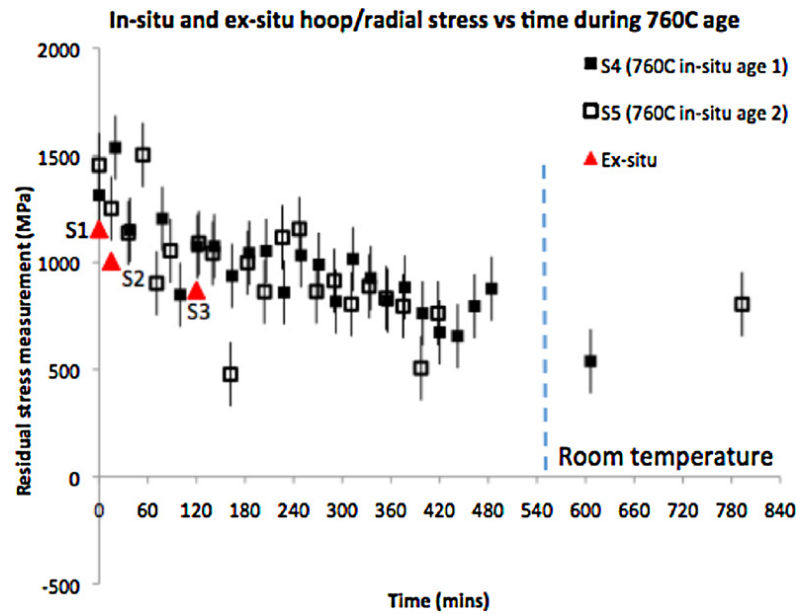
Fig. 5. Hoop and radial stress at the sample centre during an in situ ageing heat treatment at 760 °C. Data shown from both the in situ and ex situ experiments.

3. Results and discussion

The residual stress distribution in S1, S2, and S3, as obtained from the ex situ experiment are shown in Fig. 4. The results indicate peak levels of tensile residual stress approaching 1200 MPa are present in the hoop and radial direction at the centre of S1. Hoop stresses fall with radial distance to become strongly compressive towards the rim region, whereas radial stress falls to zero as it approaches the free surface at the rim. In comparison, axial stress in S1 is near zero from 0 to 20 mm radial distance. Further towards the rim of the disc a tensile 'spike' is observed followed by a rapid drop of the axial stresses into compression. Comparing residual stress levels in each of the three samples, we can assess the level of stress relaxation occurring during ageing by direction and location within the sample. It is clear from Fig. 4 that at 760 °C stress relaxation is greatest in the hoop and radial directions, and virtually non-existent in the axial direction. In the hoop direction stress relaxation of up to 300 MPa is seen in both the bore and rim regions, but this is reduced in the region in-between. Similar levels of relaxation are seen at the bore in the radial direction as the two directions as the same at the sample centre. However, moving out from the bore the level of stress relaxation in the radial direction falls until at the rim it reaches zero. In summary, the ex situ experimental data shows that the most significant stress relaxation occurs in and around the sample centre, making this location the most appropriate for the in situ experiment.

Results obtained from the in situ experiment are compared to those from the ex situ experiment in the hoop and radial direction in Fig. 5. The in situ data shows reasonable agreement between S4 and S5, indicating the experiment was repeated as faithfully as possible. However, the data does indicate a degree of scatter and anomalous measurement points, S5 in particular shows two at 150 and 380 min. Unfortunately scatter and anomalous results were a known risk in this investigation since time resolution was generally favoured over reducing experimental error. Peak fitting uncertainties in this experiment translated to ±150 MPa uncertainty in stress in this material, this will have generated some scatter although the anomalous points for S5 exceed this level of uncertainty. Comparing absolute values obtained from the two experiments, it appears the in situ data is consistently 150–200 MPa greater than the ex situ. The reason for this is not clear, although a number of factors may have contributed given the different nature of each experiment. To overcome this offset and add a further comparison between the in and ex situ experiments, the stress relaxation with time was calculated as the difference between each measurement point and the initial as-quenched measurement.

Hoop and radial stress relaxation as a function of time for both the in situ and ex situ experiments is shown in Fig. 6; agreement between the two experiments is now much stronger. The behaviour of all five samples follow a similar trend, a rapid relaxation of ∼ 200 MPa during the first 30 min and then a more linear trend for the remainder of the heat treatment. This behaviour may be indicative of a primary and secondary creep process of stress relaxation. It also suggests that even though samples S1–S5 all had been quenched in the same way, the starting stresses were different for the sample used during the in situ experiment compared to the samples generated for the ex situ experiment. This highlights the issue of possible sample to sample variations and the advantage of using in situ experiments to provide residual stress data that can be used to validate process modelling efforts.

Residual stress measurements from both the in situ and ex situ experiments in the axial direction are shown in Fig. 7; agreement between both in situ samples is high, indicating that the experimental process was repeated successfully.
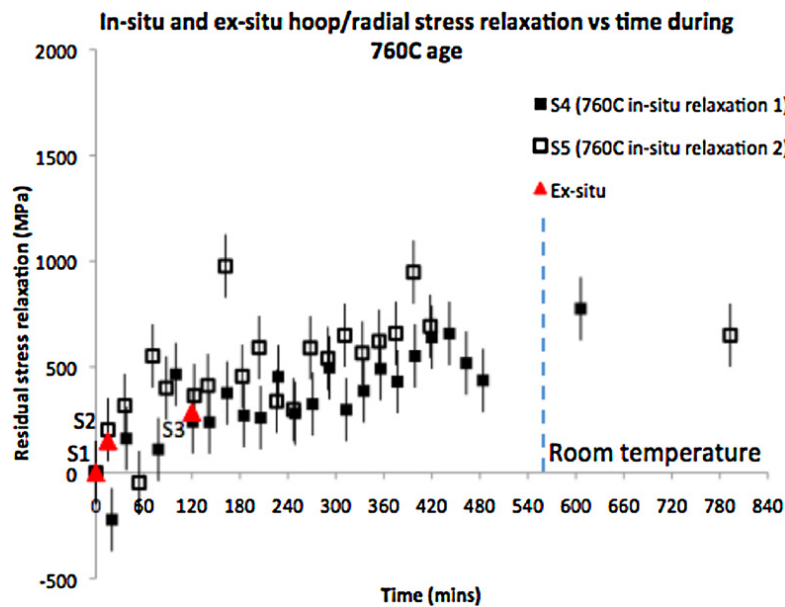
Fig. 6. Stress relaxation in the hoop and radial stress at the sample centre during an in situ ageing heat treatment at 760 °C. Data shown from both the in situ and ex situ experiments.
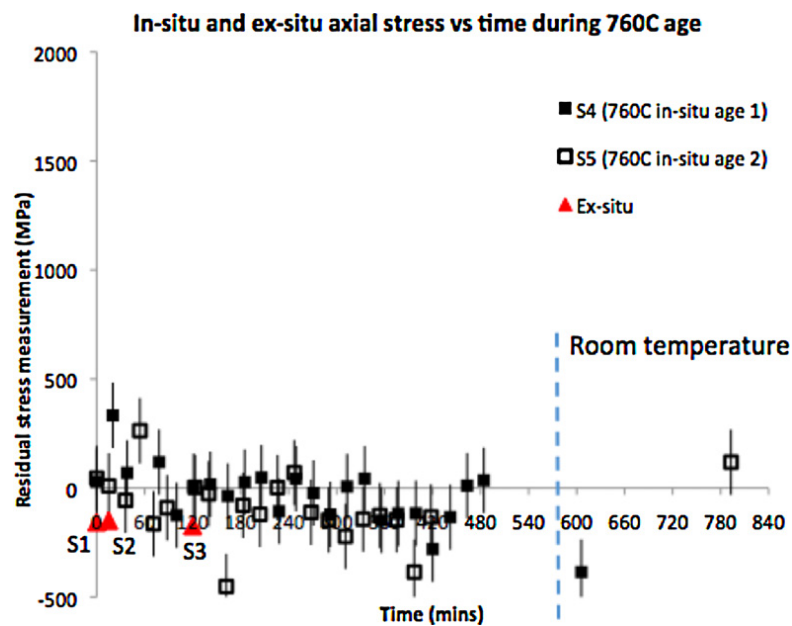
Fig. 7. Axial stress at the sample centre during an in situ ageing heat treatment at 760 °C. Data shown from both the in situ and ex situ experiments.

S4 and S5 show levels of stress very close to zero in the as-quenched state and remain relatively close to zero throughout the heat treatment although a reasonable degree of scatter is again seen in the data. In comparison, the ex situ samples, S1, S2 and S3, all indicated residual stress values of approximately −150 MPa, a difference of ∼ 150 MPa when compared to the in situ experimental data. Interestingly this same difference was seen in comparing in situ and ex situ data in the hoop/radial direction.

In terms of stress relaxation, Fig. 6 indicates that in both experiments the axial stress altered very little during the heat treatment; this being the case, axial stress relaxation with time has not been plotted. However, it is clear that whilst near zero stress relaxation was observed, it was observed equally in both experiments, which signifies agreement between in situ and ex situ measurement techniques.

4. Conclusions

The relaxation of residual stress as a result of an ageing heat treatment has been investigating using an ex situ experiment, followed by an in situ experiment. The ex situ experiment indicated that following a water quench process (S1) residual stress was found to peak at +1200 MPa in the sample centre in both the hoop and radial directions. The axial stress was found to be largely negligible with the exception of the near rim region. Following ageing heat treatments of 15 min (S2) and 120 min (S3), the bore region was found to show the greatest level of stress relaxation.

The in situ experiment was aimed at the bore region to best observe the stress relaxation during an ageing heat treatment. Two samples (S4 and S5) were measured in identical setups heating the sample to 760 °C whilst taking measurements in the sample centre every 15–20 min. Agreement between S4 and S5 was good although a large degree of experimental scatter was present in the data due to the need to reduce data acquisition times as far as possible. Comparing absolute stress values between the ex situ and in situ experiments showed almost identical trends but an offset between the two of approximately 150–200 MPa in all three strain directions. The trends in each experiment were compared by plotting the hoop/radial stress relaxation with time (Fig. 6). In terms of stress relaxation, the agreement between ex situ and in situ experiments was good; both experiments followed an initial rapid stress relaxation process followed by a slower linear rate of relaxation. It is thought that this indicates stress relaxation is occurring by a primary followed by a secondary creep process. After a 2 h age time, stress relaxation levels were: S3 (ex situ) – 285 MPa, S4 (in situ 1) – 240 MPa, and S5 (in situ 2) – 360 MPa. This places the ex situ data within the scatter of the in situ data, thus in terms of stress relaxation the two experiments are in agreement.

Acknowledgements

References

[1] P.J. Bouchard, K.H. Buschow Jr., W.C. Robert, C.F. Merton, I. Bernard, J.K. Edward, M. Subhash, V. Patrick, Residual Stresses in Lifetime and Structural Integrity Assessment, Encyclopedia of Materials: Science and Technology, Elsevier, Oxford, 2001, p. 8134.

[2] P.J. Withers, H.K.D.H. Bhadeshia, Residual stress, Part 1 – Measurement techniques, Materials Science and Technology 17 (2001) 355.

[3] P.J. Withers, Mapping residual and internal stress in materials by neutron diffraction, Comptes Rendus Physique 8 (2007) 806.

[4] M. Hofmann, R. Schneider, G.A. Seidl, J. Rebelo-Kornmeier, R.C. Wimpory, U. Garbe, H.-G. Brokmeier, The new materials science diffractometer STRESS-SPEC at FRM-II, Physica B (2006) 1035.

[5] H.J. Stone, T.M. Holden, R.C. Reed, Determination of the plane specific elastic constants of Waspaloy using neutron diffraction, Scripta Materialia 40 (1999) 353.

[6] P.J. Withers, M. Preuss, A. Steuwer, J.W.L. Pang, Methods for obtaining the strain-free lattice parameter when using diffraction to determine residual stress, Journal of Applied Crystallography 40 (2007) 891.

[7] D.J. Hughes, G. Bruno, T. Pirling, P.J. Withers, Scientific review: First impressions of SALSA: The new engineering instrument at ILL, Neutron News 17 (2006) 28.

[8] J.R. Santisteban, M.R. Daymond, J.A. James, L. Edwards, ENGIN-X: a third-generation neutron strain scanner, Journal of Applied Crystallography 39 (2006) 812.

Chapter 6

Residual Stress Generation Through Quenching of a Nickel-base Superalloy – Measurement and Prediction

This paper has been prepared for submission to the Journal *Metallurgical Transactions A.* The paper that follows is in the form in which it was submitted to the journal. This research was performed with Dr. Michael Hoffman, Dr. Alex Evans, Dr. Stan Nikov, Dr. Ranga Ramanathan, Mr. Paul Enderson, Professor Michael Preuss, Dr. Mark Hardy, and Dr. Mike Glavicic

The lead author of this paper is the author of this thesis; all of the content which follows are the words of the lead author, and all of the data gathered and presented here is the result of investigations implemented by the lead author. In terms of co-author involvement, Dr. Michael Hoffman, and Dr. Alex Evans assisted with all aspects of data acquisition through neutron diffraction. Dr. Stan Nikov and Dr. Ranga Ramanathan assisted with the finite element modelling work. Mr. Paul Enderson provided the expertise to carry out microstructural characterisations using a scanning election microscope (SEM). Feedback and overall guidance for this work was provided by Professor Michael Preuss, Dr. Mark Hardy, and Dr. Mike Glavicic.

Residual Stress Generation Through Quenching of a Nickel-base Superalloy – Measurement and Prediction

J. Rolph[1] M. Preuss[1] P. Enderson[1] M. Hofmann[2] S. Nikov[3] M. C. Hardy[3] M. G. Glavicic[4] R. Ramanathan[5] A. Evans[6]

[1] Materials Science Centre, University of Manchester, Grosvenor St, Manchester, M13 9PL, UK

[2] FRM2, TU München, Lichtenbergstr. 1, 85747 Garching, Germany

[3] Rolls-Royce Plc, PO Box 31, Moor Lane, Derby, DE24 8BJ, UK

[4] Rolls-Royce Corporation, P.O. Box 420, Speed Code T-61, Indianapolis, IN 46206-0420, USA

[5] ATI Ladish Forging, 5481 S. Packard Avenue, Cudahy, WI, 53110-8902, USA

[6] Institut Laue-Langevin, BP 156, 6, rue Jules-Horowitz, 38042 Grenoble cedex 9, France

Abstract

The residual stress generated as a result of the quenching process has been characterised in sub-scale disc forgings of the Nickel based superalloy RR1000. Three different quench media were used, air, oil and water, which allowed for three levels of residual stress to be generated. Experimental stress characterisation was made throughout the forging interior using two independent techniques: neutron diffraction and the contour method. The results indicate a good overall agreement, but with a tendency for the contour method to under-predict very large stresses. To add further comparison, the quenching process was simulated using the finite element method. Cooling data was obtained using embedded thermo-couples for each quench and the model built to replicate the measured cooling before calculating the residual through plasticity modelling. Two plasticity hardening laws were used; an isotropic law, and an Mroz multi-layer law [1], the latter allowed for a degree of kinematic hardening [2]. In the water quenched condition the isotropic model over-predicted the stress, while the Mroz model under-predicted the stress, in comparison to the experimental data. However, in the oil quenched condition the isotropic hardening law was found to show very strong agreement to the experimental data while the

Mroz model under-predicted the stress by a significant margin. In the air cooled state the model was found to under-predict the residual stresses significantly.

1. Introduction

Nickel based superalloys are a class of material capable of operating at high temperatures and loads required in gas turbines due to their finely tuned γ/γ' microstructure. The on-going development of these alloys has allowed engine manufacturers to push for greater power and efficiency through increased turbine entry temperatures. RR1000 is a polycrystalline Ni-based superalloys for disk application with improved high temperature properties due to a significantly greater volume fraction of γ' in comparison to other commercial alloys [3]. In RR1000 the γ' is employed in a tri-modal distribution. The large (1-3μm) primary γ' precipitates resist grain growth at high temperatures, while the smaller (100-300nm) secondary and (20-50nm) tertiary γ' act as obstacles to dislocations and thus resist deformation under load [4]. The finely tuned microstructure of RR1000 requires a precise heat treatment process to grow precipitates to the correct size and distribution.

Prior to heat treatment, RR1000 follows the powder metallurgy processing route, which ensures a fine grain (5-50um), equiaxed and homogeneous microstructure in the final billet [5]. Isothermal forging, just below γ' solvus, allows the fine grain size in the γ matrix to be maintained, while producing a near net shape component.

Heat treatment follows forging and consists of two stages, solution heat treatment usually below the γ' solvus and ageing. The sub γ' solvus solution heat treatment prevents grain growth, but allows dissolution of the secondary and tertiary γ' into the matrix. The quench media and hence cooling rate are known to be crucial to the γ' size distribution and morphology [6] as even very fast cooling rates do not prevent the precipitation of γ'. Ageing is carried out after cooling/quenching by holding the component at a lower temperature for a prolonged period. A common aging heat treatment temperature of γ' strengthened nickel-based superalloys is 760°C, which preferentially results in coarsening of tertiary γ' [7, 8].

While fast cooling rates and low aging temperatures might be beneficial from a microstructural point of view [9], residual stresses also have to be considered. In large Ni-based components such as compressor or turbine disks, cooling from solution heat

treatment temperature results in significant thermal gradients and hence residual stresses. The subsequent ageing process maintains the component at an elevate temperature and allows the residual stress to partially relax. The residual stress state of a component is of particular importance to engine manufacturers since it dictates in service performance and can lead to component distortion during subsequent machining stages of manufacture. Current process modelling efforts aim to characterise residual stress through manufacture to tailor material removal processes in order to minimise distortion and reworking. Furthermore, accurate residual stress predictions allow more precise lifing calculations to be made, thus increasing the working life of individual turbine components [10]. However, accurate modelling, particularly of complex and rapid processes such as quenching, requires validation and optimisation through experimental characterisation.

In the work presented here, the focus will be on the process of residual stress generation during rapid cooling. The investigation combines simulation of residual stresses by using finite element (FE) methods with experiments of characterising residual stresses buy means of neutron diffraction and the contour method. The results from each technique are compared with a view to improving the capability to predict residual stress evolution through manufacture.

2. Experimental description

Sample preparation

Three sub-scale disc forgings of the Nickel-based superalloy RR1000 (chemical composition is presented in Table 1) were individually heat treated and quenched at ATI Ladish Forgings. The sub-scale discs were 76.2mm in diameter and 25.4mm in width (Figure 1). The disc geometries were machined from a larger pancake forging at the same radial location to minimise variation in thermo-mechanical processing. Each disc was individually heat treated at a temperature of 1120°C, below the γ′ solvus, for four hours before being quenched. It was assumed that such a heat treatment removes all prior residual stresses due to forging, and that those, which existed within the geometry thereafter, were solely generated by the quenching process. Sample 1 (S1) was removed from the furnace and cooled in still air, sample 2 (S2) in an oil bath, and sample 3 (S3) in a water bath. The choice of quench media was made to reflect actual manufacturing processes, such as oil quenching, as well as

to generate a range of residual stresses. Water quenching was included in this investigation since such small geometries require rapid heat extraction in order to generate the steep thermal gradients seen in larger components.

Microstructural Characterisation

A small coupon of approximately 3mm^3 was extracted from the core of each sample in order to carry out a microstructural characterisation. Measurements were made at this location since a coupon was already made ready in order to characterise the strain-free d-spacing, d_0, for residual stress characterisation. In addition, the forging centre was thought to have experienced the most consistent cooling rate across each of the quenches. More specifically, locations outside of the core may have been subject to different cooling rates owing to the forging orientation upon quenching. Coupon extraction required electro-discharge machining (EDM) to obtain a 'matchstick' core and conventional cutting to produce a cube from the matchstick. The extraction process was only carried out after neutron diffraction and contour method techniques were completed so as to preserve the quench-induced residual stress field. Each coupon was mounted in phenolic resin and then ground using silicon carbide paper grinding discs through progressively finer grit sizes from 240 down to 1200 standard ANSI grit. The polishing stage consisted of a 6μm and 1μm diamond polish followed by a colloidal silica polish (OPS).

Chemical etching was required in order to image the γ´ distribution in a scanning electron microscope (SEM). Each coupon was removed from the mounting material before being cleaned and degreased using methanol. The etchant consisted of 10 parts water, 3 parts $HN0_3$ 3 parts HCl and approximately 1/20 parts dissolved molybdic acid powder. The coupons were placed in the etchant individually for 20-30 seconds before being thoroughly rinsed in water. Immediately following the etch, imaging was carried out using an FEI Sirion Field Emission Gun Scanning Electron Microscope (FEG-SEM). The SEM was setup to image secondary emitted electrons using a through lens detector to a resolution of ~3nm. Note, the etchant removes γ' and therefore imaging the precipitates here means imaging the holes left behind from the dissolved γ'.

Analysis of the intra-granular γ´ was made by converting the micrographs into a binary image using the image manipulation software package GIMP [11] to

distinguish the γ′ from the γ matrix. The binary image was then imported into ImageJ [12] to determine the γ′ volume fraction and size distribution.

Neutron diffraction

The method of measuring strain using neutron diffraction has been well documented in [13] and [14]. A brief overview is given here.

All neutron diffraction measurements were carried out on STRESS-SPEC, the dedicated material science diffractometer at the reactor source FRM-II, Germany [15]. A Si(400) monochromator was used to select neutrons of wavelength λ=1.55Å and strain scanning was employed here in the θ/2θ mode. Using the Ni(311) diffraction plane, this gave a scattering angle of 2θ ≈ 93° thus generating an approximately cubic gauge volume. The Ni(311) reflection was used in this case since it is known to approximate bulk behaviour, and to have a low sensitivity to plasticity induced intergranular strains [16].

The neutron gauge volume was defined using Cadmium slits set to give a 4x4x4mm gauge volume; this balanced spatial resolution with reasonable count times (< 90 minutes per point). The diffracted neutrons were recorded using a 2D area detector to give an intensity vs. diffraction angle (2θ) plot for every measurement point. The recorded data was analysed using in-house software to allow a Gaussian function to be fitted to each diffraction peak. Using the fitted function, it was possible to calculate a peak centre point as a value of 2θ, which allowed the direct calculation of the *hkl* d-spacing using Braggs law (Equation 1).

$$\lambda = 2d_{hkl}\sin\theta \tag{1}$$

The lattice strain can then be calculated using the measured d-spacing in combination with a strain-free lattice spacing, d_0 (Equation 2).

$$\varepsilon = (d - d_0)/d_0 \tag{2}$$

Strain was measured for each measurement location (Figure 1). In order to calculate stress, measurements of strain were carried out in three orthogonal directions dictated by the sample symmetry, in this case, hoop, radial and axial. Due to the disc geometry and symmetric thermal processing it was possible to assume these directions approximated the principal stresses.

The value of d_0 was obtained in a follow up experiment using the strain scanning neutron diffraction instrument, SALSA, at the ILL [17], which is in principle a similar beam line to STRESS-SPEC. A 5mm^3 cube extracted from each of the forgings was measured using the same $\theta/2\theta$ setup as the main investigation. The cube dimensions were of sufficiently small size as to be considered macro-stress free [18]; the measured d-spacings thus allowed a single value of d_0 to be obtained for each sample. Ideally, d_0 characterisation is carried out on the same instrument at the same time. However, identically processed samples were not available to machine out the required cubes at this time. To ensure data from two instruments could be used in the same calculations, a calibration measurement was performed on both instruments using a Vanadium container of RR1000 powder.

The process of quenching can generate steep thermal gradients and with them a variation in d_0. In a prior investigation it was found that the variation in d_0 following water quenching was sufficient to alter the calculated residual stress by up to 200MPa but only at locations close to the surface. However, along a centre line scan the variation in d_0 was minimal since the cooling rate across this region was similar enough to allow comparable levels of elemental diffusion [19]. Based on this result, line scans were made only at the centre line of each forging and initially a single macro-stress free cube measurement was used as the d_0 value for all neutron measurement points. However, as described later, it was found that an axial stress balance model was more suitable for appropriate d_0 determination.

Following d_0 characterisation it was possible to obtain strain (Equation 2) in each of the principal directions and hence calculate stress using a form of Hooke's law.

$$\sigma_x = \frac{E_{hkl}}{(1+v_{hkl})(1-2v_{hkl})}\left[(1-v_{hkl})\varepsilon_x + v_{hkl}\left(\varepsilon_y + \varepsilon_z\right)\right] \text{ and } \sigma_y = \cdots \tag{3}$$

The diffraction elastic constants, E_{hkl} and v_{hkl} are specific to the (311) reflection in this material. They were obtained from data generated during an in-situ loading experiment on ENGIN-X, ISIS, UK [20] and can be found in Table 2.

Uncertainty in strain was calculated from the error in peak fitting using the following relation [21].

$$u_\varepsilon = \frac{1}{\tan\theta}\left[(\delta\theta_0)^2 + (\delta\theta)^2\right]^{\frac{1}{2}} \tag{4}$$

Where $\delta\theta_0$ is the peak fit uncertainty in the stress-free measurement (d_0) and $\delta\theta$ is the uncertainty in the hkl plane spacing measurement (d).

Count times were adjusted manually throughout the experiment, which allowed measurement to an uncertainty of no more than ±50MPa. It should be noted however that in a γ/γ′ Nickel-base superalloy, the (311) reflection is a composite peak made up from contributions of both phases, γ and γ'. Measuring strain in this way assumes the γ matrix and γ′ precipitates accommodate load equally without significant partitioning which would generate an asymmetric peak shape. This proved to be a valid assumption, since a small shoulder to the main peak – suspected to be the result of load partition – was only observable in the extreme levels of stress in the water quenched forging. Furthermore, by fitting over a 2θ window, which avoided the shoulder, it was found that the impact of peak asymmetry on residual stress was no greater than experimental error.

Contour method

The contour method is a relatively new measurement technique, which allows the generation of a full 2D stress distribution normal to a cut surface. The technique is composed of three distinct stages: cutting, surface measurement and analysis (Figure 2). The cutting process allows relaxation of the residual stresses contained within a part, which causes a deformation at the cut surface. The surface is measured subsequently in one of two ways; using either a coordinate measuring machine (CMM) touch probe, or a laser scanner. The measured surface data is then manipulated and analysed using a finite element model to back-calculate the original residual stress distribution given the level of deformation and the mechanical properties of the material. Further details on this technique can be found in [22].

Each of the three forgings was cut across the diameter on a plane, which coincided with the centre of the neutron diffraction gauge volumes. The cut was made using electro-discharge machining (EDM) on a 'skim cut' setting, which allowed for a very slow and non-aggressive cutting process. This was necessary to avoid generating any additional stresses during the cut, thus compromising the measurement. The forgings were firmly clamped on both sides during the cut to reduce movement which is known to cause asymmetric material removal and generates errors [23].

The surface contours of both halves of the forging were measured using a nano-focus con-focal laser profilometer set to a step size of 100μm. Line scans were made over an area slightly greater than the cross section of the forging to allow the edges to be identified in subsequent analysis.

Data manipulation and analysis was carried out using a combination of MATLAB and ABAQUS software packages [24, 25]. A sequence of user defined MATLAB routines were used to manipulate the raw data such that a spline fit could be applied to the surface. Outliers were removed using an automated script followed by a manual check and edit of the data. In this case it was necessary to manually eliminate a 2mm cross section of contour data at the location where the wire exits the forging. At this point, the circular-profile wire breaks through the surface of the forging and leaves a curved step, which was removed to prevent an artificially generated contour being included in further analysis [26].

The two halves were analytically aligned and the average of both deformations taken. The averaging process cancelled out the equal and opposite deformation resulting from the relaxation of shear stresses on each half, and reduced errors generated from cut asymmetry. The averaged surface was fitted with a bi-variant spline function to smooth the data and provide a surface from which the model would calculate residual stress [27].

ABAQUS was used to generate a mesh for the model. The forging outline was extruded from a planar cross section to match the geometry of one half of the forging with no deformation. The part was meshed using quadratic elements of length 1mm at the cut surface reducing to ~5mm at the curved back face. The undeformed mesh was imported back into MATLAB and used along with the spline fit of the deformed surface as the initial and final boundary conditions to generate the model. By assuming elastic isotropy the model was solved in ABAQUS using bulk elastic properties (Table 2). The 2D stress maps were used for visual comparison of stress distributions, radial line scans of data were extracted for comparison to other techniques.

Finite element modelling

Modelling of the quenching process began by capturing the cooling curves using thermo-coupled geometrically identical austenitic stainless steel (304) test pieces.

Each test piece had five embedded thermo-couples; one at the bore, two in the bulk and two close to the rim. The temperature was recorded at 1s intervals from the heat treatment furnace, through the transfer to the quench tank, and throughout the quench (Figure 3a-c). The data from this experiment was employed in two distinct ways: Firstly, to derive a heat transfer coefficient (HTC) curve for each quench media, and secondly to optimise the model and accurately simulate the quenching process. HTC derivation was carried out using the following relation.

$$HTC = \frac{k(abs(T_B - T_A))}{(T_B - T_{water})d} \qquad (5)$$

Where k is the thermal conductivity, T_A, T_B and T_{water} are the temperatures at thermo-couples A, B and of the water, and d the distance between the two thermo-couples.

Using Equation 5 the temperature difference between the central (C) and near surface (NS) thermo-couples was used to calculate the heat transfer during quench for all three media (Figure 4). The near-surface location was important to characterise since the model would use surface boundary conditions to simulate heat extraction. Unfortunately, measurements on the surface could not be made reliably using the thermo-couple method, so a near surface location was used as the best approximation. It was assumed that near surface heat extraction would follow the same form as at the surface but with a slightly less aggressive level of heat extraction. Thus the derived HTC curve could be applied to the model surface providing some weighting factor could be found to replicate the more aggressive heat extraction. The weighting factors were calculated as part of the model optimisation process detailed below.

All finite element modelling work was carried out using the Rolls-Royce finite element analysis code 'SCO3' [28]. The model was defined as a two dimensional axi-symmetric problem since the quenching process was applied equally to all faces and was therefore expected to generate an approximately axi-symmetric stress distribution. The geometry was drawn up using measured dimensions and meshed using triangular elements with a typical length ~1mm. The surface of the model was broken down into thirteen sections to allow the HTC to be weighted uniquely by location on the sample surface (Figure 5).

The weighting factors were determined using an optimisation loop to iterate towards a solution of values at which the simulated cooling matched that obtained through experiment at each thermo-couple location. The optimisation process used a 'pointer'

algorithm to minimise the difference between the simulated and experimental temperatures at six discrete data points extracted from the cooling curve of each thermo-couple. Weighting factor adjustment in the optimisation loop was partially restricted to maintain a degree of continuity between neighbouring surfaces. A condition by which the difference between two adjacent weighting factors could not exceed 1/3 of the average value was used to control this. The distributions of weighting factors for each quench are given in Figure 5.

The use of weighting factors represented a significant unknown in the modelling process and had to be treated with care to avoid being used as an overriding variable, which always gave the desired result. It is important to distinguish that in this case the weighting factor was used purely to create a model, which accurately represented the experimentally measured cooling process. Once this was defined, the model was re-run using RR1000 material properties to calculate the residual stress.

The choice of hardening model was taken initially to be isotropic in accordance with work carried out to investigate quenching stresses in similar materials [29, 30]. However, initial results from the water quenched model suggested stresses far in excess of what was measured. On reflection it was decided that an Mroz multi-layer model [1] should also be considered since it took into account the reverse yielding and associated Bauschinger effect which occurs during the quench [31]. As such, the modelled results presented for the oil and water quenched forgings are those obtained from both hardening models to allow for comparison. The air cooled sample was deemed to be of sufficient slow cooling rate to assume a negligible impact from reverse yielding, and has only been plotted using isotropic hardening.

3. Results and Discussion

Microstructure

Figure 6a-c shows the primary and Figure 6d-f the secondary and tertiary γ' for each of the quenched forgings. The microstructure of the intra-granular γ' (secondary and tertiary) has also been quantified for each quench in terms of the particle size distribution in Table 3. As mentioned earlier, the samples were all extracted from the centre of the forgings; the cooling rate at this location as simulated in the model has

been give in Figure 7. The data from this location was used to calculate an average cooling rate from 1120-700°C to allow comparison between the quenches (Table 3).

Starting with the low magnification micrographs (Figure 6a-c), no variation is observed in either the primary γ´ size, or in the γ matrix grain size for the three different cooling conditions. Such a trend is expected since the solution temperature was sub γ´ solvus, with intergranular primary γ´ particles pinning γ grain boundaries.

At the higher magnification significant differences in intragranular γ' size distribution become apparent (Figure 6d-f). The intragranular γ´ size distribution is shown in Figure 8 and the mean particle sizes as well as the volume fraction of intragranular γ' are presented in Table 3. It can be seen that the air cool resulted in the largest average secondary γ' particle size of about 100 nm with a clearly distinguishable tertiary γ' family with about 20 nm. After oil quench, the secondary γ' particle size was about 60nm and tertiary about 10nm. Finally, the water quench had resulted in a broad uni-modal γ' distribution of about 30 nm. It is also noticeable that the intragranular γ' volume fraction decreases with increasing cooling rate indicating that not all γ' has formed particularly during fast cooling. However, it might be possible that with increasing cooling rate some of the very fine γ' was not captured.

The effect of the cooling rate on intragranular γ' distribution is expected. Secondary γ' nucleates during the very early stage of cooling and its growth becomes limited when cooling rates go up. As cooling proceeds, elemental diffusion rates go down. Eventually, the γ' stabilising elements do not reach secondary γ', resulting in the initiation of secondary nucleation that forms tertiary γ' in-between secondary γ'. As cooling rates go up the time difference at which secondary and tertiary γ' start nucleating decreases resulting eventually in a more uni-modal γ' size distribution.

In summary, the γ´ characterisation demonstrates clearly that even deep inside the sub-scale forgings, the different quench media had a profound effect on the resulting microstructure. This is of importance when considering the measurements of the stress-free d-spacing for the residual stress analysis and for predicting the residual stresses using FEM. Since the γ' size distribution has a profound effect on the strength of the material [32], there will be a knock on effect regarding the ability of the material to store elastic strain, i.e. build up residual stresses.

Residual stress characterisation

Experimental

The residual stress generated from each quench has been characterised along a centre-thickness radial line scan using neutron diffraction (Figure 9a-c). Initially, the d_0 had been determined by measuring small cubes as described earlier. However, in this case the S1 and S2 radial stress profiles indicated compressive radial stress at the rim. This cannot occur since the rim is a free surface in the radial direction and as a result can only have a value of zero stress. In addition, both samples were measured to have compressive axial stress across the entire line scan. Such a result appears to violate equilibrium conditions, which require the sum of the axial stresses over an axial cross section to equal zero [18]. To overcome this issue and generate an alternative d_0 value, a stress balance was imposed whereby the d_0 was calculated such that the sum of the axial stresses was zero [18]. It should be noted that ideally, such stress balance model is based on a larger data set as anomalous data points can easily skew the stress balance. As a result, the data from S1 and S2 are plotted with an additional estimated ±50MPa error bar to the measured uncertainty. The stress profiles using the imposed axial stress model, as well as the measured d_0, have been plotted in Figure 9. It can be seen that the radial stress profiles of S1 and S2 now follow the expected trend of zero radial stress at the rim. The stress balance was also used for S3 to verify the accuracy of the measured d_0. In this case the results show a very minor difference between the two d_0's (Figure 9c). Although either d_0 could be used for S3, the stress balance value will be retained for consistency across the quenches.

The measured hoop stress as obtained through the contour method is compared to neutron diffraction data along the radial line scan in Figure 10. In the water quenched, and to a lesser extent the oil quenched, there is a tendency for the contour method to measure reduced tensile stresses in comparison to the neutron diffraction data. The contour method is known to be susceptible to uncertainty when high levels of residual stress are relaxed during the cutting process [23]. The stress levels observed in S3 approach and at some points exceed the proof stress of this material (~1050MPa). At the stress levels observed, the effects of plasticity begin to generate errors as the localised region at the cut tip deforms plastically. Such deformations were minimised by secure clamping of the part. However, they would not have been eradicated and as such will have contributed to uncertainty in the contour method

data. Note that in S1 the contour method and neutron diffraction datasets show a slightly stronger correlation, possibly indicating a reduction of plasticity induced errors due to the lower magnitude residual stress distribution.

Each of the line scans in Figure 10 are made from rim to rim, thus the symmetry about the bore in terms of residual stress should reflect the symmetry of the quench. S1 exhibits the strongest level of symmetry about the bore, which reflects the slow and homogeneous air cooling process. Both S2 and S3 are approximately symmetric although both forgings exhibit an asymmetric feature at 20-25mm radial distance from the bore. This feature is thought to be the result of the cutting process as oppose to a non axi-symmetric quench since the cutting plane was chosen arbitrarily without any knowledge of the sample orientation during quench. As such, it is highly unlikely that a repeatable non axi-symmetric quenching feature would be observed in two individually quenched and measured forgings.

The feature observed in both S2 and S3 was verified post analysis to be in the half of the forging where the wire was approaching the exit point. Since this was not observed in the other half of either forging it is speculated that the cutting direction has a slight impact on the resulting stress profile when moving from tensile to compressive stress or vice-versa.

The contour method has been used to generate 2D maps of the residual hoop stress in each quench condition (Figure 11). Each dataset has been plotted using the same scale and contour demarcation for ease of comparison. As expected, the levels of imparted residual stress fall with the less aggressive quench media, i.e. water, oil and then air. In S1 the slow rate of heat extraction has resulted in residual stress levels ranging from +150 to +300MPa in the core to -150 to -300MPa at the surface. Although the stress levels are low, the trend follows what would be expected. The core cools and contracts after the surface, resulting in a tensile core balanced by a compressive surface.

The stress distribution in S2 and S3 are similar in appearance, showing a tensile core surrounded by a compressive exterior. In S2 the stress distribution is largely symmetric, indicating the quench has been applied equally to each face. However in S3 the symmetry is compromised by a large compressive feature at 30-38mm radial distance from the bore. The feature appears to be anomalous since the stress values are extreme in comparison to the opposite rim and the quenching process should have

generated an approximately axi-symmetric stress distribution as observed in S2. Such an anomalous result may have been generated during the cut; particularly since the wire was exiting the sample whilst moving through strong compressive stress in this region. Measurement errors close to the cut edge have been observed in other studies, particularly where large stresses are involved [23]. In addition, uncertainty originating from the so called 'bulge effect' and cut tip plasticity are known to be effected by the stress concentration at the cut, which would be very high in this region [23].

Comparison of experimental results to finite element model

Residual stress predictions as obtained using the finite element analysis code 'SCO3' have been compared to experimental results in Figure 12-Figure 14. Starting with S1 (Figure 12), an initial comparison of the modelled data (model-1) to the experiment produced a clear contrast. While the simulation predicts zero residual stress across the radius, both experimental techniques do not. Such a discrepancy cannot be said to be the result of an inaccurately simulated cooling process since the model and thermo-couple data have been shown to match well (Figure 3). Further investigation pointed to the material property data base, which were optimised for the commercial alloy in service, and therefore characterised the material after a more aggressive quench. The proof stress curve in particular was found not contain data for very small strains (<0.05%), meaning that the model simply extrapolated the data. As a preliminary attempt to compensate for this, a low strain material property dataset was sought through empirical trials. The low strain model based on this material data is plotted on Figure 12 as 'model-2' for comparison.

Comparing the experimental data to the low strain model shows a marginal improvement in the correlation, particularly since the trends are now comparable. It is clear however that the model still under predicts the residual stress in comparison to the experimental data. Further iterative improvements of material property data were not considered since it was recognised that a more sound material data set would be required in order to draw firm conclusions. However, after completing this initial empirical step, it is believed that a mechanical characterisation of the air cooled material would yield better results in the finite element model.

The results from next most aggressive cooling process, oil quench (S2), are given in Figure 13a-c. The trends observed largely follow the expected bounds of a quenched

disc geometry; the hoop and radial stress are the same at the bore, the axial and hoop stresses are strongly compressive at the rim whereas the radial stress falls to zero, indicating a bi-axial compressive surface. When using isotropic hardening the simulated and experimental data in S2 show very strong agreement in all three stress directions across most of the radial line scan. The only exception to this is the hoop direction, which shows a strong correlation between the predicted and measured stress in the 0-20mm region only. From 20-38mm the isotropic model has a tendency to under-predict the stresses at most locations although some improvement is seen at the rim in comparison to the neutron diffraction data. Note that the contour data at the rim is thought to be less reliable since edge effects are prevalent here.

A further comparison can be made in S2 when using the Mroz hardening model. Comparing the Mroz and isotropic models directly it is clear that a profound difference in the generation of residual stress has been predicted. The reason for this is the inclusion of the Bauschinger effect in the Mroz model [33]. The Bauschinger effect can be summarised as a reduction in the flow stress upon reverse yielding, accompanied by different hardening behaviour [31]. Thus, the use of an Mroz hardening model in S2 has brought about a reduction in the level of predicted stress since the inclusion of the Bauschinger effect has reduced the material flow stress as the forging reverse yields on final cooling.

Comparing the Mroz model to the experimental data shows a significantly reduced correlation, particularly in the hoop and radial directions where discrepancies of up to 550MPa are visible. Based on these observations, it must be concluded that the inclusion of a Bauschinger effect and the associated reduction in flow stress is not realistic for the oil quenching as carried out in the investigation. This is further verified by the strong correlation exhibited by the isotropic model, which does not take into account the Bauschinger effect.

The residual stress resulting from the final and most rapid cooling process, water quenching (S3), has been characterised in Figure 14a-c. In the hoop and radial directions, the isotropic model has predicted stresses in excess of those measured, whereas the Mroz model has predicted stresses, which are less than those measured. In the axial direction both models are in strong agreement with the data from 0-20mm, after which point the Mroz model shows a better match. Overall, neither modelling approach can be said to have a better correlation to the data, however it is

worth noting that the measured data largely lies in between the two hardening models. Based on these results, it appears that the hardening, which occurs during water quenching, is not truly isotropic or kinematic. Such a result is in contrast to much of the previous work concerning quenching stresses, which has found the isotropic model to match well with measured stress [29, 30]. Furthermore it highlights the difficulty in accurately simulating plastic behaviour when attempting to take into account complex reverse yielding.

Drawing on the data obtained for each quench, an approximate theme emerges that as the quench becomes more aggressive, the isotropic hardening model becomes less realistic and the Mroz model begins to show an improvement. This suggests that the quenching process is subject to a Bauschinger effect, and that this is more prominent as the level of reverse yielding increases with cooling rate. However, it also suggests that at present the simulation of the Bauschinger effect is too strong in this material and requires further work.

4. Conclusions

The residual stress generated through quenching from heat treatment has been characterised in sub-scale disc geometries. Three quench media were investigated; air, oil and water, giving slow, medium and fast rates of cooling. Residual stress characterisation was carried out using three independent means, neutron diffraction, the contour method and finite element modelling. Microstructural characterisation was carried out to observe the effect of cooling rate on the γ/γ' microstructure and relate it to the quenching cooling rates. The results obtained and the observations made allow the following conclusions to be drawn:

- The rate of cooling in RR1000 directly affected the γ' size distribution. Slow cooling in the air cooled forging allowed the γ' to coarsen significantly. At lower magnifications very large intragranular γ' particles were visible in some grains but not others, indicating possible chemical heterogeneity.
- In the oil and water quenched conditions the micrographs indicated that the increased cooling rate had resulted in the reduction in size of the secondary γ'. A more quantitative analysis was made and the size distributions (Table 3) found to back up what was directly observed in the microstructure.

- Residual stress was successfully characterised throughout the sample bulk using neutron diffraction. Measurements were made along a maximum pathlength of 36mm with an uncertainty of no greater than 50MPa. The quenching process was found to generate peak tensile stress in the bore with values ranging from 300MPa for air cooling, up to 1200MPa for water quenching.

- In this particular investigation two of the three d_0 cubes extracted from the core of each forging were found to be a poor representation of the actual strain free d-spacing. A stress balance was successfully implemented to obtain a best estimate of the d_0, however it is recognised that future d_0 characterisations should be made with more than one macro-stress free coupon where possible.

- The contour method provided a valuable comparison to the neutron diffraction dataset. Overall agreement was reasonable although the contour method was found to under estimate the tensile stress in bore region. A number of sources of uncertainty were considered to explain this discrepancy. It was concluded that due to the high stresses involved, plasticity at the cut tip had introduced errors into the results. Line scans across the contour data indicated a highly axi-symmetric quench in the air cooled sample. The oil and water quenches were also largely symmetric although the measurement was compromised by an artefact generated by the cutting process.

- A finite element model was generated and optimised using thermo-couple on-cooling data to characterise each quench. A heat transfer coefficient curve was successfully derived and applied as a surface boundary condition to accurately simulate the measured cooling rate.

- The model was run using two hardening models, Mroz and isotropic, to take into account the possibility of a Bauschinger effect during reverse yielding. The findings indicated the isotropic model fitted well to the oil quench, but that the same hardening model significantly over predicted the stresses resulting from a water quench. When the Mroz model was employed, the predicted stresses fell dramatically, but this resulted in an under prediction of the water quenched stresses. Overall the measured data fell largely within the upper (isotropic) and lower (Mroz) bounds of the model. Based on this observation, it is concluded that the Bauschinger effect should be taken into

account when modelling a water quench, but that it is currently over estimated for this material in the Mroz model.

Acknowledgments

List of tables:

Table 1: Nominal composition of Nickel superalloy RR1000

Alloy	Ni	Cr	Co	Mo	Ti	Al	C	B	Ta	Zr	Hf
RR1000	52.3	15.0	18.5	5.0	3.6	3.0	0.027	0.015	2	0.06	0.5

Table 2: Material properties of RR1000

Material Properties of RR1000	
Young's modulus (bulk)	224 GPa
Poisson ratio (bulk)	0.33
(311) Diffraction elastic constant	203 GPa
(311) Poisson ratio	0.3

Table 3: intra-granular γ´ characterisation by quench media (data extracted from Figure 8)

Quench media	Average Cooling rate (1200-700°C) °C/s	Intra-granular γ´ size (nm)		γ´ volume fraction %
		Secondary	Tertiary	
Still Air	2.00	110 (±20)	20 (±10)	19.8
Oil	9.03	60 (±30)	10 (±5)	16.7
Water	47.21	30 (±30) (uni-modal)		11.7
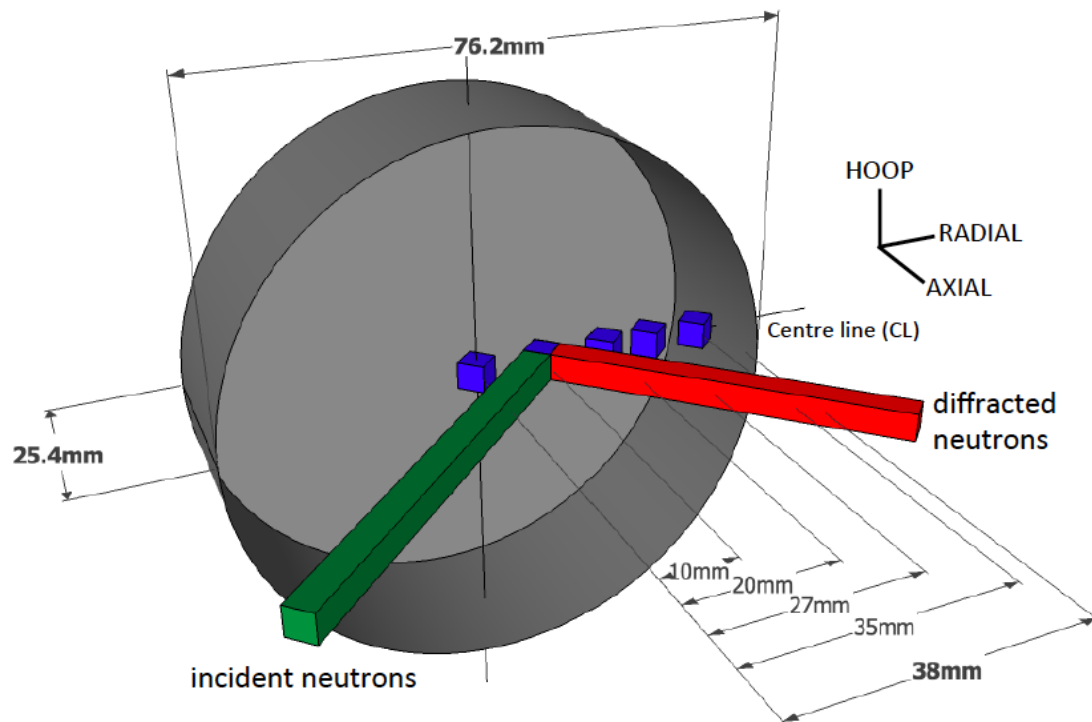
Figure 1: Schematic diagram of the sub-scale 'hockey puck' forgings with the measured gauge volumes indicated.
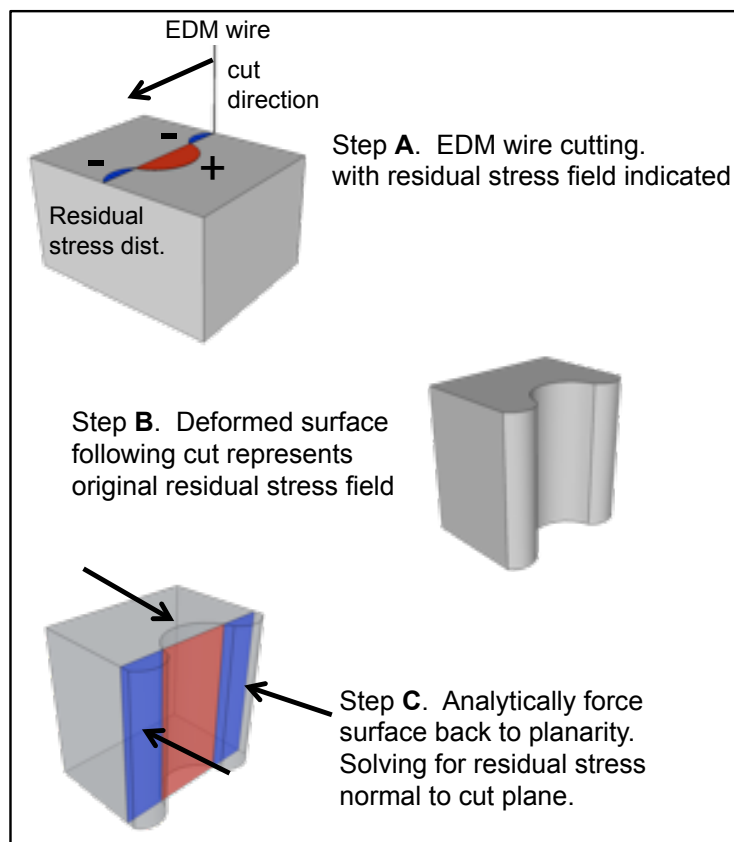
Figure 2: Schematic process of residual stress characterisation through the contour method
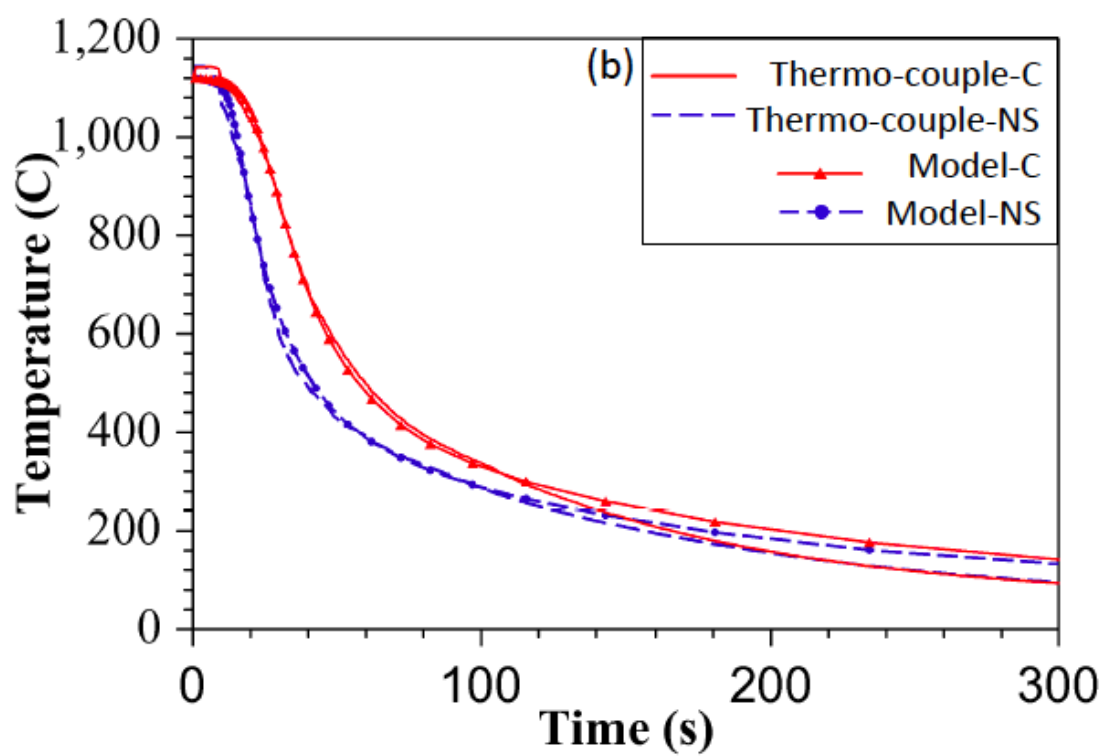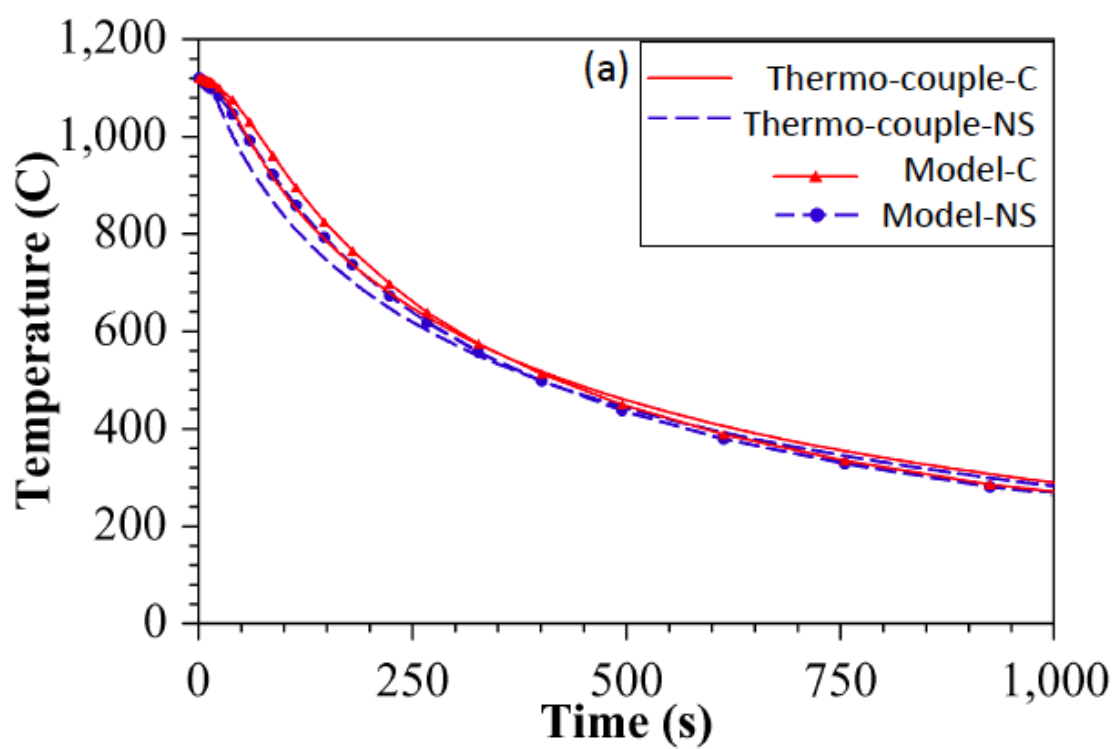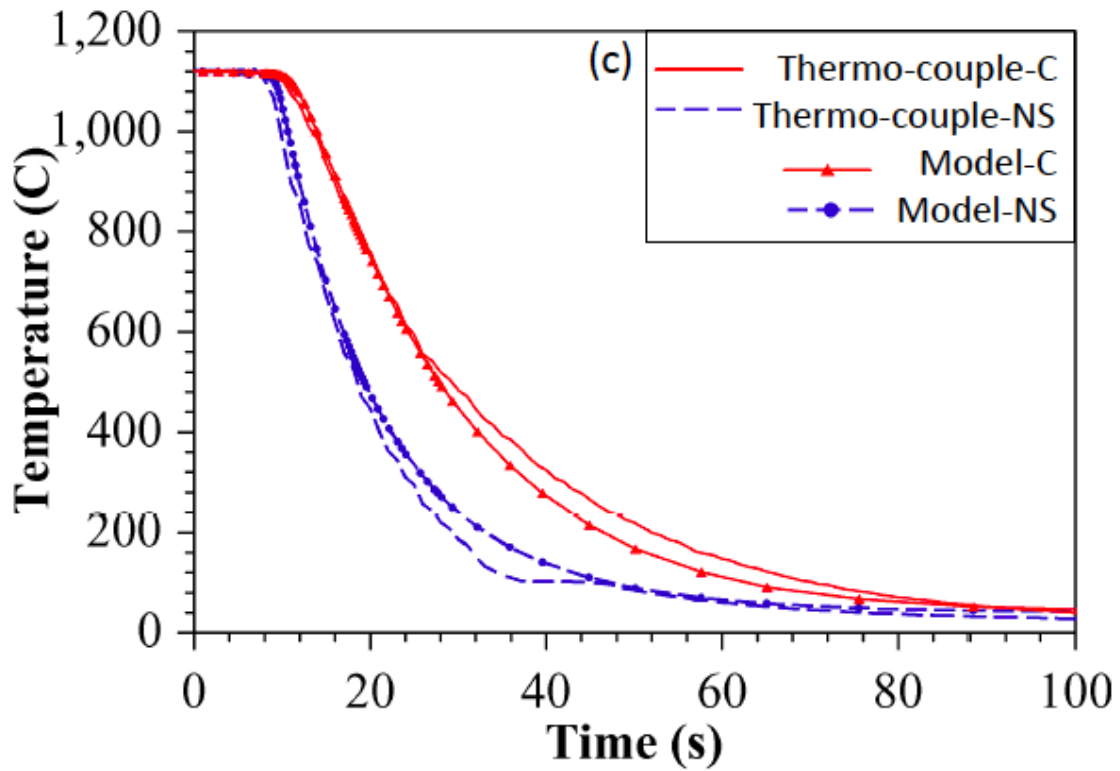
Figure 3: Comparison of the modelled and experimentally measured cooling rate during a) air cooling, b) oil quench, and c) water quench at the centre (C) and near surface (NS) of the forging.
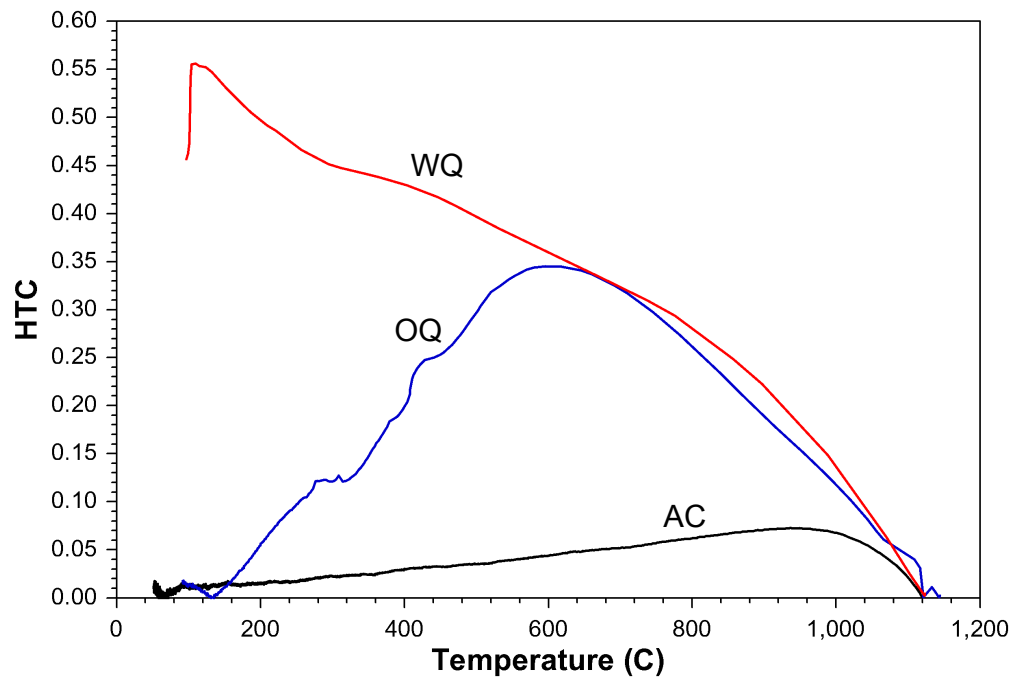
Figure 4: Derived heat transfer coefficient (HTC) curves for air cool (AC), oil quench (OQ) and water quench (WQ).
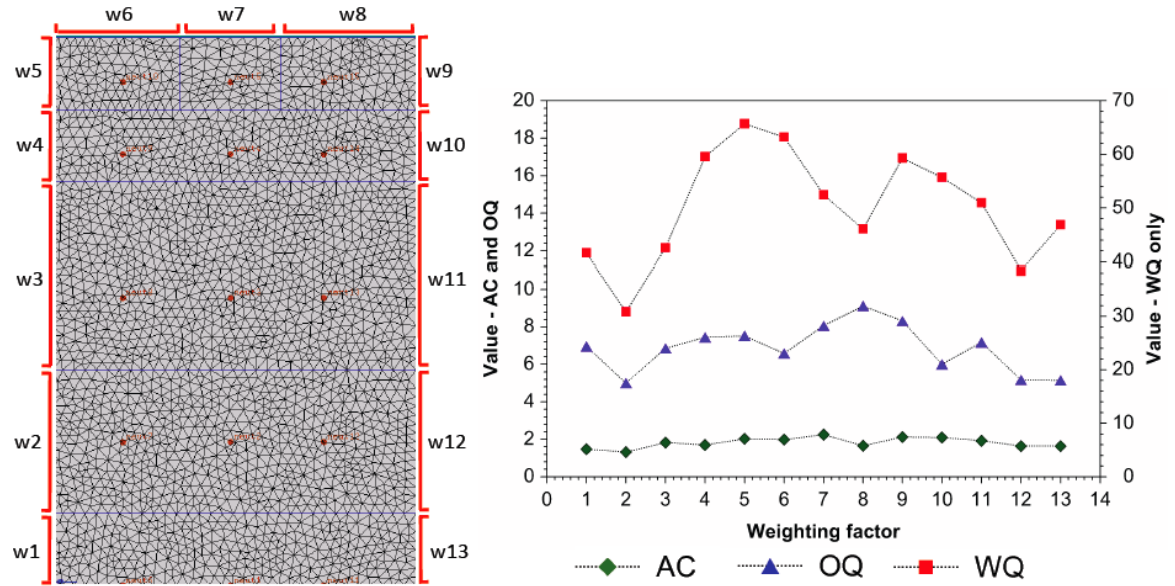
Figure 5: HTC weighting factor distribution and values as used in the FE quench model.
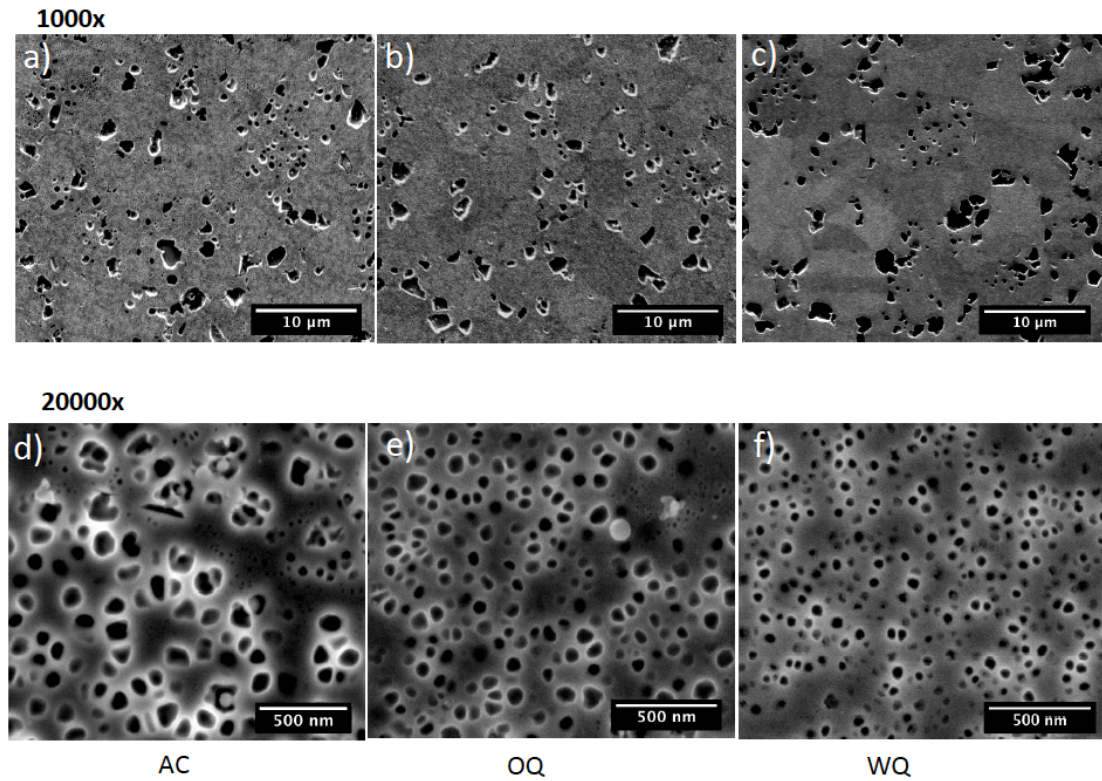
Figure 6: Micrographs characterising the γ´ particle size in each of the quenched conditions.   a-c) 1000x magnification imaging the primary γ´. d-f) 20000x magnification imaging the intragranular secondary and tertiary γ´.
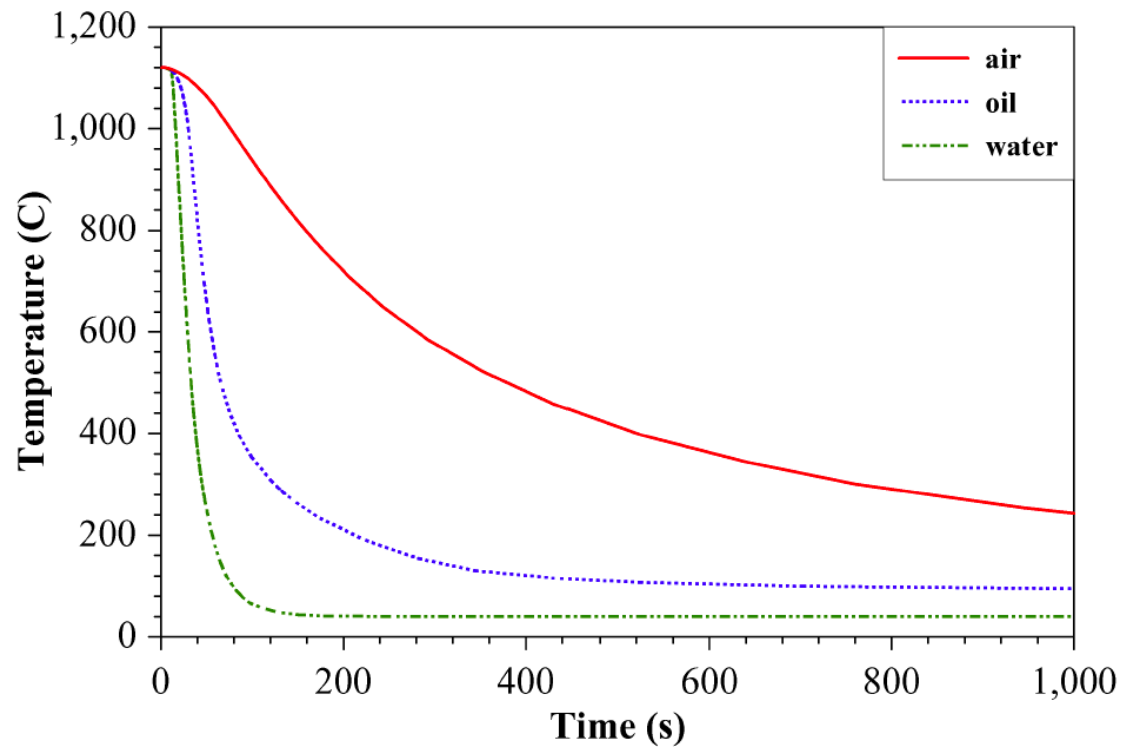
Figure 7: Modelled cooling rates at the forging centre for each quench media.
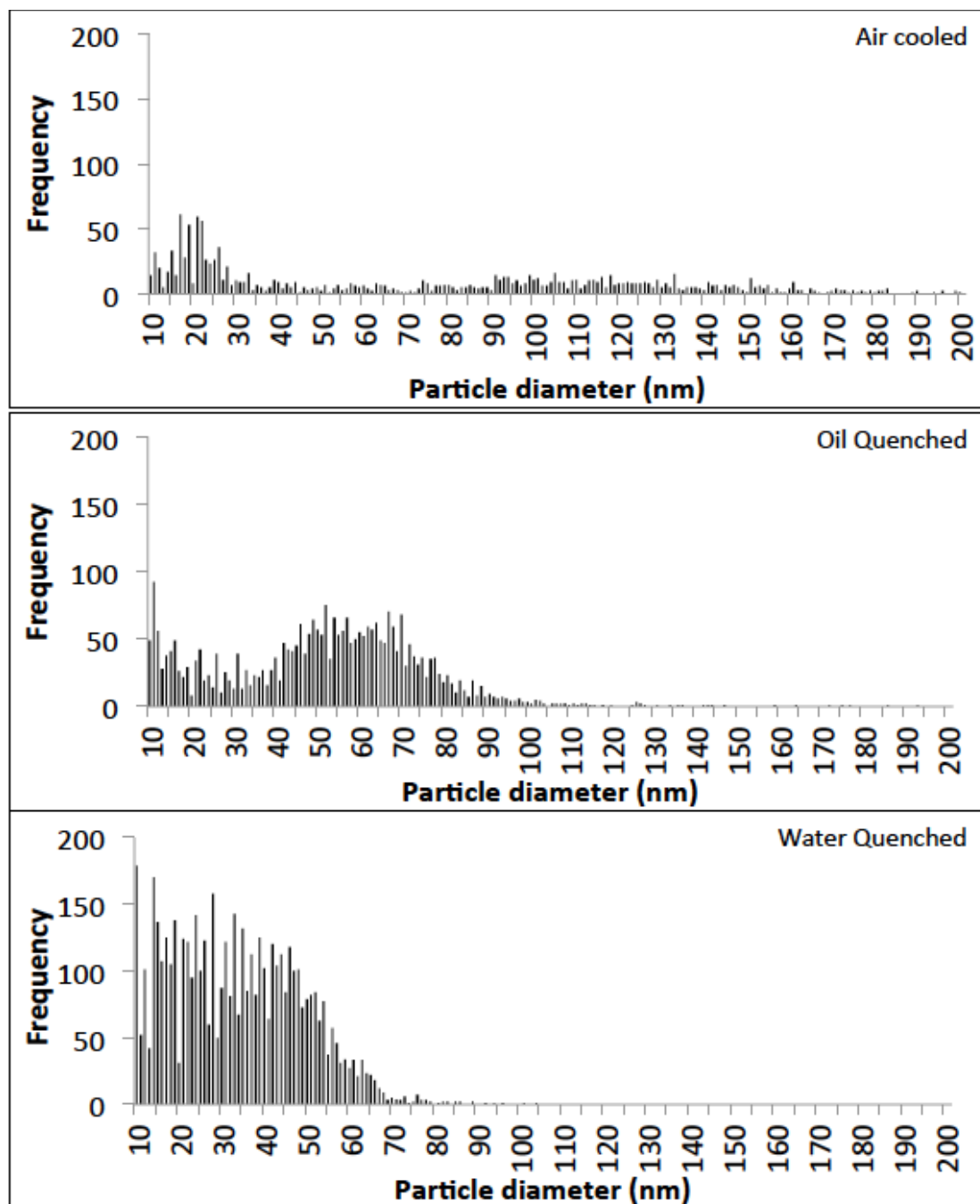
Figure 8: Intragranular γ´ particle size distribution in each of the quenched conditions.
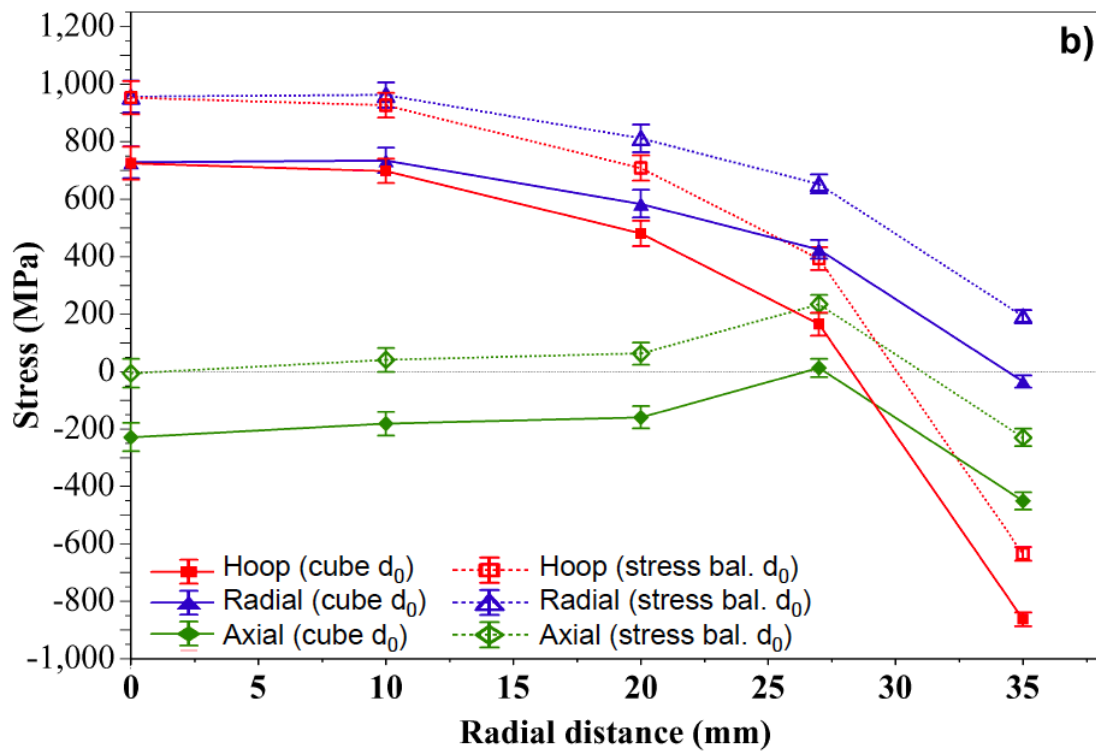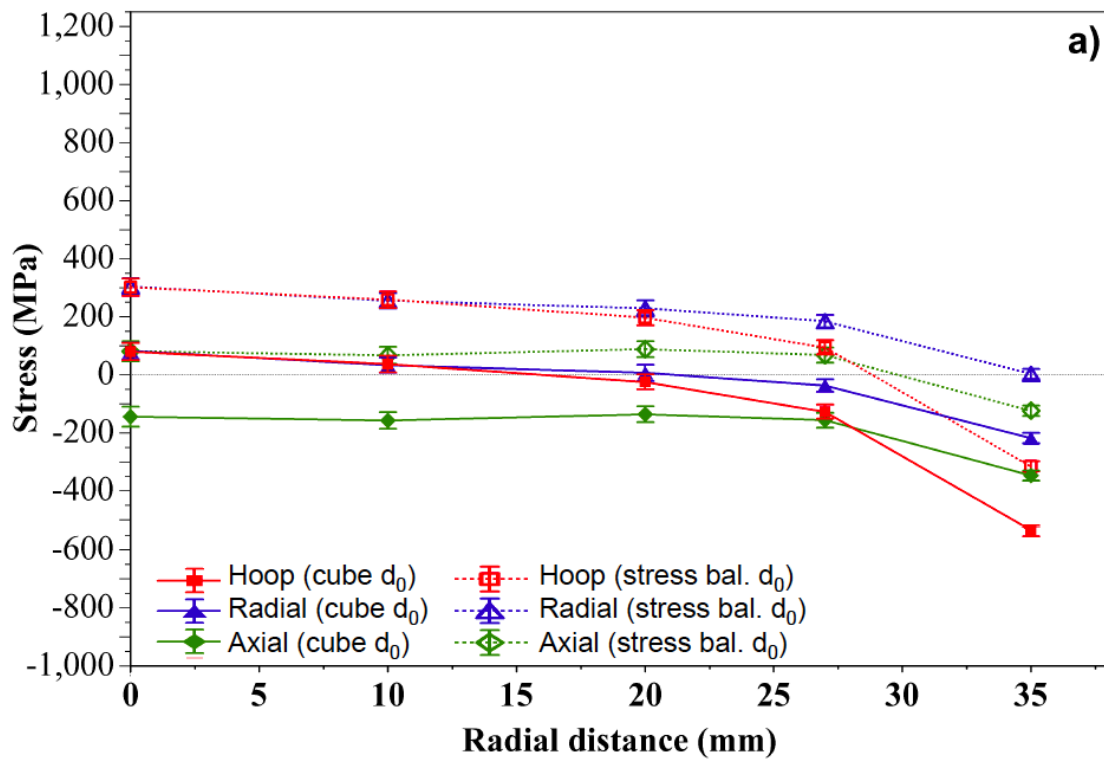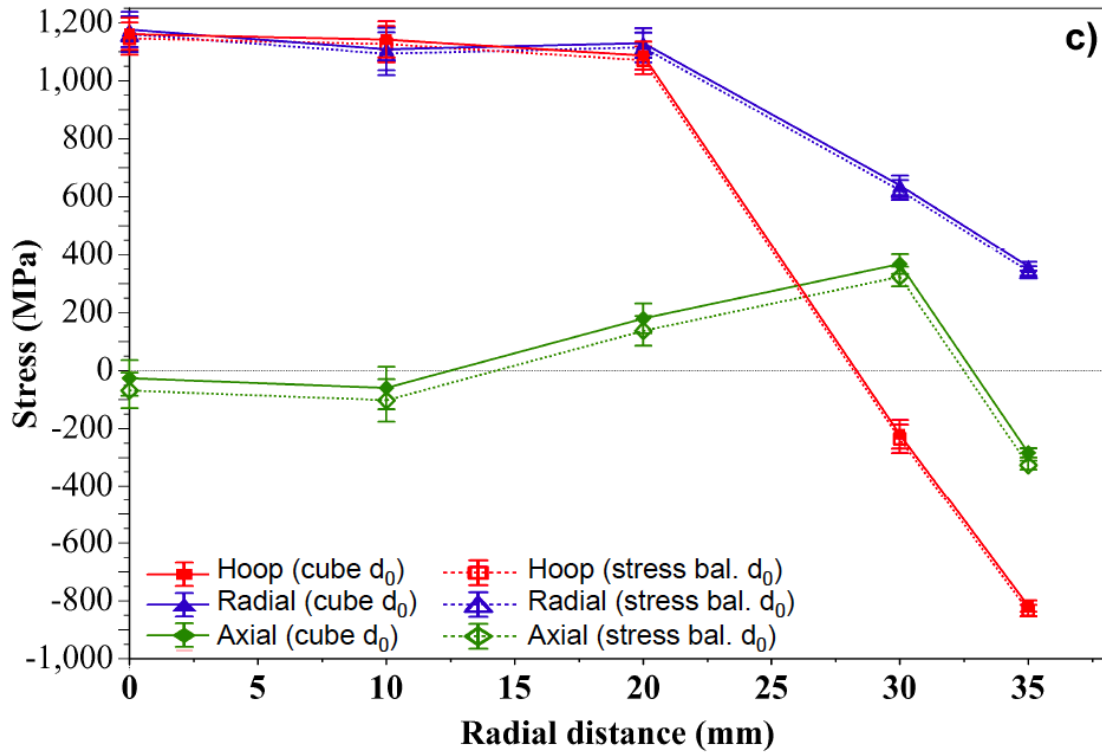
Figure 9: Residual stress characterisation by neutron diffraction in the a) air cooled, b) oil quenched, and c) water quenched condition. In each case line scans using a macro-stress free cube are compared to a d_0 obtained through an axial stress balance.
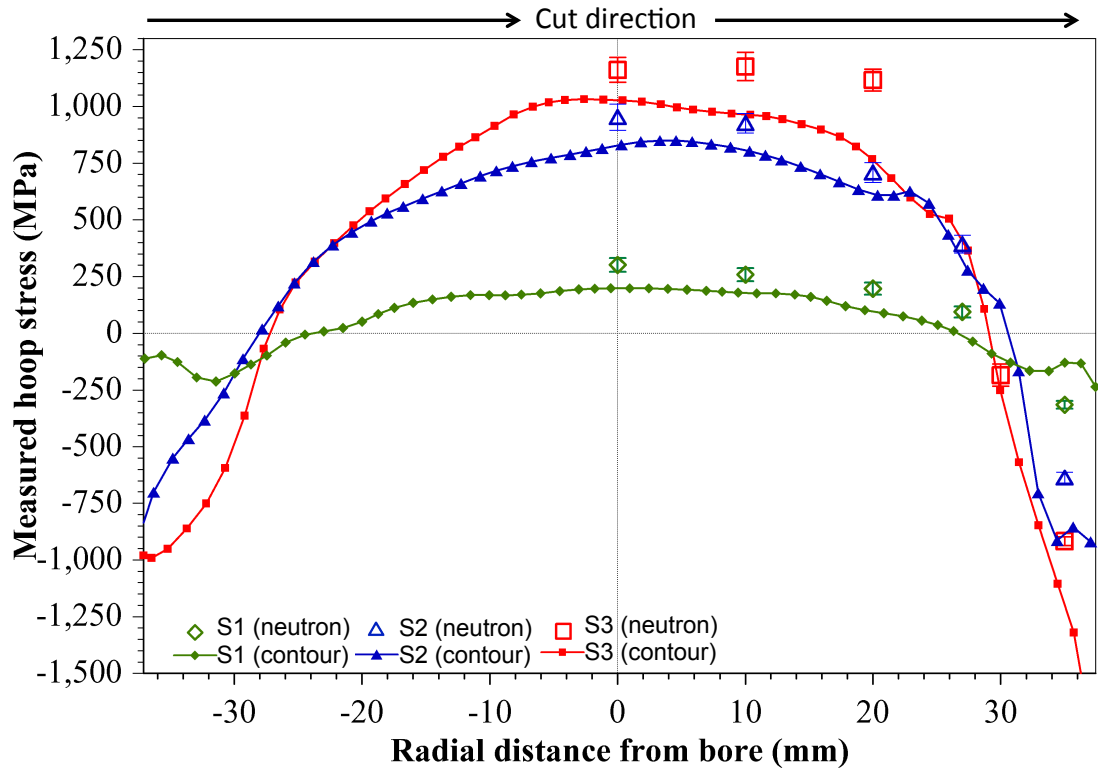
Figure 10: Comparison of the contour method and neutron diffraction line scans across the forging diameter at mid depth.
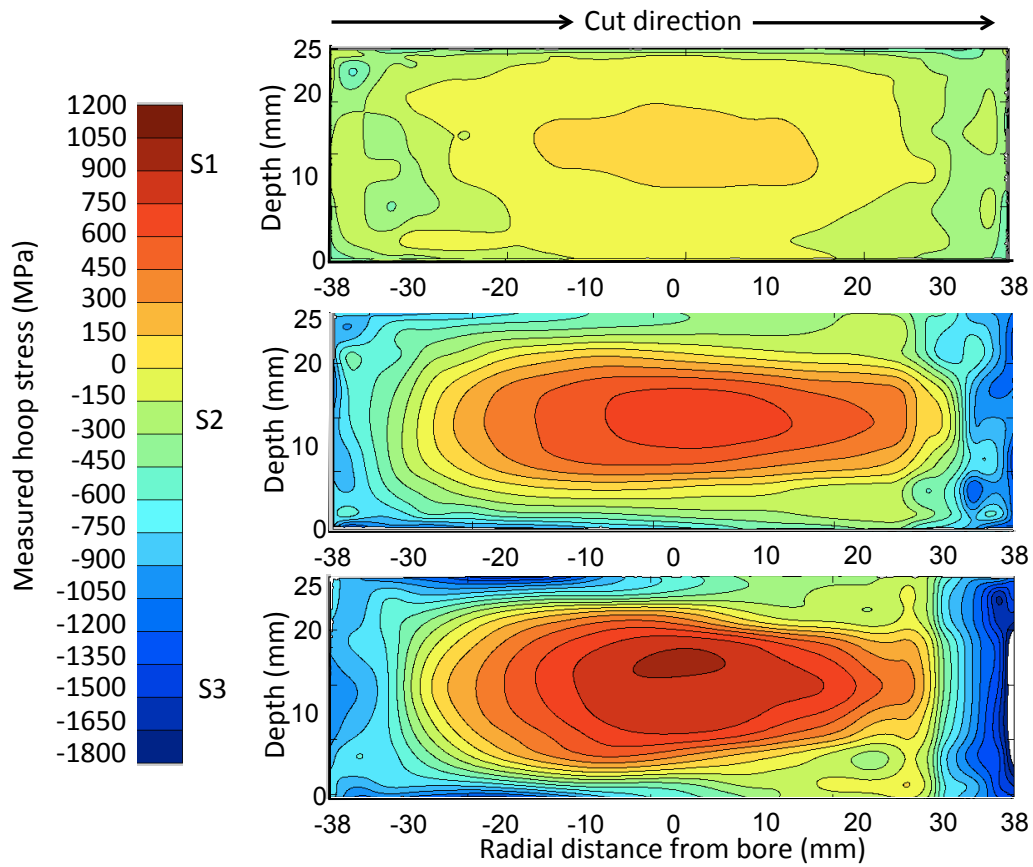
Figure 11: 2D hoop stress distribution in each quench state as obtained using the contour method
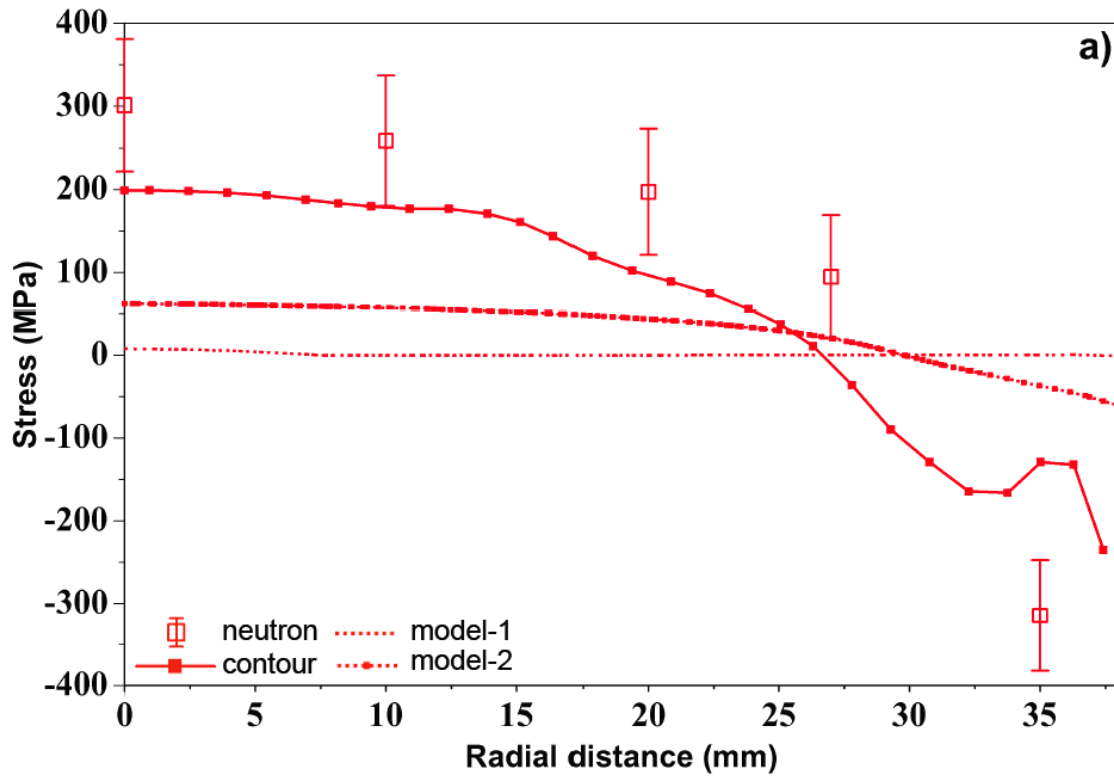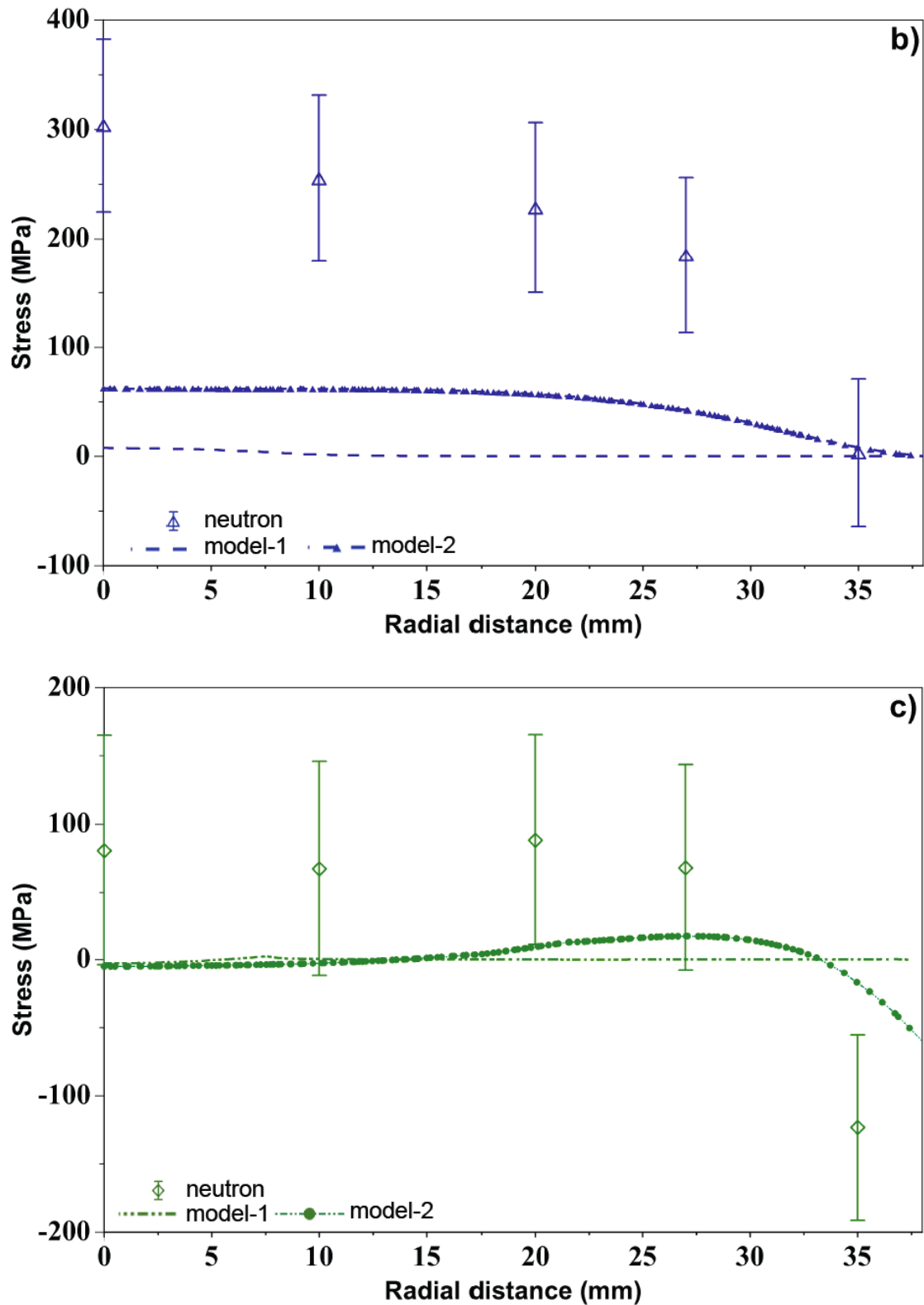
Figure 12: Comparison of residual stress characterisation in a sub-scale forging still-air cooled from solution heat treatment in the a) hoop, b) radial and c) axial stress directions. Model-1 uses standard material properties, model-2 uses modified material properties.
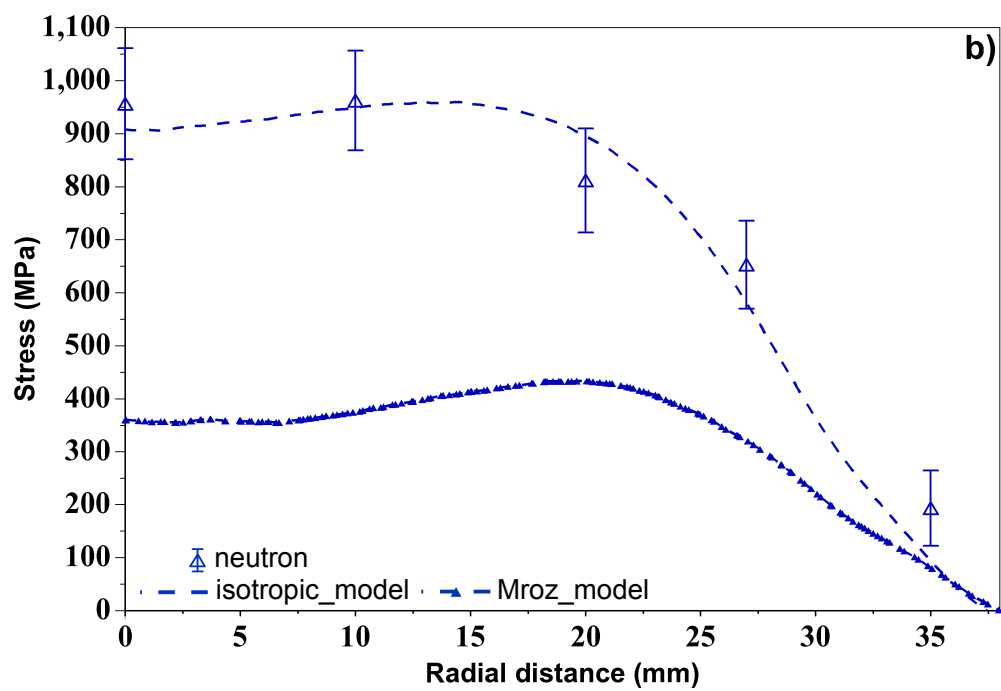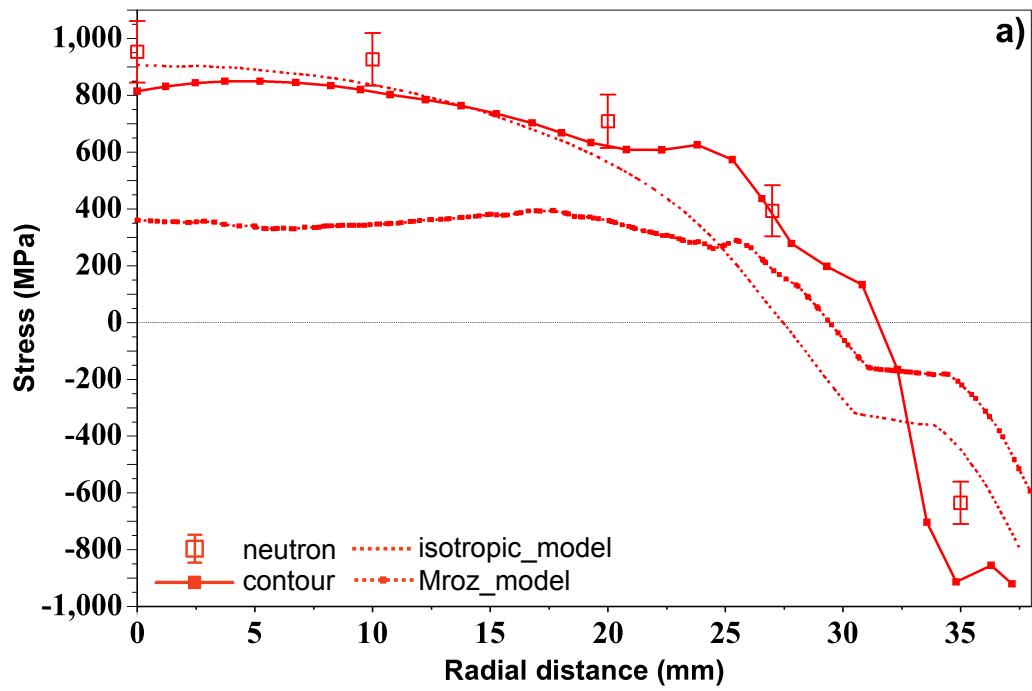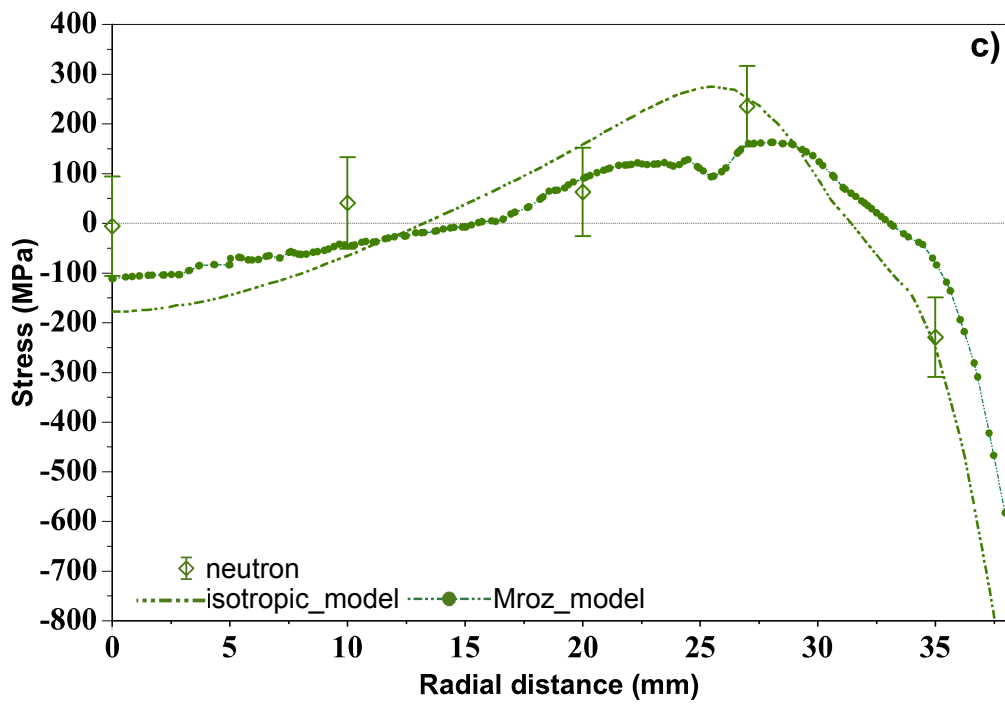
Figure 13: Comparison of residual stress characterisation in a sub-scale forging oil quenched from solution heat treatment in the a) hoop, b) radial and c) axial stress directions.
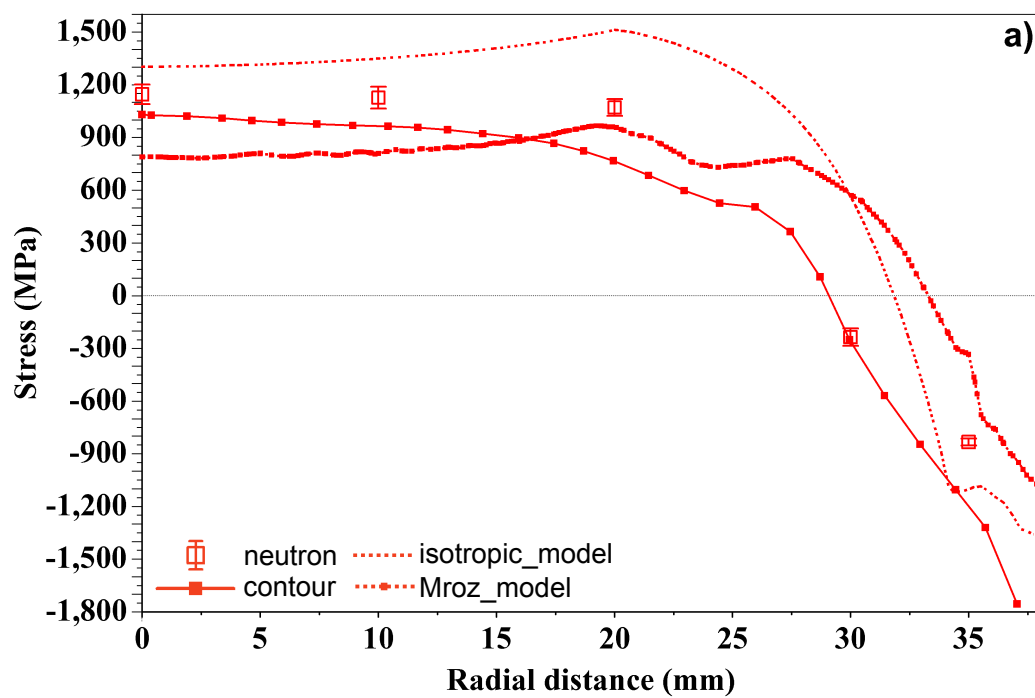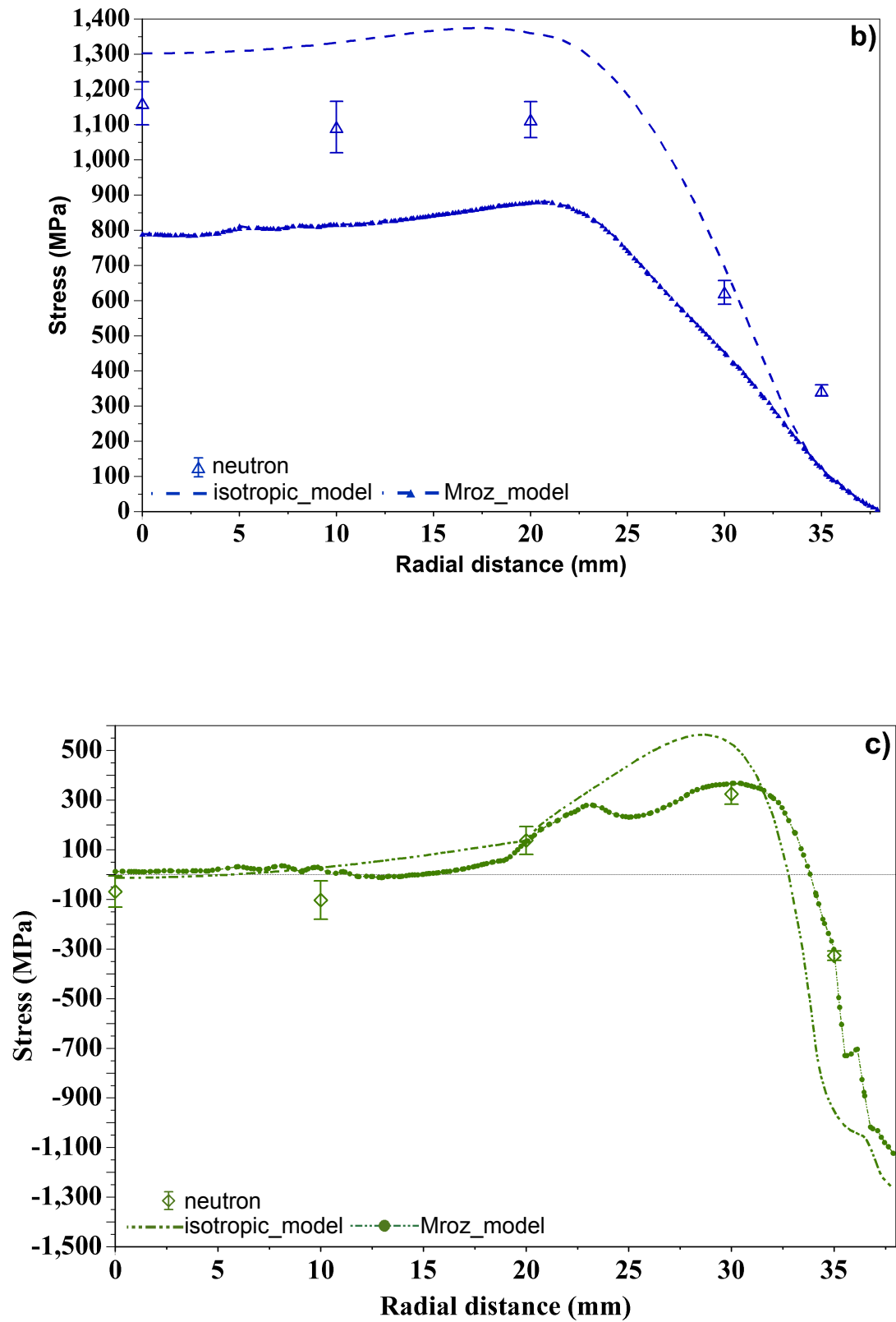
Figure 14: Comparison of residual stress characterisation in a sub-scale forging water quenched from solution heat treatment in the a) hoop, b) radial and c) axial stress directions.

References

[1] Z. Mróz, Journal of the Mechanics and Physics of Solids, 15 (1967) 163-175.

[2] N.S. Ottosen, M. Ristinmaa, 12 - Common Plasticity Models, in: The Mechanics of Constitutive Modeling, Elsevier Science Ltd, Oxford, 2005, pp. 279-319.

[3] M. Preuss, J.W.L. Pang, P.J. Withers, G.J. Baxter, Metallurgical and Materials Transactions A, 33A (2002) 11.

[4] R.C. Reed, The Superalloys - Fundamentals and Applications, Cambridge University Press, Cambridge, 2006.

[5] T.M. Pollock, S. Tin, Journal of Propulsion and Power, 22 (2006) 361-374.

[6] R.J. Mitchell, M. Preuss, M.C. Hardy, S. Tin, Materials Science and Engineering, 423 (2006) 282-291.

[7] J. Coakley, D. Dye, H. Basoalto, Acta Materialia, 59 (2011) 854-863.

[8] S. Dubiez-Le Goff, R. Couturier, L. Guétaz, H. Burlet, Materials Science and Engineering: A, 387–389 (2004) 599-603.

[9] M.P. Jackson, R.C. Reed, Materials Science and Engineering: A, 259 (1999) 85-97.

[10] D.L. Ball, B.K. Tom, R.J. Bucci, M.A. James, in: Residual Stress Summit, Tahoe City, CA, 2010.

[11] S. Kimball, P. Mattis, in, 1995.

[12] C.A. Schneider, W.S. Rasband, K.W. Eliceiri, Nat Meth, 9 (2012) 671-675.

[13] P.J. Withers, C. R. Physique, 8 (2007) 806-820.

[14] M.T. Hutchings, P.J. Withers, T.M. Holden, T. Lorentzen, Introduction to the Characterization of Residual Stress by Neutron Diffraction, Taylor and Francis, London, 2005.

[15] M. Hofmann, R. Schneider, G.A. Seidl, J. Rebelo-Kornmeier, R.C. Wimpory, U. Garbe, H.-G. Brokmeier, Physica B, (2006) 1035-1037.

[16] H.J. Stone, T.M. Holden, R.C. Reed, Acta Materialia, 47 (1999) 4435-4448.

[17] T. Pirling, G. Bruno, P.J. Withers, Materials Science and Engineering: A, 437 (2006) 139-144.

[18] P.J. Withers, M. Preuss, A. Steuwer, J.W.L. Pang, Journal of applied crystallography, 40 (2007) 891-904.

[19] J. Rolph, N. Iqbal, M. Preuss, M. Hofmann, A. Evans, M. Ganesan, (Submission in process), (2012).

[20] B. Grant, K. Elisabeth, M. Preuss, J. Quinta da Fonseca, M.R. Daymond, Advanced Materials Research, 278 (2011) 144-149.

[21] R.C. Wimpory, C. Ohms, M. Hofmann, R. Schneider, A.G. Youtsos, International Journal of Pressure Vessels and Piping, (2009) 48-62.

[22] M.B. Prime, Transactions of the ASME, 123 (2001) 162-168.

[23] M.B. Prime, A.L. Kastengren, Proceedings of the SEM Annual Conference & Exposition on Experimental and Applied Mechanics Indianapolis, (2010).

[24] Mathworks, in, Natick, MA., 2010.

[25] SIMULIA, in, Rising Sun Mills, 166 Valley Street, Providence, RI., 2011.

[26] P.G. Frankel, in: Material Science, University of Manchester, Manchester, 2008, pp. 38-40.

[27] M.B. Prime, R.J. Sebring, J.M. Edwards, D.J. Hughes, P.J. Webster, Experimental Mechanics, 44 (2004) 176-184.

[28] G.P. Bibby, in, Rolls-Royce, 1998.

[29] D. Dye, K.T. Conlon, R.C. Reed, Metallurgical and Materials Transactions A, 35A (2004) 1703-1713.

[30] M. Rist, J. James, S. Tin, B. Roder, M. Daymond, Metallurgical and Materials Transactions A, 37 (2006) 459-467.

[31] M.E. Kassner, P. Geantil, L.E. Levine, B.C. Larson, Materials Science Forum, 604-605 (2008) 39-51.

[32] M. Preuss, P.J. Withers, G.J. Baxter, Materials Science and Engineering: A, 437 (2006) 38-45.

[33] C.O. Frederick, P.J. Armstrong, Materials at High Temperatures, 24 (2007) 1-26.

Chapter 7

Residual Stress Relaxation Through Ageing of a Nickel-base Superalloy – Measurement and Prediction

This paper has been prepared for submission to a relevant peer reviewed journal. The paper that follows is in the form in which it will be submitted to the journal pending clearance from Rolls-Royce plc. and ATI Ladish Forging. This research was performed with Dr. Michael Hoffman, Dr. Alex Evans, Dr. Stan Nikov, Dr. Ranga Ramanathan, Mr. Paul Enderson, Professor Michael Preuss, Dr. Mark Hardy, and Dr. Mike Glavicic

The lead author of this paper is the author of this thesis; all of the content which follows are the words of the lead author, and all of the data gathered and presented here is the result of investigations implemented by the lead author. In terms of co-author involvement, Dr. Michael Hoffman, and Dr. Alex Evans assisted with all aspects of data acquisition through neutron diffraction. Dr. Stan Nikov and Dr. Ranga Ramanathan assisted with the finite element modelling work. Mr. Paul Enderson provided the expertise to carry out microstructural characterisations using a scanning election microscope (SEM). Feedback and overall guidance for this work was provided by Professor Michael Preuss, Dr. Mark Hardy, and Dr. Mike Glavicic.

Residual Stress Relaxation Through Ageing of a Nickel-base Superalloy – Measurement and Prediction

J. Rolph[1] M. Preuss[1] P. Enderson[1] M. Hofmann[2] S. Nikov[3] M. C. Hardy[3] M. G. Glavicic[4] R. Ramanathan[5] A. Evans[6]

[1] Materials Science Centre, University of Manchester, Grosvenor St, Manchester, M13 9PL, UK

[2] FRM2, TU München, Lichtenbergstr. 1, 85747 Garching, Germany

[3] Rolls-Royce plc, PO Box 31, Moor Lane, Derby, DE24 8BJ, UK

[4] Rolls-Royce Corporation, P.O. Box 420, Speed Code T-61, Indianapolis, IN 46206-0420, USA

[5] ATI Ladish Forging, 5481 S. Packard Avenue, Cudahy, WI, 53110-8902, USA

[6] Institut Laue-Langevin, BP 156, 6, rue Jules-Horowitz, 38042 Grenoble cedex 9, France

Abstract

Residual stress imparted by water quenching has been relieved through ageing heat treatment in sub-scale disc forgings of the Nickel superalloy RR1000. Ageing was carried out at a single elevated temperature of 760°C but with three durations of heat treatment (15, 60, and 120 minutes). The effect of the ageing process on residual stress was characterised experimentally using the neutron diffraction and contour methods. The results obtained revealed a strong correlation between the two independent approaches. Stress relaxation was observed and found to cause peak tensile stresses of 1160MPa to fall to values as low as 770MPa after a 120 minute age time. Residual stress generation as a result of quenching was simulated using isotropic hardening and an Mroz hardening law, which allowed for a degree of kinematic hardening. The model indicated an over-prediction of quenched stress when using isotropic hardening, but an under-prediction when using the Mroz hardening. The two models were aged individually and the stress values found to converge within 15 minutes at 760°C. Comparing the model to the experimental data indicated an over-prediction in the level of stress relaxation in the model. In particular, the level of primary creep was observed to be much greater in the model in

comparison to that measured in the experiment. The cause of this discrepancy is thought to be the result of increased creep strength in the sample forgings brought about by the water quench.

1. Introduction

In modern gas turbines, engine designers seek to improve power and fuel efficiency through increased compressor discharge and higher turbine entry temperatures. To allow for such improvements to be made, advanced high temperature materials are required in the turbine sections of the engine. Nickel-based superalloys are one such material. They have been developed for high-temperature strength, toughness and resistance to corrosive environments, a combination made possible through a finely tuned γ/γ' microstructure (1). In this group of alloys, the γ phase forms a disordered matrix, while the γ' exists as $L1_2$ ordered precipitates distributed throughout the matrix. The precipitates strengthen the material significantly; anti-phase boundaries set up by the ordered γ' phase resist deformation by making it energetically costly for dislocations to move through the precipitate. This is known as precipitation strengthening, or age hardening (2). In the case of Nickel-base superalloys, the γ' phase remains ordered at very high temperatures, thus the strengthening effect is retained (3).

The particle size, volume fraction, distribution, and morphology of the γ' precipitates are controlled by the alloy chemistry and metallurgical processing, they have a significant impact on the material properties of Nickel superalloy (4-6). One particular alloy, RR1000 (chemical composition - Table 1), has shown improved high temperature properties due to a significantly greater volume fraction of γ' in comparison to other commercial alloys (7). The finely tuned microstructure of RR1000 is generated through heat treatment processing, quenching followed by ageing. Quenching consists of a rapid cool from high temperature (>1100°C) and ageing a prolonged treatment at a lower temperature (typically 750-800°C). The two processes manipulate the γ', dissolving, then re-precipitating and growing the particles to get the desired microstructure. However, the rapid cooling from quench sets up steep thermal gradients and thus generates significant residual stress; the ageing process, which follows allows partial relaxation of the generated stresses.

Residual stress characterisation during and post manufacture is of great importance to turbine manufacturers since it affects component distortion levels during machining, as well as in-service performance (8, 9). Process modelling is used to predict the residual stress distribution immediately prior to machining in order to remove material in such a way as to minimise distortion. Following material removal, the residual stress distribution in the finished part is calculated and passed into the lifing model, which predicts the service life of the part. Thus, the accurate prediction of residual stress through manufacture has two key benefits, it reduces reworking or possible scrappage of parts, and it allows more accurate prediction of the in-service life.

In order to make iterative improvements to process modelling capabilities it is necessary to validate simulated results with experimental data. In this article the focus will be on the simulation and characterisation of residual stresses in the post age condition. Characterisation has been carried out experimentally on sub-scale discs using neutron diffraction and the contour method, while simulations were run using the finite element method (FEM). Microstructural changes resulting from the age have been characterised using a scanning electron microscope (SEM). The results obtained from each approach are compared with the aim of improving future process modelling capabilities.

2.   Experimental description

Sample preparation

Four sub-scale disc forgings of the alloy RR1000 (chemical composition presented in Table 1) were provided by ATI Ladish. The forgings were 76.2mm diameter and 25.4mm depth (Figure 1). The forgings were extracted from a large pancake forging which had followed the powder metallurgy processing route before being isothermally forged. Each forging was extracted from the same radial distance to reduce thermo-mechanical variation in prior processing. In order to characterise the ageing process the four forgings were all water quenched from a sub γ´ solvus (1120°C) heat treatment before being aged at 760°C for a range of hold times. The water quenching process was chosen specifically to compensate for the sub-scale geometry which would otherwise not provide a sufficient thermal gradient to generate the residual stresses observed in larger production parts. An age temperature of

760°C reflected the typical stress relief/ageing temperature of a γ' strengthened Ni-base superalloy (10). Age times of 15, 60 and 120mins were chosen since it was felt that the stress relief process would occur early in the age. Data from a water quenched forging in the as quenched condition is also included in this investigation as a baseline from which the effects of ageing can be observed. The samples are therefore numbered S1 = water quenched, S2 = 15min, S3 = 60min and S4 = 120min age.

Microstructural Characterisation

Microstructural characterisation was carried out using electron microscopy to image the γ' distribution. A 3mm^3 coupon taken from the centre of the forging was used for the measurement since material had already been extracted from this location in order obtain the strain-free d-spacing, d_0, for residual stress characterisation. Furthermore, it was felt that the sample core would experience the most consistent cooling rate across all of the quenches since the impact of forging orientation in the quench tank would be minimal here. Note that in order to preserve the residual stress field, this extraction process could only be carried out once all experimental residual stress characterisation was complete.

Each coupon was mounted in phenolic resin then ground using ANSI 240-1200 grit size silicon carbide paper. Polishing consisted of a 6μm and 1μm diamond polish followed by a colloidal silica polish (OPS). To allow imaging of the γ' phase a chemical etch was required. The etch was carried out on each coupon individually using a Nickel two part etch (Table 2) for approximately 30 seconds. The etching process dissolves the γ' but not the γ, thus the γ' distribution is observable as holes in the γ matrix. Immediately following this, the coupons were mounted in an FEI Sirion Field Emission Gun Scanning Electron Microscope (FEG-SEM). Images were captured using a secondary electron through lens detector to a maximum resolution of ~3nm.

Neutron diffraction

Each of the forgings were measured at the dedicated strain scanning instrument STRESS-SPEC at the FRM-II, Munich, Germany (11).

Each forging was mounted on a computer controlled table and aligned initially using a theodolite. Neutron entry scans were then conducted at the front face and rim to precisely align the forging with the neutron beam. The gauge volume was defined as 4x4x4mm through primary and secondary Cadmium slits, the slits were positioned as close as possible to the forgings to minimise the effects of divergence. A 4x4x4mm gauge was chosen in this case to allow for reasonable count times in the bulk (<90 minutes) whilst maintaining spatial resolution. The orientation of the gauge volumes in relation to the sample geometry and neutron beam has been given in Figure 1.

Using a Si(400) monochromator neutrons of λ=1.55Å were diffracted on the Ni(311) hkl lattice plane at a diffraction angle of approximately 2θ=92°, generating a near cubic gauge volume. The Ni(311) reflection was chosen specifically for this strain measurement since it has been shown to be a good representation of bulk behaviour and have a low sensitivity to plasticity (12).

The diffracted neutrons were measured using a 2D area detector which recorded an intensity peak at the 2θ angle required for diffraction to occur. Each peak was fitted using a Gaussian function to calculate a single value of 2θ for the peak centre. This allowed calculation of the hkl lattice plane spacing (d) using Bragg's law.

$$\lambda = 2d_{hkl}sin\theta \tag{1}$$

The lattice strain can then be calculated using the measured d-spacing in combination with a strain-free lattice spacing, d_0 (Equation 2).

$$strain\ (\varepsilon) = (d - d_0)/d_0 \tag{2}$$

The strain free lattice spacing was obtained through identical measurement of small cubes (~5mm^3) extracted from the core of each forging. The cubes were of sufficiently small dimension as be free from macrostress which allowed direct measurement of d_0 (13). Extraction and measurement of the cubes took place at a later date to the main investigation on SALSA, a strain scanning instrument of similar setup (14). In order to calibrate between d-spacings measured on two separate instruments a container of RR1000 powder was measured on both instruments.

The possibility of d_0 variation within each of the forgings was taken into account in a separate investigation using the $sin^2\psi$ technique (15). The results of this investigation found moderate d_0 variation in quenched and aged forgings, but only at locations close to the surface, the variation was minimal across the centre thickness. It is

believed that this was the result of the similar cooling rate, and therefore level of elemental diffusion, which occurred in this region. Based on these findings, a single d_0 value was used for all diffraction strain measurements made along the centre line scan.

Strain was measured in three orthogonal directions, hoop, radial and axial, which were assumed from the sample geometry to represent the principal stress directions. Using the three orthogonal strain measurements it was possible to calculate stress using a form of Hooke's law.

$$\sigma_x = \frac{E_{hkl}}{(1+v_{hkl})(1-2v_{hkl})}\left[(1-v_{hkl})\varepsilon_x + v_{hkl}(\varepsilon_y + \varepsilon_z)\right] \text{ and } \sigma_y = \cdots \tag{3}$$

The diffraction elastic constants, E_{hkl} and v_{hkl} are specific to the (311) reflection in this material (Table 3). They were obtained from data generated during an in-situ loading experiment on Engin-X, ISIS, UK (16).

Uncertainty in strain was calculated from the error in peak fitting using the following relation (17).

$$u_\varepsilon = \frac{1}{tan\theta}[(\delta\theta_0)^2 + (\delta\theta)^2]^{\frac{1}{2}} \tag{4}$$

Where $\delta\theta_0$ is the peak fit uncertainty in the stress-free measurement (d_0) and $\delta\theta$ is the uncertainty in the hkl plane spacing measurement (d). The strain uncertainties were substituted into Equation 3 in place of the strain values in order to obtain the uncertainty in stress. Using this approach it was possible to adjust count times to achieve fitting errors of <0.02° which equated to ~200µε or ~50MPa.

Contour method

The contour method is a relatively new characterisation technique developed by (18). It allows the generation of a full 2D stress distribution normal to a cut surface. Implementation of the technique comprises of three distinct stages: cutting, surface measurement and analysis. Cutting of the sample enables to the residual stresses to relax which brings with it a deformation at the cut surface. The deformation is then measured, either by CMM touch probe or a non-contact laser profilometer. The measured surface is then analysed; through Bueckners superposition principle (19), the original stress can be determined by analytically applying a force to return the

deformed surface to a planar surface through a finite element model. Further details on the technique be found in the original work published by Prime (18).

Each forging was firmly clamped before being sectioned across the diameter along the neutron diffraction measurement plane using EDM machining. The cut was made using 'skim cut' settings, a low power cut made at a slow speed; this was important to prevent the cutting process from introducing additional residual stress. The surface contour of each half was measured using a nano-focus con-focal laser surface profilometer, using a step size of 100μm. Scans were made over an area larger than the cross-section in order to clearly identify the edges as regions with zero reflected intensity from the laser.

The raw data, x-y coordinates with surface height (z), were loaded in to MATLAB for manipulation and analysis (20). Applying an user defined scripts, outliers were removed and the two contours (one from each half) were aligned analytically through minimisation of eigenstrains. Once aligned, the average of both contours was taken, which removed the effects of shear as well as any anti-symmetrical errors generated during the cut. Finally, the averaged surface contour was fitted with a bi-variant spline function to remove experimental noise and thus provide the final contour resulting from deformation through stress relief.

In order to calculate the residual stress from the surface contour a finite element model was generated in ABAQUS (21). The measured surface outline was imported into ABAQUS to generate a planar cross section. This surface was extruded and then cut to represent one half of the disc forging in the undeformed state. The part was meshed using quadratic elements ~1mm in length at the cut surface reduced to ~5mm in length at the rear face. The undeformed mesh along with the spline fit of the deformed surface contour were imported back into MATLAB to generate a second model with the undeformed and deformed surfaces set as initial and final conditions. Through assuming elastic isotropy, the model was solved in ABAQUS using bulk elastic properties (Table 3). The 2D stress maps were used for visual comparison of the stress distributions, while radial line scans of data were extracted for comparison to the neutron and finite element techniques.

Finite element modelling

Modelling residual stress in the post age condition was carried out in two stages. The first stage was to model the quench and calculate the strains generated during the rapid cooling process. The second stage was to take the strains from the quenching process and import them into a second model, which simulated the ageing heat treatment and calculated the relaxation of strain that resulted.

All residual stress simulations were carried out using the Rolls-Royce in house finite element analysis code 'SCO3' (22). A 2D axi-symmetric model was generated from the rim to the bore and meshed using triangular elements with a typical length ~1mm. Note that the 2D approach used here assumed that all heat treatment processes and the residual stresses that resulted from them were axi-symmetric.

Simulation of the quenching process was carried out by first characterising the heat extraction using embedded thermo-couples in a stainless steel test piece. The thermal data was used to generate a heat transfer coefficient using the temperature differential between two thermo-couples via the following relation.

$$HTC = \frac{k(abs(T_B - T_A))}{(T_B - T_{water})d}$$
(5)

Where k is the thermal conductivity, T_A, T_B and T_{water} are the temperatures at thermo-couples A, B and of the water, and d the distance between the two thermo-couples. The HTC curve for the water quenching process is given in Figure 2.

To simulate the cooling process the HTC curve was employed as a surface boundary condition. However, the rate of heat extraction was expected to vary by location on the sample surface, to allow for this, the HTC was utilised in combination with a weighting factor. The value of the weighting factors was set using an optimisation loop which attempted to match the simulated cooling rate to that measured at each of the five thermo-couples. In this way it was possible to generate a model, which thermally matched the quenching process. Simulated and experimental cooling rates were compared throughout and can be seen in Figure 3, the results indicate that the model was a good thermal representation of the actual quench.

The quenching model was initially run using an isotropic hardening model in accordance with prior work carried out on similar materials (23, 24). However, the results obtained indicated a large over-prediction of residual stress. It was felt that

this might be corrected by factoring in the reverse yielding and associated Bauschinger effect which can occur during the quench (25). Typically this calls for a kinematic hardening rule {Ottosen, 2005 #233}, however the SC03 model analysis code used in this investigation no longer models kinematic hardening explicitly and instead uses an Mroz multilayer hardening rule {Mróz, 1967 #255}. The Mroz rule uses layers of yield surfaces to allow expansion (isotropic hardening) and translation (kinematic hardening) of the yield surface to occur. Comparing both hardening models it was found that overall the isotropic model over-predicted, and the Mroz under-predicted, the residual stress in comparison to the experimental data. It was concluded that the actual hardening was likely to be somewhere in-between the isotropic and Mroz hardening, and that the two hardening models should be treated as an upper and lower bound for the simulation.

Upon completion of the quenching simulation the inelastic strain was imported into an ageing model. This consisted of the same 2D axi-symmetric meshed geometry, but with the simulated processes altered. The heating and cooling rates from age were captured using the same embedded thermo-couple set up utilised in the quench. From the data recorded it was found that the heating and cooling rate was sufficiently slow during ageing to consider it uniform across the entire forging. As a result, the simulation was set up such that the temperature of all elements varied uniformly, meaning that no surface boundary conditions were required to model heat input or extraction at the surface.

The heating and cooling rate was simulated in the model by linearly increasing/decreasing the temperature to specific time-temperature points extracted from the thermo-couple data, which effectively modelling the thermal profile as a sequence of straight lines. A comparison between the measured and modelled ageing thermal profile is given in Figure 4. With the thermal history of ageing well matched, the relaxation of residual stress was simulated using material specific creep behaviour. It was assumed that since the rate of heating and cooling was very slow and close to uniform across the part that no plasticity would occur, as such this was not simulated in the model.

3. Results and Discussion

Microstructure

The evolution of the γ/γ′ microstructure with ageing as observed at 1000x and 20000x magnification has been given in Figure 5 (a-d) and Figure 5 (e-h) respectively - the typical particle size for the secondary intragranular γ′ has also been given in Table 4. The thermal history at the centre location of the forging as predicted by the finite element model is also given in Figure 4.

Beginning with the low magnification micrographs (Figure 5(a-d)) it is possible to observe the intergranular primary γ′ at the grain boundaries. Over the course of the ageing heat treatment no change is seen in the primary γ′ particle distribution. This is as expected since coarsening during ageing is normally observed in the intra-granular γ′ rather than the primary γ′ at the grain boundaries (2).

At the higher magnification (Figure 5(e-h)), the evolution of intra-granular γ′ is tracked through the ageing process. Starting with the water quenched forging Figure 5e, it is possible to see a broad uni-modal size distribution of secondary γ′. After a 15 minute age (Figure 5f) very marginal coarsening of the secondary γ′ is apparent as the typical particle size increases from 30nm to 55nm. It is also just possible to observe a small number of tertiary γ′, which have precipitated out of the matrix at a number of locations. Increasing the age time to 60 and 120 minutes (Figure 5g-h) the typical particle sizes are 68nm and 56nm respectively, it is also possible to observe similar levels of tertiary γ′. However, it should be noted that it is possible that not all of the fine tertiary γ′ was captured in these images. The fact that the typical particle size appears to reduce with ageing from 60 to 120 minutes does not follow what would be expected since an increased age time should allow further coarsening of the secondary γ′. Without further investigation, it is not possible to deduce the precise cause of this microstructure, although it is acknowledged that process variation in the quenching and ageing phases is a possibility.

Overall, this characterisation verifies that the γ/γ′ microstructure of RR1000 is sensitive to the ageing heat treatment process, even after relatively short age times and deep within the bulk. The trend is for a mild coarsening of the secondary γ′ and the precipitation of tertiary γ′ following an ageing heat treatment. The effect of this

change is to strengthen the material through precipitation hardening (26), which will alter the ability of the material to accumulate plastic strain and hence reduce the ability of the material to creep relax the residual stresses during aging at 760°C.

Residual stress characterisation

Comparison of experimental residual stress results

The residual stress resulting from ageing heat treatments has been characterised experimentally using two independent techniques – neutron diffraction and the contour method. A comparison of the hoop stress as obtained for S1, S2 and S4 is given in Figure 6. The same overall trend was observed by both techniques, a tensile core surrounded by a compressive surface region, with the increased age time causing greater relaxation of the residual stresses. In S2 and S4 the neutron and contour method techniques concur to within experimental error at almost every measurement location across the radial line scan. The level of agreement between the two techniques was weakest in the water quenched condition (S1). It is thought that this is the result of the high stress levels observed, which brings with it the possibility of plasticity at the cut tip, thus generating errors in the calculated stress. Such errors are typically minimised by secure clamping of the component (27). However, the relief of such high levels of stress means that the possibility of plasticity associated errors can not be ruled out.

From Figure 6 it can be seen that the ageing heat treatment has relaxed hoop residual stresses in the bore region by as much as 150MPa after a 15 minute age (S2). However outside of this region, minimal stress relaxation was measured across the central line scan until reaching the rim. At -38mm there is a very clear relaxation of 200MPa in proximity to the rim. At +38mm the contour method data has become less reliable since it is at this point that the EDM wire was known to exit the forging. Interestingly, at a radial distance of 20-25mm an age of 15 minutes appears to cause a localised increase in residual stress by ~300MPa when characterised using the contour method. A very similar result is also seen after a two hour age in S4. The neutron diffraction data shows very good agreement with both S2 and S4 at this location but not in S1. This points to an issue with the contour method measurement of S1 over this region.

The stress profile following a two hour age contains a number of interesting features. In the bore region the residual stresses are relaxed by values up to 300MPa in comparison to S1, which is a further relaxation of 150MPa on S2 brought about by the longer age time. From 20 – 30mm radial distance the profile of S4 closely follows that of S2 but with a marginal increase in residual stress. However, from -25 to -10mm S4 exhibits a significant stress increase in comparison to S2. It therefore appears that the stresses are relaxing and re-distributing during the age to create a different profile in some locations. This behaviour is discussed in the following section with reference to the 2D residual stress distributions (Figure 7).

Considering first the water quenched contour plot (S1), strongly compressive surface regions can be seen at the top and bottom faces, particularly from -10 to -30mm radial distance. Immediately within the compressive surfaces a very steep stress gradient is observed until a large, almost uniform tensile region is reached at the sample core. Comparing this profile to S2 and S4 it appears that the ageing process has altered the residual stress profile in a number of ways. The compressive surface stresses have been reduced from approximately -1200MPa to -600MPa, and with this the steep stress gradients have moved away from the surfaces. The large tensile core has reduced in stress magnitude at the very centre but has spread radially and shrunk axially. As a result, the stress profile in S4 has a dual peak in tensile stress, and as a consequence localised regions have experienced an increase in residual stress following age. This observed behaviour explains why S4 shows a stress increase over S2 in a number of locations across the central line scan, particularly at -25 to -10mm (Figure 6).

The contour plots provide a means to qualitatively assess the symmetry of the residual stress distribution and from this infer the symmetry of the heat treatment process. In S1 a very pronounced and asymmetry region of compressive stress is visible at the +38mm rim. A similar albeit reduced feature is also visible in S2, and very marginally so in S4. However this asymmetry is not thought to be the result of the heat treatment process, but rather the result of an artefact from the cutting process. On further investigation, it was discovered that this artefact was always located in the same region of the cut – where the wire was moving from the tensile core into the compressive surface just prior to exiting the part. Furthermore the fact that the strength of the artefact is reduced as the stress levels fall points to it being the result of

the cutting/relaxation process. Such a result adds weight to the possibility of plasticity induced error, or bulge effect error, brought about by insufficient clamping at such high levels of stress (27).

In S4 the near surface cutting effects are sufficiently small that it is possible to observe a high degree of symmetry about the bore in the residual stress distribution. Since this forging was quenched and aged, the highly axi-symmetric stress distribution suggests that the heat treatment processes were applied equally to all faces.

Comparison of experimental results to finite element modelling

As already mentioned, the water quenched forging was used as the baseline level of stress from which all ageing simulations would be made. However, since the water quenching simulation was carried out using the isotropic and Mroz hardening models individually, the baseline was in reality an upper and lower bound represented by the isotropic and Mroz models respectively. The subsequent ageing models were therefore run twice, once for each baseline level of stress. The simulated quenching and ageing results, including both hardening models, have been compared to all experimental data in Figure 8-Figure 10.

The stress profiles which follow have been broken down by stress direction to enable better visualisation of the stress relaxation. Figure 8 deals with hoop stress, Figure 9 with radial stress, and Figure 10 with axial stress. As already discussed, the two hardening models are largely shown to be an over-prediction (isotropic) and an under-prediction (Mroz) of the measured residual stress. As a result, the data from both hardening models has been retained and used to characterise the stress relaxation during ageing. It is important to distinguish however that the two hardening models were in no way operating during the age simulation itself, and that the ageing models starting from each baseline were run identically.

The ageing process consisted of a 15, 60 and 120 minute hold at 760°C with a still air cool to room temperature; the resulting stress profiles have been grouped by stress direction to better visualise the relaxation process.

Beginning with the hoop direction (Figure 8a-d), it is immediately apparent from the data that after an age of just 15 minutes (8b), the two models have both predicted stress relaxation to some degree and have converged significantly, particularly in the

bore region. Such a result suggests that the driving force for relaxation originates from the immediate residual stress state. This being the case, the relaxation process is initially much faster for the isotropic stress, but then levels out once the stresses reach a similar value to those in the Mroz model. Once the two models reach a similar level of stress, the driving force and hence the rate of stress relaxation becomes equal for both models. From the data presented in Figure 8b, it appears that this has occurred within a 15 minute age time. This is further verified by the simulated results after 60 and 120 minutes (Figure 8 c-d), which show that the two models maintain the convergence.

In the radial direction (Figure 9a-d), the two hardening models follow exactly the same trend as the hoop; the isotropic stress is initially much greater than the Mroz, but the two models converge rapidly as the driving force for relaxation levels out. Since the peak stresses in the radial direction were comparable to the hoop, this result is to be expected.

In the axial direction (Figure 10a-d) the stresses in the as-quenched condition were much lower and the isotropic and Mroz models were already in relatively good agreement. The exception to this is the rim, where strongly compressive axial stresses are observed. Interestingly, the two models are still in good agreement here, which indicates reduced reverse yielding has occurred and hence very little Bauschinger effect to take into account. Upon ageing, the rim is the only region which experiences any notable stress relaxation as the compressive stress falls from approximately -1200MPa to -650MPa after a 15 minute age. Further ageing brought about very little additional relaxation, which points towards a minimum residual stress required to drive the relaxation process at 760° in this material. This also explains why the regions away from the rim, where the stresses are no greater than ~600MPa, experience little to no relaxation over the course of the age.

Comparing the simulated and experimental data it is apparent that after each ageing heat treatment the hoop stress has been under-predicted at the bore and the rim (Figure 8a-d). The same can be said of the radial stress across the entire line scan, although at the rim the stresses fall to zero and agreement improves. In the axial direction the correlation between experimental and simulated data is particularly strong in the as quenched condition. Over the course of the ageing process some discrepancy is observed in the bore region of Figure 10b and Figure 10c where the

neutron diffraction data becomes more compressive than predicted by the model. But after a two hour age, Figure 10d, the agreement is strong once again across the entire line scan. Overall, the comparison of results indicates the post age stresses are under-estimated in the model. Based on this observation, it seems that the level of stress relaxation predicted by the model is greater than that measured. In order to visualise the stress relaxation process, the stress with ageing time has been compared at the centre of the forging in Figure 11.

The data presented in Figure 11 highlights the different levels of stress relaxation observed in the experimental and simulated data. In the hoop direction, both the contour method and neutron diffraction data show an initial rapid relaxation of 200-350MPa in the first 15 minutes, followed by a slow relaxation of 50-150MPa from 15-120 minutes. The model highlights different behaviour at the early stage of the age depending on the starting stresses. The isotropic starting stresses relax rapidly while the Mroz stress relaxes at a slower rate with the net result that after a 15 minute age the two models have converged upon a value of ~520MPa. Whilst this result is ~300MPa lower than the measured stress, the gradient which follows from this point matches very well with the experimental data. This trend indicates an over prediction of the initial rapid relaxation process, a result which may be caused by the level of primary creep predicted by the model (28).

The possibility of an over estimation of primary creep points to an issue with the creep strength as specified in the material properties data. This data may not accurately reflect the creep strength of the sample forging owing to the difference in microstructure. While the sample forgings were each water quenched before being aged, the material data available in the model is that which is used for full sized production parts. Such parts are not typically water quenched since the cooling rate is too aggressive. Therefore, a forced air, or oil quench is usually used to avoid excessive distortion or cracking. The microstructure characterised by the material properties data will therefore more akin to an oil or forced air quenched, as opposed to the water quench used in the sample forgings.

In a separate study a comparison was made of the microstructures which result from an oil and water quench from sub-solvus heat treatment (29). It was found that while the water quench resulted in a broad uni-modal intragranular γ′ with particle size 30(±10)nm, by contrast the oil quench resulted in a bi-modal intragranular γ′

distribution with 60(±30)nm secondary and 10(±5)nm tertiary γ´. This is a significant result since the size distribution of the γ´ is known to have a profound effect on the mechanical properties in Nickel superalloy (26). The γ´ size and inter-particle distance in particular dictates whether a dislocation shears, loops or becomes pinned by the precipitate (30). It is therefore possible that the water quenched forging, which contained very fine tertiary γ´, had superior creep properties in comparison to the modelled microstructure, and that this in turn caused the experimental stress relaxation to appear much reduced in comparison to that which was predicted.

4. Conclusions

The relaxation of residual stresses following ageing heat treatment has been characterised in sub-scale Nickel superalloy disc forgings. The ageing process was preceded by a water quench from heat treatment 1120°C to generate high levels of residual stress in a relatively small geometry. A typical ageing/stress relief temperature for this alloy of 760°C was employed with hold times of 15, 60 and 120 minutes. The effect on the residual stress distribution was characterised experimentally using neutron diffraction and contour method techniques, while residual stress predictions were made using the finite element method. To account for the expected microstructural variations, an SEM was used to image the γ/γ´ microstructure in each of the aged conditions. Based on the results obtained and the observable trends it was possible to draw the following conclusions:

- Microstructurally the water quenching process resulted in a broad uni-modal intragranular γ´ with particle size 30(±10)nm. Upon ageing the intragranular γ´ was observed to coarsen marginally and precipitate new particles out of the matrix. Primary γ´ was found at the grain boundaries and remained unaltered by the ageing heat treatment.

- Using neutron diffraction it was possible to characterise the residual stress along a central line scan from the bore to the rim of each forging. The data indicated a typical thermally induced stress profile from the quenching phase, which was relaxed with ageing time. In the as-quenched condition hoop stresses were measured at 1160MPa at the bore and -820MPa at the rim. Following an age of 120 minutes at 760°C this fell to 770MPa at the bore and

-700MPa at the rim, indicating maximum stress relaxation levels of approximately 400MPa.

- The contour method was employed as an additional experimental method with which to contrast the neutron diffraction data. Line scans extracted from the contour data proved to a reasonable match in the quenched condition, and a particularly strong match in the aged conditions (Figure 6). In addition, the contour method provided a 2D map of the residual stress distribution across an entire cross section. It was found that while the stress distribution was largely axi-symmetric, the wire cutting process did generate some anomalous data regions close to the wire exit location.

- Residual stress simulations were carried out using a finite element model. The quenching process was modelled using an isotropic and Mroz hardening model individually. The isotropic model was found to over-predict, and the Mroz to under-predict, the residual stress generated during the quench. As such the two models were taken as an upper (isotropic) and lower (Mroz) bound for the simulated quench stress.

- The simulated quench stress from each hardening model was individually imported into the ageing model. It was found that within a 15 minute age at 760°C the two models converged despite the isotropic stress being ~500MPa greater than that predicted by the Mroz model. Based on this result it has been suggested that the immediate stress level largely drives the stress relaxation process. As a result the isotropic stress rapidly relaxed until it reached a similar level to the Mroz stress at which point a convergence was reached.

- A comparison of the modelled results to the experimental data indicated that the model had under-predicted the post age stress. Plotting the stress change with age time at the centre of the forging it became clear that the level of primary creep was over-predicted in the model in comparison to the experiment. The cause of this over prediction was thought to be the result of the material properties available to the model which characterised a production part as opposed to the water quenched sample forging. A comparison of the microstructure following a typical production quench (oil) and the water quench highlighted significant differences in the intragranular γ' particle distribution. It was felt that this lead to an increase in creep strength

in the sample forgings, which brought about the discrepancy observed in the data.

Acknowledgments

List of tables:

Table 1: Nominal composition of Nickel superalloy RR1000

Alloy	Ni	Cr	Co	Mo	Ti	Al	C	B	Ta	Zr	Hf
RR1000	52.3	15.0	18.5	5.0	3.6	3.0	0.027	0.015	2	0.06	0.5

Table 2: Chemical composition of γ´ etchant

Part I	Part II
150ml H_2O	15ml HNO_3
150ml HCl	25ml H_20
2.5g MoO_3	30ml part I

Table 3: Material properties of RR1000

Material Properties of RR1000	
Young's modulus (bulk)	224 GPa
Poisson ratio (bulk)	0.33
(311) Diffraction elastic constant	203 GPa
(311) Poisson ratio	0.3

Table 4: Typical particle sizes across the aged conditions

Age time (minutes)	Typical particle size secondary γ´ (nm)
(water quenched) - 0	30 (±10)
15	54 (±10)
60	68 (±10)
120	56 (±10)
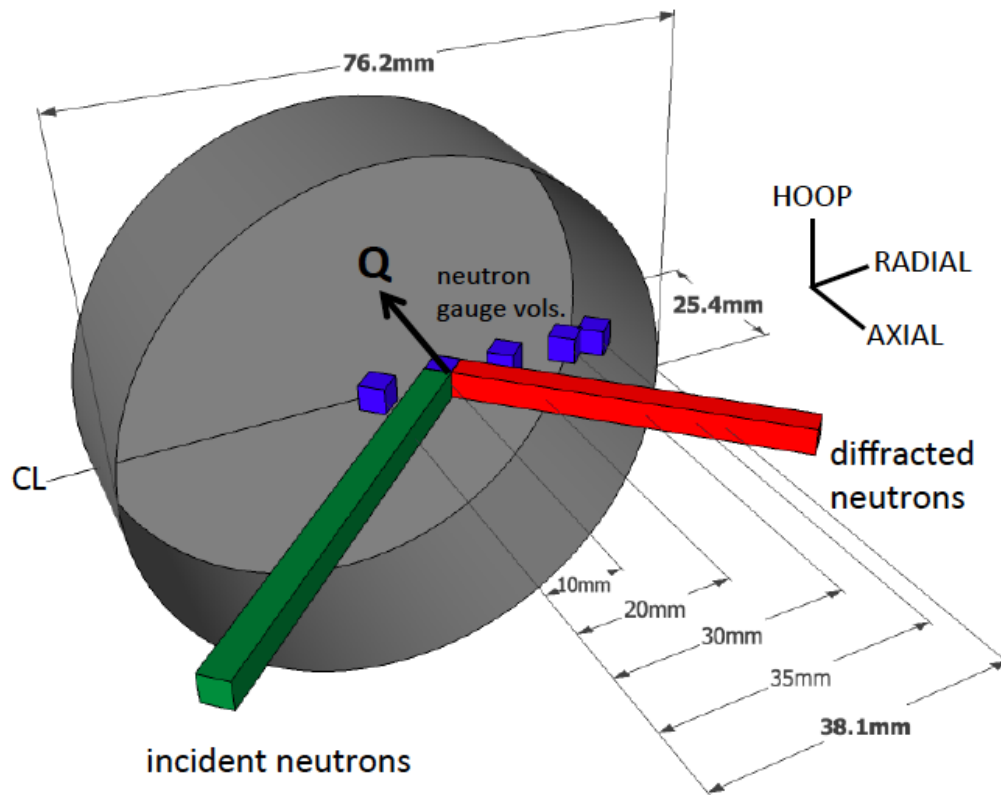
Figure 1: Schematic diagram of the sub-scale 'hockey puck' forgings with the measured gauge volumes and neutron path indicated.
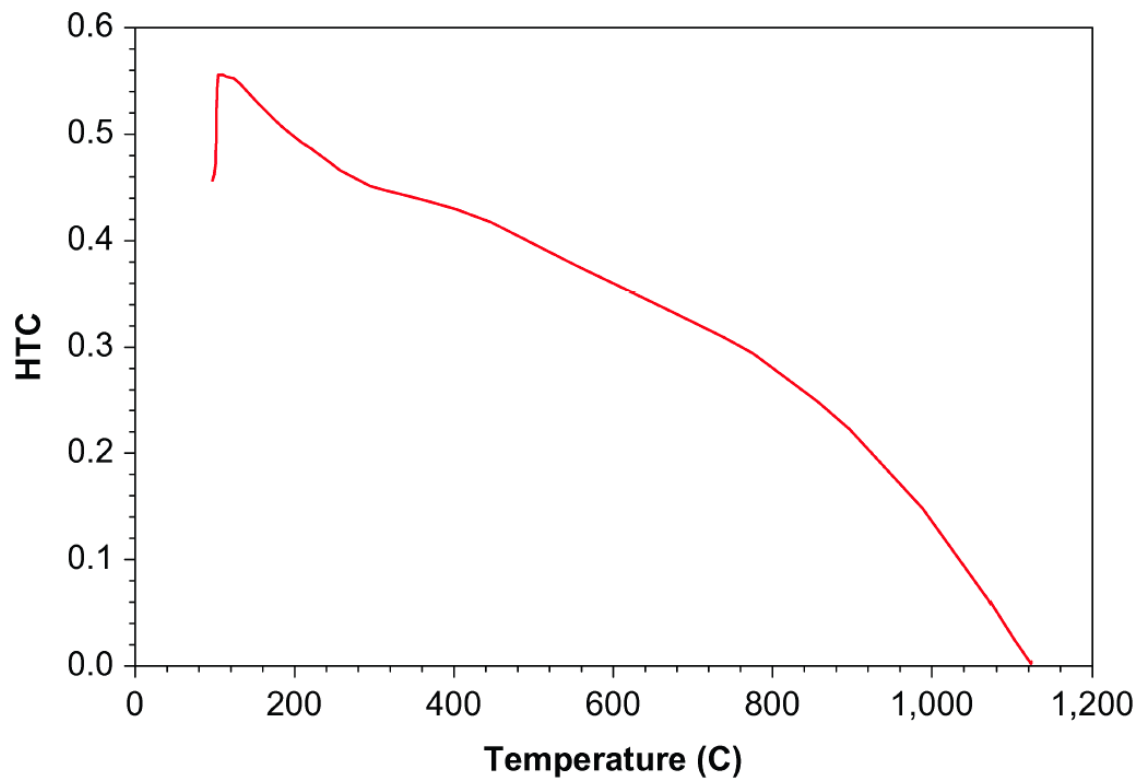
Figure 2: The derived heat transfer coefficient (HTC) for water quenching from heat treatment at 1120°C
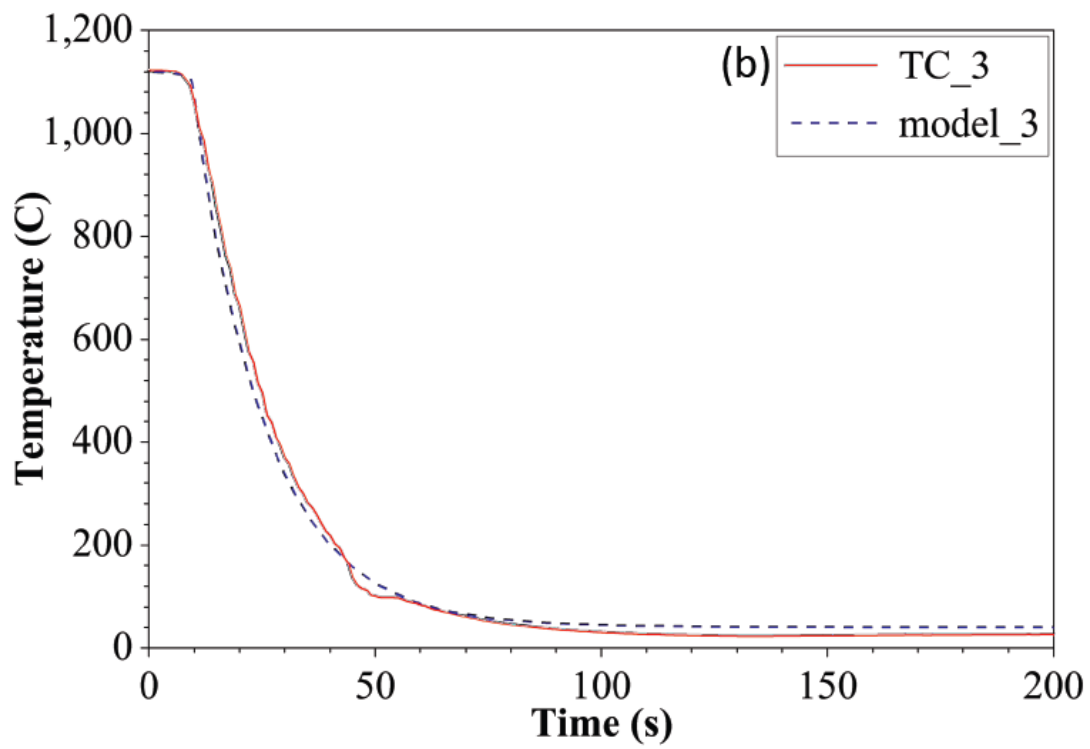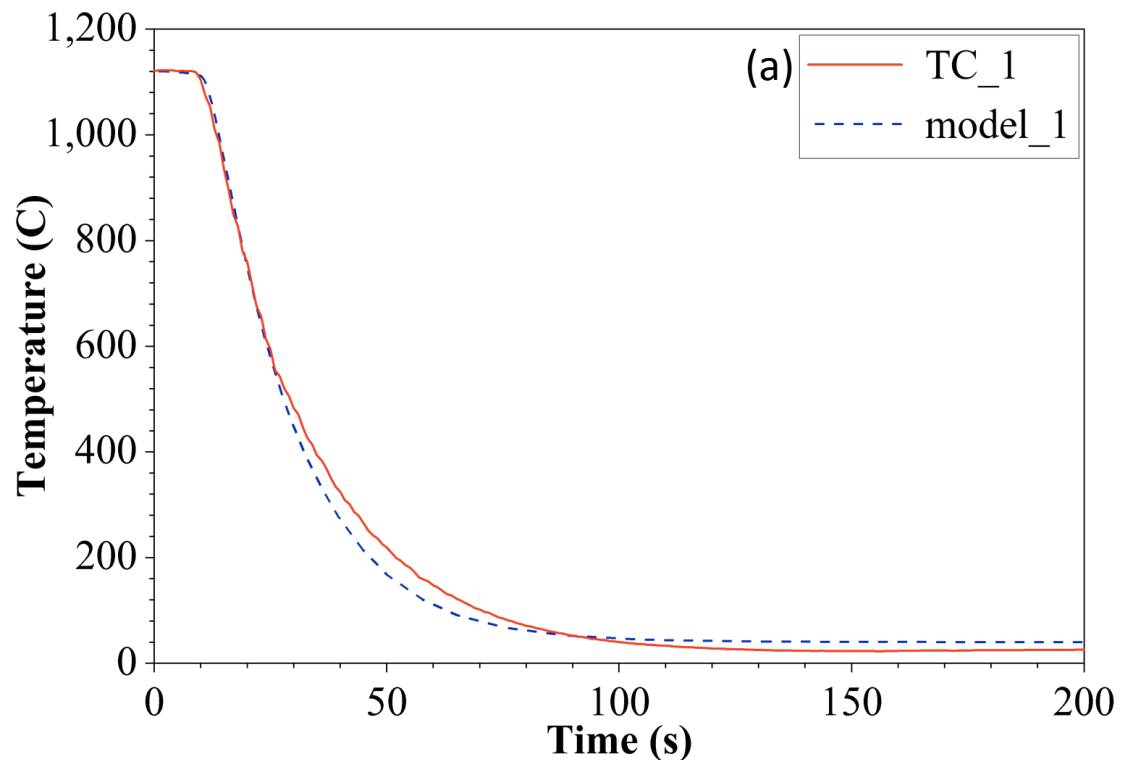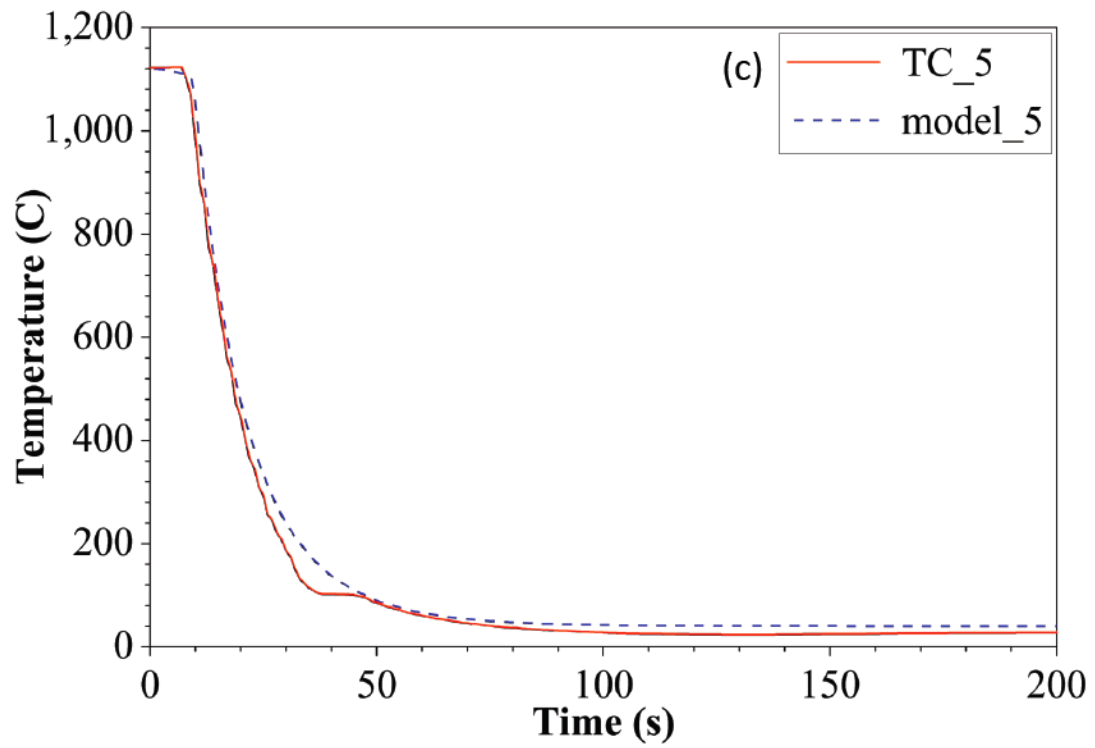
Figure 3: Comparison of the modelled and experimentally measured cooling rate during water quenching at a) bore, b) bulk, and c) rim locations
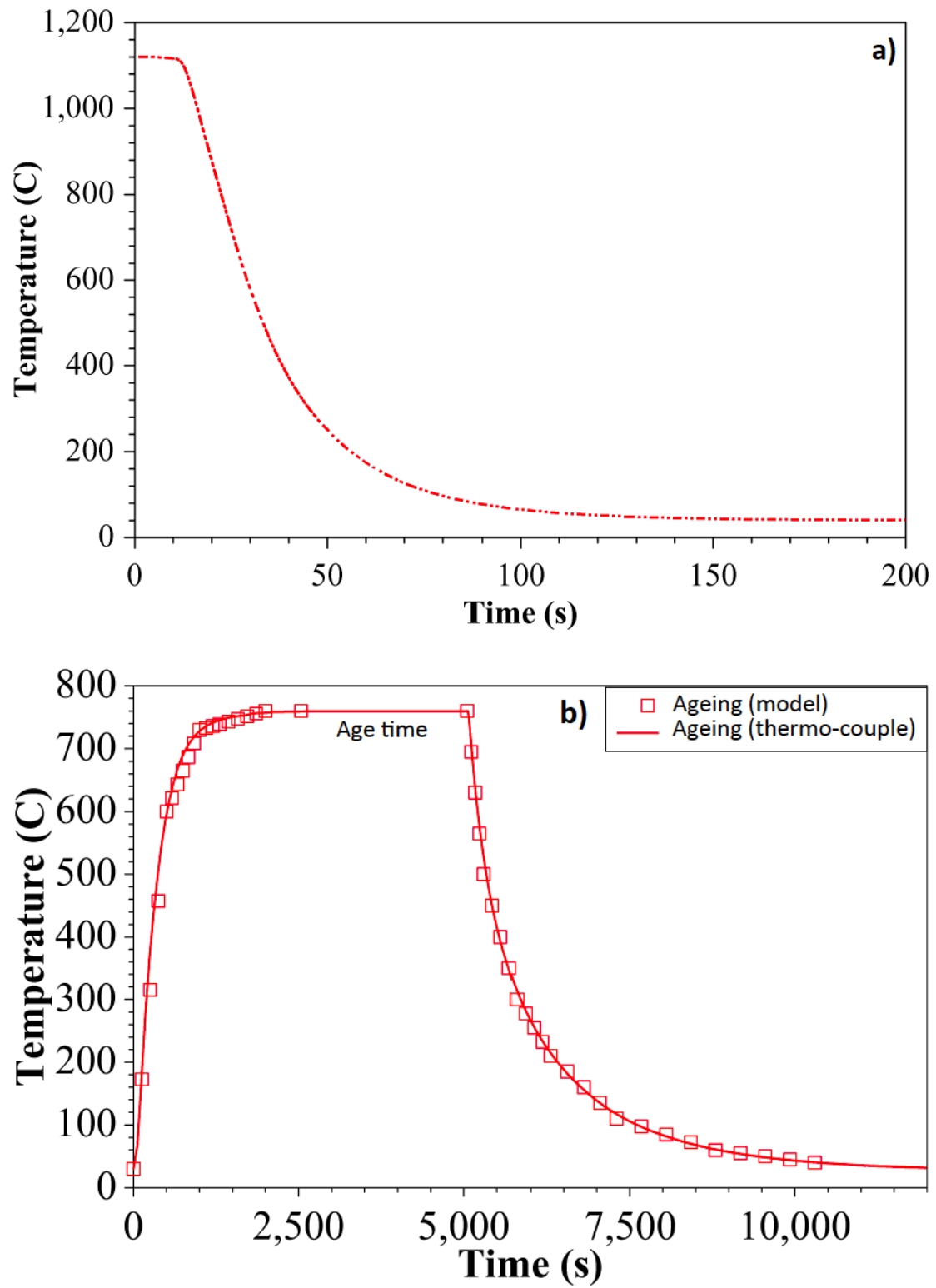
Figure 4: The thermal history through a) quenching and b) ageing at the centre of the forging.
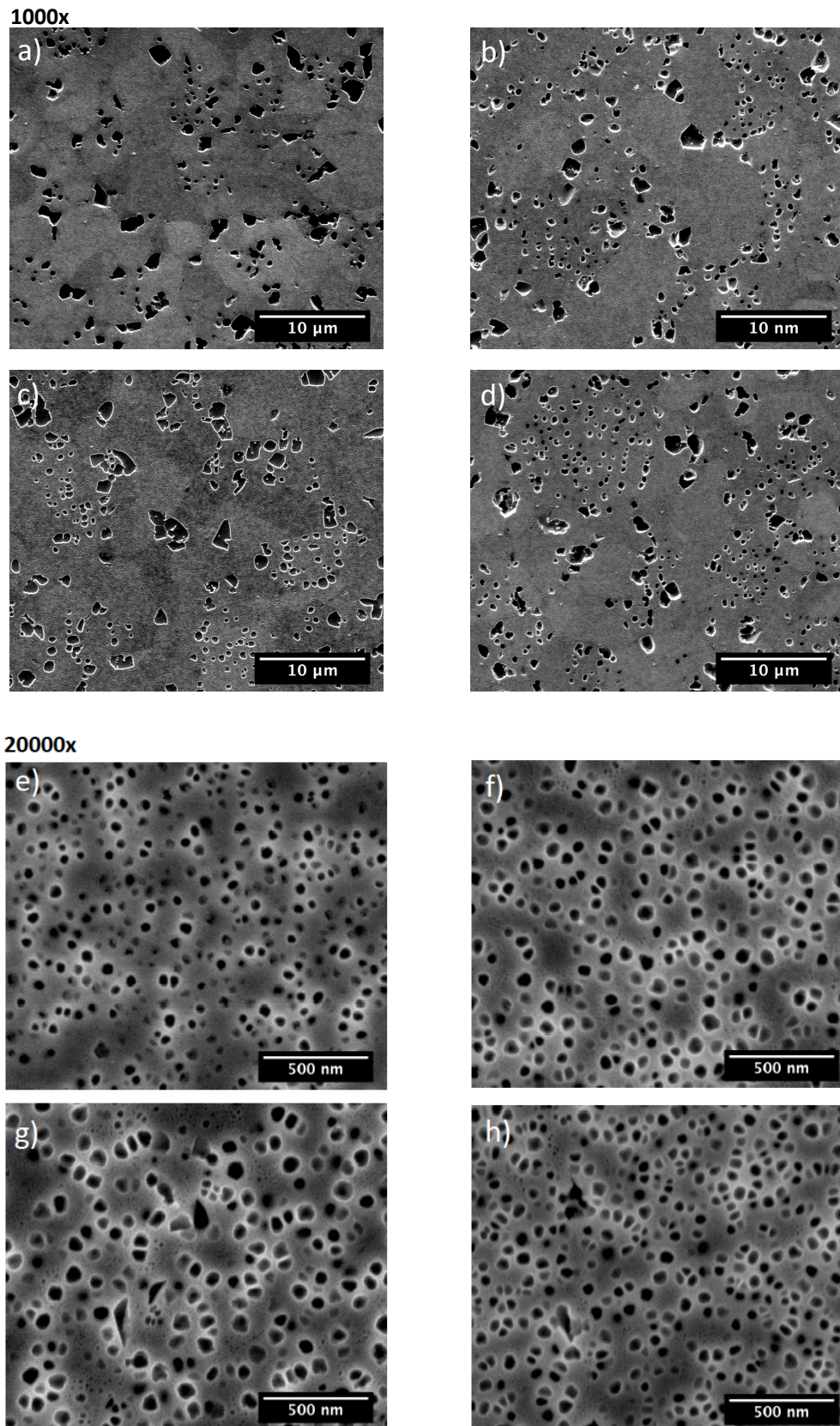
Figure 5: γ´ microstructural characterisation at 1000/20000x magnification in the water quenched condition (a/e), and 15min (b/f), 60min (c/g) and 120min (d/h) aged condition
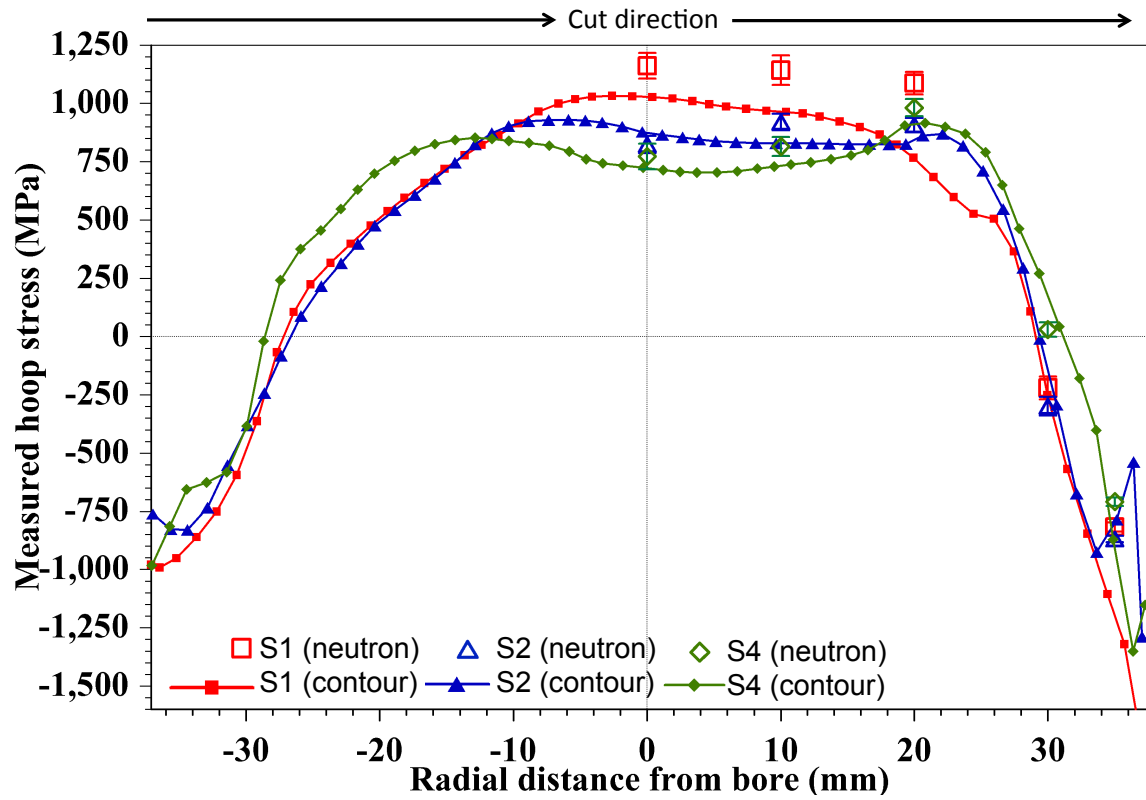
Figure 6: Comparison of the contour method and neutron diffraction line scans across the forging diameter at mid depth.
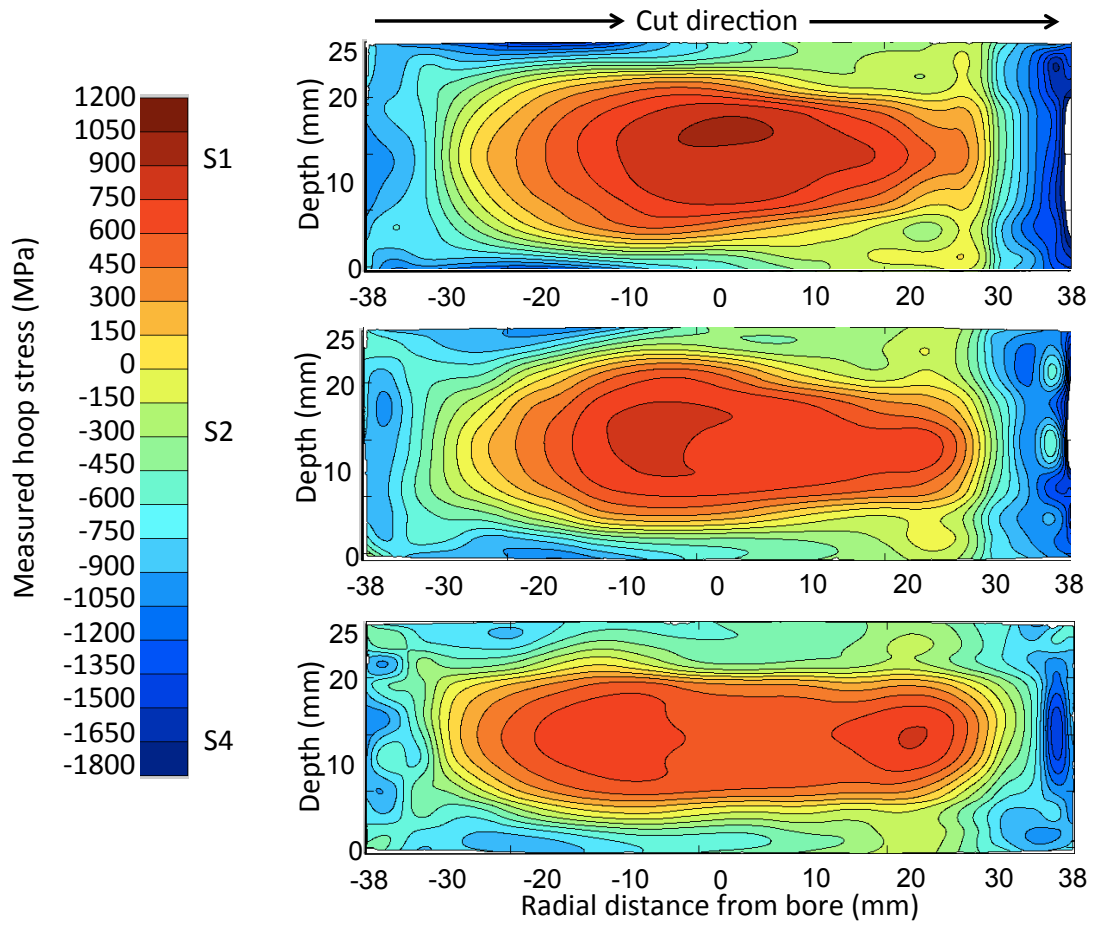
Figure 7: 2D residual stress distributions as measured using the contour method in the as quenched (S1), 15 minute age (S2) and 120 minute age (S4).
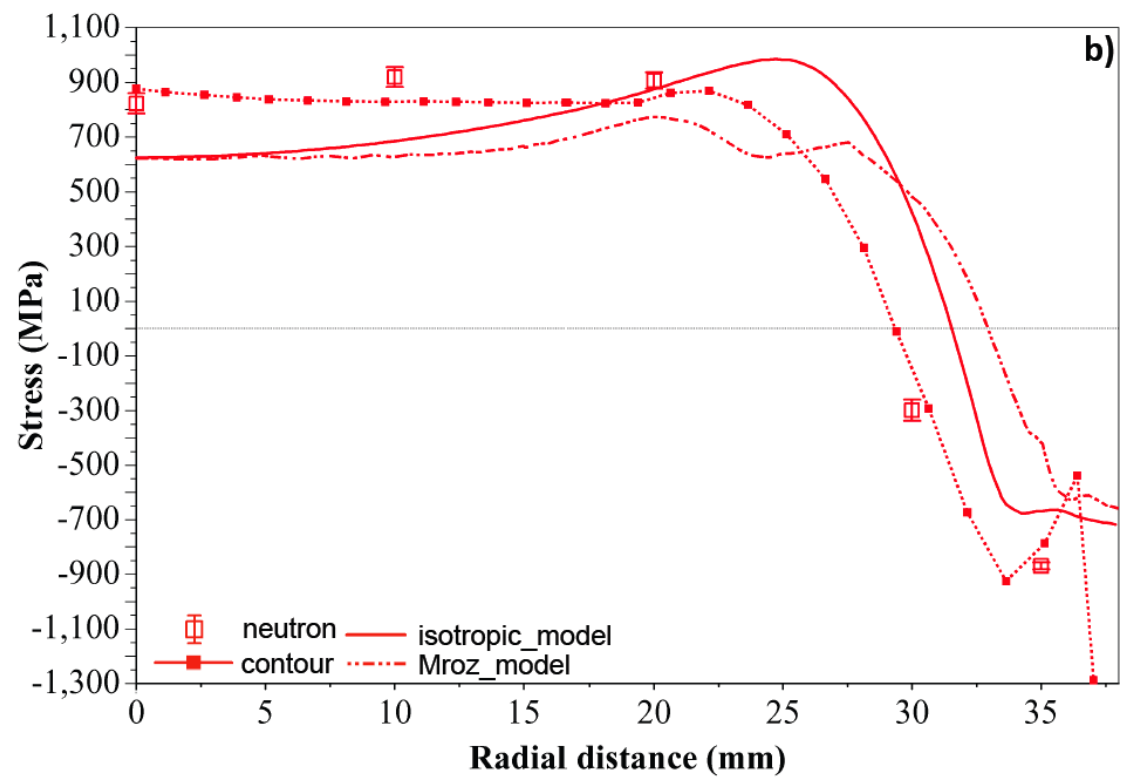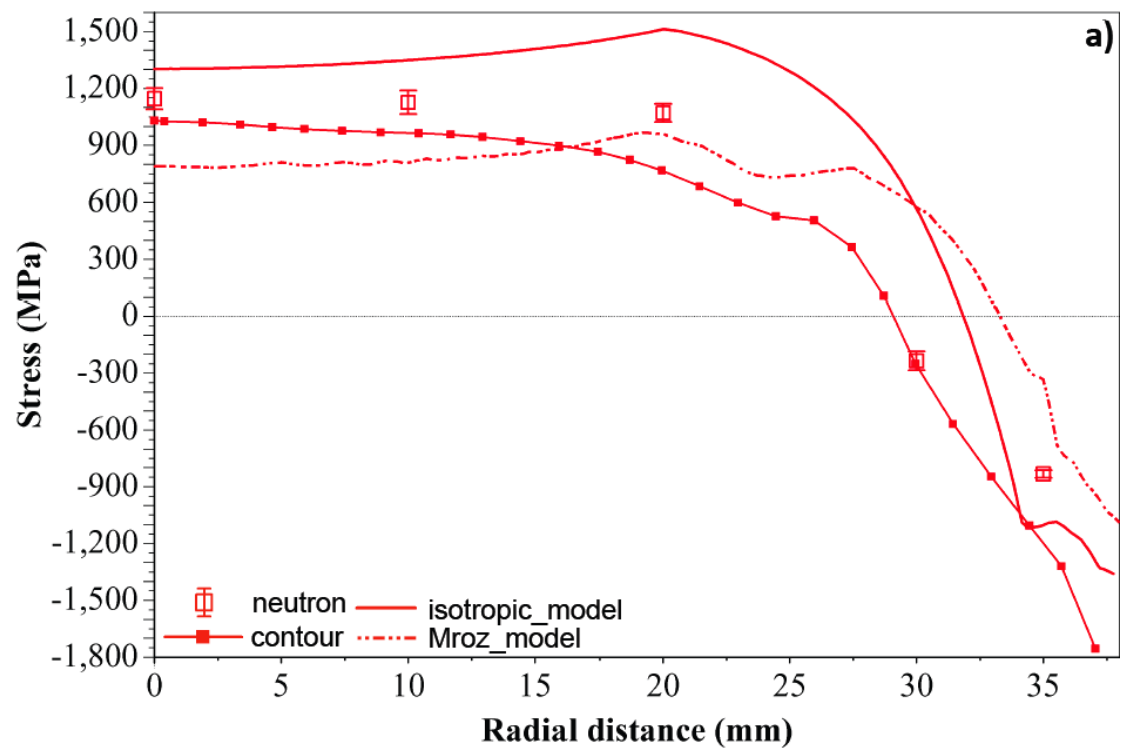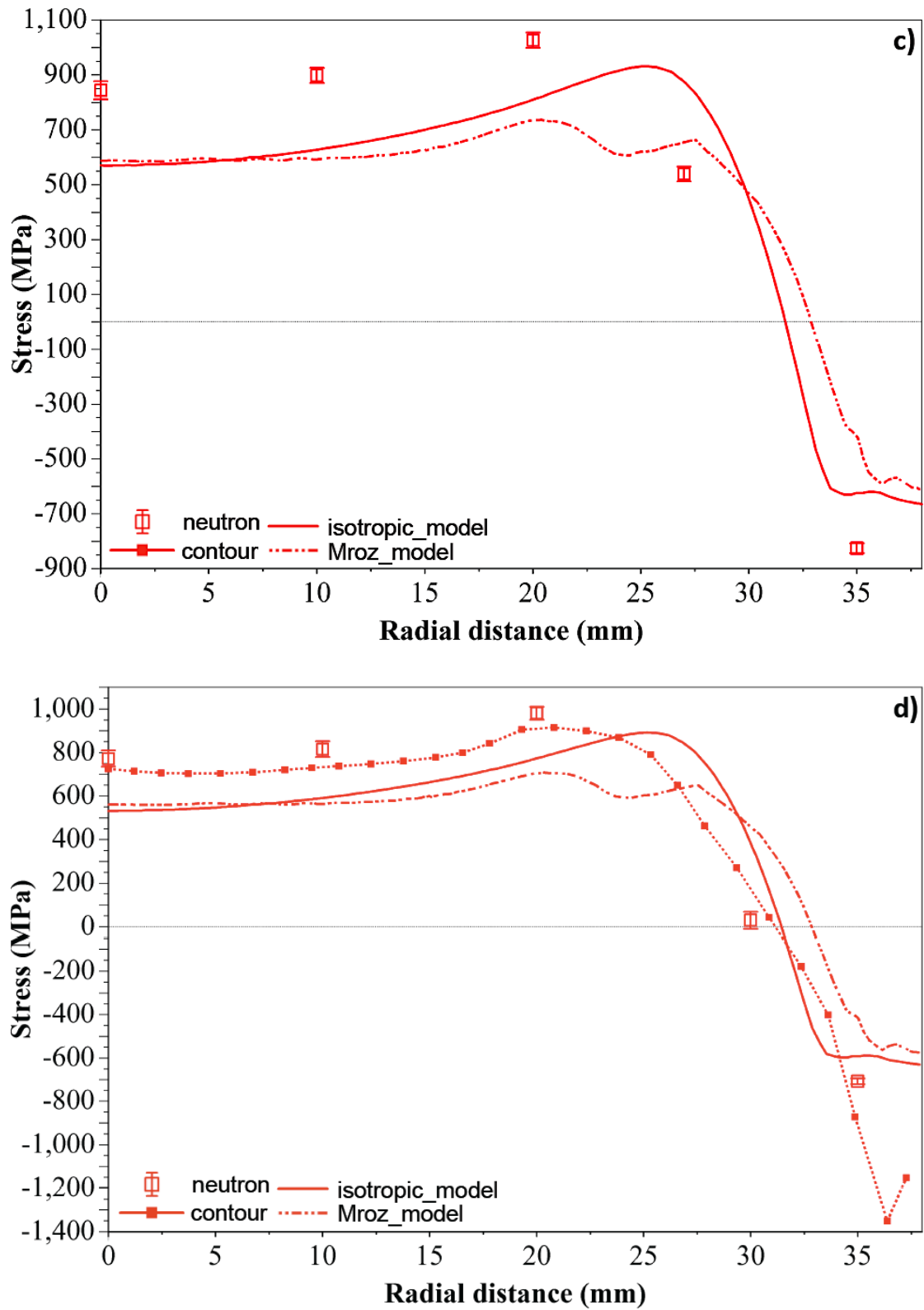
Figure 8: Residual stress prediction and measurement in the hoop direction across the central line scan in the a) as quenched condition b) 15 min, c) 60 min and d) 120 min aged condition
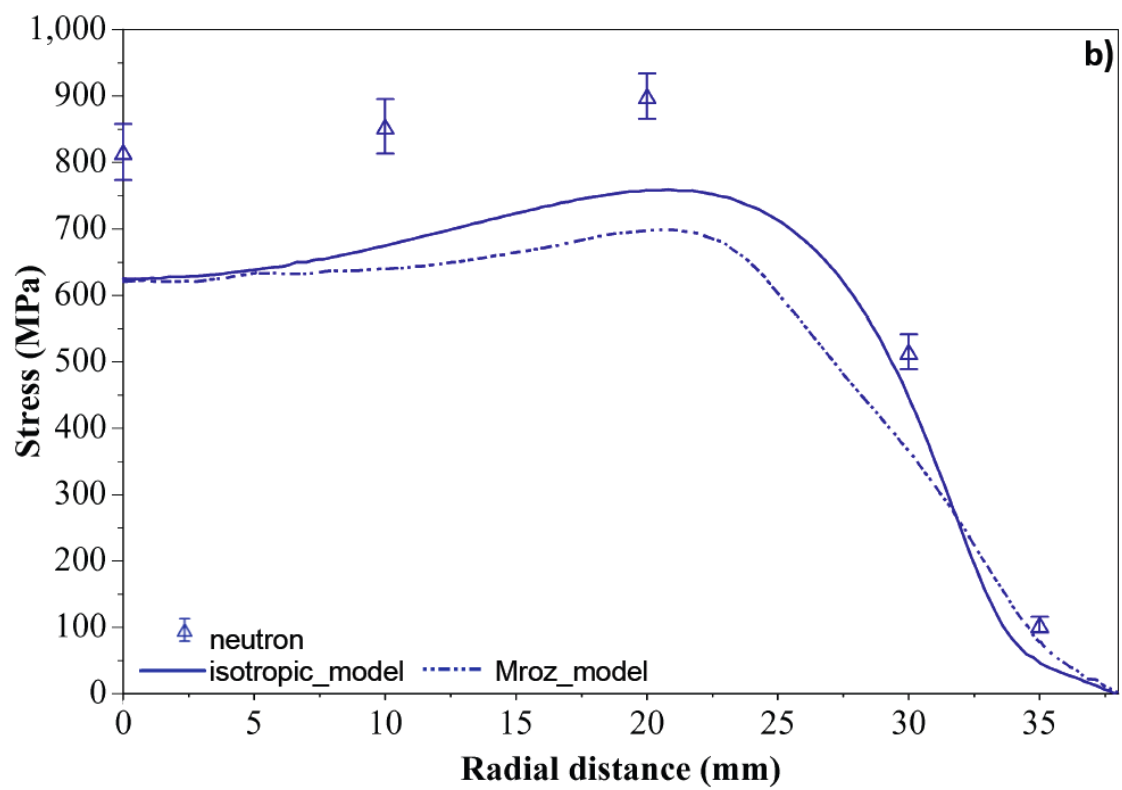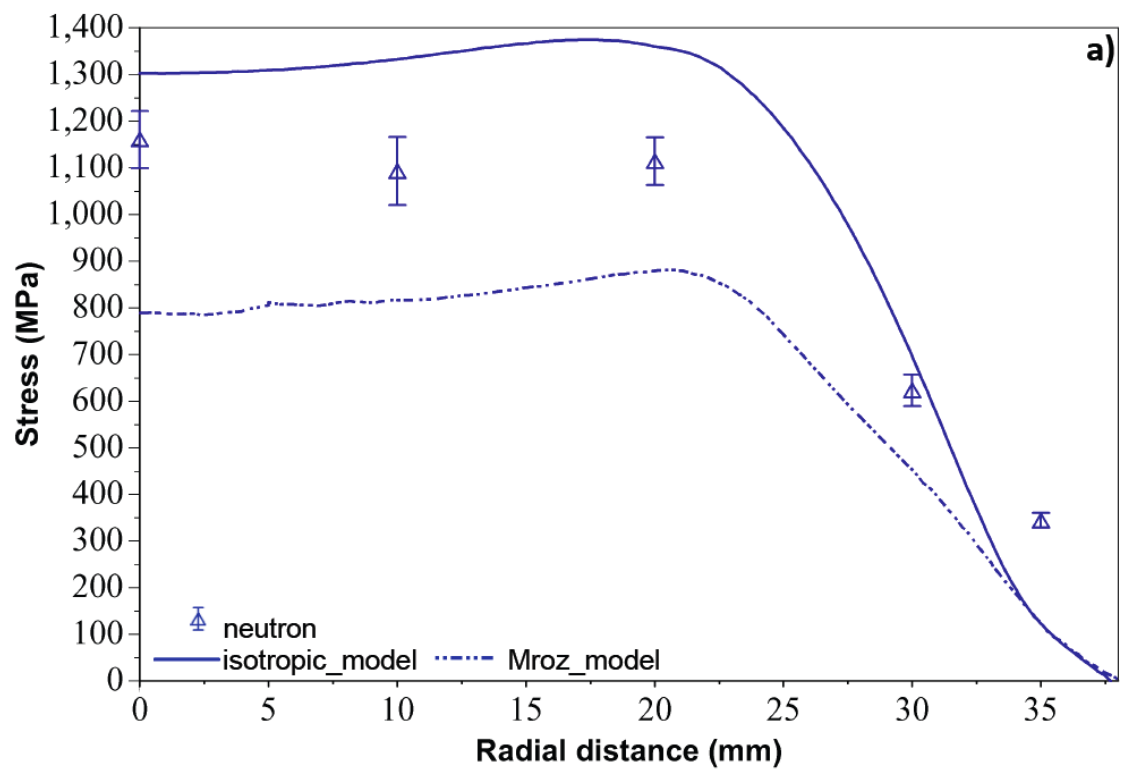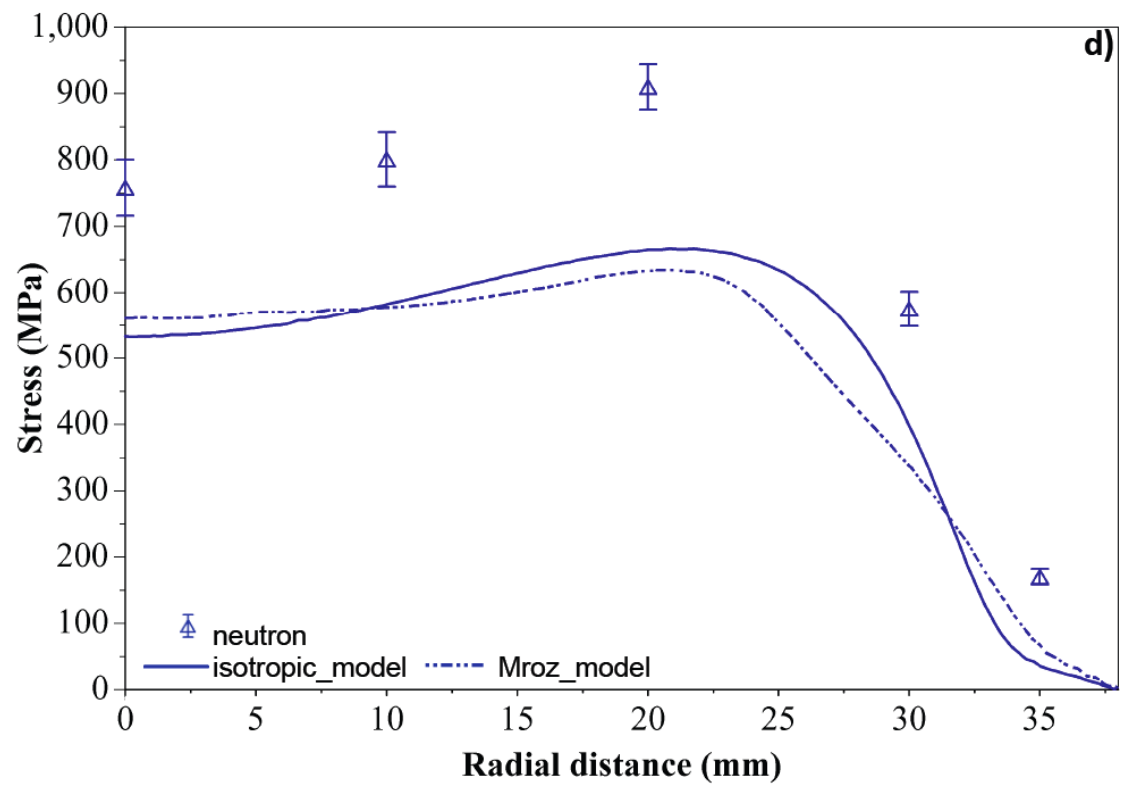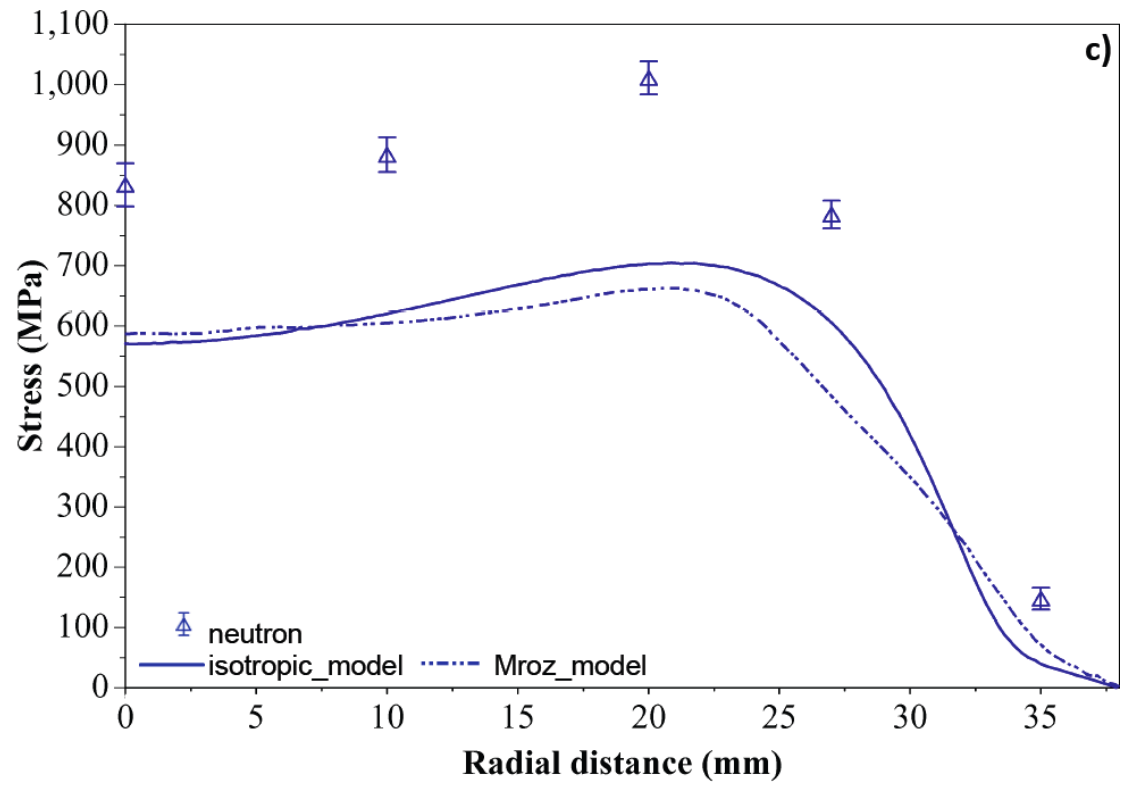
Figure 9: Residual stress prediction and measurement in the radial direction across the central line scan in the a) as quenched condition b) 15 min, c) 60 min and d) 120 min aged condition
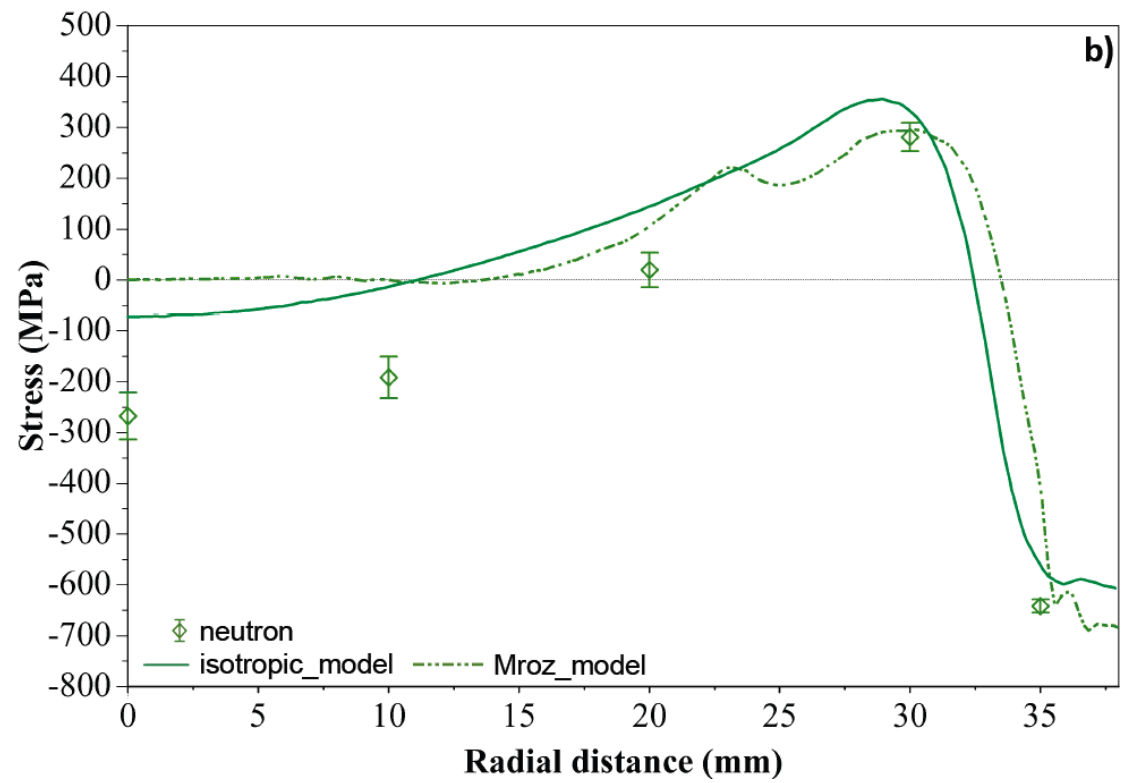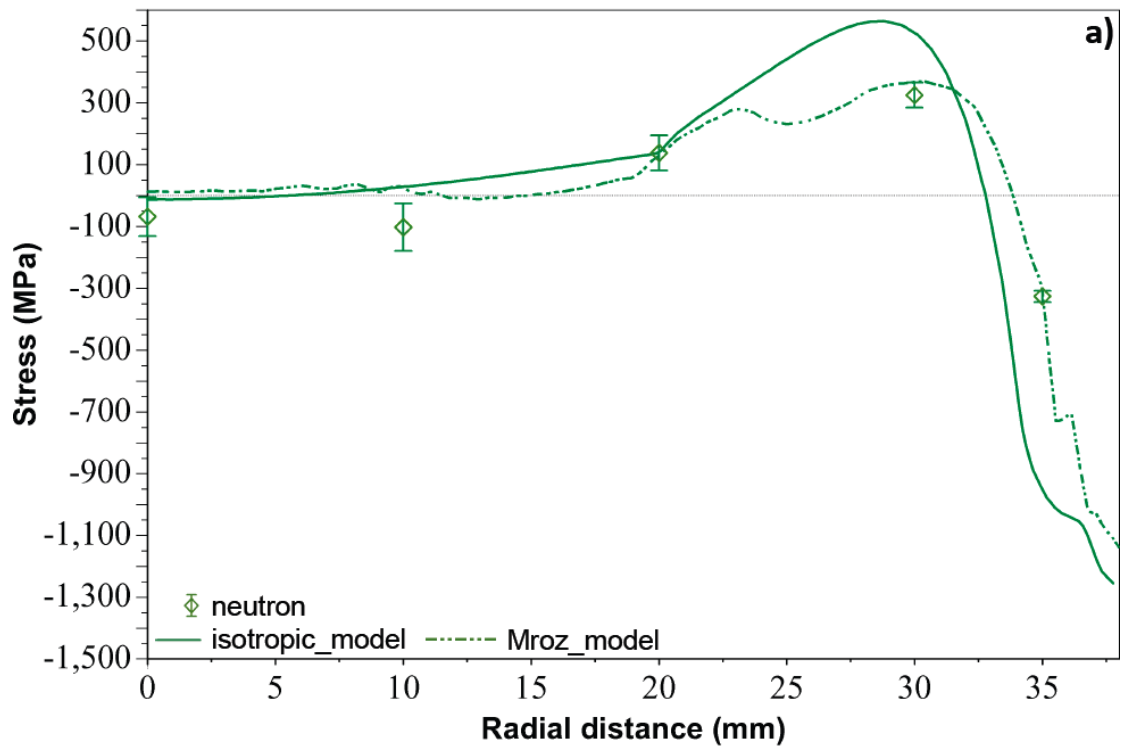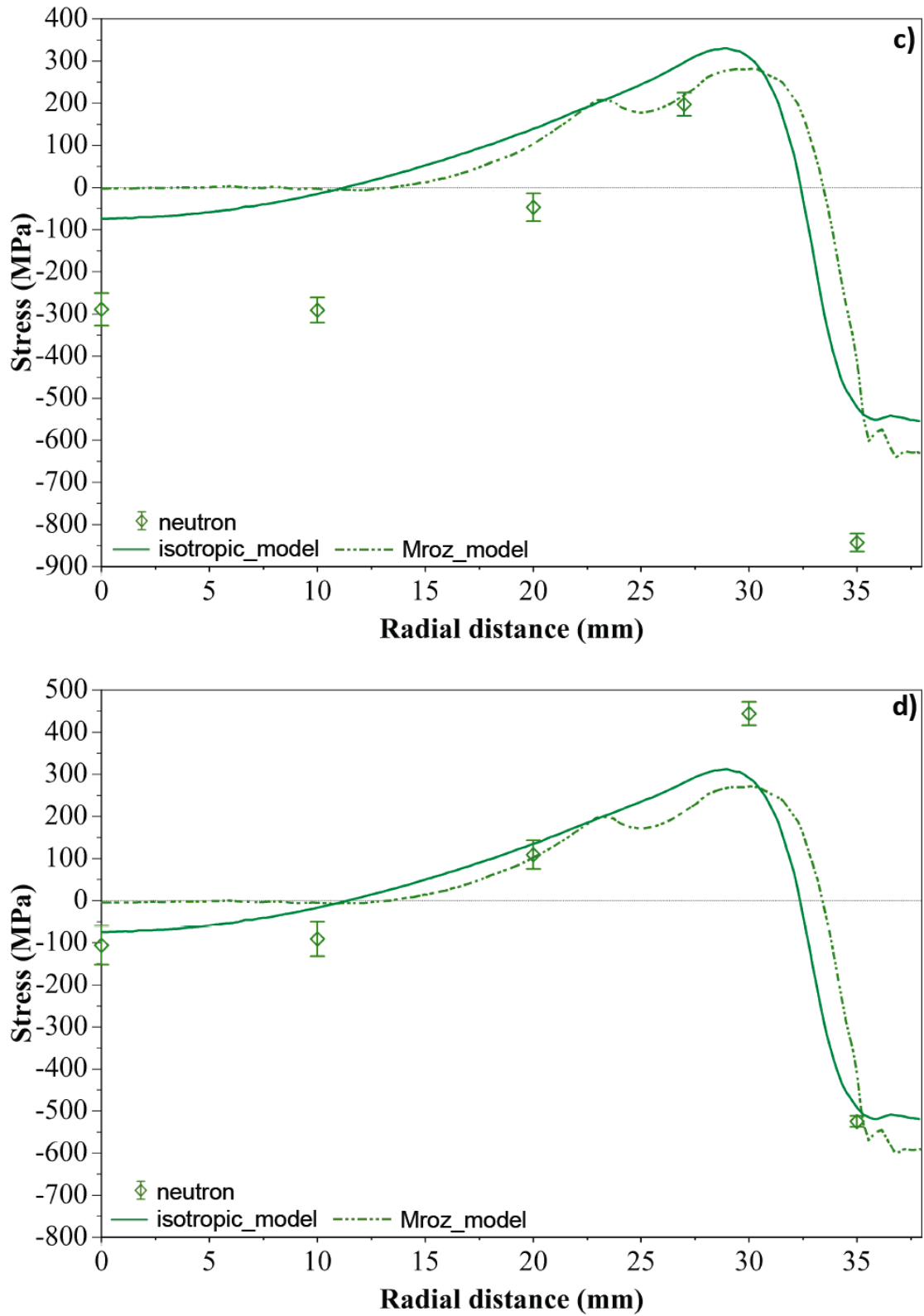
Figure 10: Residual stress prediction and measurement in the axial direction across the central line scan in the a) as quenched condition b) 15 min, c) 60 min and d) 120 min aged condition
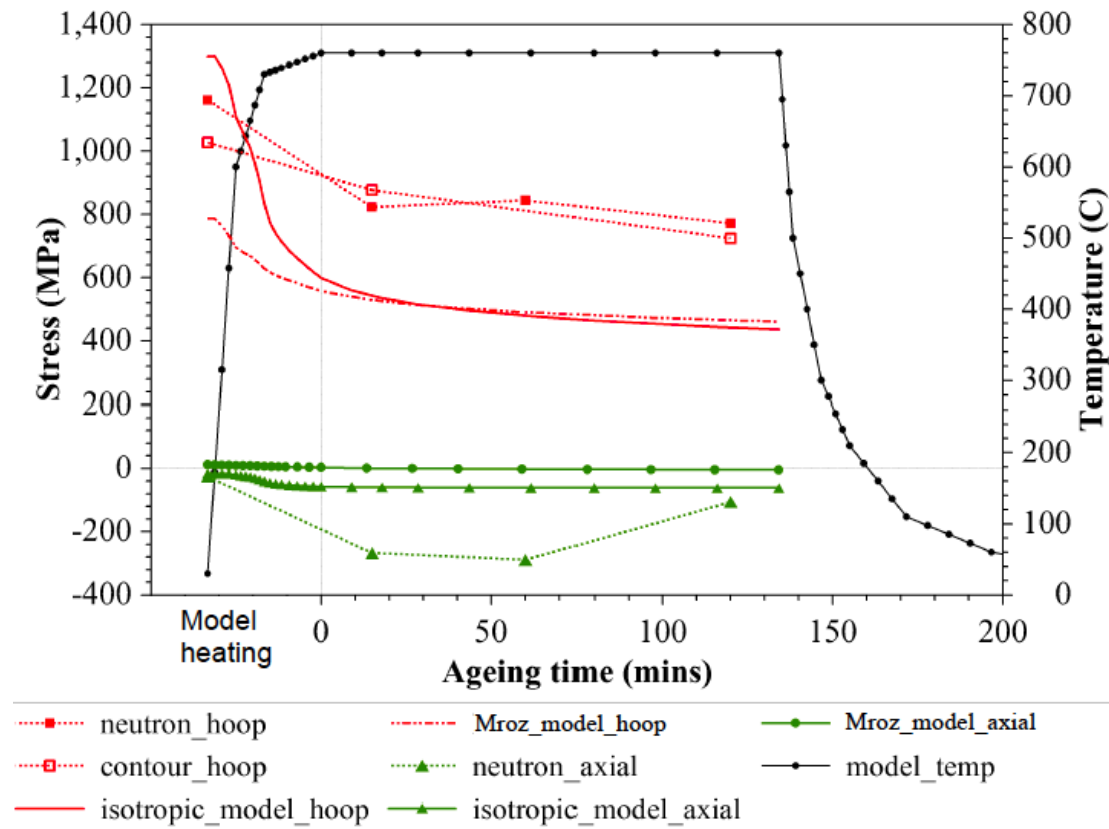
Figure 11: Residual stress with age time at the forging centre as predicted from both isotropic and Mroz starting stresses and measured experimentally. The experimental data points in the 'model heating' region are those obtained at room temperature. Note that at the forging centre the hoop and radial directions are equivalent, hence only the hoop stress has been plotted.

References

1.   Pollock TM, Tin S. Nickel-Based Superalloys for Advanced Turbine Engines: Chemistry, Microstructure, and Properties. Journal of Propulsion and Power. 2006;22(2):361-74.
2.   Reed RC. The Superalloys - Fundamentals and Applications. Cambridge: Cambridge University Press; 2006.
3.   Bhadeshia HKDH. Nickel Based Superalloys. University of Cambridge; 2003 [cited 2009 18/11]; Available from: http://www.msm.cam.ac.uk/phase-trans/2003/Superalloys/superalloys.html.
4.   Zickler GA, Schnitzer R, Radis R, Hochfellner R, Schweins R, Stockinger M, et al. Microstructure and mechanical properties of the superalloy ATI Allvac® 718Plus™. Materials Science and Engineering: A. 2009;523(1–2):295-303.
5.   Mitchell RJ, Li HY, Lemsky JA. The Influence of Cooling Rate From Solution Temperature on Microstructures and Mechanical Properties in an Advanced Polycrystalline Nickel-Base Superalloy. Engineering Issues in Turbine Machinery, Power Plant and Renewables. 2007.
6.   Mao J, Chang K-M, Yang W, Furrer DU, Ray K, Vaze SP. Cooling precipitation and strengthening study in powder metallurgy superalloy Rene88DT. Materials Science and Engineering: A. 2002;332(1–2):318-29.
7.   Hardy MC, Zirbel B, Shen G, Shankar R. Developing damage tolerance and creep resistance in a high strength nickel alloy for disc applications. Superalloys 2004. 2004:83-92.
8.   Ball DL, Tom BK, Bucci RJ, James MA, editors. Toward Understanding the Impact of Bulk Residual Stress on the Life, Weight and Cost of Primary Aircraft Structure. Residual Stress Summit; 2010; Tahoe City, CA.
9.   Bouchard PJ, Buschow KHJr, Robert WC, Merton CF, Bernard I, Edward JK, et al. Residual Stresses in Lifetime and Structural Integrity Assessment. Encyclopedia of Materials: Science and Technology. Oxford: Elsevier; 2001. p. 8134-42.
10.   Jackson MP, Reed RC. Heat treatment of UDIMET 720Li: the effect of microstructure on properties. Materials Science and Engineering: A. 1999;259(1):85-97.
11.   Hofmann M, Schneider R, Seidl GA, Rebelo-Kornmeier J, Wimpory RC, Garbe U, et al. The new materials science diffractometer STRESS-SPEC at FRM-II. Physica B. 2006:1035-7.
12.   Stone HJ, Holden TM, Reed RC. Determination of the plane specific elastic constants of waspaloy using neutron diffraction. Scripta Materialia. 1999;40(3):353-8.
13.   Withers PJ, Preuss M, Steuwer A, Pang JWL. Methods for obtaining the strain-free lattice parameter when using diffraction to determine residual stress. Journal of applied crystallography. 2007;40(5):891-904.
14.   Pirling T, Bruno G, Withers PJ. SALSA--A new instrument for strain imaging in engineering materials and components. Materials Science and Engineering: A. 2006;437(1):139-44.
15.   Rolph J, Iqbal N, Preuss M, Hofmann M, Evans A, Ganesan M. The Effect of d0 Reference Value on a Neutron Diffraction Study of Residual Stress in a Gamma/Gamma Prime Nickel-base Superalloy. (Submission in process). 2012.
16.   Grant B, Elisabeth K, Preuss M, Quinta da Fonseca J, Daymond MR. The Effect of Lattice Misfit on Deformation Mechanisms at High Temperature. Advanced Materials Research. 2011;278:144-9.

17.   Wimpory RC, Ohms C, Hofmann M, Schneider R, Youtsos AG. Statistical Analysis of residual stress determinations using neutron diffraction. International Journal of Pressure Vessels and Piping. 2009(86):48-62.

18.   Prime MB. Cross-sectional Mapping of Residual Stresses by Measuring the Surface Contour After a Cut. Transactions of the ASME. 2001;123:162-8.

19.   Bueckner HF. The Propagation of Cracks and the Energy of Elastic Deformation. Transactions of the ASME. 1958;80:6.

20.   Mathworks. MATLAB 7.10. Natick, MA.2010.

21.   SIMULIA. ABAQUS Software. Rising Sun Mills, 166 Valley Street, Providence, RI.2011.

22.   Bibby GP. Compressor Engineering SCO3 Radial Displacement Plot Facility. 14 ed: Rolls-Royce; 1998.

23.   Dye D, Conlon KT, Reed RC. Characterization and Modeling of Quenching-Induced Residual Stresses in the Nickel-Based Superalloy IN718. Metallurgical and Materials Transactions A. 2004;35A(June):1703-13.

24.   Rist M, James J, Tin S, Roder B, Daymond M. Residual stresses in a quenched superalloy turbine disc: Measurements and modeling. Metallurgical and Materials Transactions A. 2006;37(2):459-67.

25.   Kassner ME, Geantil P, Levine LE, Larson BC. Backstress, the Bauschinger Effect and Cyclic Deformation. Materials Science Forum. 2008;604-605:39-51.

26.   Preuss M, Withers PJ, Baxter GJ. A comparison of inertia friction welds in three nickel base superalloys. Materials Science and Engineering: A. 2006;437(1):38-45.

27.   Prime MB, Kastengren AL. The Contour Method Cutting Assumption: Error Minimization and Correction. Proceedings of the SEM Annual Conference & Exposition on Experimental and Applied Mechanics Indianapolis. 2010.

28.   Maldini M, Angella G, Lupinc V. Analysis of creep curves of a nickel base superalloy in a wide stress/temperature range. Materials Science and Engineering: A. 2007;462(1–2):436-40.

29.   Rolph J, Preuss M, Hardy MC, Nikov S, Ramanathan R, Hofmann M, et al. The effect of heat treatment processing on residual stress in Nickel superalloy - Part I - Quenching. Submission in process. 2012.

30.   Decker R. The evolution of wrought age-hardenable superalloys. JOM Journal of the Minerals, Metals and Materials Society. 2006;58(9):32-6.

Chapter 8

In-situ Characterisation of Residual Stress Relaxation During Ageing Through Neutron Diffraction and Finite Element Modelling

This paper has been prepared for submission to a relevant peer reviewed journal. The paper that follows is in the form in which it will be submitted to the journal pending clearance from Rolls-Royce plc. and ATI Ladish Forging. This research was performed with Dr, Alex Evans, Dr. Ania Paradowska, Dr. Michael Hoffman, Dr. Stan Nikov, Dr. Ranga Ramanathan, Mr. Paul Enderson Professor Michael Preuss, Dr. Mark Hardy, and Dr. Mike Glavicic

The lead author of this paper is the author of this thesis; all of the content which follows are the words of the lead author, and all of the data gathered and presented here is the result of investigations implemented by the lead author. In terms of co-author involvement, Dr. Alex Evans and Dr. Ania Paradowska helped to design and implement the novel in-situ neutron diffraction heat treatment setup. Dr. Michael Hoffman assisted with all aspects of the ex-situ neutron diffraction experiment. Dr. Stan Nikov and Dr. Ranga Ramanathan assisted with the finite element modelling work. Mr. Paul Enderson provided the expertise to carry out microstructural characterisations using a scanning election microscope (SEM). Feedback and overall guidance for this work was provided by Professor Michael Preuss, Dr. Mark Hardy, and Dr. Mike Glavicic.

In-situ Characterisation of Residual Stress Relaxation During Ageing Through Neutron Diffraction and Finite Element Modelling.

J. Rolph[1] M. Preuss[1] P. Enderson[1] M. Hofmann[2] S. Nikov[3] M. C. Hardy[3] M. G. Glavicic[4] R. Ramanathan[5] A. Paradowska[6] A. Evans[7]

[1] Materials Science Centre, University of Manchester, Grosvenor St, Manchester, M13 9PL, UK

[2] FRM2, TU München, Lichtenbergstr. 1, 85747 Garching, Germany

[3] Rolls-Royce Plc, PO Box 31, Moor Lane, Derby, DE24 8BJ, UK

[4] Rolls-Royce Corporation, P.O. Box 420, Speed Code T-61, Indianapolis, IN 46206-0420, USA

[5] ATI Ladish Forging, 5481 S. Packard Avenue, Cudahy, WI, 53110-8902, USA

[6] ISIS, Rutherford Appleton Laboratory, Didcot, OX11 OQX, UK

[7] Institut Laue-Langevin, BP 156, 6, rue Jules-Horowitz, 38042 Grenoble cedex 9, France

Abstract

The relaxation of residual stress in sub-scale forgings of Nickel-based superalloy has been measured during an ageing heat treatment using a novel in-situ neutron diffraction setup. Prior to ageing, high levels of residual stress were generated through water quenching from solution heat treatment. Two age temperatures were chosen for measurement: 760°C and 820°C. The stress data generated was compared to a finite element model, which was setup to closely match the in-situ experiment. A comparison of the data found that after a 400 minute age the post age stresses were under-predicted in the model by 50% and 33% in the 760° and 820°C conditions respectively. Furthermore the predicted stress relaxation profile had a stronger correlation to the experiment at the higher age temperature. This has been explained by the significant changes in microstructure, which have been observed as a result of the higher temperature age, in particular coarsening of the tertiary γ'.

1.   Introduction

Residual stress is defined as the stress which remains in a part once all external loads are removed (1). It can be generated via three distinct routes: differential thermal heating/cooling, plastic deformation, and volumetric phase changes. The manufacturing route for most engineering materials involve processes, which are known to generate residual stresses in this way. In metals, processes such as forging and quenching will induce plastic deformation and/or thermal excursions, which will result in the generation of residual stress. In precipitation strengthened alloys a subsequent process known as ageing is required following quenching in order to fine tune the microstructure (2). The ageing process consists of carefully controlled heating to a specific temperature, a holding period, and finally cooling at a pre-determined rate back to room temperature. Aside from the microstructural consequences, the ageing process can be likened to an annealing heat treatment, which relaxes residual stress. As a result, the ageing process must be considered not only in terms of microstructural changes but also in terms of residual stress relaxation.

The residual stress state of an engineering component is of particular importance to the manufacturer for two primary reasons; it governs further processing routes, and contributes to in-service performance. Further processing in this case refers specifically to machining and material removal. The removal of material will cause the removal of a region of residual stress, since the total residual stress must balance across any single free component, the removal of material will result in distortion as the stresses rebalance (3). If this is not taken into account it will lead to significant reworking of the part to achieve the required tolerances, or in the worst case, a scrapped part. Following manufacture, residual stress continues to be important but now in terms of the in-service performance of a component. Once in service, the residual stress state effects material properties such as fatigue, crack propagation, and stress corrosion, all of which contribute to the service life (4).

Given their far reaching effects, the characterisation of residual stress through manufacture is of great importance. One of the ways in which this can be done is to use finite element modelling to predict the stress evolution throughout manufacture. However, as with any model, the results require validation with experimental results. Residual stress can be characterised experimentally using a wide range of techniques, each with their own merits (5). For comparison to finite element modelling, neutron

diffraction in particular stands out for having the ability to penetrate deep within most engineering materials and being largely non-destructive (6).

Unfortunately the neutron diffraction approach to stress characterisation is usually somewhat limited when it comes to heat treatment processes. This is because measurements, particularly on engineering scale components, have to be carried out ex-situ. This means that the heat treatment is carried out away from the instrument such that a batch of samples is generated to represent each stage of interest during the heat treatment. This presents two problems, the first is sample-to-sample variation in processing, and the second is the low level of time resolution available without generating a very large batch of samples. The solution to these problems is to carry out the characterisation *in-situ* so that measurements are being made while the heat treatment process is occurring. This has the advantage of removing all sample-to-sample variation and allows a time resolution only limited by the instrument capabilities.

In this investigation the focus has been on the stress relief brought about by ageing heat treatment in a Nickel-base superalloy for turbine disc application. An in-situ neutron diffraction experiment has facilitated stress characterisation throughout an eight hour ageing process with a time resolution of approximately 15 minutes. The results obtained from this experiment have then been compared to the results from a finite element model.

2. Experimental description

Sample preparation

The component under investigation was that of a turbine disc, owing to the large size and complexity of a production part, the samples used here were of a sub-scale and simplified geometry (Figure 1a). The material used to manufacture the experimental samples was representative of those used in full scale production, in this case the Nickel-base superalloy RR1000 (Chemical composition - Table 1). RR1000 is an advanced alloy designed for disc application which has improved high temperature capabilities owing to a greater volume fraction of γ' in comparison to previous Ni-base superalloys (7). For this experiment, three forgings of RR1000 were provided by ATI Ladish, each having a diameter of 76.2mm and a depth of 25.4mm. Each forging was machined out from a large iso-thermally forged disc at the same radial distance to

minimise thermo-mechanical in-homogeneity. Once removed, each forging was subjected to an eight hour sub γ´ solvus heat treatment at 1120°C followed by immersion in a water bath. The water quench process was chosen in this instance since it allowed for significant residual stress to be generated in the sub-scale geometries which would then be relaxed during the in-situ experiment.

Microstructural Characterisation

A microstructural characterisation was carried out as it was expected that the different age temperatures would bring about a change in the γ´ distribution. To observe the microstructural changes, which occurred early in the age, small coupons were prepared to represent a 15 and 120 min age time for each temperature. Since all of the in-situ forgings had experienced the full duration of age it was necessary to prepare these samples separately after the neutron diffraction experiment. Four 3mm³ coupons were taken from the centre of a water quenched forging and aged individually using a tube furnace at the required time and temperature. The heating and cooling rates of the furnace were programmed to match closely those of the in-situ experiment.

Each heat treated coupon was mounted in phenolic resin then ground using ANSI 240-1200 grit size silicon carbide paper. This was followed by a diamond polish at 6μm and 1μm and finally a colloidal silica polish (OPS). Imaging the γ´ required a chemical etch, which attacks the precipitates but not the matrix. The resulting holes are then used to map the γ´ distribution. The etch was carried out on each coupon individually using a Nickel two part etch (Table 2) for approximately 30 seconds. Immediately following this, the coupons were mounted in an FEI Sirion Field Emission Gun Scanning Electron Microscope (FEG-SEM). Images were captured using a secondary electron and through lens detector to a maximum resolution of ~3nm.

Neutron Diffraction

The process of strain measurement for stress characterisation is a now well established technique, details of which can be found in (8) and (1). In this investigation strain measurements were made using an in-situ heat treatment setup on the strain scanning instrument ENGIN-X at ISIS, Oxford, UK (9).

ENGIN-X receives neutrons from a pulsed source, as such it operates under the 'time-of-flight' (TOF) setup, details of which can be found in (1) and (10). One of the many significant differences between a TOF instrument and a $\theta/2\theta$ instrument is that TOF operates at a fixed diffraction angle of 90°. This has the advantage of providing simultaneous use of two detectors, one at 2θ +90° and one at -90°, which allows measurement of two strain directions at the same time (Figure 1c). By using both detectors, and by measuring at the exact centre of the sample where hoop and radial direction are equivalent, it was possible to measure all three strain directions simultaneously. This was essential for a successful experiment since the primary goal was to capture stress relaxation during ageing with a high resolution in time.

Measurement of strain on a TOF instrument can be done in one of two ways, either the single peak fitting process, i.e. scanning 2θ, or a multi-peak refinement to obtain the lattice parameter (11). For this investigation strain was calculated in the $\theta/2\theta$ setup to allow faster acquisition times and to maintain consistency with prior neutron diffraction experiments. As such, it was necessary to choose an *hkl* lattice plane on which to diffraction neutrons. By fitting a Gaussian function to the recorded peak it was possible to obtain a single figure in 2θ for the peak position, this was translated into a value of d-spacing using Bragg's law.

$$\lambda = 2d_{hkl}sin\theta \tag{1}$$

The measured d-spacing was used in combination with a strain-free reference value (d_0) to calculate strain using the following relation.

$$\varepsilon = (d - d_0)/d_0 \tag{2}$$

The value of d_0 can be calculated or measured in a variety of different ways, a detailed review of which can be found in the literature (12). In this particular investigation the value of d_0 was measured by recording a diffraction peak in a 6x6x6mm cube. This approach relies on the coupon being of sufficiently small dimension as to be free from macro-stress, thus the d-spacing measured can be taken as the value for d_0.

Since this experiment involved heating, it was expected that due to thermal expansion the value of d_0 would not be the same from room temperature to ageing temperature. It was therefore necessary to measure the value of d_0 at the ageing temperature. In order to achieve this a 6x6x6mm d_0 cube in the same as quenched condition was

attached to the top of the forging using ceramic glue (Figure 2). Care was taken to ensure a good conductive contact between the forging and the cube to ensure temperature continuity was maintained across the two.

The d_0 cube was measured at room temperature before and after ageing, and at the beginning and end of the elevated temperature holding period to account for d_0 variation during the age. The difference between the two d_0 measurements at temperature was used to linearly interpolate a d_0 value for each measurement point made during the heat treatment.

Having fully characterised d_0 it was possible to calculate stress from the measured strain using a variation of Hooke's law.

$$\sigma_x = \frac{E_{hkl}}{(1+v_{hkl})(1-2v_{hkl})}\left[(1-v_{hkl})\varepsilon_x + v_{hkl}(\varepsilon_y + \varepsilon_z)\right] \; and \; \sigma_y = \cdots \qquad (3)$$

Where E_{hkl} and v_{hkl} represent the elastic constants specific to the (311) reflection in this material (Table 3). The values of E_{hkl} and v_{hkl} were obtained at room temperature and at ageing temperature using data generated during an in-situ loading experiment on Engin-X, ISIS, UK. (13).

Accuracy in the measurement processs was calculated using the peak fit uncertainty, which was translated to an accuracy in strain (and hence stress) using the following relation.

$$u_\varepsilon = \frac{1}{tan\theta}\left[(\delta\theta_0)^2 + (\delta\theta)^2\right]^{\frac{1}{2}} \qquad (4)$$

The measurement procedure began by mounting each forging securely on a computer controlled stage and aligned to the beam using a theodolite and entry scans at the surfaces. To carry out the ageing heat treatment a blanket of sintered alumina beads, containing high resistance Ni-Cr wire, was wrapped around the forging. The blanket was clamped firmly to each face using bolted steel plates attached to a water cooled stage. This ensured strong heat conduction between the blanket and the forging whilst protecting the instrument from the heat. To reduce the heat radiating away into the surroundings, and maintain a homogeneous temperature within the heated blanked, a series of insulating layers were arranged around the outside. Through a sequence of preliminary tests it was found that almost all of the layers placed around the forging would attenuate the neutron beam to a certain extent. As a consequence it

was necessary to arrange a window in the heated blanket, clamp, and outer heat proof blankets to avoid compromising the measurement.

Temperature control across the forging and d_0 cube was monitored using five surface mounted thermo-couples distributed as indicated in Figure 2. The central thermo-couple was used as the input to the furnace controller, which maintained the temperature to within 10°C across each of the thermo-couples. The heating and cooling rates were matched to those of a typical heat treatment using thermo-couple data provided by ATI Ladish (Figure 3).

Neutrons arrived at the instrument through a neutron guide tube via a beam chopper which was set for this experiment to 50Hz, providing a neutron bandwidth of λ=0.7-2.2Å. This crucially included the Ni(311) reflection which was selected for strain measurement owing to the good approximation to bulk behaviour and low sensitivity to plastic strain (14). The neutron gauge volume on ENGIN-X is set using a beam window at the end of the guide tube immediate adjacent to the sample, combined with the width of two sets of collimators. The collimators sit immediately in front of the detectors on either side of the sample. For this experiment it was planned to use the largest collimators available, which had a width of 4mm, combining this with a 4x4mm window would give a 4x4x4mm gauge volume. However during preliminary tests it was found that using this setup it was only possible to achieve count times of the order of 40min, which was much slower than the 15min target. In order to achieve the targeted 15min count time and maintain realistic levels of uncertainty the neutron window was increased to 8x8mm. However the collimators could not increase in size, therefore to maintain a cubic gauge volume the collimators were rocked laterally to achieve an effective 8x8x8mm volume. Such a large gauge volume normally brings with it the issue of averaging out stresses even in moderate stress gradients. However, from the stress distributions predicted by the model (Figure 4) it was know that the forging centre contained a negligible stress gradient in all measured direction. As such, a large gauge volume was not expected to cause any significant averaging of the stress.

The first two heat treatments were both carried out at 760°C. The repeated measurement was necessary to understanding the repeatability and stability of this novel experimental process. The measurement procedure began and ended with a room temperature data point, which was measured for a longer count time to reduce

uncertainty while time resolution was not a priority. The heating and cooling of S1 was executed without any issue and the thermal profile is clearly seen to match well with the thermo-couple data (Figure 3). In S2 however, an issue was encountered at the end of the heat treatment process, which prevented the furnace from being turned off. As a result S2 experienced an age of 10 hours as opposed to the 8 hours of S1. This was an unfortunate error, however it only effects the measured strains after 8 hours, therefore all data up until a 8 hour age is comparable between S1 and S2.

The final heat treatment was for an age at 820°C for 8 hours, the overall procedure remained the same as at 760°C. However, this heat treatment could not be carried out for the full 8 hours since the increased temperature placed additional loads on the electrical systems, which failed after 6 hours. All data up until this point remained valid however, and can be compared to the finite element simulations.

Finite element modelling

Finite element modelling was carried out using SCO3 – a Rolls-Royce in house analysis code (15). The problem was defined as a 2D axi-symmetric mesh (Figure 5a). Setting up the model in this way has the advantage of fast run times, but makes the assumption that heat treatment processes were carried out equally around the circumference of the part. The model was meshed with triangular elements with an approximate 1mm dimension across the entire cross section.

The modelling of the quench process has been described in detail in a separate investigation into residual stress generation during quenching (16). The basic steps were:

- Carry out a thermo-couple trial experiment of the quench from 1120°C to capture the rate of cooling across the forging. The thermo-couples were arranged as per Figure 6.
- Use the temperature differential between the core and rim thermo-couple during the cooling to calculate a heat transfer coefficient (HTC) curve (Figure 5b) using the following relation.

$$HTC = \frac{k(abs(T_B - T_A))}{(T_B - T_{water})d} \qquad (5)$$

- Take the derived HTC curve and apply it as a surface boundary condition to the 2D model (Figure 5a). Then increase or decrease the HTC were necessary

using weighting factors (Figure 5c) until the thermo-couple cooling curves were accurately replicated in the model. The simulated and experimental cooling curves for thermo-couples 1, 3 and 5 are given in Figure 7.

- Upon completion of a thermally accurate model, the same parameters are retained using a thermo-mechanical model complete with RR1000 material properties in order to calculate residual stress. In this case the quenching stresses were predicted using an isotropic hardening law. While it was expected that this would over-predict the level of residual stress, the alternative kinematic hardening law would under-predict the stress, which would not allow the stress relaxation behaviour to be visualised as clearly.

The inelastic strain data from the quenching model was imported into the ageing model. The ageing model consisted of the same geometry and meshing but did not require the use of an HTC curve for surface boundary conditions. This is because the heating and cooling rates were sufficiently slow, and the geometry sufficiently small, that it was possible to treat the entire component as a single entity in terms of temperature. As such the heating/cooling rate was set using 'ramp points' – user determined points of time and temperature for the entire geometry between which the model tracks linearly. Using 11 ramp points it was possible to accurately simulate the thermo-couple data captured during the in-situ heat treatment (Figure 3). The simulated and experimental temperature profiles indicate that the ageing model was a very close match to the actual in-situ heat treatment. Data was extracted from the model as a series of time-stress plots for the central node in the hoop/radial and axial directions.

3. Results and discussion

Each in-situ heat treatment required a characterisation of d_0 through the age in order to account for d_0 variation as a result of elemental diffusion in the material while at temperature. However, since time resolution was a priority, it was not possible to make a d_0 measurement for every measurement point during the heat treatment. Therefore in order for the variation in d_0 to be taken into account a d_0 measurement was made at the beginning and end of the hold period (i,e, while still at 760°C). The measured values of d_0 in S1 and S2 have been given in Figure 8. It was noted that the difference between the two measurement d_0 values was relatively small, no greater

than ~350$\mu\varepsilon$. As a result, a linear interpolation between the two measured points could be used generate a d_0 variation across the entire heat treatment without having a large impact on the calculated strain.

Unfortunately the failure of the heating element control system during the 820°C age prevented a d_0 measurement from being made at the end of the ageing heat treatment. As such the d_0 variation could not be quantified or taken into account in the stress calculations. Based on the variations seen at the lower ageing temperature, the minimum error this could have caused is ~400$\mu\varepsilon$ which in this material equates to an under-estimation of residual stress ~100MPa. However, this error is only likely to be prevalent in the latter stages of the age; measurements made shortly after the first d_0 measurement will still be accurate. As such, high confidence can be retained in the stress values calculated towards the beginning of the age.

The results as obtained from the in-situ ageing experiment have been given in Figure 9. Of particular note is the 760°C age (Figure 9a-b) which was carried out twice to assess the repeatability of this experimental technique. Considering first the hoop/radial direction (Figure 9a), it appears that two measured samples agree to within experimental error in almost all cases throughout the age. In the axial direction (Figure 9b), the experimental data shows a good degree of scatter without a clear trend, but this is repeated for both S1 and S2 which is at least an indicator of a repeatable experimental procedure. Overall the experimental data from all of the in-situ heat treatments exhibit high levels of scatter and uncertainty. This was to be expected in the experiment since the priority was to achieve a good time resolution during the ageing process, which forced count times down.

Comparing the experimental data to the simulation (Figure 9), it is immediately apparent that the stress relaxation profile in the hoop/radial direction is very different to the axial direction. The reason for this is that the quenching stress at the centre of the forging is close to zero in the axial direction but at peak tension in the hoop/radial direction. As a result, the relaxation behaviour resulting from ageing is best observed in the hoop/radial dataset. A detailed comparison of the simulated and experimental stress relaxation in the hoop/radial direction has been made with three considerations: 1) initiation of stress relaxation, 2) the relaxation profile, and 3) the total level of relaxation, which results from the age.

Initiation of stress relaxation

In the hoop direction (Figure 9a&c) the stress relaxation is predicted to begin at an earlier point than that which was measured at either age temperature. As the forging is heated to ageing temperature the simulated stresses begin to relax as early as 150°C, with very rapid relaxation beginning at approximately 550°C. Although measurements could not be made over the heating process, a measurement before and after heating indicates very little change in stress during this stage. Given that the starting stresses and the temperature profiles were almost identical in both experiment and simulation, this result is surprising. On further investigation it was found that some of the very early relaxation observed over the range of 150-550°C was caused by the thermal elastic response in the model. Upon cooling, a similar stress change was observed with the opposite sign, which was taken to be the reversal of this response and thus helped to explain some of the initial relaxation at low temperature in the model. However, even taken this into account the stress relaxation in either quench model is still occurring far in advance of what was measured experimentally.

Stress relaxation profile

In the hoop/radial direction (Figure 9a&c) the predicted stress relaxation follows a similar profile through each age condition. In each case the predicted stress falls rapidly over a period of approximately 200 minutes before entering a steady state of slow relaxation for the remainder of the heat treatment. However in the axial direction, the quenching stresses are very low, as such there is very little relaxation to observe or compare between prediction and experiment.

Comparing the predicted trend to experiment in the hoop/radial direction (Figure 9a&c) highlights a difference between the 760°C and the 820°C ageing heat treatments. At 760°C the predicted and measured profiles differ significantly during the early stages of the age. While the predicted profile exhibits a sharp and significant initial relaxation, the experiment does not. In the latter stages of the age, the predicted and measured profiles follow a similar gradient but with very different absolute values of stress. At an age temperature of 820°C the predicted stress profile in the hoop/radial directions shows a much stronger agreement to the experimental data (Figure 9c). Both profiles clearly show a sharp initial relaxation followed by a steady secondary relaxation.

Further insight into the predicted stress relaxation profile can be gained by considering the level of creep through each ageing heat treatment (Figure 10). The creep curves for each age show three distinct regions. As the profile leaves the x-axis there is a period of ~50 minutes at a steady but steep gradient (marked (a)), after this point a very rapid accumulation of creep occurs (b), which then tails off into a steady rate (c). It is notable that in either age the transition from region (a) to (b) appears to be brought on by the temperature exceeding ~700°C. Furthermore according to the model, the only difference in the two age temperatures is the extent to which stage (b) occurs. Based on these observations, it is possible that the discrepancy between prediction and experiment at 760°C can be attributed to the rapid relaxation process (b), which was initiated in the model but not in the experiment

Total relaxation

The total level of stress relaxation resulting from the full age can be compared directly without regarding the profile if it is only the final stress level after age that is of concern. In the 760° age the experimental data indicates a stress level after 400 minutes of approximately 800MPa in comparison to the predicted 400MPa. This equates to a 50% under prediction in the post age stress according to the model. At the 820°C age the model comes closer to matching experimental data, however the model still under-predicts the post age stress. After the same 400 minute interval the experiment measured ~300MPa and the model 200MPa, this corresponds to a 33% under prediction in the post age stress according to the model.

Considering all of the above observations the overall trend is one of improved correlation in the 820°C age over the 760°C age. To gain further insight into this behaviour the microstructure has been compared after 15, and 120mins in each age temperature.

The intragranular γ´ has been imaged at 20000x magnification through a 760°C age (Figure 11a-c), and through a 820°C age (Figure 11a,d,e). The 760°C age shows a small change in the microstructure in comparison to the water quench. A small amount of coarsening in the secondary γ´ is visible with typical particle sizes increasing from 30nm to 55nm after a 15 minute age. Increasing this time to 120 minutes brings about a negligible change with a typical particle size of 56nm in the secondary γ´. However, it is possible that tertiary γ´ has precipitated out of the matrix

at this temperature but is not visible at this magnification. Comparing these trends to the 820°C age it is clear that the higher age temperature has had an impact on the microstructure. After a 15 minute age there appears to be some coarsening of the existing secondary γ′, but more noticeably, the total number of precipitates has increased dramatically. Increasing the age time to 120 minutes brings about some additionally coarsening of the secondary γ′ whilst maintain the large number of precipitates.

One possibility for the increased number of precipitates at 820°C is that some of the previously unobserved tertiary γ′ has been significantly coarsened at the higher age temperature and is now visible at this magnification. This has not occurred to the same extent at 760° since the diffusion of γ′ elements to coarsen the precipitates occurs at a slower rate at the lower temperature. This result also correlates well with what was observed in the quenched forgings, which found the water quench to contain the lowest volume fraction of intragranular γ′ in comparison to an air and oil quench (16). This indicates a significant amount of the γ′ stabilising elements remained in the matrix as a result of the rapid quench, and so it should be expected that significant coarsening will occur given sufficient energy (i.e. temperature).

In terms of the mechanical properties of the material, significant coarsening of the tertiary γ′ will lead to an reduction in in strength (17). This may explain why such a rapid relaxation was observed experimentally in the 820°C age in comparison to the 760°C. Considering the simulated data, the improved correlation at 820°C indicates that the mechanical properties of the alloy in the model are more closely matched to those of the alloy at 820° in comparison to 760°C. Since the creep strength will be reduced at the higher temperature, it can be inferred that the material data used in the model predicted a reduced creep strength in comparison to the water quenched sub-scale forging used in this study.

4. Conclusions

A novel in-situ ageing heat treatment experiment has been carried out with the view to making detailed comparisons to finite element modelling of the ageing process. Ageing temperatures of 760°C and 820°C were achieved using a furnace arrangement constructed from a high resistance heating blanket situated on a neutron diffraction

beamline to measure strain and hence residual stress. A finite element model was generated to thermally match the in-situ experiment based on the temperature profiles captured by surface mounted thermo-couples. The results from each approach have been compared such that the following conclusions may be drawn.

- The use of a heating blanket placed in contact with the forging surface allowed a stable heat treatment process to be carried out with a temperature range no greater than 10°C. With careful arrangement of the heating elements and surrounding insulation it was possible to get the neutron beam in and out of the forging without and tangible attenuation. With this setup it was possible to measure strain at intervals of approximately 15 minutes with a peak fit uncertainty which equated to ±70MPa in the final stress calculation.

- The results from the in-situ experiment found a contrast in the measured stress relaxation behaviour in the 820°C age in comparison to the 760°C age. While the 820°C age exhibited a significant rapid relaxation process, the 760°C age was much reduced in comparison. However, both experimental profiles then entered a steady relaxation process of similar gradient.

- Comparing stress predictions to experiment, it was apparent that the simulations predicted a greater level of stress relaxation than that observed in either heat treatment. From the data extracted from the model (Figure 10), it is thought likely that this can be attributed to the large accumulation of creep at the early stages of the heat treatment.

- A microstructural characterisation found that the 820°C age resulted in a significantly altered microstructure in comparison to the 760° age. Of particular note was the coarsening of tertiary γ', which it is speculated will reduce the mechanical strength of the alloy.

- The change in microstructure at 820°C has been correlated to an improved agreement between the model and the experiment. Since the microstructure is intrinsically linked to the mechanical properties of the material, it is possible that the observed change in microstructure has resulted in a material, which is more in line with the material properties of the model. As such it is speculated that an improved correlation could be achieved by further materials characterisation work, particularly of the water quenched alloy prior to ageing.

Acknowledgments

List of tables:

Table 1: Nominal composition of Nickel superalloy RR1000

Alloy	Ni	Cr	Co	Mo	Ti	Al	C	B	Ta	Zr	Hf
RR1000	52.3	15.0	18.5	5.0	3.6	3.0	0.027	0.015	2	0.06	0.5

Table 2: Chemical composition of γ´ etchant

Part I	Part II
150ml H_2O	15ml HNO_3
150ml HCl	25ml H_2O
2.5g MoO_3	30ml part I

Table 3: Material properties of RR1000

Material Properties of RR1000			
	Room temp.	760°C	820°C
Young's modulus (bulk)	224 GPa	174GPa	168GPa
Poisson ratio (bulk)	0.33	0.37	0.38
(311) Diffraction elastic constant	203 GPa	155GPa	147GPa
(311) Poisson ratio	0.3	0.34	0.35

a)

76.2mm

Diffracted
neutrons

25.4mm

Hoop

Radial   Axial

Q

Neutron beam

b)

Q'   Q

Detector bank 1 - Transmission.
(Q) Hoop and Radial direction

Detector bank 2 - Reflection.
(Q') Axial direction

Gauge
volume

50Hz
neutron beam
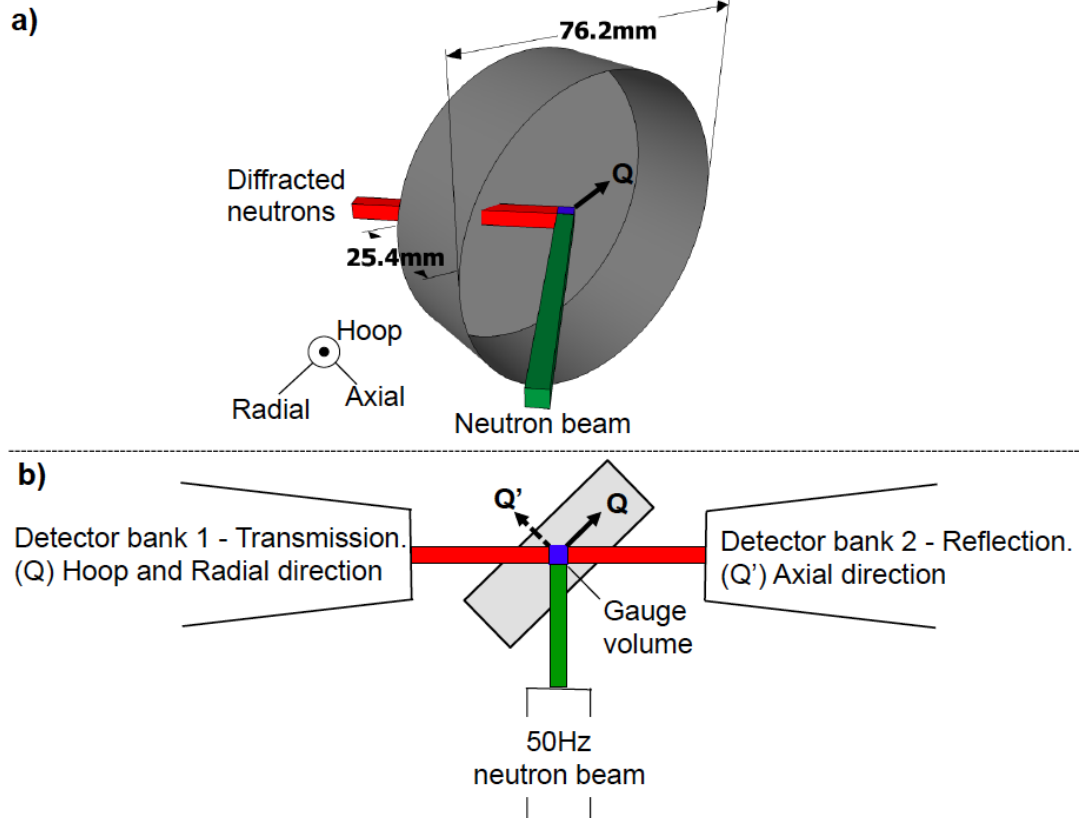
Figure 1: Schematic diagram of the sub-scale forging – a) with the central measurement gauge volume indicated and b) as measured on the spallation source in-situ experiment.

d_0 cube

Vertical 27mm

Bulk

Horizontal
27mm

Furnace
control
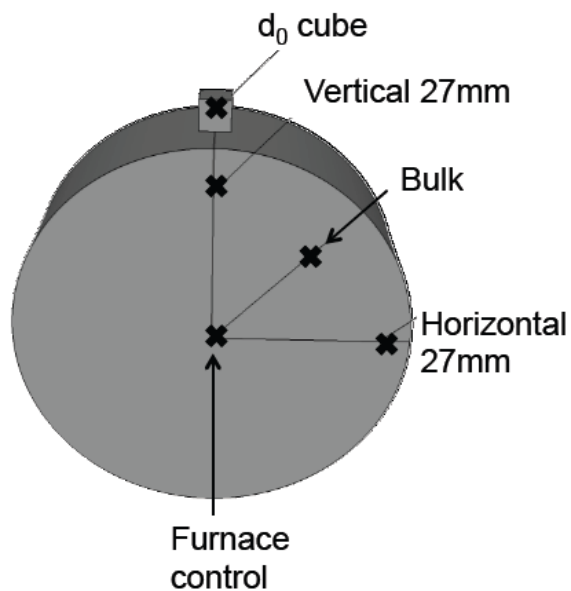
Figure 2: Schematic illustration of the thermo-couple locations for the in-situ experiment temperature control.
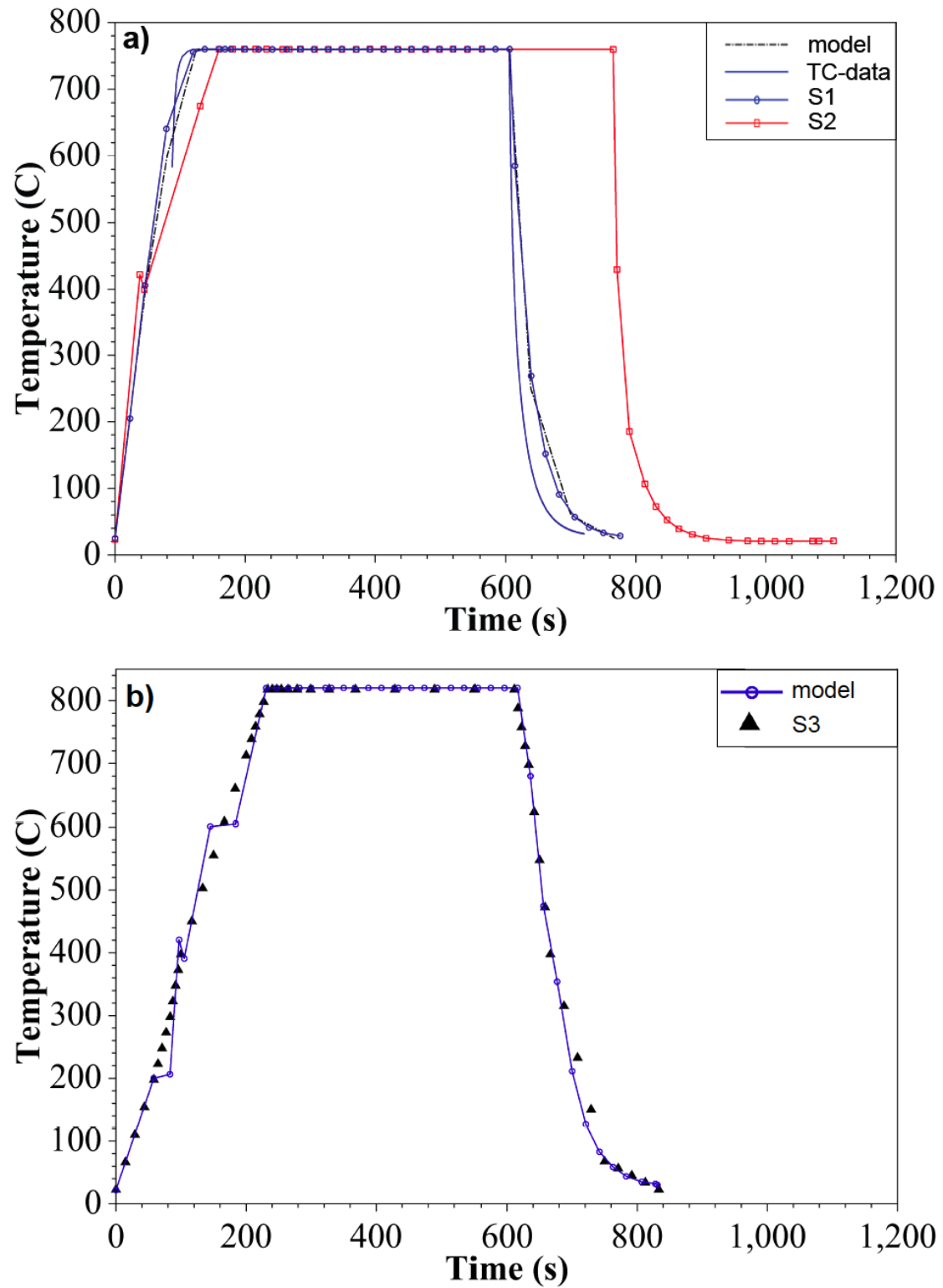
Figure 3: Comparison of the in-situ and modelled ageing thermal profile over a) the 760°C age (S1 &S2) and b) the 820°C age (S3).
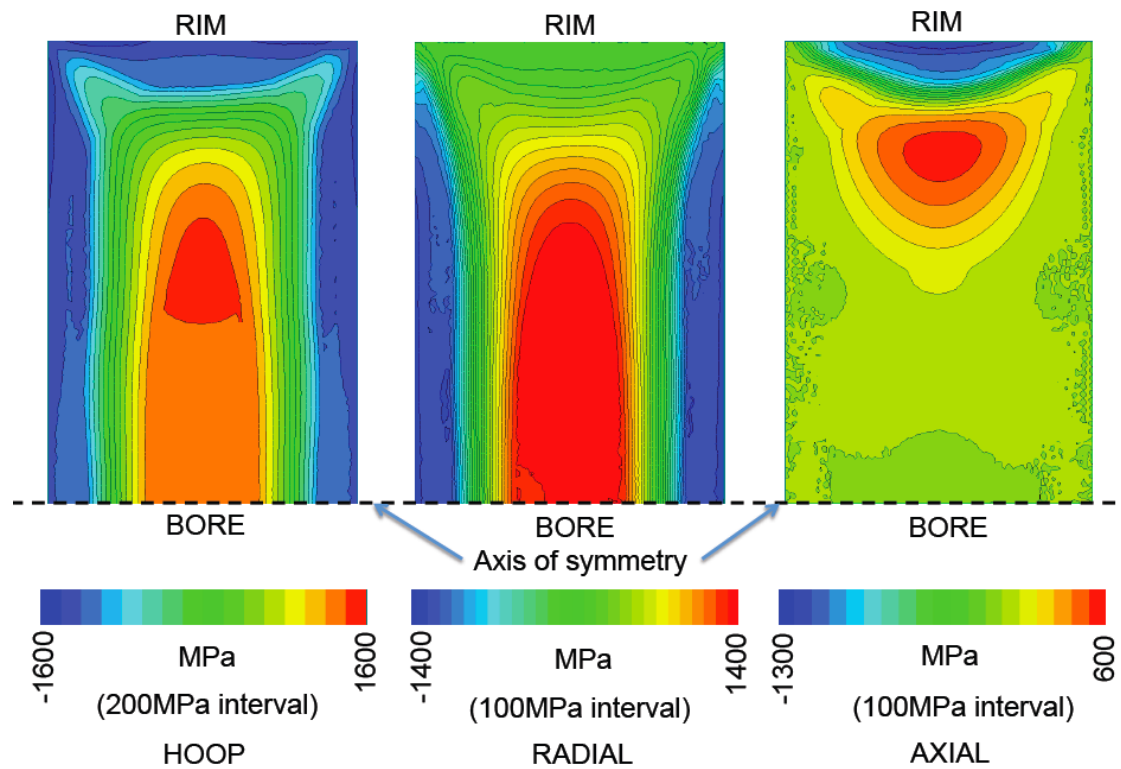
Figure 4: Residual stress predictions in the as quenched condition. Very low stress gradients are clearly present in the forging centre
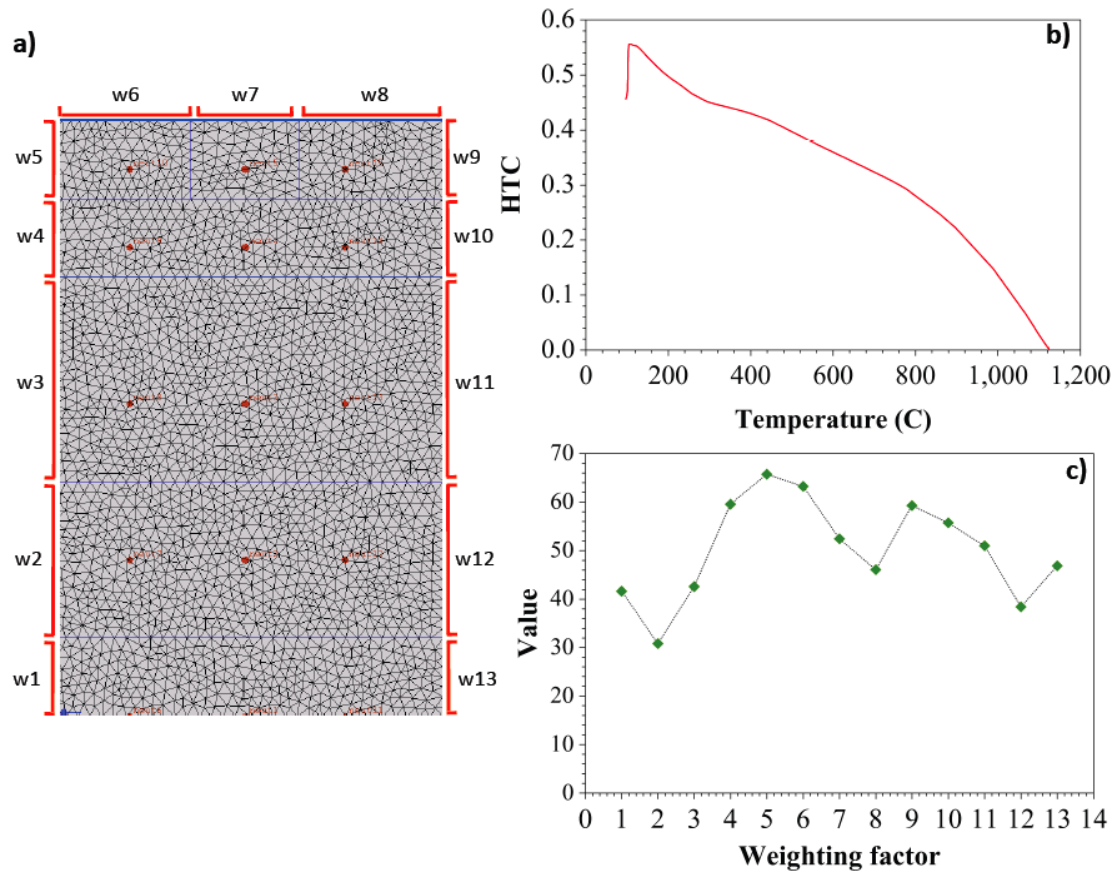
Figure 5: a) distribution of weighting factors along the boundary of the 2D axi-symmetric model, b) the HTC curve for water quenching, and c) the weighting factor values used in the final model for calculating stress
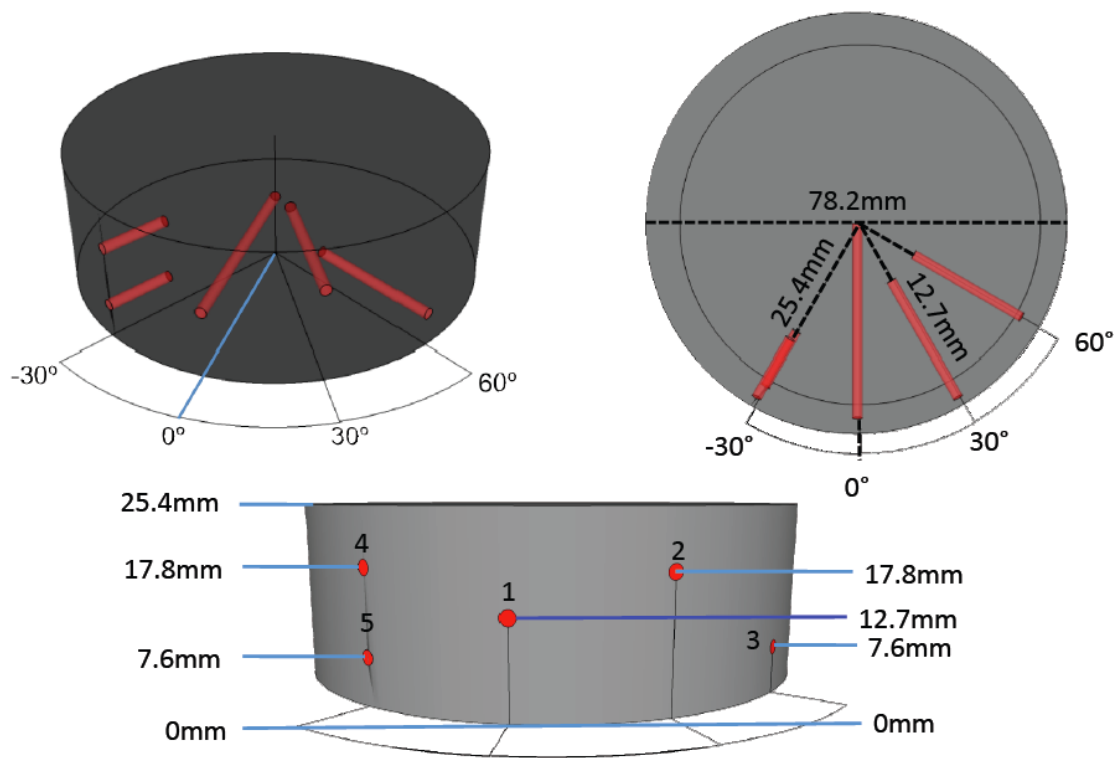
Figure 6: Thermo-couple locations in the stainless steel test piece used to capture the thermal profile of quenching and ageing.
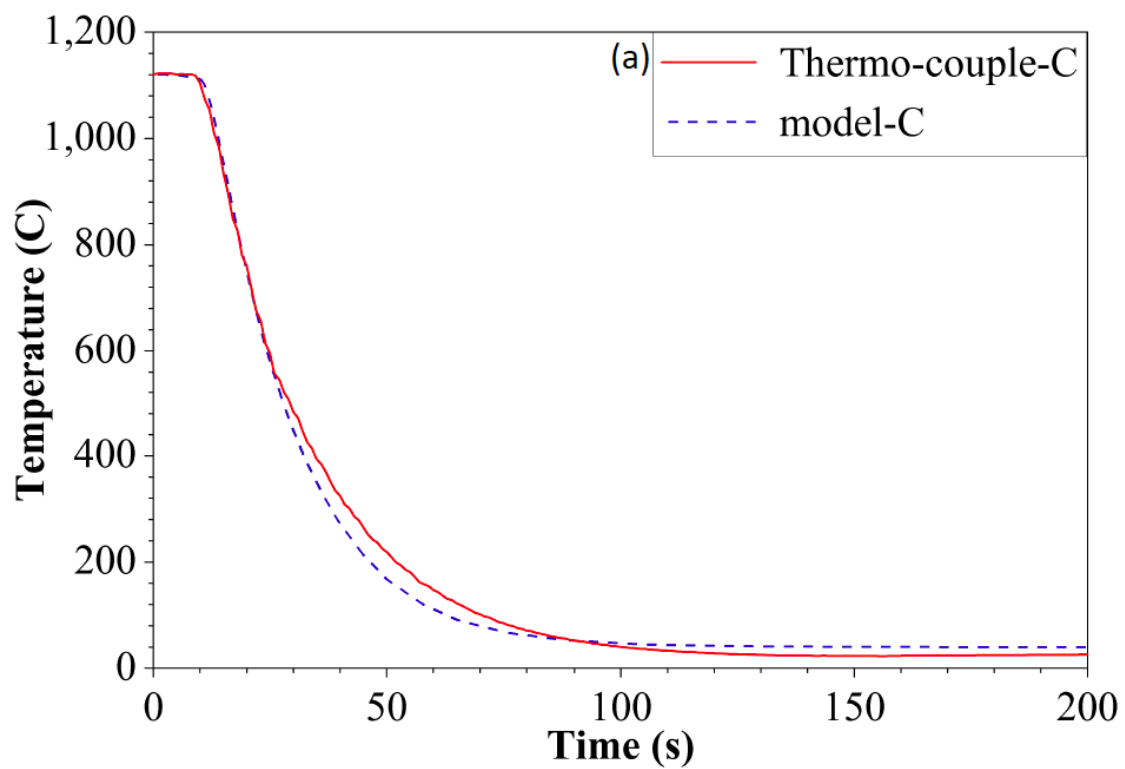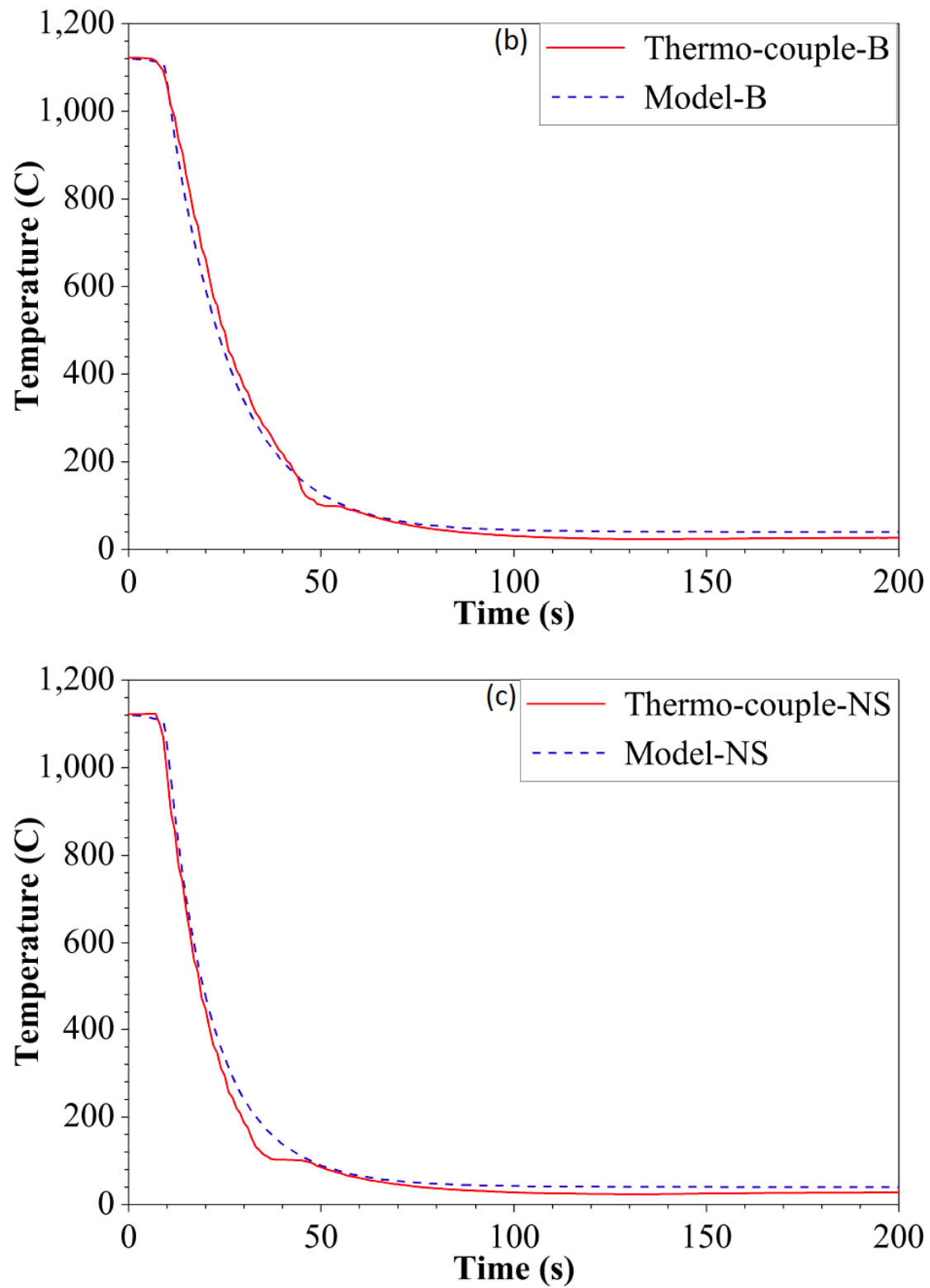
Figure 7: Comparison of quenching cooling curves at the a) the core (C), b) the bulk (B) and c) the near surface (NS) region as measured by the thermo-couples and predicted by the model.
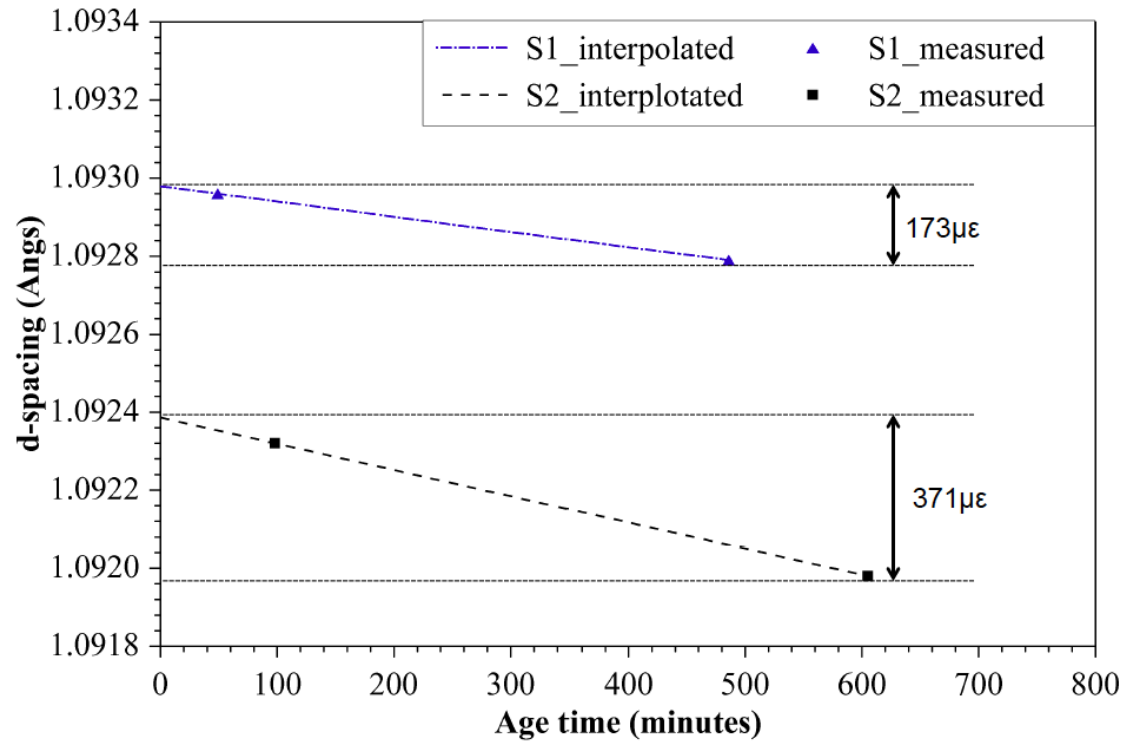
Figure 8: The value of d_0 as measured at the beginning and end of the in-situ age treatment at 760°C. The significance of the d_0 variation has been given in terms of a microstrain. The interpolation of d_0 using the two data points is also shown.
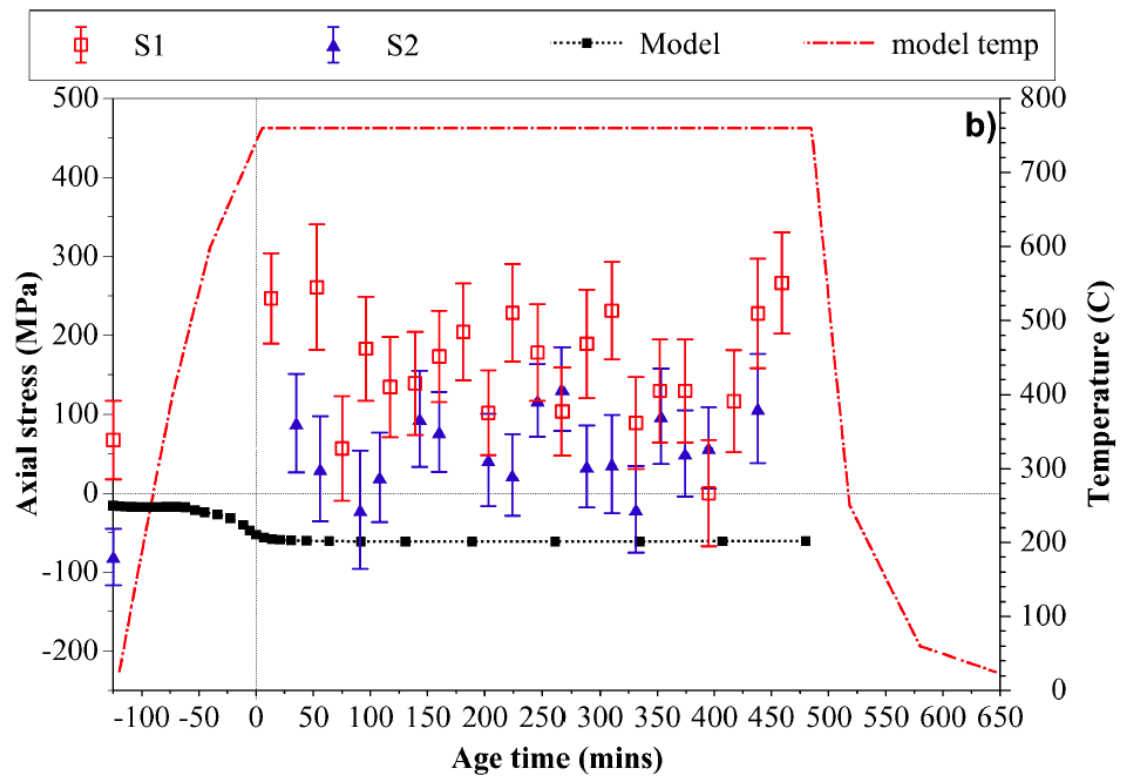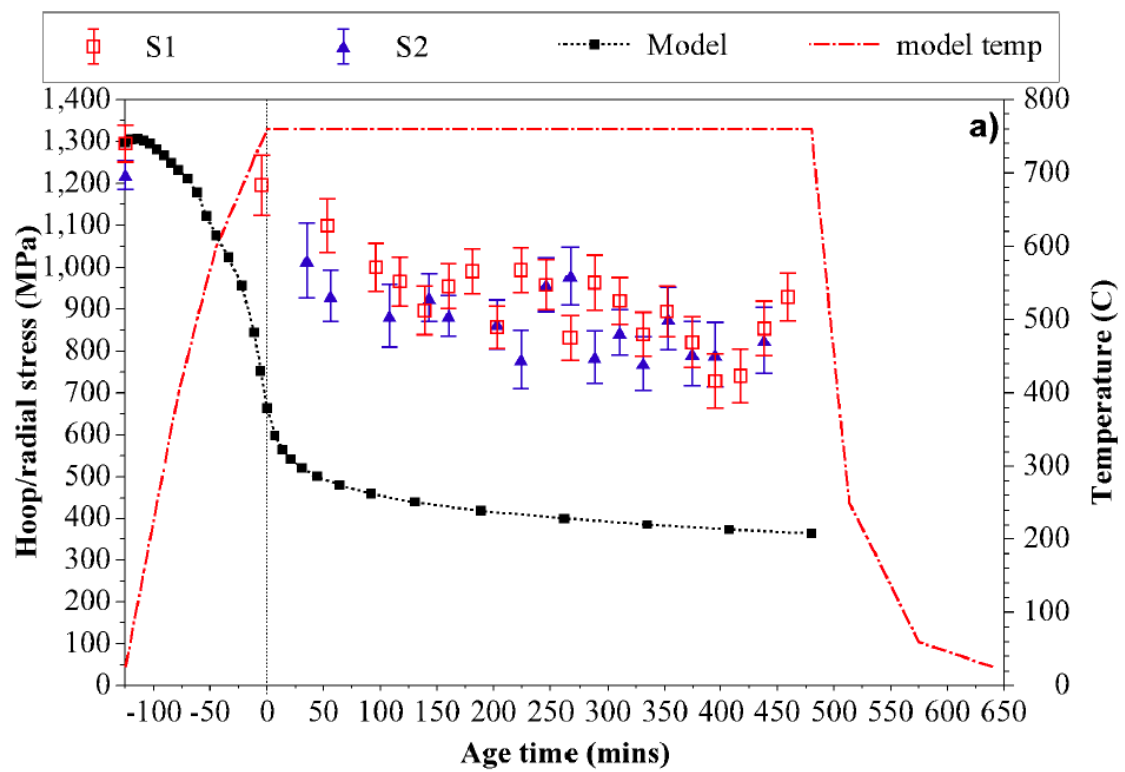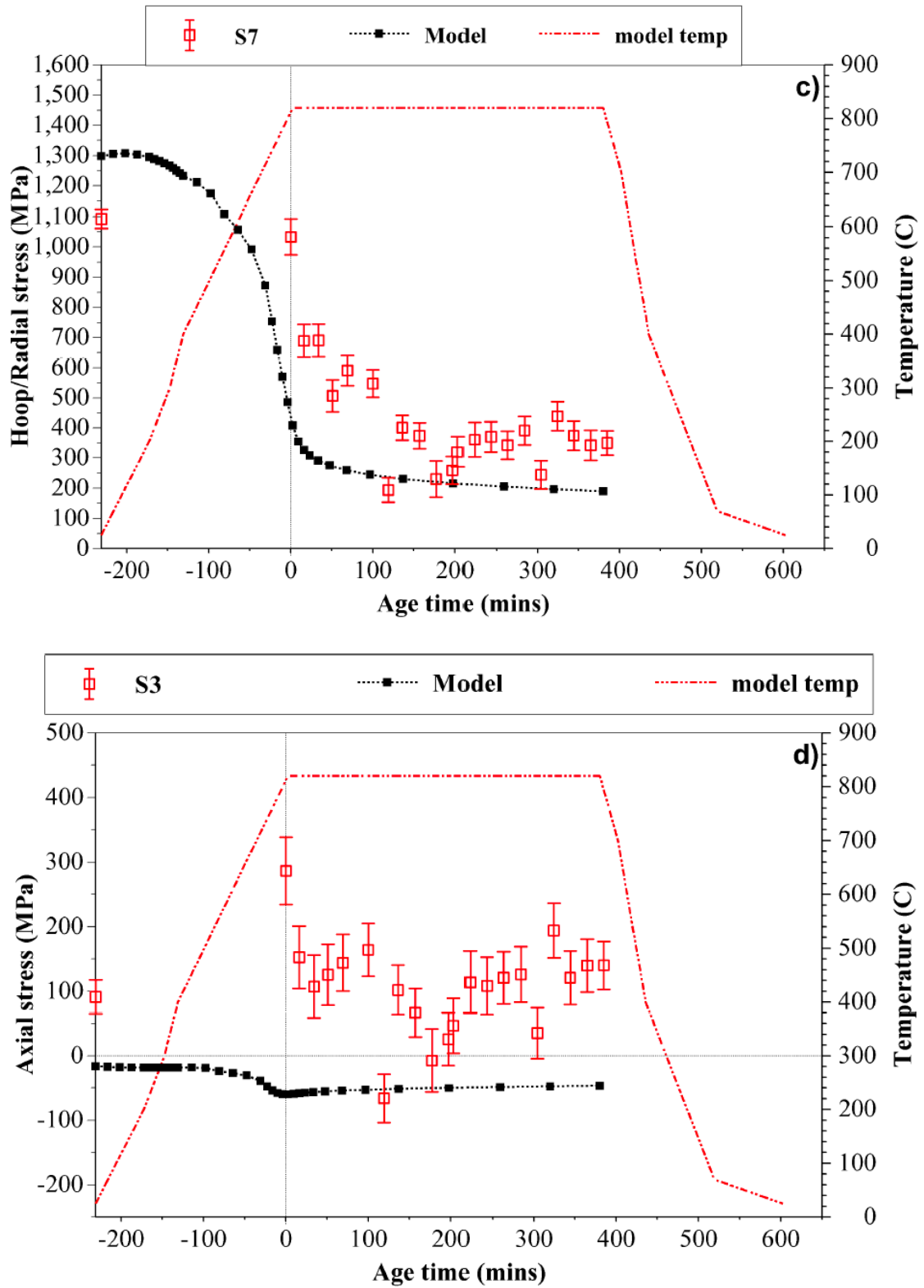
Figure 9: Comparison of residual stress characterisation by in-situ neutron diffraction and finite element modelling methods through: 760°C age – hoop (a) and axial direction (b), and 820°C age – hoop (c) and axial direction (d)
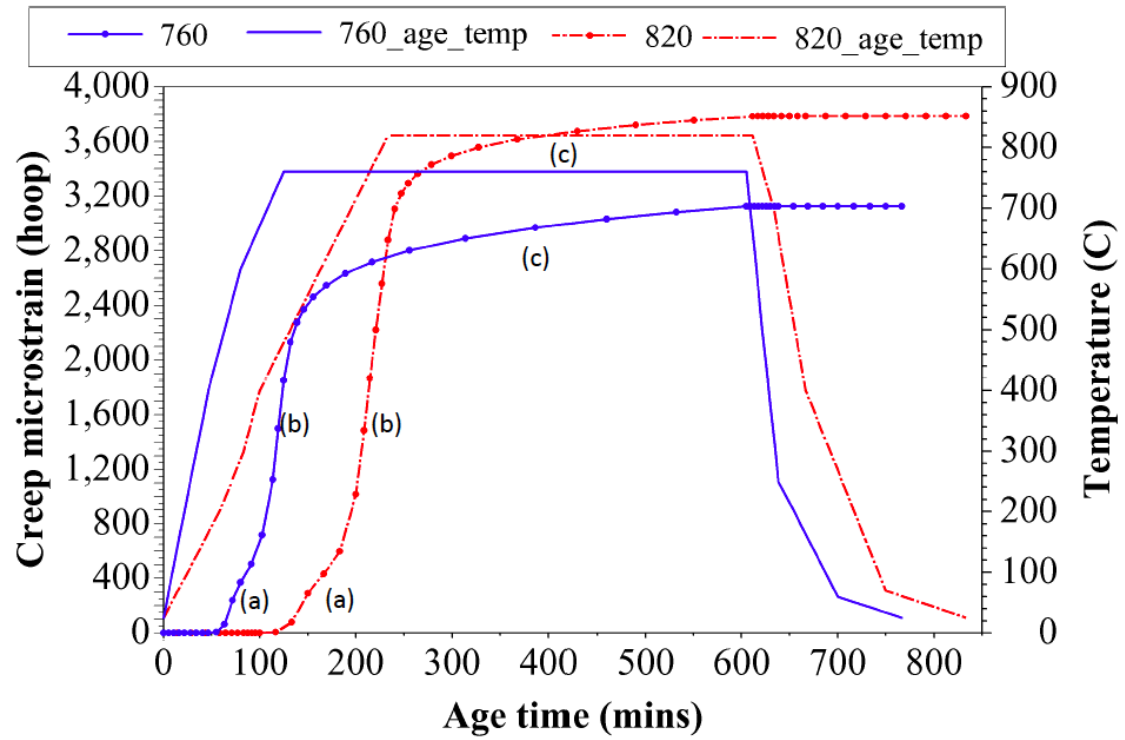
Figure 10: Creep strain accumulation at the forging centre in the hoop direction throughout the in-situ heat treatment at 760°C and 820°C.
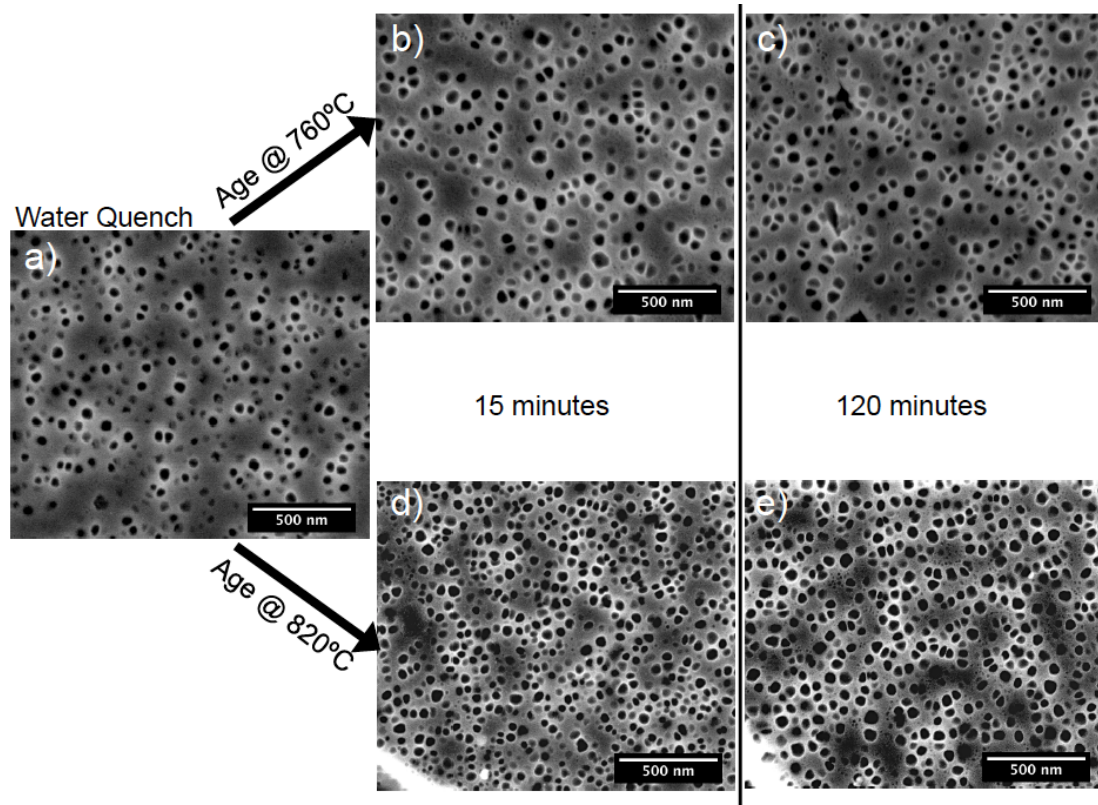
Figure 11: Intragranular γ´ imaged at 20000x magnification in the a) water quenched condition, b) 15min @ 760°C, c) 120min @ 760°C d) 15min @ 820°C and e) 120min @ 820°C

References

1.   Hutchings MT, Withers PJ, Holden TM, Lorentzen T. Introduction to the Characterization of Residual Stress by Neutron Diffraction. London: Taylor and Francis; 2005.

2.   Reed RC. The Superalloys - Fundamentals and Applications. Cambridge: Cambridge University Press; 2006.

3.   Rist M, James J, Tin S, Roder B, Daymond M. Residual stresses in a quenched superalloy turbine disc: Measurements and modeling. Metallurgical and Materials Transactions A. 2006;37(2):459-67.

4.   Webster GA, Ezeilo AN. Residual stress distributions and their influence on fatigue lifetimes. International Journal of Fatigue. 2001;23, Supplement 1(0):375-83.

5.   Withers PJ, Bhadeshia HKDH. Residual Stress Part 2 - Nature and Origins. Materials Science and Technology. 2001;17:366-75.

6.   Withers PJ. Mapping residual and internal stress in materials by neutron diffraction. C R Physique. 2007;8:806-20.

7.   Hardy MC, Zirbel B, Shen G, Shankar R. Developing damage tolerance and creep resistance in a high strength nickel alloy for disc applications. Superalloys 2004. 2004:83-92.

8.   Lodini A. Analysis of Residual Stress by Diffraction using Neutron and Synchrotron Radiation. London: Taylor and Francis; 2003.

9.   Santisteban JR, Daymond MR, James JA, Edwards L. ENGIN-X: a third-generation neutron strain scanner. Journal of applied crystallography. 2006;39(6):812-25.

10.   Dann JA, Daymond MR, Edwards L, James JA, Santisteban JR. A comparison between Engin and Engin-X, a new diffractometer optimized for stress measurement. Physica B: Condensed Matter. 2004;350(1–3, Supplement):E511-E4.

11.   Rietveld HM. A profile refinement method for nuclear and magnetic structures. Journal of applied crystallography. 1969;2(2):8898.

12.   Withers PJ, Preuss M, Steuwer A, Pang JWL. Methods for obtaining the strain-free lattice parameter when using diffraction to determine residual stress. Journal of applied crystallography. 2007;40(5):891-904.

13.   Grant B, Elisabeth K, Preuss M, Quinta da Fonseca J, Daymond MR. The Effect of Lattice Misfit on Deformation Mechanisms at High Temperature. Advanced Materials Research. 2011;278:144-9.

14.   Stone HJ, Holden TM, Reed RC. Determination of the plane specific elastic constants of waspaloy using neutron diffraction. Scripta Materialia. 1999;40(3):353-8.

15.   Bibby GP. Compressor Engineering SCO3 Radial Displacement Plot Facility. 14 ed: Rolls-Royce; 1998.

16.   Rolph J, Preuss M, Hardy MC, Nikov S, Ramanathan R, Hofmann M, et al. The effect of heat treatment processing on residual stress in Nickel superalloy - Part I - Quenching. Submission in process. 2012.

17.   Decker R. The evolution of wrought age-hardenable superalloys. JOM Journal of the Minerals, Metals and Materials Society. 2006;58(9):32-6.

Chapter 9

Residual Stress Evolution During the Manufacture of Aerospace Forgings

This paper was submitted for publication as part of the peer reviewed proceedings to the *TMS Superalloys 2012* conference. This paper was accepted for inclusion in the conference on the 30th April 2012. The paper which follows is in the form in which it will appear in the proceedings to the 12th International Symposium on Superalloys (Pittsburgh 2012). This research was performed with Dr. Naveed Iqbal, Dr. Michael Hoffman, Dr. Alex Evans, Stan Nikov, Dr. Ranga Ramanathan, Professor Michael Preuss, Dr. Mark Hardy, and Dr. Mike Glavicic

The lead author of this paper is the author of this thesis; all of the content which follows are the words of the lead author, and all of the data gathered and presented here is the result of investigations implemented by the lead author. In terms of co-author involvement, Dr. Naveed Iqbal, Dr. Michael Hoffman, and Dr. Alex Evans assisted with all aspects of data acquisition through neutron diffraction. Dr. Stan Nikov and Dr. Ranga Ramanathan assisted with the finite element modelling work. Essential guidance and feedback was provided through Professor Michael Preuss, Dr. Mark Hardy, and Dr. Mike Glavicic.

Residual stress evolution during the manufacture of aerospace forgings.

J. Rolph[1] M. Preuss[1] N. Iqbal[1] M. Hofmann[2] S. Nikov[3] M. C. Hardy[3] M. G. Glavicic[4] R. Ramanathan[5] A. Evans[6]

[1] Materials Science Centre, University of Manchester, Grosvenor St, Manchester, M13 9PL, UK

[2] Forschungs-Neutronenquelle Heinz Maier-Leibnitz (FRM II), TU München, Lichtenbergstr. 1,
85747 Garching, Germany

[3] Rolls-Royce plc, PO Box 31, Moor Lane, Derby, DE24 8BJ, UK

[4]Rolls-Royce Corporation, Indianapolis, IN, USA

[5] ATI Ladish Forging, 5481 S. Packard Avenue, Cudahy, WI, 53110-8902, USA

[6] Institut Laue-Langevin, 6 rue Jules-Horowitz, BP 156, 38042 Grenoble cedex 9, France

Keywords: Residual stress, Nickel superalloy, Neutron diffraction, Contour method, Finite element modelling

Abstract

The residual stresses present through the quenching, ageing, and machining processes in sub-scale turbine disc forgings of RR1000 have been measured experimentally using neutron diffraction, and the contour method. The disc samples, 88.9mm in diameter, and 25.4-50.8mm thickness were of small enough geometry to allow neutron strain measurement in 3 directions throughout most of the bulk. The contour method was employed successfully to generate a full 2D map of the hoop stress in the as-aged and machined samples. The two experimental data sets have been shown to agree very well. Finite element modelling predictions based on an experimentally derived heat transfer coefficient (HTC) curve allowed further comparison and generated additional data. Agreement between the experimental and simulated data was found to be reasonable with some discrepancy visible in the axial direction. The water quenching process was found to generate peak stresses up to 1400MPa in the hoop and radial direction, which were relaxed by as much as 700MPa through ageing. Material removal by machining had a less significant impact in most cases, relaxing residual stress by 100-200MPa.

1. Introduction

Aero-engine manufacturers seeking to increase turbine power and efficiency traditionally look to utilise higher turbine entry temperatures, and increase compressor discharge temperatures. To cope with the greater demands of such a design, it is now increasingly necessary to employ the next generation of nickel-base superalloys in the hottest sections of the engine. One such disc alloy is RR1000; developed by Rolls-Royce, it has a γ' volume fraction of close to 50 vol.% and typically a tri-modal γ' distribution. The design temperature capability of RR1000 is 1000°K [1]. To achieve the required mechanical performance, which is closely linked to the microstructure of the material, each component is processed using a sequence of forging and heat treatments before being machined in stages to the finished geometry. In disc components, the best mechanical performance is achieved when a fine γ' particle size distribution is produced, which requires fast cooling rates from solution heat treatment. However, this generates steep thermal gradients resulting in high levels of residual stress, which can be partially relaxed and re-distributed by the ageing and machining processes respectively.

The precise residual stress distribution is of importance to engine manufacturers for two distinct reasons. Firstly, machining processes remove constraint, which cause the component to distort as residual stresses re-distribute to reach a new equilibrium state. If unaccounted for, such distortions can lead to significant re-working of the component, or additional machining operations. Secondly, residual stresses have a direct impact on the performance of a component as they add to the applied stresses during operation. In the case of tensile residual stresses, they can deteriorate fatigue life and are ultimately passed on to component lifing predictions for service [2]. For these reasons, it has become increasingly important to employ validated process models that predict residual stresses during and post manufacture to tailor individual processes and improve the accuracy of lifing predictions.

Model validation on full-scale production parts can only be carried out in a handful of cases due to the high cost and difficulty in measuring large and complex geometries. In addition, large production geometries limit viable measurement techniques to near surface methods such as hole drilling or lab x-ray diffraction, which can only penetrate to a maximum depth of 1-2mm in this material. The hole drilling technique in particular is subject to a higher level of uncertainty once residual stress levels exceed 60% yield [3]. However, alternative methods such as neutron and high energy synchrotron x-ray diffraction [4, 5] as well as the so-called contour method [6] enable one to measure residual stresses from the near surface to deep inside the component. Furthers details on these residual stress measurement techniques including typical penetration into engineering materials can be found in [7].

In the present study residual stresses have been characterised in the alloy RR1000 using simplified sub-scale disc geometries to represent the quenching, ageing and machining processes of full scale discs. The geometry of the sub-scale disc was designed to allow neutron diffraction measurements deep inside the samples and the application of the contour method technique whilst maintaining similar levels of residual stress to production parts. The experimental residual stress results from neutron diffraction and contour method have been compared with finite element modelling predictions of the residual stress state with a view to improving current process modelling predictions. To date, the only industrially standardised technique available for model validation is that of hole drilling, thus the measurement of bulk residual stress represents an alternative approach to process model validation.

2. Experimental description – Sample preparation

Sample preparation

Three sub-scale disc forgings of RR1000 were provided by ATI Ladish Forgings. The nominal chemical composition of RR1000 is given in Table 1. Samples 1 (S1) and 2 (S2) had a diameter of 88.9mm, a bore width of 50.8mm and rim width of 25.4mm, the sample cross section has been provided in Figure 1. Sample 3 (S3) differs dimensionally in being machined on both faces to give a uniform width of 25.4mm.

Table 1: RR1000 nominal composition (wt%)

Alloy	Ni	Cr	Co	Mo	Ti	Al	C	B	Ta	Zr	Hf
RR1000	Bal.	15	18.5	5	3.6	3	0.027	0.015	2	0.06	0.5

In each case, sample processing began with extraction from a large pancake forging at the same radial distance to ensure a closely matched thermo-mechanical history for each part. S1 was then subjected to a sub γ′ solvus heat treatment at 1120°C for 4 hours before being water quenched. S2 was processed identically with the addition of a 16 hour ageing heat treatment at 760°C. S3 was processed as S2 with a follow up machining operation, which removed material from each face of the bore region (Figure 1). Note that the initial sub γ′ solvus heat treatment is assumed to reduce all forging stresses to zero. Therefore all residual stresses analysed in this study are those initiated from the quenching process alone.
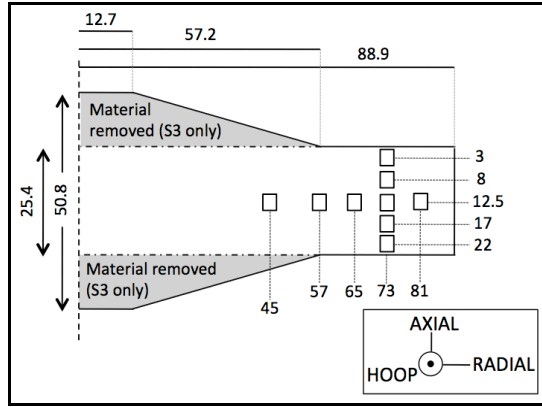

Figure 1: An axi-symmetric cross section of S1, S2, and S3 (with material removal indicated), with neutron diffraction gauge volume locations. All dimensions in mm.

A water quench process was chosen in this sub-scale geometry to achieve high levels of residual stress despite the small geometry of the sample, whilst an ageing temperature of 760°C was chosen because it is a typical stress relief/ageing temperature for γ' strengthened nickel-base superalloys. The machining operation carried out on S3 was designed as a simplified representation of a reduction in cross-section, as carried out in full-scale disc manufacture when moving from heat treatment geometry to finished component.

2.1 Residual stress analysis by neutron diffraction

All neutron diffraction measurements were carried out at the dedicated strain scanning instrument STRESS-SPEC at FRM-II, Germany [8].

Two samples were mounted simultaneously and aligned initially using a computer controlled translator table and theodolite, followed by entry scans with the neutron beam for accurate positioning. The Ni (311) reflection was chosen for the measurement of elastic strain in this alloy as it is known for having low sensitivity to plasticity induced intergranular strains and to exhibit a good representation of bulk behaviour [9]. It is acknowledged however, that in RR1000 the (311) diffraction peak is composed of contributions from both the γ and γ′ phases. The two phases are indistinguishable in most neutron diffraction experiments since they have almost identical lattice parameters; thus a single peak is observed where the two contributions overlap. Measuring bulk strain with a composite peak such as this assumes both the γ and γ′ phases accommodate load without any significant partitioning, which would otherwise alter the peak shape. Throughout peak fitting and analysis, care was taken to ensure peak symmetry was observed and the Gaussian fit could be

applied without generating any offset in peak-centre position. The instrument monochromator was set do give a wavelength of λ = 1.55Å which allowed measurement of the (311) reflection at 2θ=92°, thus providing an approximately cubic gauge volume.

To allow calculation of stress, strain was measured in three perpendicular directions, namely hoop, radial and axial as indicated on Figure 1. These directions can be assumed to approximate the principle stress directions from the disc geometry. A radial line scan at mid width in combination with an axial line scan at 73mm from the bore made a total of nine measurement points arranged in a cross formation. To balance spatial resolution with count statistics, a gauge volume of 4x4x4 mm^3 was chosen and defined using primary and secondary slits. Data analysis was carried out using in-house software by fitting and subtracting background intensity, followed by a Gaussian fit of the peak itself. This allowed each diffraction peak centre to be expressed in terms of a value of 2θ, which was converted to a value of d-spacing using Bragg's law (Equation 1).

$$\lambda = 2d\sin\theta \qquad (1)$$

Strain is calculable from measured d-spacings and a reference (d_0) value using the following relation (Equation 2).

$$\varepsilon = \frac{d^{hkl} - d_0^{hkl}}{d_0^{hkl}} \qquad (2)$$

One technique to obtain the stress-free d-spacing (d_0) is to measure individual cubes of material extracted from specific locations in an identically processed specimen at the time of the neutron diffraction experiment. If these cubes are sufficiently small in dimension they may be considered free from macro-stress and allow the true lattice strain to be deduced via Equation 2 [10]. In this study identically processed cubes were not available at the time of the experiment. Instead, cubes were extracted from each sample at a later date and measured in a follow up experiment. The cubes were extracted using Electro-Discharge Machining (EDM) and measured using the strain scanning instrument SALSA at the ILL, Grenoble [11]. To ensure the measured d-spacings from two different instruments could be used to calculate strain, a reference sample of RR1000 powder was measured on each instrument. The measured powder d-spacing was then employed as a scale factor to the data obtained from each instrumental setup.

The water quenching process was known to have set up severe thermal gradients. Consequently, it was expected that a d_0 variation might exist approaching the rim of the disc [12]. In order to compensate for this a cube was extracted from each sample at three radial locations coinciding with neutron measurement points; 45mm, 73mm, and 81mm from the bore centre. The 45mm cube was also used as a d_0 for the 57mm, and 63mm neutron measurement points since they were not affected by near surface d_0 variation.

Upon completion of d_0 measurement, it was possible to calculate strain in the three principal directions, and from this stress using the following relation.

$$\sigma_x = \frac{E_{hkl}}{(1+v_{hkl})(1-2v_{hkl})}\left[(1-v_{hkl})\varepsilon_x + v_{hkl}(\varepsilon_y + \varepsilon_z)\right] \quad \text{and} \quad \sigma_y = ...etc. \qquad (3)$$

Note that in this case, E and v represent the (311) plane specific diffraction elastic constants (DECs) at room temperature, as given in Table 2. The (311) DECs given here were measured previously during an in-situ loading neutron diffraction experiment on the

strain scanning instrument Engin-X, (Didcot, UK) [13]. The experiment measured multiple diffraction peaks through increased load in the longitudinal and transverse direction simultaneously. From this data it was possible to calculate the (311) plane specific elastic modulus and Poisson ratio.

Peak position accuracies were calculated in real time during the experiment from the fit uncertainty of each peak using the method outlined by Wimpory [14]. Using this methodology it was possible to adjust count times to account for variations in neutron pathlength depending on measurement position and direction. In doing so a residual stress accuracy of ±50MPa or better was achieved.

Table 2: Material properties of RR1000

Material Properties of RR1000	
Young's modulus (bulk)	224 GPa
Poisson ratio (bulk)	0.33
(311) Diffraction elastic constant	203 GPa
(311) Poisson ratio	0.3

2.2 Residual stress analysis using the contour method

The contour method for residual stress characterisation is a destructive technique for obtaining a 2D map of the residual stress normal to a cut surface. The technique consists of three stages, cutting, surface measurement, and analysis. These are shown schematically in Figure 2. The cutting processes (A) causes residual stresses within the component to relax. The resultant deformation of the cut surfaces is representative of the original residual stress distribution (B). Measurement of both deformed surfaces is carried out using either a CMM touch probe or laser scanner and the deformed surfaces loaded into an FE model. Analysis is then carried out by virtually iterating the deformed surface back to planarity (C) and the residual stress field is calculated from the total force required to do this.
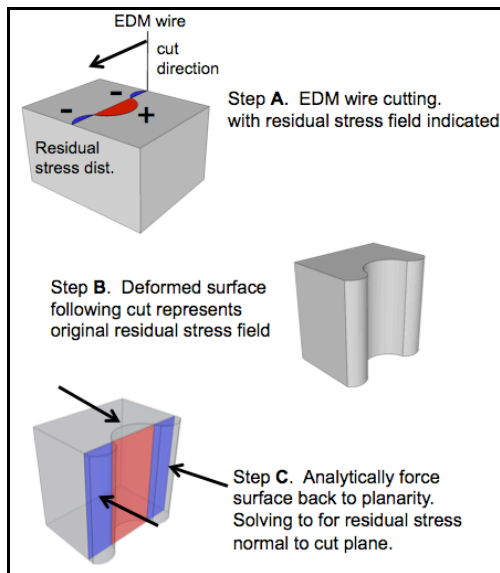

Figure 2: Schematic methodology for obtaining residual stress using the contour method

It is worth noting that two key assumptions are made using this method. First, the relaxation of residual stress and the resulting surface deformation are purely elastic. Second, the cutting process is sufficiently slow and non-aggressive that no additional stresses are introduced during the process. An in-depth description of the contour method can be found in [6].

Due to time and cost constraints only S2 and S3 were measured using the contour method. Each sample was sectioned across the diameter using Electro-Discharge Machining (EDM), with the cut plane aligned to pass through each of the neutron diffraction measurement gauge volumes. The EDM cut was made using so called 'skim cut' settings, which ensure a slow and fine cut that does not contribute to the residual stress state. Each sample was firmly clamped on both sides of the cut to reduce non-symmetric errors which would contribute to the final residual stress calculation [15]. The surface contour of each sample was measured using a Nanofocus confocal laser profilometer at a step size of 100μm. The sample outline was defined as the point at which reflectivity dropped below 80%, thus indicating that the laser had scanned over the edge of the sample; all data points with reflectivity less than 80% were set to a default "mask" value to allow easy identification in later stages of analysis.

Surface contour data sets were manipulated and analysed using a combination of user defined routines in MATLAB [16] and ABAQUS [17]. MATLAB was used to remove "masked" data points and clean outliers. In both cases a 5mm width of contour data was removed in the regions where the wire entered and exited the workpiece to eliminate artifacts generated here [18]. Data from both halves were aligned analytically through minimisation of eigenstrains and the average of both displacements taken. This averaged displacement is then assumed to be exclusively the result of the elastic relaxation of stresses normal to the cut; all other effects including shear and Poisson contribution are averaged out at this stage of the process. Lastly, experimental noise was removed by fitting a bi-variant spline function to the averaged measured surface. Further details on data analysis can be found in [19].

The spline fit represented the initial condition in the model. From this condition the model worked 'backwards' to the final condition of one sample half with a planar surface, and in doing so calculated the stress. The final condition was generated by first importing the sample outline into ABAQUS in order to generate a planar cross-section. The remaining 3D geometry was generated using built-in extrude and cut functions. The part was meshed using quadratic elements with typical length 1mm at the cut surface, which reduced to 3.5mm at the rim of the disc. This allowed relatively short calculation times (60 minutes) whilst maintaining adequate resolution. By assuming elastic isotropy, bulk elastic properties were used (Table 2) and the model was solved using ABAQUS.

The model was subsequently interrogated to obtain residual stress distributions. Two dimensional maps of the stress normal to the surface were generated to visualise the distribution, and undertake first comparisons between S2 and S3. To compare data sets in detail, contour stress data were exported as either radial or axial line scans between any two user-defined points on the sample surface.

3. Process modelling

Model generation
All finite element modelling work was carried out using the Rolls-Royce in-house analysis code 'SCO3' [20]. The problem was defined as a two dimensional cross-section from bore to rim only. This was known to be a valid approximation due to the propensity of all manufacturing processes in this study to generate

approximately axi-symmetric residual stress distributions. The geometry was drawn in SCO3 using measured dimensions and meshed using ~1mm length triangular elements throughout the entire cross section (Figure 3).
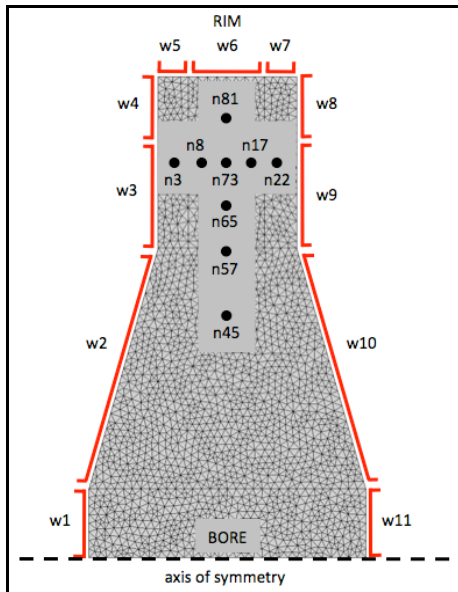

Figure 3: The meshed part as generated in SCO3, complete with neutron diffraction target values ('n' prefix points) and HTC weighting factors (w1-11) indicated.

Quench
The quenching process was modelled through heat extraction at the surfaces of the geometry. Heat extraction comprised of two key stages; firstly, surface radiation during transfer from furnace to quench tank, and secondly, convection currents once immersed in the quench medium. The level of heat extraction during sample transfer was sufficiently low that a simple constant of emissivity could be used to simulate this stage of the quench process. However, once the sample was in contact with water it was necessary to use a heat transfer coefficient (HTC) curve to define the level of heat extraction at any given temperature.
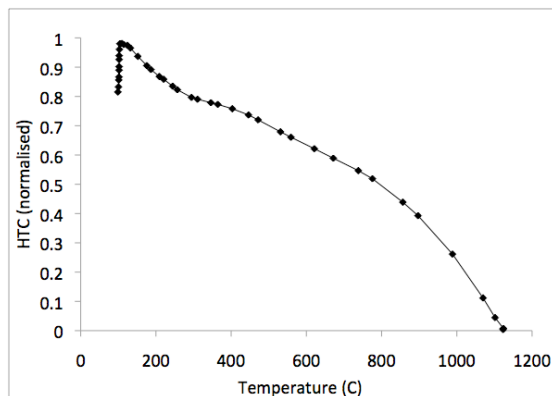

Figure 4: Normalised water quenching HTC curve for a sub-scale disc forging of the nickel-base superalloy RR1000.

The HTC curve was obtained in a separate investigation using a stainless steel test piece with multiple embedded thermocouples to record the change in temperature during quench (Figure 4). After taking into account the material properties, the difference in temperature between two proximal thermocouples was used to derive the level of heat transfer throughout the quenching process and hence the HTC curve of that setup (Figure 4).

The HTC curve was initially applied uniformly to the model as a temperature dependant coefficient of heat extraction on each surface. However, this did not accurately define the process; factors such as sample geometry and orientation when entering the quenching tank caused differential cooling by surface location. To better describe the quenching process the part was broken down into 11 surface regions and a further 'weighting factor' (WF) was employed at each surface to allow cooling rates to vary by location (Figure 3). The method for deriving each WF has been described in later sections as the *inference method*.

Age
Experimentally, S2 and S3 were both water quenched before being aged for sixteen hours at 760°C followed by cooling in still air for a further hour. This process was simulated by interpolating strains from the quench model output into a new model of identical geometry but using ramp points that reflected the thermal history through the ageing process. Stresses were expected to relax via creep during ageing. Therefore, material specific creep rates were added to the simulation process at this stage. The rate of heating and cooling was of sufficiently slow rate during ageing that it was possible to treat the sample as a uniform thermal entity without straying far from the actual manufacturing process.

Machine
The machining process modelled in this investigation was strictly aimed at characterising the re-balancing of residual stresses after material removal, therefore stresses induced from machining itself were in no way considered. This being the case, the simulation of machining was completed by removing the appropriate elements, directly transposing the aged condition (S2) strains onto the new mesh, and then running the model to regain force balance.

In addition, it was assumed that the order in which material was removed did not seriously affect the net residual stress distribution once the machining process was completed [21]. This assumption was tested in a preliminary investigation by modelling material removal on each side first, then both sides at the same time. It was found that the order of material removal made no difference to the final residual stress distribution. It was therefore possible to model the machining sequence by removing all of the relevant elements in one step.

Model execution
The quench model was loaded into an optimisation software package known as 'iSight' [22] to carry out the so called 'inference method' of deriving HTCs. Data from the neutron diffraction study was used to define the target residual stress values in nine locations within the bulk of the sample (Figure 3).

The optimisation process used a 'pointer' algorithm to adjust the eleven weighting factors to minimise the sum of residuals between experimental and modelled residual stresses. However, weighting factor adjustment was restricted during optimisation to maintain a degree of continuity between neighbouring surfaces. Contained within the optimisation loop was a condition by which the maximum allowable difference between neighbouring weighting factors must be less than two thirds of the average between them. Using this method the HTC weighting factors for water quenching were derived as shown in Figure 5. The distribution of weighting factors indicates a rapid cooling at the

bore, and near symmetric cooling rate about the centre line (w6). Each derived weighting factor value was multiplied by the HTC curve to give a heat transfer function for each surface region. A final simulation was carried out using this set up to obtain the modelled residual stress following water quench.
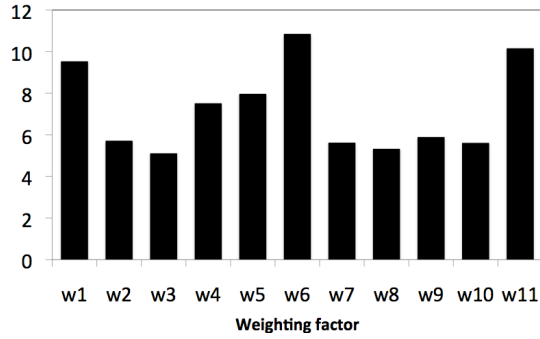
Figure 5: HTC curve weighting factors for the water quenching process as derived using the inference method.

It was recognised that whilst the use of HTC weighting factors would likely achieve high agreement with the experimental residual stress distribution, it potentially masks any underlying issues in the model at the quenching stage. In particular, inaccuracies in thermal or mechanical properties, which would otherwise lead to an incorrect stress prediction, could be at least partially corrected for by the HTC optimisation. To check the HTC inference method was generating realistic levels of cooling throughout the disc, time-temperature curves from the model were compared to measured data from the thermo-couple experiment (Figure 6). Overall the modelled cooling correlates well with the measured data. In the regions close to the rim (P3 & P5), the agreement is high, indicating a well matched cooling rate in proximity to the neutron measurement locations. Closer to the bore, (P1 and P11) the high level of agreement has been maintained, thus the derived HTC weighting factors gave a realistic representation of cooling for the entire sample surface. However in the region deep within the sample bulk the model did not correlate well to the measured cooling (P7). At P7 the model cooled too slowly, yet at the surrounding surface this was not the case (P1&P11).
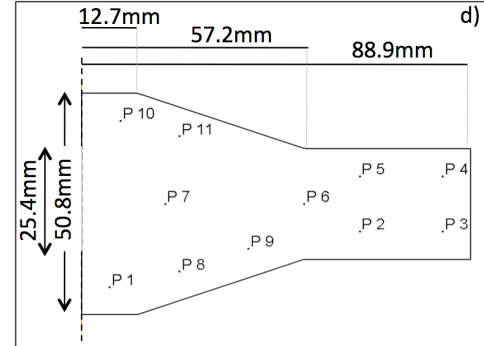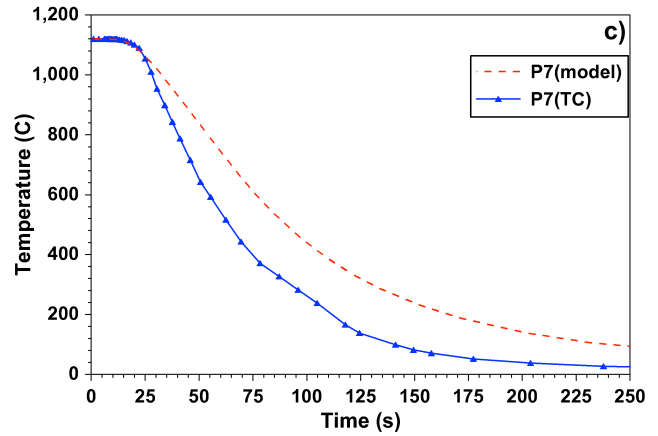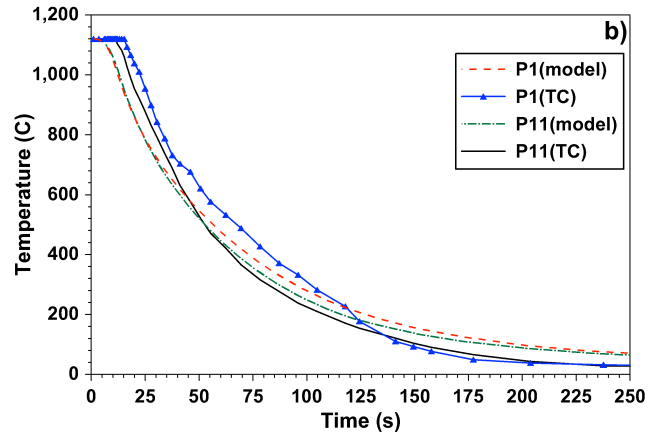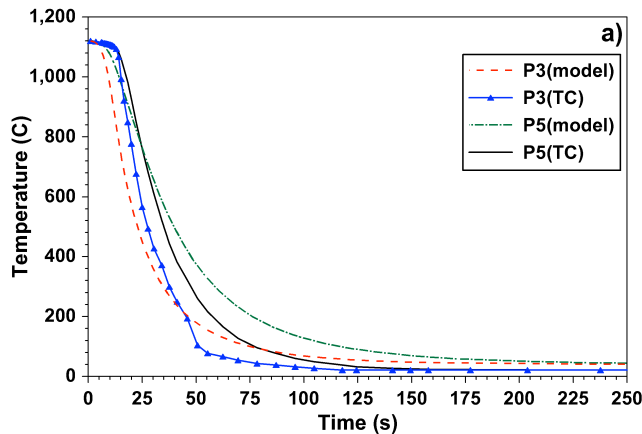
Figure 6: (a-c) Time-temperature history through water quench as obtained by FE simulation (model) and thermo-couple (TC) experiment and d) the thermo-couple locations.

This indicates a possible error in the level of internal conduction rather than surface heat extraction as controlled by the HTC. This being the case, it is possible that the simulated residual stresses will show some disagreement to measured results in the bore region of this disc.

Ageing and machining
Both ageing and machining models were executed without parameter optimisation; thus the simulated residual stress values after age and after machining are representative of the model alone and allow for a more direct comparison of results.

4. Results and Discussion

Neutron diffraction

Figure 7 shows mid-section residual stress evolution in the hoop (a), radial (b) and axial (c) directions using neutron diffraction following quenching, ageing and machining processes. The trends observed following quenching largely follow the expected behaviour. Initial surface cooling over a hot core causes tensile yield in the hoop and radial directions on each face and axial yield around the circumference. After a period of time this process reverses as the core cools and contracts and attempts to draw in the outer surface, thus leaving the surface in biaxial compression and the core in tension [23] .

Following quench, peak tensile stresses are observed in the regions close to the bore in both the hoop and radial directions. Hoop stress falls until reaching the compressive layer at the surface, whereas the radial stress remains tensile throughout. The radial stresses must fall to zero at the free surface of the rim, and the falling trends shown in Figure 7b do indicate that this is likely to be the case. Axially, residual stresses are generally smaller in magnitude when compared to the hoop and radial directions. It is likely that this is the result of a reduced thermal gradient in this direction brought about by the geometry of the disc. The expected compressive axial stress at the disc rim was not captured in this measurement, although a balancing tensile region behind this is just observable. This was due to the need to avoid partial immersion of the large gauge volume, which would have caused the generation of pseudo-strains [7]. Hence the first measurement point is 8mm from the surface.

Beyond this region, moving towards the bore, the stress profile becomes flat, with a roughly constant value of -375MPa. This is a surprising result since disc like geometries are only expected to have significant non-zero axial stress in the rim region, due to edge effects [24]. The issue of non-zero axial stress in disc like geometries has been discussed in the literature [25], and suggested to be the result of residual microstress built up in a particular reflection. Microstresses develop in polycrystalline materials due to elastic and plastic anisotropy. During loading, the stiffness of each grain depends on its orientation to the loading direction, and thus corresponds to the strain accommodated. Upon unloading a residual microstrain develops as neighbouring grains unload strains of a differing magnitude. The stresses resulting from the microstrain are superposed onto that of the bulk [26].

Whilst microstress may be a contributing factor to non-zero axial stress, the Ni (311) reflection is known to exhibit a low sensitivity to this effect, making any contribution small. In addition, the extracted macro-stress free cube will still have contained the microstress field, thus the measured difference between the sample and reference value should be that of the bulk macro-strain only.

In the hoop direction the ageing heat treatment has relaxed tensile stresses in the bulk by up to 450MPa, and compressive stresses at the rim by up to 200MPa. The level of relaxation is reduced at 57mm and 65mm to 280MPa and 40MPa respectively. This indicates that the level of relaxation is likely to be related to the initial residual stress state in terms of level of plasticity, and relaxed via creep [27]. However, at 73mm, ageing appears to have increased the residual stress by at least ~140MPa. Since this is also in strong agreement with S2 contour data at the same location (Figure 8a), it is unlikely that this is an erroneous result in the S2 measurement. Notably, the profile after ageing is quite

different to that after quench; a 'peak-like' feature is seen at 65-73mm which was previously not visible.
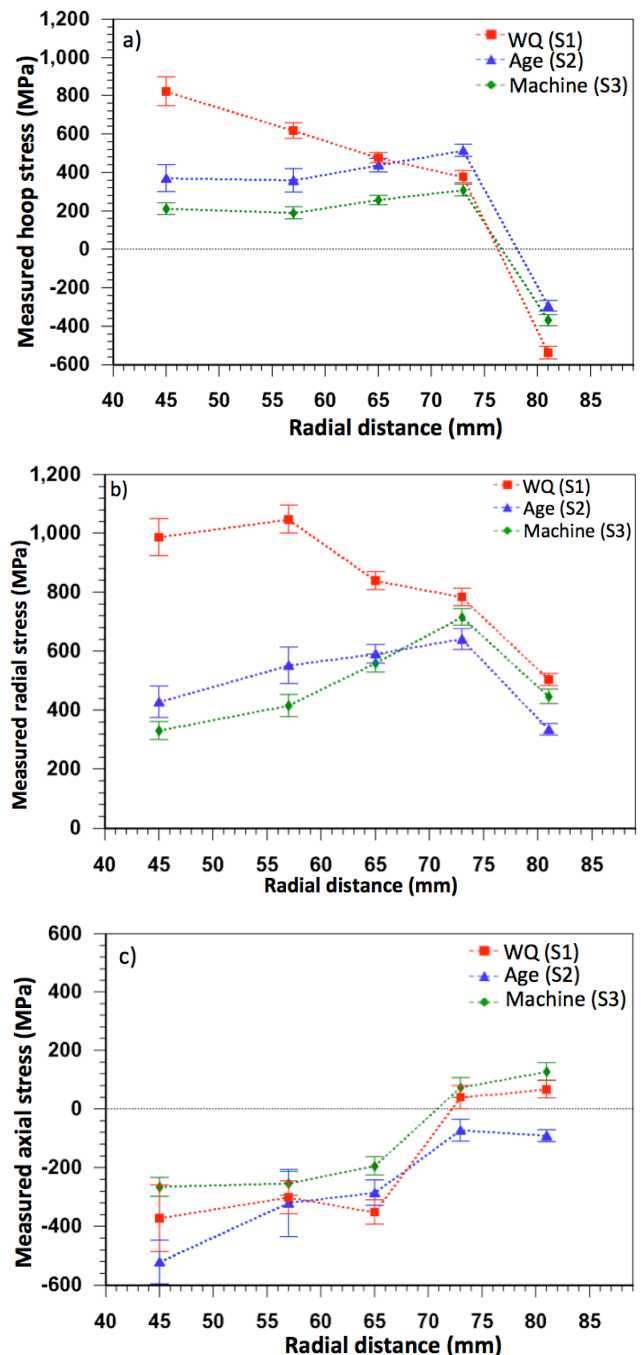
Figure 7: Residual stress as a result of quenching, ageing and machining in the a) hoop, b) radial, and c) axial direction of a sub-scale disc forging. Lines are a guide for the eye only.

Two possibilities for this result offer themselves for consideration. Firstly that the quench process in S2 differed significantly to S1 and that this generated a different initial profile, which remained even after ageing. This is unlikely however since great care in processing was taken to avoid this, and the level of variation to cause this result would be significant. The other possibility is that ageing causes a complex redistribution of residual stress, which

has been observed here in the hoop direction. Further investigation of this behaviour could be carried out by re-measuring a quenched sample after ageing to remove any sample to sample variation.

Radially, the ageing heat treatment has relaxed stresses by up to 550MPa in the near bore regions. As was the case in the hoop direction, larger quench stress has again led to increased relaxation during age. However, ageing does not appear to increase the residual stress at any location, although it does still alter the profile.

In comparison the axial direction exhibits very little relaxation from the ageing treatment, which corresponds to the lower initial residual stress from quench. The apparent increase in residual stress following age at 45mm can be discounted once errors are taken into account. The particularly long path length in the axial direction at 45mm in S1 and S2 made larger uncertainty inevitable at this location.

The machining processes have reduced tensile hoop stress in the bulk by 150-200MPa across the 45-73mm line scan. This indicates that material machined from each face (0-57mm radial distance – Figure 1) has caused the bulk residual stress to re-balance. The removal of much of the compressive surface region has caused the tensile region in the sample core to reduce in magnitude in order to maintain equilibrium.

The effect of material removal on the radial stress in the 45-67mm range is much reduced in comparison to the hoop. It is possible therefore that the material removed did not contain such a strong stress field in the radial direction. It appears that the stresses at the 73mm and 81mm locations have increased slightly, despite the material removal being at least 16mm away. This suggests the re-balancing of residual stress following material removal may have far reaching effects.

The Contour Method
Contour method data allowed comparison of residual stress in the hoop direction using a completely independent technique and thus add significant weight to the experimental data set. The results for S2 (age) and S3 (Op1 machine) as measured by the contour method are compared to neutron diffraction data in Figure 8

The contour method **radial line scan** (Figure 8a) of S2 indicates peak tension at the bore and throughout most of the bulk, with a narrow compressive layer at the rim. Following machining (S3) much of this profile is retained although the stress magnitude reduces at almost every location. Notably, even though material was removed in the just ±57mm radius the stress rebalancing extends beyond this range through the whole of the sample. The contour method **axial line scan** (Figure 8b) shows reduction of tensile stresses by ~175MPa at the bore. At the rim (-12.5mm) stress falls by ~300MPa, but at the opposite rim (+12.5mm) they remain the same.

Figure 8a also compares contour data (line) to neutron diffraction data (discrete points) across the **radial line scan**. It is clear that in both S2 and S3 very strong agreement is seen between the two data sets. In the S2 the agreement is marginally worse, particularly close to the bore. This is associated with the larger bore cross-section of S2, which increased the neutron path length at the 45 and 53mm measurement locations. This effect is clearly visible in the larger error bars at these locations in comparison all other measurement points. Close to the rim the contour method data indicates an extremely steep stress gradient is present from

75-89mm, approximately 100MPa/mm. The agreement between neutron and contour method data in this region is therefore subject to an averaging of stresses over the neutron gauge volume. In this case strong agreement was achieved, however steep gradient measurements are usually less reliable when a large gauge is employed.

Some discrepancies exist between the contour method and neutron diffraction data in the **axial line scan**. Whilst a correlation is maintained near the centre line, this is reduced in proximity to the surface. In particular the neutron diffraction data at ±9.5mm in both samples is more compressive than that measured using the contour method.
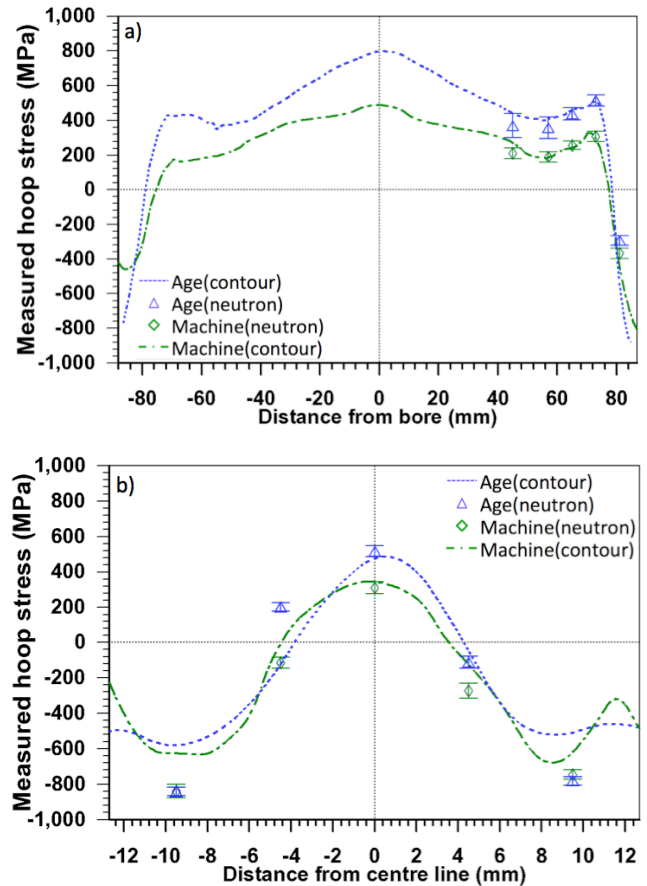
Figure 8: Hoop residual stress distributions over a) a radial line scan at the centre thickness and b) an axial line scan at 73mm radial distance, in S2 and S3 as measured by the contour method and by neutron diffraction.

The trends observed in the contour data are highly symmetric about the bore and about the centre thickness, particularly in the aged sample (S2). From this result it is inferred that the quench and ageing heat treatments were carried out reasonably homogeneously at each surface. The only exception to this trend is seen in S3 at the rim; from -80mm to the rim (-89mm) the residual stress appears to level off and then marginally increase. Since this profile is not observed at the other rim, or at all in the other sample it is suspected that this result be anomalous. The wire cutting direction was recorded and it is known that at this location the wire was leaving the sample. It is possible that as the wire exited the sample, it could have moved in the clamp, or that

some transient effect of the cutting process may have affected the surface contour at this position.

Finite element modelling
Simulated residual stress profiles across the centre-thickness radius, have been modelled in the hoop, radial and axial directions (Figure 9). Each profile has been compared to all available experimental data.

In the hoop direction, the simulated quench stress matches well with experimental data at the neutron diffraction locations. At the bore, simulated quench stresses reach 1400MPa, which exceeds yield in this material. However, once the other two directions are taken into account, the Von-Mises stress is found to peak at ~1100MPa at the bore; below yield. Following age, the simulated data is compared to both the contour and neutron diffraction data sets. The contour and neutron data clearly correlate very strongly, but this can only be said of the model at the 45, 57 and 81mm locations. At 65-73mm the model under-predicts the post-age stress in such a way as to miss a peak-like feature in the experimental data. At the bore and the rim the model also under-predicts the residual stress in comparison to experimental data. Such a discrepancy may be the result of the modelled creep behaviour, which is currently only well defined in a post age microstructure rather than as-quenched.

The material removal following machining was predicted to reduce stresses in the bore region, and marginally increase them in the rim region. The experimental data agrees with this overall trend, although localised variations captured by the neutron and contour techniques are not visible in the simulated data. At the bore the model still under-predicts the magnitude of residual stress, although the level of relaxation from S2 to S3 is well matched. Interestingly, at the 73mm location both S2 and S3 experimentally exhibit a similar peak-like feature not observed in the model. Since the two samples were measured identically but independently, the measured feature at 73mm seems to be real. Clearly this is not observed in the simulated data which points to an issue in the ageing model. The fact that the machining model did not match this result in S3 is not surprising, since the model used the as-aged model result as a starting point.

The radial stresses (Figure 9b) are generally well predicted throughout the processing stages. In the as-quenched condition (S1), the measured and simulated data sets follow the same trend, although discrepancy is clearly observed at the 45mm and 65mm locations. Without additional data it is not clear whether this is due to an issue with the experimental or simulated data. The ageing process is predicted to reduce residual stress by as much as 750MPa at the bore, and the nearest neutron measurement point in S2 indicates this to be an accurate prediction. Overall, agreement in the aged condition is high with the exception of the 73mm location, which is under-predicted in a similar way to that observed in the hoop direction. Given that quenched stresses are well predicted in both hoop and radial directions, it would appear that stress relaxation through ageing is not well simulated in this region of the disc.

Machining is predicted to reduce radial stress exclusively in regions from which material has been removed, i.e. over 0-57mm radial distance. Experimentally this is mostly borne out, as only the 45mm and 57mm data points show a reduction in stress following machining and the 65mm location shows no change. At 73mm and 81mm, the model predicts no change following machining whereas the neutron data showed a small increase in

stress. This indicates stress re-distribution following material removal may extend beyond the localised region, although this is not predicted in the radial direction.
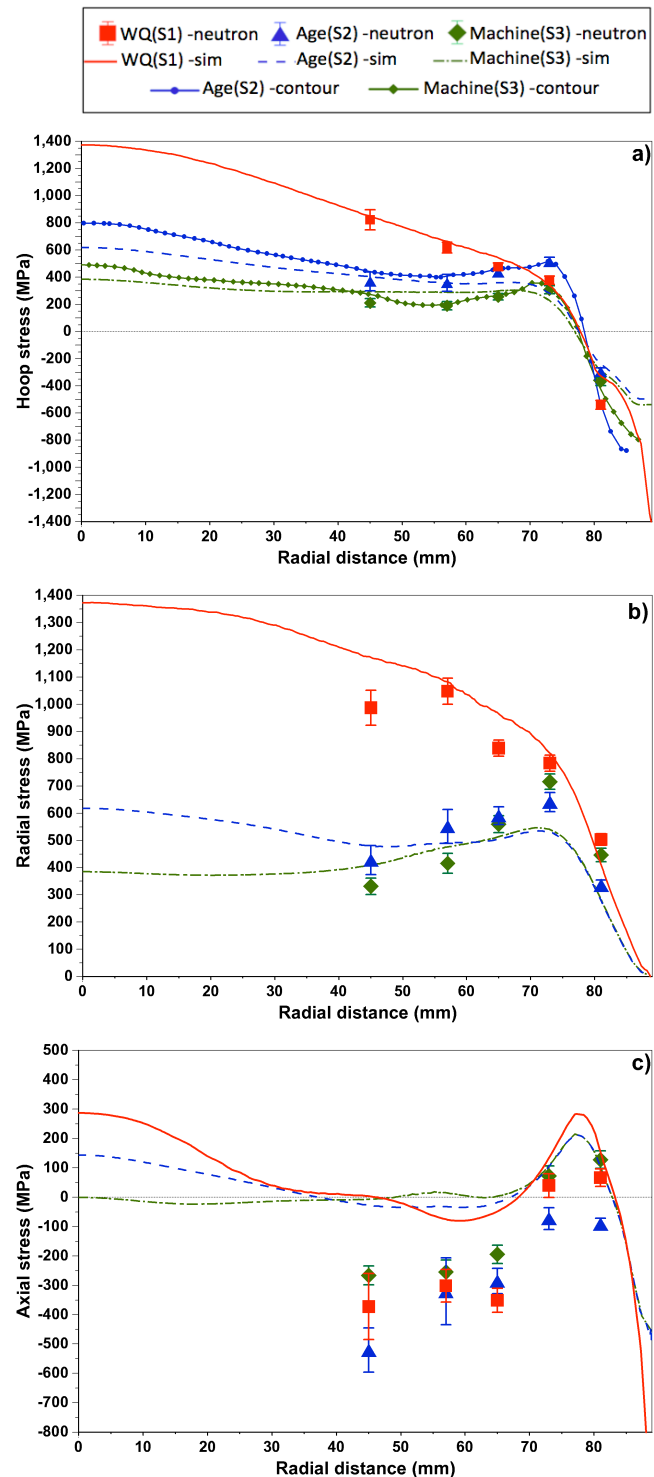

Figure 9: Simulated and experimental residual stress distributions over a radial line scan in the a) hoop b) radial and c) axial stress directions.

In the axial direction the simulated and experimental data sets generally show quite different trends. In the as-quenched

condition the two datasets match only at 73mm and 81mm radial distance; the region of balancing tensile stress behind the strongly compressive surface. The agreement here is relatively weak, but stress gradients around this feature are high. It is likely that neutron diffraction gauge volume averaging, due to spatial resolution of ~6mm along the scattering vector, has reduced agreement. Since the neutron measurements were not made closer than 8mm to the rim surface it is not possible to comment whether the modelled surface compressive region would have also been observed experimentally. However, since the tensile feature associated with the compressive surface is visible experimentally, it is reasonable to assume that the predicted trend at the surface is realistic.

From 0-67mm radial distance, the predicted and measured quenched stresses are markedly different in magnitude. Whilst the model predicts tension at the bore slowly falling to near zero at 45mm radial distance, the experimental data is strongly compressive over the 45-67mm region. The same discrepancy is seen here in both the aged and machined samples, which suggests this result is not a measurement, or model user-setup error. In earlier discussion it was highlighted that residual microstresses are unlikely to be the cause of the experimental values seen here. Ideally, more experimental data would be available from 0-45mm radial distance to fully characterise this behaviour, however neutron pathlengths within the thicker cross-section were prohibitively long.

Ageing is predicted to relax bore tensile stress by ~120MPa, rim compressive stress by ~300MPa, and the tensile peak (73-81mm) by ~100MPa. Experimental data was not obtained for the bore/rim regions due to pathlength, and near surface issues in the neutron diffraction experiment. At the tensile peak the measured change in stress, following age, is felt to be unrealistic in magnitude. Given the low axial stress in this region it would be expected that neither ageing nor machining would have a large impact on stress relaxation at the 73-81mm measurements locations. S1 and S3 agree with the expected behaviour, as does the model, it is therefore particularly surprising that S2 does not. Since peak fitting errors are low close to the rim, and a more than adequate d_0 characterisation was carried out, it is illogical to cite a measurement error in this instance. Given that the discrepancy is relatively minor, and within a region of rapidly changing stresses by virtue of being close to the rim; it is felt that minor process variations are likely to have generated this result.

The machining operation removed material to reduce the axial cross-section over the 0-57mm radial distance. The simulated results (Figure 9c) indicate that removal of this material reduces the cross-section to the point that axial stresses fall from ~100MPa to zero for much of the bore region. No experimental data was obtained for the 0-45mm region, but from the data obtained beyond this point it appears unlikely that the axial stress datasets would agree here. In the regions were experimental data was obtained (45-81mm), the absolute values in S3 differ to the simulation, most likely due to the original discrepancy in S1. However the negligible level of relaxation, following material removal, does approximately correlate in both the simulated and experimental data.

5. Conclusions

In this article, residual stresses in three sub-scale disc geometries of the nickel superalloy RR1000 have been characterised following key manufacturing processes. Experimental datasets obtained using the neutron diffraction and contour method techniques have been compared to finite element modelled predictions. Based on the results obtained, the following conclusions can be drawn.

1. It was possible to use neutron diffraction to map the generation and subsequent redistribution of bulk residual stress in sub-scale discs through the quenching, ageing, and machining processes.

2. In the disc geometries measured, hoop and radial stresses were significantly larger than axial stresses post quench. As a consequence, the ageing process had the greatest impact on residual stress relaxation in the hoop and radial directions.

3. The contour method of measuring residual stress was demonstrated to agree very strongly with the neutron diffraction technique in the as-aged and machined conditions. The full diameter stress profiles generated by the contour method highlighted the strongly axi-symmetric stress distribution in the hoop direction.

4. Thermocouple trials were used to derive a heat transfer coefficient curve for water quenching. The curve was scaled up at each surface using the inference method to match measured and simulated bulk residual stress values. The subsequent modelled cooling rates were found to match well with the original thermocouple trial data, thus validating this approach.

5. Finite element modelling predictions generally correlated well with experimental data; a number of observations were made:
   a. Quench stresses were very well predicted in the hoop direction across the centre line scan. In the radial direction some discrepancy was visible at the 45mm and 65mm measurement locations.
   b. The predicted hoop stress post age differed from both, the contour and neutron diffraction data, in a number of locations. This was also observed to a lesser extent in the radial direction. A possible source of error was identified in the currently available creep data.
   c. The residual stress following machining was well predicted in the hoop direction, showing stronger agreement with both the neutron and contour data. At the bore the stresses were under-predicted by ~100MPa, but the level of relaxation was well matched to experimental data.
   d. In the radial direction the effect of machining was largely localised to the region of material removal. Measured values did indicate some stress redistribution beyond the localised region, which was not predicted in the model.
   e. The axial direction showed the worst overall agreement between simulated and measured residual stress in every sample. Away from the rim the model predicted near zero stresses whereas the measured data indicated compression up to 400MPa. However, both the simulated and measured results indicated the ageing and machining processes had little effect on the residual stress profile in this direction.

The next stages of this research should be targeted towards understanding the observed discrepancies between the measured and simulated values presented here. In particular the relaxation

of residual stresses during an ageing heat treatment, which resulted in differing profiles in the predicted and measured results in the hoop and radial direction. To facilitate this, the use of in-situ ageing measurement capabilities may be required to reduce sample processing variations and therefore to fine-tune the ageing model. The poor agreement in the axial direction is highly significant since stresses are of very different magnitude and the opposite sign. Such a result requires more experimental data in the bore region to fully characterise this issue. Finally, in order for quenching simulations to be well tested and improved, it is necessary for the HTC curve to be defined independently a priori. Once this has been achieved, detailed comparisons can be made between the measured and predicted stress profiles following quenching. In the long term, this will lead to an improved capability in forward-predicting residual stresses throughout manufacture.

REFERENCES

[1]   Hardy MC, Zirbel B, Shen G, Shankar R. Developing damage tolerance and creep resistance in a high strength nickel alloy for disc applications. Superalloys 2004:83-92.

[2]   Ball DL, Tom BK, Bucci RJ, James MA. Toward Understanding the Impact of Bulk Residual Stress on the Life, Weight and Cost of Primary Aircraft Structure. Residual Stress Summit. Tahoe City, CA, 2010.

[3]   Schajer GS. Residual Stresses: Measurement by Destructive Testing. Encyclopedia of Materials: Science and Technology. Elsevier, 2001. p.8152-8158.

[4]   Hutchings MT, Withers PJ, Holden TM, Lorentzen T. Introduction to the Characterization of Residual Stress by Neutron Diffraction. London: Taylor and Francis, 2005.

[5]   Lodini A. Analysis of Residual Stress by Diffraction using Neutron and Synchrotron Radiation. London: Taylor and Francis, 2003.

[6]   Prime MB. Cross-sectional Mapping of Residual Stresses by Measuring the Surface Contour After a Cut. Transactions of the ASME 2001;123:162-168.

[7]   Withers PJ, Bhadeshia HKDH. Residual Stress Part 1 - Measurement Techniques. Materials Science and Technology 2001;17:355-365.

[8]   Hofmann M, Schneider R, Seidl GA, Rebelo-Kornmeier J, Wimpory RC, Garbe U, Brokmeier H-G. The new materials science diffractometer STRESS-SPEC at FRM-II. Physica B 2006:1035-1037.

[9]   Stone HJ, Holden TM, Reed RC. Determination of the plane specific elastic constants of waspaloy using neutron diffraction. Scripta Materialia 1999;40:353-358.

[10]   Withers PJ, Preuss M, Steuwer A, Pang JWL. Methods for obtaining the strain-free lattice parameter when using diffraction to determine residual stress. Journal of applied crystallography 2007;40:891-904.

[11]   Pirling T, Bruno G, Withers PJ. SALSA--A new instrument for strain imaging in engineering materials and components. Materials Science and Engineering: A 2006;437:139-144.

[12]   Rolph J, Iqbal N, Preuss M, Hofmann M, Evans A, Ganesan M. The Effect of d0 Reference Value on a Neutron Diffraction Study of Residual Stress in a Gamma/Gamma Prime Nickel-base Superalloy. (Submission in process) 2012.

[13]   Grant B, Elisabeth K, Preuss M, Quinta da Fonseca J, Daymond MR. The Effect of Lattice Misfit on Deformation Mechanisms at High Temperature. Advanced Materials Research 2011;278:144-149.

[14]   Wimpory RC, Ohms C, Hofmann M, Schneider R, Youtsos AG. Statistical Analysis of residual stress determinations using neutron diffraction. International Journal of Pressure Vessels and Piping 2009:48-62.

[15]   Prime MB, Kastengren AL. The Contour Method Cutting Assumption: Error Minimization and Correction. Proceedings of the SEM Annual Conference & Exposition on Experimental and Applied Mechanics Indianapolis 2010.

[16]   Mathworks. MATLAB 7.10. Natick, MA., 2010.

[17]   SIMULIA. ABAQUS Software. Rising Sun Mills, 166 Valley Street, Providence, RI., 2011.

[18]   Frankel PG. Residual Stresses in Aerospace Components. Material Science, vol. EngD. Manchester: University of Manchester, 2008. p.38-40.

[19]   Prime MB, Sebring RJ, Edwards JM, Hughes DJ, Webster PJ. Laser surface contouring and spline data smoothing for residual stress measurement. Experimental Mechanics 2004;44:176-184.

[20]   Bibby GP. Compressor Engineering SCO3 Radial Displacement Plot Facility. Rolls-Royce, 1998.

[21]   Hesketh G, Goetz R, Matlik J, Shen G. Disc Residual Stress Modelling. Rolls-Royce plc, 2011.

[22]   SIMULIA. iSight Optimization software. Rising Sun Mills, 166 Valley Street, Providence, RI., 2011.

[23]   Dye D, Conlon KT, Reed RC. Characterization and Modeling of Quenching-Induced Residual Stresses in the Nickel-Based Superalloy IN718. Metallurgical and Materials Transactions A 2004;35A:1703-1713.

[24]   Fletcher AJ, Lewis C. Effect of free edge on thermal stresses in quenched steel plates. Materials Science and Technology 1985;1:780-785.

[25]   Cihak U, Staron P, Clemens H, Homeyer J, Stockinger M, Tockner J. Characterization of residual stresses in turbine discs by neutron and high-energy X-ray diffraction and comparison to finite element modeling. Materials Science and Engineering A 2006;437:75-82.

[26]   Dye D, Stone HJ, Reed RC. Intergranular and interphase microstresses. Current Opinion in Solid State Materials Science 5 2001:31-37.

[27]   Zhou Z, Gill AS, Qian D, Mannava SR, Langer K, Wen Y, Vasudevan VK. A finite element study of thermal relaxation of residual stress in laser shock peened IN718 superalloy. International Journal of Impact Engineering 2011;38:590-596.

Chapter 10

Conclusions and Future Work

The work presented in this thesis concerns the development of residual stress through the manufacturing process of aero-space forgings, specifically, the turbine disc. As a result of this thesis being presented in the alternative format, it is recognised that the individual publications already have a concluding section. As such, the conclusions made here concern the project as a whole, drawing upon each of the publications to form a broader set of conclusions. This section also seeks to tie in the publications into a succinct discussion, as a result the following conclusions go into more depth than is typical.

The conclusions from each of the publications can be split into two sub-categories: conclusions, which can be drawn about the methods used, and conclusions which can be drawn about the results obtained.

10.1 Methods-based conclusions

10.1.1 Experimental methods

The experimental characterisation of residual stress consisted of the neutron diffraction and contour method techniques. By following the procedures outlined in Chapter 2 it was possible to use neutron diffraction to determine bulk residual stress in RR1000 with a pathlength of 35mm to an accuracy of ±30MPa in acquisition times of no greater than 90 minutes. It should be noted however that the alloy contained appreciable levels of Cobalt (18.5wt%), which are highly neutron absorbing and therefore increased the acquisition times. Other common nickel-base superalloys such as Udimet 720Li, Waspaloy and Inconel 718 should display shorter counting times in comparison. The contour method was employed as detailed in Chapter 2, and provided a full 2D map of the hoop stresses in seven of the disc forgings. The stress data generated by the contour method showed exceptionally good agreement to the neutron diffraction data, indicating that both techniques were able to reliably characterise the stress. However the contour method was found to be less reliable in regions close to the wire exit in the most highly stressed samples such as the water and oil quenches. It is likely that the high stresses were a factor in this since it

increases the forces attempting to move the sample in the clamps, and the effects of plasticity at the cut tip.

The neutron diffraction technique required the determination of the strain-free lattice spacing (d_0). A separate study was conducted using laboratory x-rays in the $\sin^2\psi$ technique (Chapter 4) to provide a value for d_0, and assess whether the value varied by location within the forging. A number of important methodological conclusions were drawn from this study:

- A d_0 variation could be observed across a water quenched forging, and to a much lesser extent an aged forging. If not taken into account, the change in d_0 value could create an error in the measured stress of up to 200MPa in a water quenched component. However, the variation was found to be limited to the near surface (~5mm), meaning that little variation and hence little impact on the measured stress was observed in the bulk region.

- Values of d_0 as measured by the x-ray diffraction instrument could not be used directly in a strain calculation using neutron diffraction d-spacings. Stress calculated in such a way had a consistent offset of ~400MPa in comparison to stresses calculated using alternative d_0's or the contour method. It is thought that this is the result of the negative neutron scattering properties of titanium, which makes up 3.6wt% the alloy, thus creating an offset between the x-ray and neutron diffraction data.

- Although the x-ray derived d_0 could not be used directly in a strain calculation, it was possible to use the measured variation as a position dependant correction factor to a global d_0 value if required.

- A global d_0 such as that obtained by a macro-stress free cube can be used for a heat treated forging with a minimal impact on the measured stress providing measurement locations are not close to the surface.

The neutron diffraction technique was developed further by implementation of a novel in-situ heat treatment setup for large components (Chapter 5). The setup enabled ageing to be carried out at 760° and 820°C for 8 hours while measuring strain. The results from this study indicated a possible time resolution of 15 minutes, and an uncertainty in measured stress of ±50MPa when measuring through 35mm of

RR1000. By carrying out a repeat measurement, the setup was found to be a reliable means to measure stress relaxation through heat treatment in-situ.

10.1.2 Simulation methods

The simulation of residual stress development was carried out using a finite element (FE) model as detailed in Chapter 3. Prior to the calculation of stresses it was necessary for studies to be carried out to thermally characterise the heat treatment processes of quenching and ageing. From the approach taken and the results obtained, it is possible to make the following concluding remarks about the method:

- Thermal characterisation of the quenching process was made using five embedded thermo-couples in a sub-scale disc forging to derive a heat transfer coefficient (HTC) which was applied as a surface boundary condition. However, while the derived HTC followed a logical profile, it was too low in magnitude to extract heat at a fast enough rate due to the fact that the embedded thermo-couples were not close enough to the surface. As such, it is reasonable to conclude that in order to improve the derivation of an accurate HTC, the placement of thermo-couples must include locations as close the surface as possible.

- Despite the derived HTC being of reduced magnitude, it was demonstrated that the use of an additional weighting factor multiplied by the entire curve could provide an accurate thermal simulation of the quench. An optimisation loop was setup to repeatedly run a thermal model using different weighting factors until a solution was arrived upon whereby the simulated cooling matched that measured using the embedded thermo-couples.

At present the approach for predicting quenching stress cannot be said to be entirely 'forward predicting'. The model requires experimental thermal data in order for an optimisation loop to be run to generate weighting factors to bring the model in to line with the actual process. If any of the quenching parameters were to change, such as component geometry, quenchant, or heat treatment temperature, it would be necessary for a new set of weighting factors to be established.

The simulation of ageing differed from that of quenching since the heating and cooling rates were slow enough to model the age by simply altering the temperature of the part as a whole, without the need for heat transfer at the surface. This therefore

represented a forward predicting aspect of the model since the stresses could be calculated without reference to an experimental characterisation of the process. However, if the cooling rate from age was increased by for instance oil or water quenching, the procedure would have to revert to that of the quench model, i.e. derivation of HTCs for a surface boundary condition.

10.2 Results-based Conclusions

Three manufacturing processes were investigation in terms of the development of residual stress, namely, quenching, ageing and machining. Residual stress characterisation was completed using two independent experimental techniques (contour method, neutron diffraction) in addition to a finite element simulation and microstructural characterisation. Taking into account all of the observations made it is possible to make the following concluding remarks.

The residual stress distribution, which resulted from quenching was found to be that of a compressive surface surrounding a tensile core. Furthermore the stress distribution was observed to be largely axi-symmetric in each quench. The peak stresses were observed to correlate well with the quench media, having values of approximately 200MPa, 900MPa and 1200MPa in the still-air, oil and water quenches respectively. The impact on the γ/γ' microstructure was equally distinct with the most observable change being that of the secondary γ' size which had typical values of 110nm in air, 60nm in oil and 30nm (uni-modal) in water. The modelling of quench induced stress and the comparison of results to experimental data highlighted the following:

- The residual stress resulting from the still-air quench was under-predicted by the model in comparison to either experimental technique. It was determined that this was the result of the material property database, which did not account specifically for the low strains generated in the still-air quench. The significantly coarsened γ' microstructure in the still-air quench also represented a departure from the model in terms of the material property database, and thus contributed to this discrepancy.
- The oil quenched residual stress profile was very well predicted by the model in all stress directions when assuming isotropic strain hardening. The model was initially setup to model the strain hardening isotropically, subsequently an

mroz multi-layer model was also run to assess whether reverse yielding of the material required the inclusion of a Bauschinger effect. However, from the data produced it was clear that the inclusion of a Bauschinger effect significantly reduced the correlation to experimental data. It was therefore concluded that the strain hardening behaviour during an oil quench could be simulated isotropically.

- As was the case with the oil quench, the water quenching model was run twice, once with an isotropic hardening law, and once with an mroz multi-layer hardening law. On comparing the predictions to the experimental data, it was evident that the isotropic model had over-predicted, and the mroz multi-layer model under-predicted, the residual stress. The level of over/under prediction was such that it was not possible to deduce which hardening law was more appropriate for the water quench. Based on this result, it was concluded that the actual hardening process was a mixture of the isotropic and mroz multi-layer laws employed, meaning that the two models could be treated as upper and lower bounds on the predicted residual stress.

The comparison between simulated and experimentally characterised residual stress now moved onto ageing. In this investigation the ageing heat treatments were always carried out on a component, which had already been water quenched in order to first generate high levels of residual stress which could be relaxed during the heat treatment. Since the water quenching simulations were made using the isotropic and mroz multi-layer hardening laws as upper and lower bounds, the ageing process was also modelled twice, once for each starting stress distribution resulting from each hardening model. The results from in-situ and ex-situ experimental characterisations as well as those generated through finite element modelling allow the following conclusions to be drawn:

- The two starting stress distributions resulting from the mroz multi-layer and isotropic water quenching models were aged at 760°C for periods of 15, 60, and 120 minutes to compare to ex-situ experimental data. After a 15 minute age at 760°C the isotropic stress fell from 1300MPa to 600MPa, while the mroz multi-layer stress fell from 800MPa to 600MPa. It is therefore apparent from the data that the very different stress levels predicted by the two hardening laws rapidly converged to a common stress value as a result of

ageing. Such a trend indicates that the driving force for stress relaxation is related to the immediate value of the residual stress.

- Throughout all of the 760°C ageing heat treatments, a comparison between the experimental and simulation data indicated a very strong tendency for the model to over-predict the level of stress relaxation. Using the in-situ relaxation data (Chapter 8), the contrast in simulated and experimental behaviour was clear. While the model predicted a large primary creep stage the experiment data did not. Since the model was thermally accurate to the in-situ experiment, and the starting stresses very similar, this pointed to the modelled material having a lower creep strength than that of the experimental forging. One possible explanation for this was that the water quenched microstructure was not typical of a manufactured component, and therefore not well characterised in the material property database in terms of creep strength.

- At an age temperature of 820°C the measured stress relaxation differed to the 760°C age by exhibiting significant primary creep relaxation. A comparison of the 760°C and 820°C aged microstructures signalled a clear increase in the number of secondary γ′ particles as a result of the higher age temperature. It is thought that this was the result of highly coarsening tertiary γ′, and that this brought with it an increase in the inter-particle spacing and a corresponding reduction in the creep strength at the higher temperature (100).

- The change in microstructure at 820°C correlates with an improved agreement between the model and the experiment. It is therefore possible that the observed microstructural change has resulted in a material, which is more in line with the material properties of the model; in particular a reduction in creep strength.

The final manufacturing process characterised in this study, in terms of residual stress development, was that of material removal by machining. The observed behaviour in the experimental and simulated data has led to the following conclusions:

- The machining process carried out on the large disc forgings (Chapter 9) removed large regions of compressive hoop and radial stress (Appendix 1). The remaining stresses re-balanced, with stresses of the opposite sign to those, which were removed being reduced in order to maintain equilibrium.

This resulted in a fall in tensile hoop and radial stress in bore region of up to 300MPa.

- The re-balancing of stress was not limited to the locality of material removal. In this particular measurement, hoop stress was found to re-balance across the entire component.

10.3 Recommendations For Future Work

Ultimately the aim of this work is to improve the understanding of residual stress development through the manufacturing processes with a view to improving the capabilities of stress predicting models. In the ideal case, the prediction of residual stress should be 'forward predicting' – meaning that the stresses resulting from a manufacturing process can be accurately predicted simply by clearly defining the process in the model. Comparing current residual stress predictions to the results obtained in studies such as this allow the shortcomings in the current modelling capability to be identified. Based on these findings it is possible to target areas for improvement and move one step nearer to an accurate forward-predicting stress model.

10.3.1 Characterisation of heat transfer

The conclusions drawn about the finite element methodology highlighted the fact that the simulation of quenching stress was not a forward predicting aspect of the model. Central to this simulation was the use of a heat transfer coefficient (HTC) which governed the rate at which heat was transferred from the sample surface to the quenchant. Heat also flowed through the sample bulk from the interior to the surface as the sample cooled. This was simulated using a coefficient of thermal conduction specific to the material. Thermally, these are the only parameters, which dictate the way in which the component cools, and therefore the thermal gradients which are setup. The thermal conduction will only vary by the component material, and is thus relatively easy to characterise for a given component quench. In contrast to this, the HTC can vary by component geometry/orientation, heat treatment temperature, quenchant, and the quench tank arrangement (i.e. size, agitation).

The key to creating a thermally accurate model is therefore to improve the understanding of the HTC during quenching. In the ideal case it should be possible to alter component geometries and quench tank arrangements and still be able to

accurately predict the HTC and therefore the quenching stress. Such a capability could be developed by modelling the quench in terms the fluid dynamics of the quenchant and comparing the predicted HTC to that captured using surface mounted thermo-couples.

10.3.2 Modelled material behaviour

The contour method and neutron diffraction techniques used in this study have been shown to have strong agreement with each other, indicating a robustness to the approach taken in each case. Furthermore, both techniques characterised the residual stress deep within the bulk of the forging, and with an uncertainty of no greater than ±50MPa. As such, the residual stress values obtained experimentally have been quoted with high confidence, and any discrepancy with the model scrutinised.

From the conclusions drawn in the previous section, three significant discrepancies are identified, namely, the under-prediction of air-cooled stress, the issue of hardening law in water quenching and the level of creep induced stress relaxation during ageing. Since each of these models was known to be thermally accurate to the process, the cause of the discrepancy must be a result of the mechanical model and the associated material property database. The next stages of this project should therefore be to implement further material characterisation to address these issues to see if an improvement could have been seen in the predictions.

10.3.3 Characterisation techniques

The neutron diffraction technique was developed further as part of this investigation by carrying out a large scale in-situ heat treatment to measure stress relaxation through ageing. The data generated and presented in this thesis is some of the first obtained from a larger component and therefore opens the door for future studies of a similar nature. Further studies made using this technique may be able to achieve even faster acquisition times by making measurements in thinner sections, or by measuring materials which are less absorbing of neutrons. As seen in the present work, the residual stress data recorded during the in-situ experiment showed some significant scatter. The particular interest from such an in-situ experiment in respect of model validation is that it should enable one to follow the exact stress relaxation at a particular point in the component. Hence a comparison between experimental and modelling data could focus on the stress relaxation rate rather than only absolute

values. It is worth mentioning that these very first in-situ aging experiments carried out on ENGIN-X have been used to make a case for a new PhD project funded by the ILL to develop such in-situ experiments at the strain imaging beam line SALSA. This project is due to start in October 2012.

References

1. Winholtz RA. Residual Stresses: Macro and Micro Stresses. Encyclopedia of Materials: Science and Technology (Second Edition). Oxford: Elsevier; 2001. p. 8148-51.
2. Hossain S, Daymond MR, Truman CE, Smith DJ. Prediction and measurement of residual stresses in quenched stainless-steel spheres. Materials Science and Engineering: A. 2004;373(1–2):339-49.
3. Hammersley G, Hackel LA, Harris F. Surface prestressing to improve fatigue strength of components by laser shot peening. Optics and Lasers in Engineering. 2000;34(4-6):327-37.
4. Smallman RE, Ngan AHW. Chapter 8 - Advanced alloys. Physical Metallurgy and Advanced Materials Engineering (Seventh Edition). Oxford: Butterworth-Heinemann; 2007. p. 447-80.
5. Bouchard PJ. Residual Stresses in Lifetime and Structural Integrity Assessment. Encyclopedia of Materials: Science and Technology. Oxford: Elsevier; 2001. p. 8134-42.
6. Carnot S, Fox R. Reflexions on the motive power of fire: Manchester University Press; 1986.
7. Lodini A. Calculation of Residual Stress from Measured Strain. Analysis of Residual Stress by Diffraction using Neutron and Synchrotron Radiation. London: Taylor and Francis; 2003. p. 47-58.
8. Hutchings MT, Withers PJ, Holden TM, Lorentzen T. Introduction to the Characterization of Residual Stress by Neutron Diffraction. London: Taylor and Francis; 2005.
9. Winholtz RA. Characterization of Macrostresses. Analysis of Residual Stress by Diffraction using Neutron and Synchrotron Radiation. London: Taylor and Francis; 2003. p. 60-6.
10. Dye D, Conlon KT, Reed RC. Characterization and Modeling of Quenching-Induced Residual Stresses in the Nickel-Based Superalloy IN718. Metallurgical and Materials Transactions A. 2004;35A(June):1703-13.
11. Withers PJ, Bhadeshia HKDH. Residual Stress Part 2 - Nature and Origins. Materials Science and Technology. 2001;17:366-75.
12. Oliver EC, Mori T, Daymond MR, Withers PJ. Neutron diffraction study of stress-induced martensitic transformation and variant change in Fe–Pd. Acta Materialia. 2003;51(20):6453-64.
13. Prevey PS, Shepard MJ, Smith PR. The Effect of Low Plasticity Burnishing (LPB) on the

HCF Performance and FOD Resistance of Ti-6Al-4V. Proceedings: 6th National Turbine Engine High Cycle Fatigue (HCF) Conference. 2001:10.
14. Withers PJ, Bhadeshia HKDH. Residual Stress Part 1 - Measurement Techniques. Materials Science and Technology. 2001;17:355-65.
15. Pritchard SE. The use of ultrasonics for residual stress analysis. NDT International. 1987;20(1):57-60.
16. Buttle D, Scruby C. Residual Stresses: Measurement using Magnetoelastic Effects. In: Editors-in-Chief: KHJB, Robert WC, Merton CF, Bernard I, Edward JK, Subhash M, et al., editors. Encyclopedia of Materials: Science and Technology (Second Edition). Oxford: Elsevier; 2001. p. 8173-80.

17.	Novion CHd. The use of Neutrons for Materials Characterization. Analysis of Residual Stress by Diffraction using Neutron and Synchrotron Radiation. London: Taylor and Francis; 2003. p. 3-20.

18.	Cullity BD. Elements of X-Ray Diffraction. 2 ed. Reading, Massachusetts: Addison-Wesley; 1978.

19.	Hook JR, Hall HE. Solid State Physics: John WIley; 1991.

20.	SEA standard J784a, Residual Stress Measurement by X-Ray Diffraction1971.

21.	Stone HJ, Holden TM, Reed RC. Determination of the plane specific elastic constants of waspaloy using neutron diffraction. Scripta Materialia. 1999;40(3):353-8.

22.	Ezeilo AN, Webster GA, Webster PJ, Wang X. Characterisation of elastic and plastic deformation in a nickel superalloy using pulsed neutrons. Physica B: Condensed Matter. 1992;180–181, Part 2(0):1044-6.

23.	Webster GA, Youtos AG, Ohms C, Wimpory RC. Draft standard for the measurement of residual stresses by neutron diffraction. Recent Advances in Experimental Mechanics. 2002:467-76.

24.	Withers PJ. Residual Stresses: Measurement by Diffraction. In: Editors-in-Chief: KHJB, Robert WC, Merton CF, Bernard I, Edward JK, Subhash M, et al., editors. Encyclopedia of Materials: Science and Technology (Second Edition). Oxford: Elsevier; 2001. p. 8158-69.

25.	Quesnel DJ, Meshii M, Cohen JB. Residual stresses in high strength low alloy steel during low cycle fatigue. Materials Science and Engineering. 1978;36(2):207-15.

26.	Romero J, Attallah MM, Preuss M, Karadge M, Bray SE. Effect of the forging pressure on the microstructure and residual stress development in Ti–6Al–4V linear friction welds. Acta Materialia. 2009;57(18):5582-92.

27.	Arunachalam RM, Mannan MA, Spowage AC. Residual stress and surface roughness when facing age hardened Inconel 718 with CBN and ceramic cutting tools. International Journal of Machine Tools and Manufacture. 2004;44(9):879-87.

28.	Luo Q, Jones AH. High-precision determination of residual stress of polycrystalline coatings using optimised XRD-sin2ψ technique. Surface and Coatings Technology. 2010;205(5):1403-8.

29.	Steuwer A, Santisteban JR, Turski M, Withers PJ, Buslaps T. High-resolution strain mapping in bulk samples using full-profile analysis of energy-dispersive synchrotron X-ray diffraction data. Journal of applied crystallography. 2004;37(6):883-9.

30.	Rietveld HM. A profile refinement method for nuclear and magnetic structures. Journal of applied crystallography. 1969;2(2):8898.

31.	Pirling T, Bruno G, Withers PJ. SALSA--A new instrument for strain imaging in engineering materials and components. Materials Science and Engineering: A. 2006;437(1):139-44.

32.	Price JWH, Ziara-Paradowska A, Joshi S, Finlayson T, Semetay C, Nied H. Comparison of experimental and theoretical residual stresses in welds: The issue of gauge volume. International Journal of Mechanical Sciences. 2008;50(3):513-21.

33.	Daymond MR, Johnson MW, Sivia DS. Analysis of Neutron Diffraction Strain Measurement Data from a Round Robin Sample. Journal of Strain Analysis. 2002;37(1):13.

34.	Withers PJ. Mapping residual and internal stress in materials by neutron diffraction. C R Physique. 2007;8:806-20.

35.	Cihak U, Staron P, Clemens H, Homeyer J, Stockinger M, Tockner J. Characterization of residual stresses in turbine discs by neutron and high-energy X-

ray diffraction and comparison to finite element modeling. Materials Science and Engineering A. 2006;437:75-82.

36.   Wimpory RC, Ohms C, Hofmann M, Schneider R, Youtsos AG. Statistical Analysis of residual stress determinations using neutron diffraction. International Journal of Pressure Vessels and Piping. 2009(86):48-62.

37.   Withers PJ, Preuss M, Steuwer A, Pang JWL. Methods for obtaining the strain-free lattice parameter when using diffraction to determine residual stress. Journal of applied crystallography. 2007;40(5):891-904.

38.   Krempaszky C, Werner EA, Stockinger M, editors. Residual Stresses in IN718 Turbine Discs. Superalloys 718 and Derivatives; 2005: TMS.

39.   Beghini M, Bertini L. Recent Advances in the Hole Drilling Method for Residual Stress Measurement. Journal of Materials Engineering and Performance. 1998;7(2):10.

40.   Schajer GS. Residual Stresses: Measurement by Destructive Testing. Encyclopedia of Materials: Science and Technology: Elsevier; 2001. p. 8152-8.

41.   Prime MB. Cross-sectional Mapping of Residual Stresses by Measuring the Surface Contour After a Cut. Transactions of the ASME. 2001;123:162-8.

42.   Bueckner HF. The Propagation of Cracks and the Energy of Elastic Deformation. Transactions of the ASME. 1958;80:6.

43.   Prime MB. RESIDUAL STRESSES MEASURED IN QUENCHED HSLA-100 STEEL PLATE. Proceedings of the 2005 SEM Annual Conference & Exposition on Experimental and Applied Mechanics; Portland, OR USA2005.

44.   Kelleher J, Prime MB, Buttle D, Mummery PM, Webster PJ, Shackleton J, et al. The Measurement of Residual Stress in Railway Rails by Diffraction and Other Methods. Journal of Neutron Research. 2003;11(4):7.

45.   Brown DW, Holden TM, Clausen B, Prime MB, Sisneros TA, Swenson H, et al. Critical comparison of two independent measurements of residual stress in an electron-beam welded uranium cylinder: Neutron diffraction and the contour method. Acta Materialia. 2011;59(3):864-73.

46.   Prime MB, Gnäupel-Herold T, Baumann JA, Lederich RJ, Bowden DM, Sebring RJ. Residual stress measurements in a thick, dissimilar aluminum alloy friction stir weld. Acta Materialia. 2006;54(15):4013-21.

47.   Prime MB, Kastengren AL. The Contour Method Cutting Assumption: Error Minimization and Correction. Proceedings of the SEM Annual Conference & Exposition on Experimental and Applied Mechanics Indianapolis. 2010.

48.   Sommer C, Sommer S. Complete EDM handbook: Advance Pub; 2005.

49.   Hatamleh O, Lyons JED, Forman R. Laser peening and shot peening effects on fatigue life and surface roughness of friction stir welded 7075-T7351 aluminum. Fatigue & Fracture of Engineering Materials & Structures. 2007;30(2):115-30.

50.   Johnson G. Residual Stress Measurements using the Contour Method. Manchester: University of Manchester; 2008.

51.   Schoenberg IJ. Contributions to the problem of approximation of equidistant data by analytic functions, Part A - On the problem of smoothing of graduation, a first class of analytic approximation. Quarterly of Applied Mathematics. 1946;4:45-88.

52.   Frankel PG. Residual Stresses in Aerospace Components. Manchester: University of Manchester; 2008.

53.   Robert DC. Finite Element Modeling for Stress Analysis: John Wiley & Sons, Inc.; 1995.

54.   Ottosen NS, Ristinmaa M. The Mechanics of Constitutive Modeling: Elsevier; 2005.

55.   Needleman A, Van der Giessen E. Elasticity: Finite Element Modeling. In: Editors-in-Chief: KHJB, Robert WC, Merton CF, Bernard I, Edward JK, Subhash M, et al., editors. Encyclopedia of Materials: Science and Technology (Second Edition). Oxford: Elsevier; 2005. p. 1-6.

56.   Dye D, Roder B, Tin S, Rist M, James J, Daymond MR, editors. MODELING AND MEASUREMENT OF RESIDUAL STRESSES IN A FORGED IN718 SUPERALLOY DISC. Superalloys 2004; 2004; Pittsbirgh: TMS.

57.   Rist M, James J, Tin S, Roder B, Daymond M. Residual stresses in a quenched superalloy turbine disc: Measurements and modeling. Metallurgical and Materials Transactions A. 2006;37(2):459-67.

58.   Kassner ME, Geantil P, Levine LE, Larson BC. Backstress, the Bauschinger Effect and Cyclic Deformation. Materials Science Forum. 2008;604-605:39-51.

59.   Ottosen NS, Ristinmaa M. 12 - Common Plasticity Models. The Mechanics of Constitutive Modeling. Oxford: Elsevier Science Ltd; 2005. p. 279-319.

60.   Karadge M, Grant B, Withers PJ, Baxter GJ, Preuss M. Thermal Relaxation of Residual Stresses in Nickel-Based Superalloy Inertia Friction Welds. Metallurgical and Materials Transactions A. 2011;42(8):11.

61.   Tawfik D, Mutton PJ, Chiu WK. Experimental and numerical investigations: Alleviating tensile residual stresses in flash-butt welds by localised rapid post-weld heat treatment. Journal of Materials Processing Technology. 2008;196(1–3):279-91.

62.   Hossain S, Truman CE, Smith DJ, Peng RL, Stuhr U. A study of the generation and creep relaxation of triaxial residual stresses in stainless steel. International Journal of Solids and Structures. 2007;44(9):3004-20.

63.   Reed RC. The Superalloys - Fundamentals and Applications. Cambridge: Cambridge University Press; 2006.

64.   Williams JC, Starke Jr EA. Progress in structural materials for aerospace systems. Acta Materialia. 2003;51(19):5775-99.

65.   Sims CT, Hagel WC. The superalloys: Wiley-Interscience; 1972.

66.   Cumpsty N. Jet Propulsion: A Simple Guide to the Aerodynamic and Thermodynamic Design and Performance of Jet Engines: Cambridge University Press; 2003.

67.   Donachie MJ, Donachie SJ. Superalloys: A Technical Guide. 2 ed2003.

68.   Jackson MP, Reed RC. Heat treatment of UDIMET 720Li: the effect of microstructure on properties. Materials Science and Engineering: A. 1999;259(1):85-97.

69.   Mitchell RJ, Preuss M, Hardy MC, Tin S. Influence of composition and cooling rate on constrained and unconstrained lattice parameters in advanced nickel-base superalloys. Materials Science and Engineering. 2006;423:282-91.

70.   Gayda J, Gabb T, Kantzos P. Heat Treatment Technology for Production of Dual Microstructure Superalloy Disks2002 April 2002 Contract No.: NASA TM 2002-211558.

71.   Connor LD, Rae CMF, Mitchell RJ, Hardy MC, Lemsky J. Dual Microstructure Heat Treated Discs: Microstructural Characterisation. Power Generation in an Era of Climate Change; Glasgow, UK: Parsons; 2007. p. 321-32.

72.   Blobaum KJ, Van Heerden D, Gavens AJ, Weihs TP. Al/Ni formation reactions: characterization of the metastable Al9Ni2 phase and analysis of its formation. Acta Materialia. 2003;51(13):3871-84.

73.   Brooks CR. Heat Treatment, Structure, and Properties of Nonferrous Alloys: American Society for Metals; 1982.

74.   Nabarro F. Plastic deformation and fracture of materials. Edited by Haël Mughrabi, Volume 6 of Materials Science and Technology—A Comprehensive

Treatment, VCH, Weinheim 1992, 697 pp., hardback, DM 430, ISBN 3-527-26819-7. Advanced Materials. 1993;5(10):773-4.

75.	Reppich B. Particle Strengthening. Materials Science and Engineering, Volume 6: Plastic Deformation and Fracture1993. p. 311-57.

76.	Furillo FT, Davidson JM, Tien JK, Jackman LA. The effects of grain boundary carbides on the creep and back stress of a nickel-base superalloy. Materials Science and Engineering. 1979;39(2):267-73.

77.	Choudhury A. Vacuum metallurgy: ASM International; 1990.

78.	Benz MG. Preparation of Clean Superalloys. In: Briant CL, editor. Impurities in Engineering Materials: Marcel Dekker; 1999. p. 31-48.

79.	Gessinger GH, Bomford MJ. Modern Methods of Powder Metallurgical Processing of Superalloys. High Temperature Materials in Gas Turbines.345-79.

80.	Davis JR. Tool Materials: ASM International; 1995.

81.	Preuss M, Withers PJ, Baxter GJ. A comparison of inertia friction welds in three nickel base superalloys. Materials Science and Engineering: A. 2006;437(1):38-45.

82.	Brinksmeier E, Lübben T, Fritsching U, Cui C, Rentsch R, Sölter J. Distortion minimization of disks for gear manufacture. International Journal of Machine Tools and Manufacture. 2011;51(4):331-8.

83.	Hauk V. Structural and Residual Stress Analysis by Nondestructive Methods: Evaluation - Application - Assessment: Elsevier; 1997.

84.	Hofmann M, Schneider R, Seidl GA, Rebelo-Kornmeier J, Wimpory RC, Garbe U, et al. The new materials science diffractometer STRESS-SPEC at FRM-II. Physica B. 2006:1035-7.

85.	Withers PJ, Johnson MW, Wright JS. Neutron strain scanning using a radially collimated diffracted beam. Physica B: Condensed Matter. 2000;292(3–4):273-85.

86.	Santisteban JR, Daymond MR, James JA, Edwards L. ENGIN-X: a third-generation neutron strain scanner. Journal of applied crystallography. 2006;39(6):812-25.

87.	axs B. D8 Discover with GADDs. 2012 [18/8/12]; Available from: http://www.bruker-axs.com/discover_with_gadds.html.

88.	Fitzpatrick ME, Fry AT, Holdway P, Kandil FA, Shackleton J, Suominen L. NPL Good Practice Guide No. 52: Determination of Residual Stress by X-ray Diffraction. 2002.

89.	nanofocus. uscan custom. 2012 [18/08/12]; Available from: http://www.nanofocus-us.com/uscan-custom.html?&L=2.

90.	Mathworks. MATLAB 7.10. Natick, MA.2010.

91.	Xiong YS, Kelleher J, Frankel PG, Withers PJ, editors. From surface profile to residual stress using the contour method. ICRS; 2008; Denver Colorado.

92.	Mathworks. Spline Toolbox. 2001; Available from: http://www.mathworks.com/products/splines/.

93.	SIMULIA. ABAQUS Software. Rising Sun Mills, 166 Valley Street, Providence, RI.2011.

94.	Bibby GP. Compressor Engineering SCO3 Radial Displacement Plot Facility. 14 ed: Rolls-Royce; 1998.

95.	Williams S, Machlachan D. SC03 Creep and Plasticity. 2012.

96.	Basoalto H, Vermeulen B, Brooks JW, Coventry G, Williams S, Mason-Flucke J, et al. A new hyberbolic tangent modelling approach for the creep behaviour of the single crystal nickel-based superalloy CMSX4. Superalloys; Pittsburgh: TMS; 2008. p. 515-20.

97.   SIMULIA. iSight Optimization software. Rising Sun Mills, 166 Valley Street, Providence, RI.2011.

98.   Mróz Z. On the description of anisotropic workhardening. Journal of the Mechanics and Physics of Solids. 1967;15(3):163-75.

99.   Egerton RF. Physical Principles of Electron Microscopy: An Introduction to TEM, SEM, and AEM: Springer; 2005.

100.   Decker R. The evolution of wrought age-hardenable superalloys. JOM Journal of the Minerals, Metals and Materials Society. 2006;58(9):32-6.